

AD-A173 185

PIEZOELECTRIC AND ELECTROSTRICTIVE MATERIALS FOR
TRANSDUCER APPLICATIONS(U) PENNSYLVANIA STATE UNIV
UNIVERSITY PARK MATERIALS RESEARCH LAB

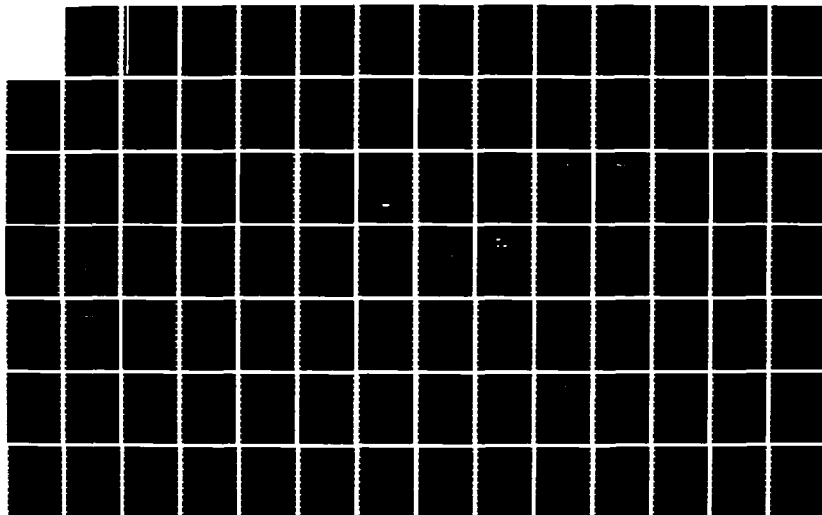
174

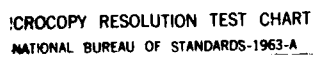
UNCLASSIFIED

L E CROSS ET AL JUL 86 N00014-82-K-0339

F/G 9/1

NL





PHOTOCOPY RESOLUTION TEST CHART
NATIONAL BUREAU OF STANDARDS-1963-A

AD-A173 185

**PIEZOELECTRIC AND ELECTROSTRICTIVE MATERIALS
FOR TRANSDUCER APPLICATIONS**

Period January 1 to December 31, 1985

Annual Report

OFFICE OF NAVAL RESEARCH

Contract No. N00014-82-K0339

DTIC
ELECTE
OCT 21 1986
S D

APPROVED FOR PUBLIC RELEASE - DISTRIBUTION UNLIMITED

Reproduction in whole or in part is permitted for
any purpose of the United State Government

L.E. Cross
R.E. Newham
G.R. Barsch
J.V. Biggers

July 1986

DTIC FILE COPY



THE MATERIALS RESEARCH LABORATORY

THE PENNSYLVANIA STATE UNIVERSITY

UNIVERSITY PARK, PENNSYLVANIA

86 10 21_014

AD-A173185

SECURITY CLASSIFICATION OF THIS PAGE

REPORT DOCUMENTATION PAGE

1a. REPORT SECURITY CLASSIFICATION		1b. RESTRICTIVE MARKINGS	
2a. SECURITY CLASSIFICATION AUTHORITY		3. DISTRIBUTION/AVAILABILITY OF REPORT Reproduction in whole or in part is permitted for any purpose of the United States Government.	
2b. DECLASSIFICATION/DOWNGRADING SCHEDULE		5. MONITORING ORGANIZATION REPORT NUMBER(S)	
4. PERFORMING ORGANIZATION REPORT NUMBER(S) N00014-82-K0339		7a. NAME OF MONITORING ORGANIZATION	
6a. NAME OF PERFORMING ORGANIZATION Materials Research Laboratory	6b. OFFICE SYMBOL (If applicable)	7b. ADDRESS (City, State and ZIP Code)	
6c. ADDRESS (City, State and ZIP Code) The Pennsylvania State University University Park, PA 16802		8. PROCUREMENT INSTRUMENT IDENTIFICATION NUMBER	
8a. NAME OF FUNDING/SPONSORING ORGANIZATION Office of Naval Research	8b. OFFICE SYMBOL (If applicable)	10. SOURCE OF FUNDING NOS.	
8c. ADDRESS (City, State and ZIP Code) 619 Ballston Tower 800 W. Quincy Street Arlington, VA 22217		PROGRAM ELEMENT NO.	TASK NO.
11. TITLE (Include Security Classification) Piezoelectric and Electrostrictive Mtls. for Transducer Applications		PROJECT NO.	WORK UNIT NO.
12. PERSONAL AUTHOR(S) L.E. Cross, R.E. Newham, G.R. Barsch, J.V. Biggers			
13a. TYPE OF REPORT Annual	13b. TIME COVERED FROM 1/85 TO 12/85	14. DATE OF REPORT (Yr., Mo., Day)	15. PAGE COUNT
16. SUPPLEMENTARY NOTATION <i>Fig 10 to the minus 100</i>			
17. COBATI CODES		18. SUBJECT TERMS (Continue on reverse if necessary and identify by block number)	
FIELD	GROUP	SUB. GR.	
19. ABSTRACT (Continue on reverse if necessary and identify by block number) This annual report documents work carried out on the third year (January 31, 1985 to February 1, 1986) under ONR Contract No. N00014-82-K-0399, "Piezoelectric and Electrostrictive Materials for Transducer Applications." On the topic of piezoelectric composites, work over the year has focused primarily upon materials with 0:3 phase connectivity. Using chemically co-precipitated powders with high purity and surface perfection, it has been possible to raise the poling field substantially and realize markedly improved properties in lead titanate based materials. X-ray measurements confirm excellent poling and the d_{33} figure of merit of $4200 \times 10^{-15} \text{ m}^2/\text{V}$ is comparable to the best PZT materials. Work on fired composites which use a low temperature pre-firing yield materials with high d_{33} and g_h values which pole at low fields. New studies of piezoelectrics generated using paint technology permit surprisingly high powder loading and show promising properties for large area receptors. Modelling studies of 'Safari' type 3:1 and 3:2 composites using			
20. DISTRIBUTION/AVAILABILITY OF ABSTRACT UNCLASSIFIED/UNLIMITED <input type="checkbox"/> SAME AS RPT. <input type="checkbox"/> DTIC USERS <input type="checkbox"/>		21. ABSTRACT SECURITY CLASSIFICATION	
22a. NAME OF RESPONSIBLE INDIVIDUAL	22b. TELEPHONE NUMBER (Include Area Code)	22c. OFFICE SYMBOL	

19. Abstract

finite element methods show excellent agreement with measured properties and provide new insights into complex stress distributions in Holey composites. To explore the possibility of patterning ceramics by semiconductor type techniques, etches have been explored for PZT family materials and photo resist defined structures have been produced.

In electrostriction, the basic theoretical work has continued upon CaF_2 , SrF_2 and BaF_2 . Good agreement is found for calculations of third order elastic constants, and for hydrostatic electrostriction, but Q_{11} and Q_{12} show large discrepancies with both theoretical models tried. Experimental studies have now moved to glass systems and new measurements have been made on sodium trisilicate, sodium aluminosilicate and on borosilicate glasses.

Practical electrostrictor work has concentrated on high permittivity relaxor compositions contributing new understanding to the superparaelectric model, including a new and logical explanation for the aging effects in MnO doped lead magnesium niobates. New work exploring techniques to stabilize the perovskite phase in lead zinc niobate:lead titanate compositions near to the morphotropic phase boundary have shown that very small additions of BaTiO_3 will stabilize the structure and materials superior to PbTiO_3 for actuators have now been produced.

Conventional piezoelectrics in the PZT family continue to be the object for phenomenological theoretical study with emphasis now upon the single cell:multicell transition in the PbZrO_3 rich rhombohedral ferroelectric compositions. The new model now takes account of both electrostrictive strain due to polarization, and rotostriction due to tilts in the oxygen octahedron network. The model also addresses the problem of the tricritical behavior in the 8 mole% PbTiO_3 composition.

Anisotropic materials in the doped lead titanate family are under study in cooperation with North American Philips Corporation. The latest work shows that complex dielectric elastic and PIEZOELECTRIC constants are needed in order to quantitatively describe the resonance behavior and that the zero values of d_{31} evident at certain temperatures are due to a decrease to zero and a change of sign in the real part of d_{31} for these systems.

Associated programs have explored crystal growth of KInF_3 and KlgF_3 , growth of tungsten bronze crystals in the $\text{Pb}_{1-x}\text{Ba}_x\text{NbO}_6$ solid solution field and the flux growth of $\text{PbZn}_{1/3}\text{Nb}_{2/3}\text{O}_3$ perovskites.

Program faculty have also been involved with work on the polar glass ceramics in the fresnoite family, and with sol-gel preparation, chemical co-precipitation and hydrothermal methods for preparation of perovskite structures powders.

TABLE OF CONTENTS

	Page
1.0 INTRODUCTION.	1
2.0 PIEZOELECTRIC COMPOSITES.	1
2.1 Introduction	1
2.2 Poling Studies on 0:3 PT:Polymer Composites.	1
2.3 Fired Composites	2
2.4 Piezoelectric Paints	2
2.5 Finite Element Modelling of Composites	2
2.6 Composite Sound Absorbers.	3
2.7 Etched PZT Structures.	3
3.0 ELECTROSTRICTION.	3
3.1 Basic Theory	3
3.2 Basic Experiments.	5
3.3 Practical Electrostrictors	6
3.3.1 Relaxor Ferroelectrics (Theory)	6
3.3.2 Relaxor Ferroelectrics (Measurements)	6
3.3.3 Relaxor Ferroelectrics (Aging).	6
3.3.4 Relaxor Ferroelectrics (New Compositions)	8
4.0 CONVENTIONAL PIEZOELECTRIC CERAMICS	8
4.1 Phenomenological Theory.	8
4.2 Anisotropic Piezoceramics.	9
5.0 ASSOCIATED PROGRAMS	9
5.1 Preparative Studies.	9
5.1.1 Single Crystals	9
5.1.2 Glass Ceramics.	10
5.1.3 Ceramics.	11
6.0 PUBLICATIONS, PRESENTATIONS, HONORS AND AWARDS.	11
6.1 Publications	11
6.2 Presentations at National and International Meetings	15
6.2.1 Invited Papers.	15
6.2.2 Contributed Papers.	16
6.3 Honors, Awards, Prizes	19
6.4 Degrees Earned	20
6.4.1 Graduate Thesis Project	20
6.4.2 Undergraduate Thesis Projects	20



des	
Dist	Avail and/or Special
A-1	

TABLE OF CONTENTS (Continued)

	<u>Page</u>
6.5 Collaboration and Interaction with Other Institutions.	20
6.6 Patent Disclosures	21
6.7 Applied Science Apprenticeships.	21

APPENDICES

1.0 INTRODUCTION

This annual report documents the work accomplished on the third year (January 31, 1985 to February 1, 1986) under ONR Contract No. N00014-82-K0339 "Piezoelectric and Electrostrictive Materials for Transducer Applications." It has become customary to document the work largely through reprints and preprints of papers published by investigators on the program and this method is continued in the current report. To supplement this large assemblage which is carried in the technical appendices, a brief overview summary is given which highlights the points of major progress. To improve convenience in the use of the report which is now circulated to more than 160 users both summary and appendices are divided in four major topic areas.

1. Piezoelectric Composites
2. Electrostrictive Materials
3. Conventional Piezoelectric Ceramics
4. Associated Programs

2.0 PIEZOELECTRIC COMPOSITES

2.1 Introduction

Over the current year more emphasis has been placed upon the 0:3 composites. Following the work of G. Giniewicz it became clear that very significant improvement could be made by changing to a lower permittivity ferroelectric phase, while the parallel studies in the Group by G.A. Sa-Gong underscored the cardinal importance of the poling process in realizing improved 0:3 materials.

2.2 Poling Studies on 0:3 PT:Polymer Composites

Over the current contract year, it has become clear that not only is the composition of the piezoelectric filler powder quite critical in achieving good poling behavior, but also the surface perfection is similarly most

important. Powders produced by comminution generally have a damaged surface layer which for some reason inhibits the poling and reduces the breakdown field of the composite. Using carefully chemically co-precipitated powders d_{33} values greater than 60 pC/N have been realized at poling fields ~ 100 kV/cm giving materials with $d_h g_h \sim 4200 \times 10^{-15} \text{ m}^2/\text{N}$. For these composites, recent x-ray studies suggest that the poling is better than the optimum 90° cone for a tetragonal ferroelectric symmetry so that we may be achieving particle rotation at these very high field levels.

2.3 Fired Composites

A new and simple method has been developed for forming 0:3 composites with loadings of piezoelectric powder phase in excess of 70 volume% by using a low temperature firing step on the shaped powder, followed by a post impregnation with the polymer. Results with PbTiO_3 powders are most encouraging giving d_{33} values of 70 pC/N and g_h values above $70 \cdot 10^{-3} \text{ Vm/N}$. Poling is now possible at much lower fields (less than 50 kV/cm).

2.4 Piezoelectric Paints

0:3 composites have been prepared from water-based methacrylic copolymer emulsions and various PZT, PbTiO_3 and $(\text{PbBi})(\text{TiFe})\text{O}_3$ piezoelectric powder compositions. A typical paint base which includes surfactants and rheology control agents was used. Results with the lead titanate filler show the possibility of achieving a 60 volume% loading, d_{33} values of 35 pC/N and $d_h g_h$ values above $1,000 \cdot 10^{-15} \text{ m}^2/\text{N}$.

2.5 Finite Element Modelling of Composites

In conjunction with the NRL Washington, a significant effort has been expended to develop finite element methods to model more precisely the stress and field distribution in 3:1 and 3:0 composite structures. For the 3:1

"Safari" type materials, calculation of the hydrostatic response show good Safari agreement with experimental measurement. Similarly in 3:0 'holey' composites, the modelling has produced new insights into the complex stress distributions which will be of major help in refinement of the design of these systems.

2.6 Composite Sound Absorbers

The emphasis of this study has been to set up the experimental techniques for exploring sound absorption and damping in composite materials so as to be able to sort out and quantify the additional absorption mechanisms which should be available in ferroic combinations.

2.7 Etched PZT Structures

The objective of these studies are to develop chemical etchants and etching techniques which will permit the development of patterned structures in PZT ceramics. Photo-resist techniques are being explored for masking, and acid etches based on HCl, HNO₃ and H₃PO₄ are being examined for the uniformity of etching in both poled and unpoled materials.

3.0 ELECTROSTRICTION

3.1 Basic Theory

In view of the success last year in measuring the full family of electrostriction constants Q_{11} , Q_{12} and Q_{44} for the fluorite structure halides CaF_2SrF_2 and BaF_2 effort was concentrated upon using the shell model theories of Axe (1965) and of Catlow and Nargett (1973) to calculate the electrostriction constants. A comparison of experimental and theoretical their order elastic (T.O.E.) constants and electrostriction (E.S.) constants is given in Tables 3.1 and 3.2. It is evident that for both T.O.E. and E.S. constants, the coefficients are only moderately model dependent. There is

Table 3.1. Third Order Elastic Constant (in 10^{10} N/m²) for CaF₂, SrF₂, BaF₂.

		C ₁₁₁	C ₁₁₂	C ₁₂₃	C ₁₄₄	C ₁₆₆	C ₄₅₆
CaF ₂	Exp. ^a	-124.6	-40.0	-25.4	-12.4	-21.4	-7.5
	Model A	-95.5	-44.2	-27.9	-11.4	-25.3	-9.1
	Model B	-107.8	-33.8	-17.5	-10.5	-24.2	-7.9
SrF ₂	Exp. ^b	-82.1	-30.9	-18.1	-9.5	-17.5	-4.2
	Model A	-68.6	-36.5	-23.7	-8.8	-19.2	-6.0
	Model B	-76.7	-31.4	-18.6	-8.7	-18.0	-4.4
BaF ₂	Exp. ^c	-58.4	-29.9	-20.6	-12.1	-8.9	-2.7
	Model A	-47.0	-32.9	-23.1	-5.3	-12.9	-1.7
	Model B	-54.6	-28.4	-18.5	-5.4	-11.8	-1.8

^aAlterowitz and Gerlich (1969)

Model A: Axe (1965);

^bAlterowitz and Gerlich (1970)

Srinivasan (1968)

^cGerlich (1968)

Model B: Batlow and Norgett (1973)

Table 3.2. Electrostriction Coefficients (in m⁴/C²) for CaF₂, SrF₂ and BaF₂.

		Q ₁₁	Q ₁₂	Q ₄₄	Q _h [*]	Q _s ^{**}
CaF ₂	Exp. ^a	-.563	+.499	+.546	+.435	-1.062
	Model A	+.218	+.149	+.459	+.516	+.069
	Model B	+.129	+.12		+.379	+.019
SrF ₂	Exp. ^a	-.588	+.524	+.664	+.490	-1.082
	Model A	+.252	+.154	+.474	+.559	+.098
	Model B	+.162	+.100		+.363	+.062
BaF ₂	Exp. ^a	-.384	+.442	+.535	+.500	-0.826
	Model A	+.242	+.115	+.454	+.473	+.128
	Model B	+.202	+.041		+.284	+.161

$$^*Q_h = Q_{11} + 2Q_{12}$$

$$^{**}Q_s = Q_{11} - Q_{12}$$

^aMeng, Sun and Cross (1984)

Model A: Axe (1965); Srinivasan [corrected] (1968).

Model B: Catlow and Norgett (1973).

fair to good agreement in all T.O.E. constants and for the hydrostatic electrostriction $Q_h = Q_{11} + 2Q_{12}$ and for Q_{44} , but Q_{11} and Q_{12} show large discrepancies in both magnitude and sign. Possible causes of the present discrepancies may be the neglect of many body interactions, the approximate nature of the Born-Mayer potential used, anisotropy in the electronic polarizability and perhaps also the effects of temperature. In the future it is proposed to explore the effect of short range three body interactions and to look at mode softening effects in perovskite oxides and fluorides.

3.2 Basic Experiments

While the efforts are in progress to grow larger halide perovskite crystals for electrostriction measurements, it was proposed to use the compressometer to explore electrostriction in silicate glass. An advantage for these measurements is that because of the ∞ fold rotational symmetry in glass there are only two independent electrostriction constants Q_{11} and Q_{12} . Q_{11} may be measured directly in the compressometer then Q_{12} deduced from the hydrostatic data $Q_h = Q_{11} + 2Q_{12}$. Measurements on sodium trisilicate and sodium aluminosilicate glasses show that there is a frequency dependence of Q_{11} associated with sodium ion motion, which is more severe in the alkali silicate, but less evident in the aluminosilicate presumably due to the more open network in the modified glass. An unexpected result has come from recent measurements on a Corning borosilicate (707) glass which gives Q_{11} of opposite sign to the other two silicates. Clearly further work to identify the possible roles of network modifiers in silicates upon both the magnitude and sign of electrostriction is now called for.

3.3 Practical Electrostrictors

3.3.1 Relaxor Ferroelectrics (Theory)

Last year (1984-85) we made a major breakthrough in understanding the polarization processes in relaxor ferroelectrics. By combining data from order:disorder studies, thermal expansion and optical birefringence and electrostriction measurements, it was possible to demonstrate the superparaelectric character.

This year, in a second major forward step, it has become clear that the difference between local symmetry at the polar micro-region and the global symmetry of the whole crystals must relieve the Devonshire requirement of completely equivalent polar orientations (Fig. 3.1).

With this new realization, it becomes possible to explain:

- (a) The poling:depoling behavior of relaxor PLZTs.
- (b) Aging effects in PLZTs and in PMN relaxors.
- (c) Observations on micro-domains by TEM.
- (d) Some grain size effects in PLZTs.

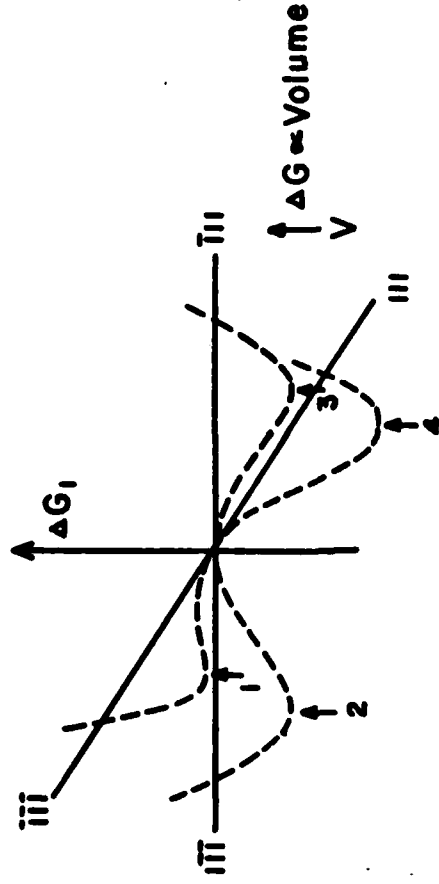
3.3.2 Relaxor Ferroelectrics (Measurements)

New measurements of direct electrostriction in pure lead magnesium niobate have been used together with earlier single crystal data to define a completely self consistent family of electrostriction constants. An apparent temperature dependence of the converse effect measurements has been traced to the temperature dependence of the relaxation behavior and is eliminated by extrapolating all data to very low frequency (equilibrium).

3.3.3 Relaxor Ferroelectrics (Aging)

Extensive studies of dielectric aging in pure and doped lead magnesium niobate and PMN:lead titanate solid solutions has shown that in carefully prepared stoichiometric PMN and PMN:PT, no aging occurs even at temperatures

Model for a Relaxor Ferroelectric



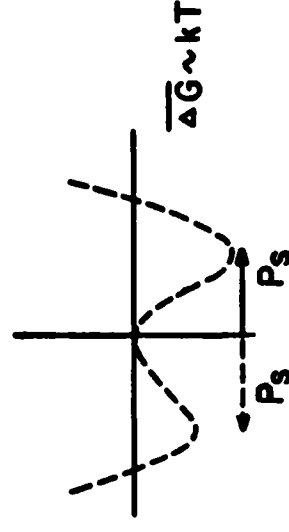
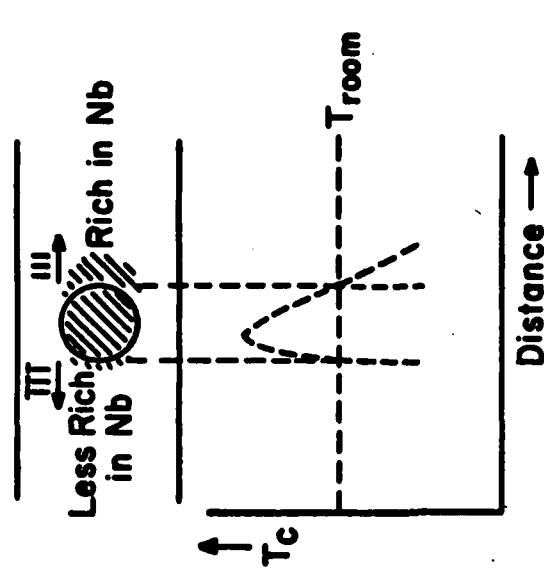
$$\text{Volume} \sim (200 \text{ \AA})^3 \quad \Delta G \sim 5kT$$

In perfect single crystal symmetry dictates

all $\langle \eta \rangle$ directions are equivalent

\therefore Minima 1, 2, 3, 4 are identical.

Two Dimensional Model for Real Relaxor



Spends less time along η well is less deep.

Spends longer time along η well is deeper.

Figure 3.1

below the Curie maximum. In doped or in non-stoichiometric compositions, however, an aging almost exactly similar to that in PLZT relaxor compositions, i.e. a major decrease in the frequency dependent (dispersive) part of the permittivity both at and above the aging temperature, but complete recovery of dispersion at lower temperatures. This ability to control and eliminate aging is clearly of major importance for the use of ferroelectric relaxor compositions in actuators for surface deformable mirrors.

3.3.4 Relaxor Ferroelectrics (New Compositions)

New compositions in the $\text{BaTiO}_3:\text{PbZn}_{1/3}\text{Nb}_{2/3}\text{O}_3\text{PbTiO}_3$ family are being investigated for application in high strain actuators. In compositions in which just enough of the larger Ba^{2+} cation is used to stabilize against pyrochlore formation, the PbTiO_3 content can be used to tune the T_c to obtain compositions with high strain capability superior to the PMN:PT family. These materials are also of major interest for their high field dielectric properties.

4.0 CONVENTIONAL PIEZOELECTRIC CERAMICS

4.1 Phenomenological Theory

Work has continued in cooperation with Dr. R. Halemene at Bell Telephone Laboratories to extend and refine the phenomenological equations to describe the PZT family of ferroelectrics. Concentration this year has been upon the single cell:multicell phase change associated with the 'rocking' transition of the oxygen octahedra framework and with making the model consistent with the observed tricritical behavior at T_c for composition close to 8 mole% PbTiO_3 in PbZrO_3 . Using a function in which the full family of parameters up to sixth order in both polarization and oxygen octahedron tilt angle are permitted, it has been possible to devise parameter which fit well with measured phase

stability. The full family of shape changes is now being explored by using the permitted electrostriction and rotostriction parameters.

4.2 Anisotropic Piezoceramics

The effort here is in close cooperation with North American Philips Company and has been concerned with investigations of the nature of the very high piezoelectric anisotropy in lead titanate based compositions doped with calcium or samarium. New more detailed measurements of the transverse resonance indicate that it is necessary to include both real and imaginary components in dielectric, elastic and piezoelectric response to adequately describe the phenomenon. From this new analysis, it is clear that d_{31}' changes sign at the temperature where k_t goes to zero, but that d_{31}'' remains finite. In the calcium containing family new compositions have been explored which maintain $k_t = 0$ but permit higher levels of s_{33} .

5.0 ASSOCIATED PROGRAMS

Faculty upon the ONR sponsored program also have association with a number of other sponsored programs and are involved in joint work to further these studies.

5.1 Preparative Studies

5.1.1 Single Crystals

Work has continued on improving the bridgeman growth of KMnF_3 and KMgF_3 and samples with dimensions large enough for compressometer studies of the electrostriction parameters are now to hand.

For the $\text{Pb}_{1-x}\text{Ba}_x\text{Nb}_2\text{O}_6$ tungsten bronze compositions, work has been focused upon the compositions on the orthorhombic side of the morphotropic composition near the $\text{Pb}_{0.6}\text{Ba}_{0.4}\text{Nb}_2\text{O}_6$ composition.

Early dielectric measurements upon these crystals have shown that the high ϵ_{33} which occurs over the whole temperature range below T_c freezes in with RELAXATION CHARACTER at temperatures below -100°C . New low temperature measurements on the compositions on the tetragonal side of the boundary confirm that the high ϵ_{11} in these compositions also freezes in at low temperature.

We believe that this is the first clear evidence of a strong relaxation component in these tungsten bronzes in the ferroelectric ordered state, and may give very strong supporting evidence to the hypothesis that the local symmetry may be lowered by composition heterogeneity.

Work has continued on the flux growth of $\text{PbZn}_{1/3}\text{Nb}_{2/3}\text{O}_3$ crystals using excess PbO and B_2O_3 fluxes, and is being extended to compositions in the $\text{PbZn}_{1/3}\text{Nb}_{2/3}\text{O}_3:\text{PbTiO}_3$ solid solution system to generate crystals with compositions close to the morphotropic phase boundary.

5.1.2 Glass Ceramics

In cooperation with NSF and ARO sponsored programs, analysis has continued on the properties of the fresnoite analogue polar glass ceramics. Compositions in the barium titanium silicate family have been shown to have SAW properties which can be trimmed to zero temperature coefficient of delay by suitable doping of the glass phase.

In the barium titanium germanate family, there is now good evidence of a ferroelastic:ferroelectric first order phase change near 20°C on heating and -50°C on cooling. The transition is interesting in that the ferroelectric phase is one of the few known examples of a reorientable but irreversible phase emergent from a polar point group as prototype.

5.1.3 Ceramics

Extensive preparative studies have been required to develop the sol-gel methods needed to produce PZTs of precise stoichiometry for our phase diagram studies. Cooperative work with Rutgers University initiated the exploration of sol-gel prepared lead titanate for composite powder preparation, and lead on to our own studies of chemical co-precipitation, and hydrothermal methods for the preparation of filler powders.

Over the year we have been going through an extensive re-equipment of our furnace room, to put all furnaces onto centralized microprocessor control with some of the versatility of our fast firing system.

6.0 PUBLICATIONS, PRESENTATIONS, HONORS, AND AWARDS

6.1 Publications

1. R.E. Newnham, "Composite Electroceramics," Ferroelectrics (Special Issue).
2. R.E. Newnham, "Ferroelectric Composites," Proc. Sixth International Meeting on Ferroelectricity, Jpn. J. Appl. Phys. 24(24-2):16-17 (1985).
3. R.Y. Ting, A. Halliyal and A.S. Bhalla, "New Materials for Hydrophone Applications-Single Crystals and Polar Glass Ceramics," Proc. Sixth International Meeting on Ferroelectricity, Jpn. J. Appl. Phys. 24(24-2):982-983 (1985).
4. G. Sa-Gong, A. Safari, S.J. Jang and R.E. Newnham, "Poling Flexible Piezoelectric Composites," Ferroelectrics Letters 5:131-142 (1986).
5. J. Runt, A. Safari, E.C. Galgoci and R.E. Newnham, "The Influence of Interfacial Adhesion on the Piezoelectric Response of Electroceramic/Polymer Composites," Ferroelectrics Letters 5:15-20 (1985).

6. S. DaVanzo, W. Carlson, R.E. Newnham and A. Safari, "Finite Element/Different Modeling of Electroceramics,"
7. A. Safari, G. Sa-Gong, J. Giniewicz and R.E. Newnham, "Composite Piezoelectric Sensors," Proc. Symposium on Tailoring Multiphase and Composite Ceramics (in press).
8. S. Pilgrim, R.E. Newnham, T.R. Gururaja and A. Safari, "Piezoelectric Ceramic-Polymer Composites as Transducers and Vibration Absorbers," American Chemical Society, Rubber Division.
9. M.J. Haun and R.E. Newnham, "An Experimental and Theoretical Study of 1-3 and 1-3-0 Piezoelectric PZT-Polymer Composites for Hydrophone Applications," Ferroelectrics (Special Issue).
10. M.J. Haun, W.A. Schulze and R.E. Newnham, "1-2-3 and 1-2-3-0 Piezoelectric Composites for Hydrophone Applications,"
11. E.C. Galgoci, D.G. Schreffler, B.P. Devlin and J. Runt, "Pyroelectricity in 1-3 PZT/Polymer Composites," Ferroelectrics (Special Issue).
12. K.A. Hu, J. Runt, A. Safari and R.E. Newnham, "Electroceramic-Polymer Composite Thermistors," Ferroelectrics (Special Issue).
13. Jayne R. Giniewicz, "(Pb,Bi)(Ti,Fe)O₃/Polymer 0-3 Composite Materials for Hydrophone Applications," Master of Science Degree, The Pennsylvania State University (August, 1985).
14. P. Asadipour, U. Kumar, S.J. Jang, A.S. Bhalla and L.E. Cross, "Electrostriction Properties of Oxygen Octahedron Ferroelectrics," Proc. Sixth International Meeting on Ferroelectricity, Jpn. J. Appl. Phys. 24(24-2):742-743 (1985).
15. H.M. Chan, M.P. Harner, A. Bhalla and L.E. Cross, "TEM of the Relaxor Material Pb(Sc_{0.5}Ta_{0.5})O₃," Proc. Sixth International Meeting on Ferroelectricity, Jpn. J. Appl. Phys. 24(24-2):550-552 (1985).

16. W.Y. Pan, E. Furman, G.O. Dayton and L.E. Cross, "Lead Titanate Relaxor Ferroelectric Ceramics," *J. Am. Ceram. Soc.* (submitted).
17. W.Y. Pan and L.E. Cross, "Direct and Converse Electrostrictive Effects in $\text{Pb}(\text{Mg}_{1/2}\text{Nb}_{2/3})\text{O}_3$ Ceramics," *J. Mat. Sci.* (submitted).
18. W.Y. Pan, P. Moses and L.E. Cross, "Antiferroelectric to Ferroelectric Switching in Lead Zirconate Titanate Stannate Ceramics," *Materials Letters* (submitted).
19. T.R. Halemane, M.J. Haun, L.E. Cross and R.E. Newnham, "Ferroelectric Phase Transitions in PZT with Octahedral Tilts," *Proc. Sixth International Meeting on Ferroelectricity, Jpn. J. Appl. Phys.* 24(24-2):212-214 (1985).
20. M.J. Haun, T.R. Halemane, R.E. Newnham and L.E. Cross, "A Phenomenological Theory for the $\text{PbZrO}_3\text{:PbTiO}_3$ Solid Solution System with the Spontaneous Polarization and Oxygen Octahedral Tilt Angle as Order Parameters," *Proc. Sixth International Meeting on Ferroelectricity, Jpn. J. Appl. Phys.* 24(24-2):209-211 (1985).
21. A. Amin and L.E. Cross, "Effect of Electric Boundary Conditions on Morphotropic $\text{Pb}(\text{Zr,Ti})\text{O}_3$ Piezoelectrics," *Proc. Sixth International Meeting on Ferroelectricity, Jpn. J. Appl. Phys.* 24(24-2):229-231 (1985).
22. W.R. Xue, J.N. Kim, S.J. Jang, L.E. Cross and R.E. Newnham, "Temperature Behavior of Dielectric and Electromechanical Coupling Properties of Samarium Modified Lead Titanate Ceramics," *Proc. Sixth International Meeting on Ferroelectricity, Jpn. J. Appl. Phys.* 24(24-2):718-720 (1985).
23. J.N. Kim, M.J. Huan, S.J. Jang and L.E. Cross, "Low Temperature Dielectric and Piezoelectric Properties of Doped PZT Ceramics,"
24. D.L. Monroe, J.B. Blum and A. Safari, "Sol-Gel Derived PbTiO_3 -Polymer Piezoelectric Composites," *Ferroelectrics Letters* 5:39-46 (1986).

25. A. Halliyal, A.S. Bhalla, S.A. Markgraf, L.E. Cross and R.E. Newnham, "Unusual Pyroelectric and Piezoelectric Properties of Fresnoite ($\text{Ba}_2\text{TiSi}_2\text{O}_8$) Single Crystal and Polar Glass-Ceramics," Ferroelectrics 62:27-38 (1985).
26. A. Halliyal, A.S. Bhalla and L.E. Cross, "Phase Transitions, Dielectric, Piezoelectric and Pyroelectric Properties of Barium Titanium Germanate $\text{Ba}_2\text{TiGe}_2\text{O}_8$ Single Crystals," Ferroelectrics 62:3-9 (1985).
27. S.A. Markgraf, A. Halliyal, A.S. Bhalla, R.E. Newnham and C.T. Prewitt, "X-Ray Structure Refinement and Pyroelectric Investigation of Fresnoite, $\text{Ba}_2\text{TiSi}_2\text{O}_8$," Ferroelectrics 62:17-26 (1985).
28. A. Halliyal, A.S. Bhalla, L.E. Cross and R.E. Newnham, "Dielectric, Piezoelectric and Pyroelectric Properties of $\text{Sr}_2\text{TiSi}_2\text{O}_8$ Polar Glass-Ceramic: A New Polar Material," J. Mat. Sci. 20:3745-3749 (1985).
29. A.S. Bhalla, L.E. Cross and R.W. Whatmore, "Pyroelectric and Piezoelectric Properties of Lithium Tetraborate Single Crystal," Proc. Sixth International Meeting on Ferroelectricity, Jpn. J. Appl. Phys. 24(24-2):727-729 (1985).
30. C.F. Clark, W.N. Lawless and A.S. Bhalla, "Quantum Ferroelectricity in $(\text{Cd,Pb})_2(\text{Nb,Ta})_2\text{O}_7$," Proc. Sixth International Meeting on Ferroelectricity, Jpn. J. Appl. Phys. 24(24-2):266-268 (1985).
31. A.S. Bhalla, L.E. Cross and R.E. Newnham, "Glass Bonded Crystalline Boracite Composites for Pyroelectric Applications," Proc. Sixth International Meeting on Ferroelectricity, Jpn. J. Appl. Phys. 24(24-2):454-456 (1985).
32. S.W. Meeks, B.A. Auld and R.E. Newnham, "Ferroelastic Bubbles and Periodic Gratings in Neodymium Pentaphosphate," Proc. Sixth International Meeting on Ferroelectricity, Jpn. J. Appl. Phys. 24(24-2):568-570 (1985).

33. S.L. Swartz, A.S. Bhalla and L.E. Cross, "Low Temperature Dielectric Properties of SrTiO_3 Glass-Ceramics," Proc. Sixth International Meeting on Ferroelectricity, Ann. J. Appl. Phys. 24(24-2):979-981 (1985).
34. C.W. Nies, A. Safari, T.R. Gururaja and R.E. Newnham, "Measurement Method for Transducers for On-Line Sonication," Presented at 87th American Ceramic Society Annual Meeting,

6.2 Presentations at National and International Meetings

6.2.1 Invited Papers

1. R.E. Newnham, Ferroelectric Composites. IMF6, Kobe, Japan (Aug., 1985).
2. L.E. Cross, Electroactive Ceramics and Composites. VI Whitney Symposium, Schenectady, NY (June, 1985).
3. R.E. Newnham, Electroceramic Composites. 2nd US:Japan Symposium on Dielectric and Piezoelectric Ceramics, Williamsburg, VA (Nov., 1984).
4. R.E. Newnham, Electroceramics. W. Coast Gordon Conference on Chemistry of Electronic Materials, La Jolla, CA (Feb., 1985).
5. R.E. Newnham, Piezoelectric Composites. Northern Ohio Section of the American Ceramic Society Outstanding Speaker Award Lecture (March, 1985).
6. R.E. Newnham, Active Vibration Absorbers. American Chemical Society, Rubber Division, San Francisco, CA (April, 1985).
7. T.R. Gururaja, Composite Piezoelectric Transducers for Ultrasonic Medical Imaging. 7th Annual Conference, Biomedical Division IEEE, Chicago, IL (Sept., 1985).
8. L.E. Cross, Active Electroceramic Composites. Penn State Meeting on Multiple Scattering of Waves in Discrete Random Media (June, 1985).
9. R.E. Newnham, Holey Crystals. American Crystallographic Assn. National Meeting, Stanford (Aug., 1985).

10. R.E. Newnham, Sensors, Transducers and Actuators. IEEE G.S.U. National Lectureship I, University of Texas, Austin (Sept., 1985).

6.2.2 Contributed Papers

1. M.J. Haun, T.R. Halemane, R.E. Newnham and L.E. Cross, "A Phenomenological Theory for the $\text{PbZrO}_3\text{:PbTiO}_3$ Solid Solution System." Presented at the 87th Annual Meeting of the American Ceramic Society, Electronics Division, Cincinnati, OH (May, 1985).
2. M.J. Haun, T.R. Halemane, R.E. Newnham and L.E. Cross, "A Phenomenological Theory for the $\text{PbZrO}_3\text{:PbTiO}_3$ Solid Solution System." Presented at the Sixth International Meeting on Ferroelectricity, Kobe, Japan (August, 1985).
3. T.R. Halemane, M.J. Haun, L.E. Cross and R.E. Newnham, "Ferroelectric Phase Transitions in PZT with Octahedral Tilts." Presented at the Sixth International Meeting on Ferroelectricity, Kobe, Japan (August, 1985).
4. C.W. Nies, A. Safari, T.R. Gururaja and R.E. Newnham, "Measurement Methods for Transducers for Sonication Applications." Presented at the American Ceramic Society 87th Annual Meeting (May 6, 1985).
5. A. Safari, G. Sa-Gong, J. Giniewicz and R.E. Newnham, "Composite Piezoelectric Sensors." Presented at the Symposium on Tailoring Multiphase and Composite Ceramics. The Pennsylvania State University (July, 1985).
6. S.M. Pilgrim, R.E. Newnham and T.R. Gururaja, "Acoustic Properties of Some Piezoelectric Ceramic-Polymer Composites." Presented at the 87th American Ceramic Society, Cincinnati, OH (May, 1985).

7. C.M. Pilgrim, R.E. Newnham, T.R. Gururaja and A. Safari, "Piezoelectric Ceramic-Polymer Composites as Transducers and Vibration." Presented at the 87th American Ceramic Society Meeting Rubber Division, Los Angeles, CA (April, 1985).
8. A.E. Semple, S.M. Pilgrim, W. Thompson, Jr. and R.E. Newnham, "Wave Absorption in Piezoceramic-Polymer Composites." Presented at the 21st Multiphase Ceramic Conference, The Pennsylvania State University (August, 1985).
9. S.M. Pilgrim, et al. Poster Presentation on "Wave Abs. in Piezoceramic-Polymer Comp." 1st Annual Polymer Symposium, The Pennsylvania State University, Pennsylvania Ceramic Society (October, 1985).
10. S. Markgraf, A.S. Bhalla and R.E. Newnham, "Polar Properties of Hemimorphite." ACA Annual Meeting, Collected Abstracts, 69 (1985).
11. B.N.N. Achar and G.R. Barsch, "Static Shell Model Calculation of Electrostriction for CaF_2 ." 1984 Annual Meeting of the Southeastern Section of the American Physical Society, Memphis, TN (October 25-27, 1984).
12. K.A. Hu, D. Moffatt, J. Runt, A. Safari and R.E. Newnham, "Electroceraic-Polymer Composite Thermistors." Penn State Polymer Symposium (July, 1985).
13. A. Safari, J. Giniewicz, T.R. Gururaja, J. Runt and R.E. Newnham, "Piezoelectric Polymer Composite Transducers." Penn State Polymer Symposium (July, 1985).
14. E.C. galgoci and J. Runt, "Interfacial Adhesion in Polymer/Electroceraic Composites." American Physical Society, Baltimore (1985).
15. B.S. Wen, S.J. Jang, L.E. Cross and A. Safari, "Composite Bimorph Structure." 87th Annual American Ceramic Society Meeting, Cincinnati, OH (1985).

16. G. Sa-Gong, A. Safari, S.J. Jang and R.E. Newnham, "Easily Poled Flexible Composite for Transducer Applications." 87th Annual American Ceramic Society Meeting, Cincinnati, OH (1985).
17. M.T. Lanagan, J.H. Kim, S.J. Jang and R.E. Newnham, "High Frequency Dielectric Properties of PbZrO_3 ." 87th Annual American Ceramic Society Meeting, Cincinnati, OH (1985).
18. K. Rittenmyer, A.S. Bhalla and L.E. Cross, "Determination of the Electrostriction Coefficients M_{11} , M_{12} and M_{44} for Single Crystals of Calcium Fluoride." American Ceramic Society (1985).
19. H.M. Chan, M.P. Harmer, A. Bhalla and L.E. Cross, "TEM of the Relaxor Material $\text{Pb}(\text{Sc}_{0.5}\text{Ta}_{0.5})\text{O}_3$." Proc. IMF6, Japan (August, 1985).
20. A.S. Bhalla, L.E. Cross and R.E. Newnham, "Glass Bonded Crystalline Boracite Composite for Pyroelectric Applications." Proc. IMF6, Japan (August, 1985).
21. A.S. Bhalla and L.E. Cross, "A Simple Phenomenological Approach to Evaluating Materials for Application in Pyroelectric Vidicons." Proc. IMF6, Japan (August, 1985).
22. N.S. Dalal, A.S. Bhalla and L.E. Cross, "EPR and Endor Investigations of Structural Change in Ionic Fluctuation in Phosphate and Arsenate Substituted TGS." Proc. IMF6, Japan (August, 1985).
23. A.S. Bhalla, L.E. Cross and R.W. Whatmore, "Pyroelectric and Piezoelectric Properties of Lithium Tetraborate Single Crystal." Proc. IMF6, Japan (August, 1985).
24. P. Asadipour, U. Kumar, S.J. Jang, A.S. Bhalla and L.E. Cross, "Electrostriction Properties of Oxygen Octahedron Ferroelectrics." Proc. IMF6, Japan (August, 1985).

25. R.Y. Ting, A. Halliyal and A.S. Bhalla, "New Materials for Hydrophone Applications - Single Crystals and Polar Glass Ceramics." Proc. IMF6, Japan (August, 1985).
26. C.F. Clark, W.N. Lawless and A.S. Bhalla, "Quantum Ferroelectricity in the $(\text{CdPb})_2(\text{NbTa})_2\text{O}_7$ System." Proc. IMF6, Japan (August, 1985).
27. A. Halliyal, A.S. Bhalla and L.E. Cross, "Phase Transitions, Dielectric Constant, Piezoelectric and Pyroelectric Properties of Barium Titanium Germanate $\text{Ba}_2\text{TiGe}_2\text{O}_8$ Single Crystals." 2nd U.S.:Japan Seminar on Electronic Ceramics, Williamsburg, VA (November 4-7, 1984).
28. J. McColl, L.J. Bowen, A. Halliyal and A.S. Bhalla, "Piezoelectric Applications of Glass Ceramics." 2nd U.S.:Japan Seminar on Electronic Ceramics, Williamsburg, VA (November 4-7, 1984).
29. C.W. Lee, L.J. Bowen, J.M. Browne, A. Halliyal, A.S. Bhalla and E. Ylo, "Acoustic Wave Properties of Fresnoite Glass-Ceramics." IEEE Ultrasonic Symposium, Dallas, TX (November 14-16, 1984).

6.3 Honors, Awards, Prizes

Dr. L.E. Cross

Elected Evan Pugh Professor of Electrical Engineering at Penn State.

Elected Fellow of the Optical Society of America.

Co-recipient of the Ross Coffin Purdy Award of the American Ceramic Society.

Nominated to the National Materials Advisory Board (NMAB) of the National Academy of Engineering.

Dr. R.E. Newnham

President of the American Crystallographic Association.

IEEE National Lecturer in Sonics and Ultrasonics.

6.4 Degrees Earned

6.4.1 Graduate Thesis Project

1. J.R. Giniewicz, "(Pb,Bi)(Ti,Fe)O₃/Polymer 0-3 Composite Materials for Hydrophone Applications." M.S. Thesis (May, 1985).

6.4.2 Undergraduate Thesis Projects

Graduated May, 1985

1. D. Moffatt, PZT-PZN Piezoelectric Ceramics.
2. Robert Naugler, Electrical and Structural Properties of SrPbO₃-BaPbO₃ Ceramics.
3. Lori Rohlfing, PFN Composition for Use as Hydrostatic Pressure Gage.
4. Walter Wright, Silver Iodide Composite Thermistors.
5. Eric Rothdeutsch, Electrical Characteristics of a Conductor-Filled Polymer: BaPbO₃ - Epoxy.

6.5 Collaboration and Interaction with Other Institutions

1. K. Rittenmyer, A.S. Bhalla and L.E. Cross, "Determination of the Electrostriction Coefficients M_{11} , M_{12} and M_{44} for Single Crystals of Calcium Fluoride." American Ceramic Society (with Navy, Orlando).
2. R.Y. Ting, A. Halliyal and A.S. Bhalla, "New Materials for Hydrophone Applications - Single Crystals and Polar Glass Ceramics." Proc. IMF6, Japan (August, 1985) (with Navy, Orlando).
3. H.M. Chan, M.P. Harmer, A. Bhalla and L.E. Cross, "TEM of the Relaxor Material Pb(Sc_{0.5}Ta_{0.5})O₃." Proc. IMF6, Japan (August, 1985) (with Lehigh University).
4. N.S. Dalal, A.S. Bhalla and L.E. Cross, "EPR and Endor Investigations of Structural Change in Ionic Fluctuation in Phosphate and Arsenate Substituted TGS." Proc. IMF6, Japan (August, 1985) (with University of West Virginia).

5. A.S. Bhalla, L.E. Cross and R.W. Whatmore, "Pyroelectric and Piezoelectric Properties of Lithium Tetraborate Single Crystal." Proc. IMF6, Japan (August, 1985) (with Plessey, Co.; U.K.).
6. C.F. Clark, W.N. Lawless and A.S. Bhalla, "Quantum Ferroelectricity in the $(\text{CdPb})_2(\text{NbTa})_2\text{O}_7$ System." Proc. IMF6, Japan (August, 1985) (with CeramPhysics, OH).

6.6 Patent Disclosures

1. M.J. Haun and R.E. Newnham, "Piezoelectric 1-3-0 Composites for Hydrophone Applications." Assignee: The Office of Naval Research.
2. M.J. Haun, W.A. Schulze and R.E. Newnham, "Transversely Reinforced 1-3 and 1-3-0 Piezoelectric Composites for Hydrophone Applications." Assignee: The Office of Naval Research.
3. J.R. Giniewicz, R.E. Newnham, A. Safari and L.E. Cross, " $(\text{Pb,Bi})(\text{Ti,Fe})\text{O}_3$ -Polymer Composites with 0-3 Connectivity for Transducer Applications." (Invention Disclosure - 4/13/84).
4. J.R. Giniewicz, A. Safari, R.E. Newnham and L.E. Cross, "Improved Piezoelectric Filler for Flexible Piezoelectric Composites." (Invention Disclosure - 6/17/85).

6.7 Applied Science Apprenticeships

It is the purpose of this program to provide opportunity for high school students to become acquainted, during their summer break, with the workings of a major research laboratory and the fascination of research and discover. The objective is to have a maximum of four students in this category who could work closely with the postdoctoral fellows and graduate assistants in the Materials Research Laboratory on problems associated with our ONR program in the Center for Dielectric Studies and on the program of research on Piezoelectric and Electrostrictive Materials for Transducer Applications.

These programs which encompasses the preparation, characterization, and measurement of properties of a wide range of new electroceramic and ceramic-plastic composites offer many opportunities in which the "extra pair of hands" and quick perceptions of a well motivated high school student provides invaluable assistance.

We believe that the relaxed atmosphere and constant interchange between faculty, postdoctoral fellows, graduate assistants, and technical aides, and the continuous presence of many eminent foreign visiting scientists provides a very stimulating environment for the young student who may be at a critical juncture in making decisions as to longer range career plans.

A secondary but not insignificant advantage of the program is in the additional component which it provides in the education of our graduate students. Most of these young men and women will go out into responsible positions in Government and Industry where they will be called upon to organize and supervise the work of many junior engineers and technicians. This program, which attaches the technical aid to a graduate assistant, gives him the chance to organize the work of a second person to speed his own program, but also the responsibility of the associated human problems of scheduling and humane management. We believe it has been a most valuable experience for the graduate assistants who have participated and has given them very useful insights into both the problems and the rewards of "people management."

For the last three years, we have developed a much closer relationship with the University's Upward Bound Program, who are able to draw well motivated black students from the Philadelphia School System. Over the years it has become our custom to issue each student participant a certificate on

completion of the term, at a small internal ceremony in MRL. Copies of certificates given to our last four successful apprentices are appended.

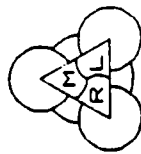
THE MATERIALS RESEARCH LABORATORY

PENNSYLVANIA STATE UNIVERSITY

1985

Office of Naval Research
Apprentice Program Certification
for successful completion of the 8 week project/study program
in Electronic Ceramics

Selena Brownfield



SEL
The Pennsylvania State University

THE MATERIALS RESEARCH LABORATORY

PENNSYLVANIA STATE UNIVERSITY

1985

Office of Naval Research
Apprentice Program Certification
for successful completion of the 8 week project/study program
in Electronic Ceramics

Dana Balthus



SEL
The Pennsylvania State University

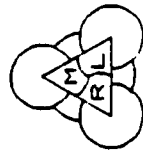
THE MATERIALS RESEARCH LABORATORY

PENNSYLVANIA STATE UNIVERSITY

1985

Office of Naval Research
Apprentice Program Certification
for successful completion of the 8 week project/study program
in Electronic Ceramics

Kathy Barlow



SEL
The Pennsylvania State University

THE MATERIALS RESEARCH LABORATORY

PENNSYLVANIA STATE UNIVERSITY

1985

Office of Naval Research
Apprentice Program Certification
for successful completion of the 3 week project/study program
in Electronic Ceramics

Kathy Barlow



SEL
The Pennsylvania State University

COMPOSITE ELECTROCERAMICS

R.E. Newnham

COMPOSITE ELECTROCERAMICS

R. E. NEWNHAM

*Materials Research Laboratory, Pennsylvania State University, University
Park, PA 16802 U.S.A.*

(Received January 7, 1986)

Some of the concepts employed in composite electroceramics are reviewed in this paper: connectivity, sum and product properties, coupled phase transformations, polychromatic percolation, mechanical stress and electric field concentration, and symmetry rules. Electronic applications are described for most of the ideas.

INTRODUCTION

Composite materials have found a number of structural applications but their current use in the electronics industry is relatively limited. As the advantages and disadvantages of electroceramic composites are better understood we can expect this picture to change.

In this paper we review some of the basic ideas underlying composite electroceramics: sum and product properties, connectivity patterns leading to field and force concentration, the importance of periodicity and scale in resonant structures, the symmetry of composite materials and its influence on physical properties, polychromatic percolation and coupled conduction paths in composites, varistor action and other interfacial effects, coupled phase transformation phenomena in composites, and the important role that porosity and inner surface area play in many composites.

SUM AND PRODUCT PROPERTIES

The basic ideas underlying sum and product properties were introduced by Van Suchtelen.¹ For a sum property, the composite property coefficient depends on the corresponding coefficients of its constituent phases. Thus the stiffness of a composite is governed by the elastic stiffnesses of its component phases.

Product properties are more complex and more interesting involving different properties in its constituent phases with the interactions between the phases often causing unexpected results. In a magnetoelectric composite, for instance, the magnetostrictive strain in one phase creates an electric polarization in an adjacent piezoelectric phase. Examples of sum and product phases are described in the following sections.

Sum Properties

Dielectric constant will be used to illustrate a simple sum property. Series and parallel mixing rules for dielectric constant are shown in Figure 1. The mixing rules involve only the dielectric constants K_A and K_B of the two phases and their volume fractions v_A and v_B . When plotted as a function of composition, the dielectric constant of the composite, \bar{K} , decreases smoothly from K_A to its minimum value at K_B .

The series and parallel models represent extremes for the mixing rules. Maximum values are obtained with parallel mixing, and minimum for the series case. There are, of course, other mixing rules which lie between these extremes.

Two examples of dielectric composites are illustrated in Figures 2 and 3. The microwave foamed glass in Figure 2 has an extremely low dielectric constant. By introducing 60 volume percent porosity in a lithium aluminum silicate glass, its dielectric constant is reduced from 5.6 to 2.1 (Partridge, 1983). Decreasing the dielectric constant increases the speed of electromagnetic waves travelling along conducting wires embedded in the composite. The speed is doubled by replacing alumina ($K \sim 9$) with porous glass ($K \sim 2$).

Composite ceramics are also useful in high voltage applications. The dielectric constant of BaTiO_3 multilayer capacitors decreases substantially under high voltage fields, often by 100% or more. This is normal behavior for ferroelectric materials where the polarization saturates, but antiferroelectric substances such as NaNbO_3 behave differently. The dielectric constant of sodium niobate is nearly independent of bias field (Figure 3) as its metastable ferroelectric structure begins to influence the permittivity under high fields.

Capacitor compositions with enhanced permittivity at high fields have been manufactured from composites made from BaTiO_3 and NaNbO_3 . Fast-firing a mixture of BaTiO_3 and NaNbO_3 causes the NaNbO_3 to melt and coat the grains of BaTiO_3 , producing a composite structure with ferroelectric grains and antiferroelectric grain boundaries. By adjusting the composition and firing schedule, a capacitor with field-independent permittivity is produced. Coating the grains with NaNbO_3 prevents growth of the BaTiO_3 grains, further enhancing the dielectric properties of the composite, and causing it to exceed both component phases at high voltages.

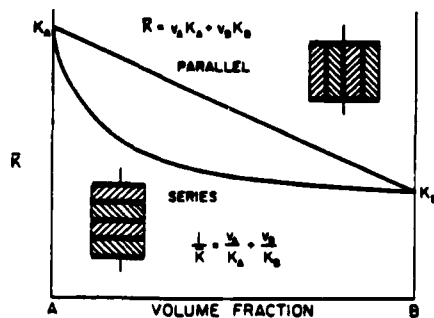


FIGURE 1 Dielectric constant plotted as a function of composition for series and parallel mixing

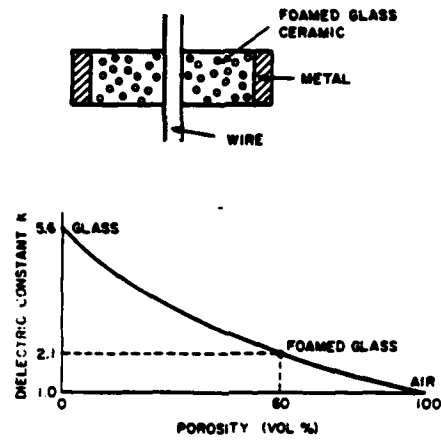


FIGURE 2 Dielectric constant of a porous glass used in microwave lead-through seals.

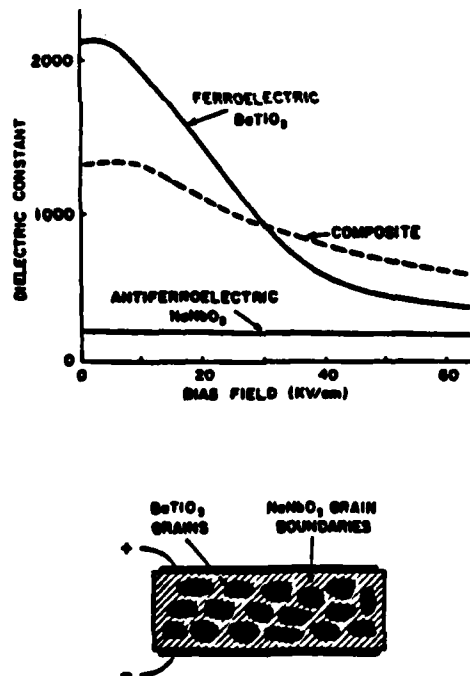


FIGURE 3 Composite capacitor dielectric consisting of BaTiO_3 grains in a NaNbO_3 matrix. The dielectric constant shows relatively little variation with field.

Combination Properties

For simple mixing rules, the properties of the composite lie between those of its constituent phases. This is not true for combination properties which involve two or more coefficients. Poisson's ratio is a good example of a combination property since it is equal to the ratio of two compliance coefficients. As is well known, some composite materials have extremely small values of Poisson's ratio, smaller than those of the materials used to make the composite.

Another example of interest in electronic applications is the acoustic wave velocity which determines the resonant frequency of piezoelectric devices. For a long, thin rod, the velocity of waves propagating along the length of the rod is $v = (E/\rho)^{1/2}$ where E is Young's modulus and ρ is the density. Fiber-reinforced composites often have very anisotropic wave velocities. Consider a compliant matrix material reinforced with parallel fibers. Long, thin rods fashioned from the composite have different properties when the fibers are oriented parallel or perpendicular to the length of the rod. Much faster wave velocities are measured for longitudinal orientation than for transverse orientation of the fibers (Figure 4). For the longitudinal case,

$$v_L = \sqrt{\frac{(E_f - E_m)v_f + E_m}{(\rho_f - \rho_m)v_f + \rho_m}}$$

and for transverse fibers,

$$v_t = \sqrt{\frac{E_m(1 + 2\nu_f)}{\rho_m + (\rho_f - \rho_m)(1 - \nu_f)}}$$

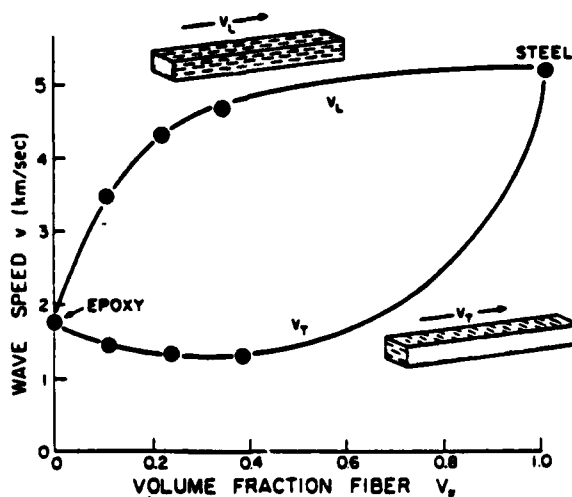


FIGURE 4 Speed of stress waves in composite materials made from steel filaments in epoxy. Waves travelling parallel to the filaments travel faster than transverse waves; the transverse waves are slower than waves in the pure epoxy matrix.⁴

where E_f and E_m are the Young's modulus values for the fibers and matrix, respectively, ρ_f and ρ_m are the densities, v_f the fiber volume fraction, and where n , is

$$n = \frac{(E_f/E_m) - 1}{(E_f/E_m) + 2}$$

Experimental data⁴ for composites made from steel filaments embedded in epoxy resins conform closely to the equations for v_L and v_T . Note the v_T , the wave velocity for waves traveling transverse to the fibers, is less than the velocity of both epoxy resin and steel, the two phases which make up the composite. The slowness of this wave is caused by the fact that density and stiffness depend differently on volume fraction. This difference in mixing rules for E and ρ causes the combination property v_T to lie outside the range of the end members. The longitudinal wave, v_L , behaves more normally. In this case E and ρ follow the same mixing rule and the values for v_L lie between those of the end members.

Another example of unusual wave behavior occurs in composite transducers made from poled ferroelectric fibers embedded in an epoxy matrix.⁵ When driven in thickness resonance, the regularly-spaced fibers excite resonance modes in the polymer matrix causing the matrix to vibrate with much larger amplitude than the piezoelectric fibers. The difference in compliance coefficients causes the non-piezoelectric phase to respond far more than the stiff ceramic piezoelectric. Composite materials are therefore capable of mechanical amplification.

Product Properties

A product property utilizes different properties in the two phases of a composite to produce yet a third property through the interaction of the two phases. By combining different properties of two or more constituents, surprisingly large product properties are sometimes obtained with a composite. Indeed, in a few cases, product properties are found in composites which are entirely absent in the phases making up the composite. Table I lists a few of the hundreds of possible product properties, several of which are described in the following paragraphs.

In the magnetoresistive field plate developed by Weis,⁶ a composite of InSb and NiSb is directionally solidified to form parallel NiSb needles in an InSb matrix. A

TABLE I
Examples of product properties

Property of Phase I	Property of Phase II	Composite Product Property
Thermal Expansion	Electrical Conductivity	Thermistor
Magnetostriction	Piezoelectricity	Magnetoelectricity
Hall Effect	Electrical Conductivity	Magnetoresistance
Photoconductivity	Electrostriction	Photostriction
Superconductivity	Adiabatic	Electrothermal
	Demagnetization	Effect
Piezoelectricity	Thermal Expansion	Pyroelectricity

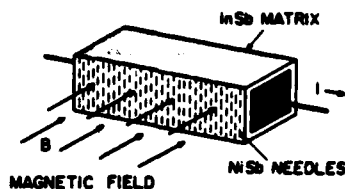


FIGURE 5 Magnetoresistive field plate made from indium antimonide and nickel antimonide. The plate is used as a magnetic field sensor and a noncontacting variable resistor.

long rectangular segment of the composite is electroded across the ends with the NiSb fibers parallel to the electrodes and transverse to the length of the composite (Figure 5). InSb is a semiconductor with a large Hall Effect and NiSb is metallic with large electrical conductivity.

When an electric current flows along the length of the bar, and a magnetic field is applied perpendicular to the current and perpendicular to the NiSb needles, the current is deflected because of the Hall Effect. Normally this would result in an electrical field transverse to the current and the magnetic field, but in this case the NiSb needles short out the field. Electric current continues to be deflected as long as the magnetic field is present. The resulting product property is a large magnetoresistance effect.

A second example of a product property is the superconducting stabilizer developed by W. N. Lawless.⁷ The superconducting cable made of Nb_3Sn is sheathed with a paramagnetic ceramic of $CdCr_2O_4$. Temperature fluctuations cause portions of the superconducting cable to revert to normal metallic behavior, thereby decreasing the superconducting electric current and the surrounding magnetic field it generates. The decrease in magnetic field demagnetizes the paramagnetic $CdCr_2O_4$ and lowers its temperature. This in turn cools the Nb_3Sn cable causing it to return to the superconducting state (Figure 6).

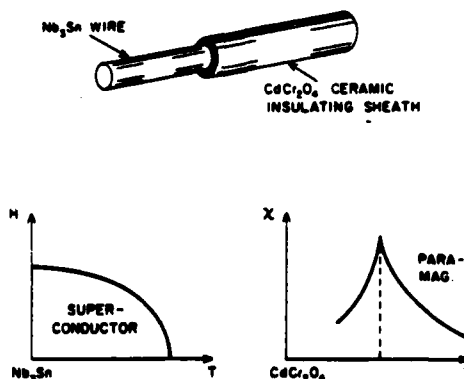
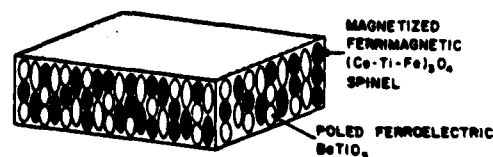


FIGURE 6 Superconducting wire of Nb_3Sn surrounded by a paramagnetic sheath of $CdCr_2O_4$.



PRODUCT PROPERTY

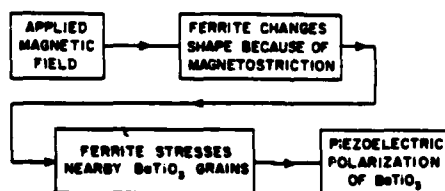


FIGURE 7 Magnetolectric transducer making use of the magnetostrictive effect of a ferrite mechanically coupled to piezoelectric barium titanate.

A magnetolectric composite made from ferroelectric BaTiO_3 and ferrimagnetic cobalt titanium ferrite has been studied by scientists from Philips Laboratory.^{8,9} A dense intimate mixture of the perovskite and spinel-structure phases was obtained by directional solidification, and then electrically poled to make the BaTiO_3 phase piezoelectric (Figure 7). When a magnetic field is applied to the composite, the ferrite grains change shape because of magnetostriction. The strain is passed along to the piezoelectric grains resulting in an electrical polarization. Magnetolectric effects a hundred times larger than those in Cr_2O_3 are obtained this way. Subsequent research¹⁰ has led to the development of a broadband magnetic field probe with an exceptionally flat frequency response up to 650 kHz.

TRANSPORT PROPERTIES OF COMPOSITES

Conductor-filled composites are discussed in this section, emphasizing the importance of percolation in random and segregated mixes. Differential thermal expansion between matrix and filler sometimes leads to remarkable variations in resistance with temperature. Composite PTC thermistors and humidity sensors based on these ideas are described in this section.

Percolation and Segregated Mixing

Some of the principles can be illustrated with the work on wax-graphite composites carried out by Rajagopal and Satyam.¹¹ After melting the wax, the graphite particles are stirred in and the composites pressed to remove porosity. Graphite grains 45 to 215 μm in size were used in the study. A typical variation of conductivity with composition is shown in Figure 8. At approximately 20 volume percent graphite the

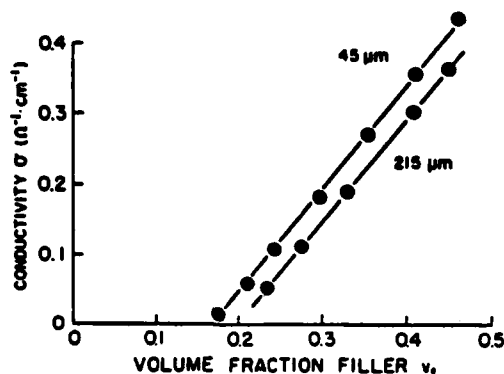


FIGURE 8 Electrical conductivity of wax-graphite composites plotted as a function of composition. Critical volume fraction for percolation is determined by extrapolating the conductivity to zero.¹¹

resistance decreases rapidly as the graphite particles begin to contact one another. This critical volume fraction v_f is referred to as the percolation limit, and is evaluated by plotting conductivity on a linear scale versus volume fraction conducting filler (Figure 8). The electrical conductivity of composites rich in filler is controlled by contacting graphite particles, whereas below the percolation limit it is controlled by the polymer. Near the percolation limit the conductivity is controlled by thin polymer layers between graphite particles. As shown in Figure 8, the critical volume fraction for 45 μm graphite particles is smaller than that for 215 μm particles.

The smaller particles show *segregated mixing*. The effect of particle size on mixing is illustrated in Figure 9, which compares the situations when the conducting

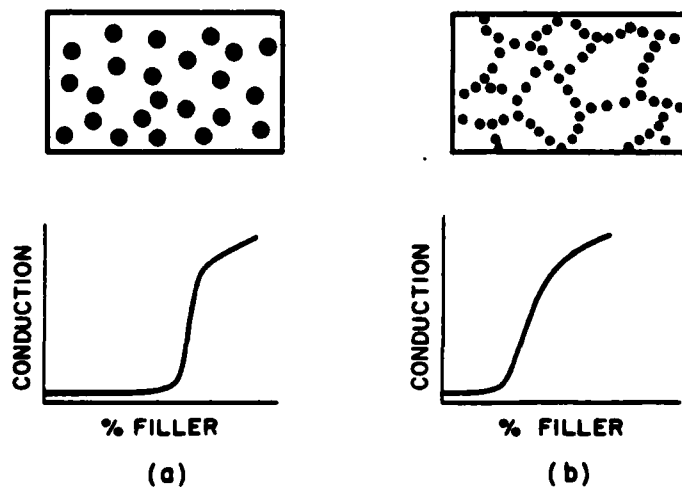


FIGURE 9 Mixing of (a) equal size particles and (b) large and small particles. The percolation limit is smaller when the conducting particles are segregated into interstitial sites between larger insulating particles.

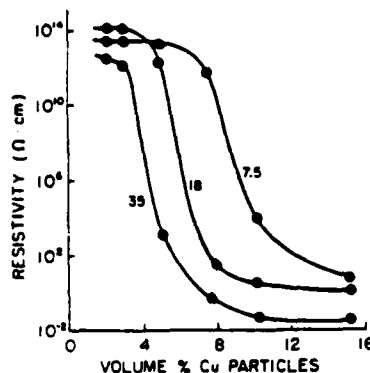


FIGURE 10 Resistivity of Cu-PVC composites for several size ratios of PVC/Cu particles. Percolation occurs easily when the Cu particles are small and concentrated in grain boundary regions.¹²

particles are comparable in size to the insulating particles, and when the conducting particles are much smaller than the insulating particles. Percolation requires a larger volume fraction when the two types of particles are comparable in size. When the conducting particles are small, they are forced into interstitial regions between the insulating particles; this forces the conducting particles in contact with one another, resulting in a low percolation limit.

These ideas are borne out by experiments on copper particles embedded in a matrix of polyvinylchloride.¹² Figure 10 shows the resistivity of Cu-PVC composites plotted as a function of volume fraction copper. The critical volume fraction decreases markedly when the Cu particles are far smaller than the polymer particles. When the size ratio is 35 : 1, the critical volume percent is only 4% Cu. This highly segregated mixing establishes contact between conducting copper particles at a very low ratio of conductor to insulator.

Composite Thermistors

A second interesting effect is the dependence of electrical resistance on temperature. PTC thermistors are characterized by a positive temperature coefficient of electrical resistance. Doped barium titanate (BaTiO_3) has a useful PTC effect in which the resistance undergoes a sudden increase of four orders of magnitude just above the ferroelectric Curie temperature (130°C). The PTC effect is caused by insulating Schottky barriers created by oxidizing the grain boundary regions between conducting grains of rare earth-doped BaTiO_3 .

Similar PTC effects are observed when polymers are loaded near the percolation limit with a conducting filler. The Polyswitch overload protector¹³ is made from high density polyethylene with carbon filler. At room temperature the carbon particles are in contact giving resistivities of only $1 \Omega\text{-cm}$, but on heating the polymer expands more rapidly than carbon, pulling the carbon grains apart and raising the resistivity. Polyethylene expands very rapidly near 130°C , resulting in a pronounced PTC effect comparable to that of BaTiO_3 . A rapid increase in resistivity of six orders of magnitude occurs over a 30° temperature rise (Figure 11).

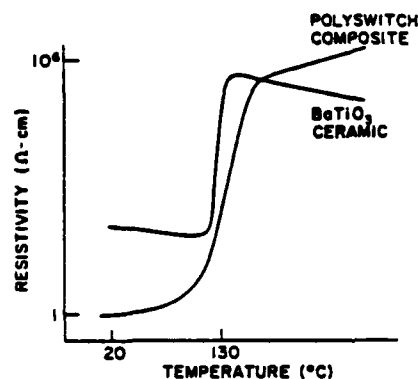


FIGURE 11 Comparison of the PTC effects in BaTiO_3 and carbon-polyethylene composites. The PTC effect is caused by the volume expansion of the polyethylene during an amorphous-crystalline phase transformation.

As pointed out by Doljack,¹³ the carbon-ethylene PTC thermistor has several advantages over BaTiO_3 : (i) the room resistivity is lower, (ii) it shows PTC behavior at high temperature, (iii) the resistance is insensitive to voltage, and (iv) the device has good thermal shock resistance. The principal drawback with Polyswitch composites seems to be the slow recovery time. Several hours are required for the resistance to return to within 10% of its initial value at room temperature. The slow recovery of base resistance is caused by polymer melting followed by secondary recrystallization and gradual reformation of the carbon black chains responsible for conduction.

Similar, but less dramatic, changes in resistivity are observed in wax-graphite composites where a three-fold increase in resistivity occurs over a 20°C temperature rise.¹¹ Not all composites show a PTC effect, however. Magnetite-alumina composites¹⁴ made by arc plasma spray possess NTC behavior with a decrease of four orders of magnitude in resistivity on heating from 100° to 300°K . For composites containing 60 volume percent Fe_3O_4 , the magnetite particles remain in contact throughout the temperature range.

Combined NTC-PTC composites have also been constructed.¹⁵ Vanadium sesquioxide (V_2O_3) has a metal-semiconductor transition near 160°K with a large increase in conductivity on heating.¹⁶ This material can be incorporated in a composite by mixing V_2O_3 powder in an epoxy matrix. The filler particles are in contact at low temperatures and exhibit an NTC resistance change similar to that observed in V_2O_3 crystals and single phase ceramics. On heating above room temperature, the polymer matrix expands rapidly, pulling the V_2O_3 grains apart and raising the resistance by many orders of magnitude. This produces a PTC effect similar to the Polyswitch composite. The net result is an NTC-PTC thermistor with a conduction "window" in the range -100°C to $+100^\circ\text{C}$. This is a good example of the use of coupled phase transformations in composites.

Many interesting experiments remain to be done using electroceramic fillers in polymer matrices. In addition to the conducting particles just discussed, there are

interesting combinations of piezoelectric, magnetic, pyroelectric, ferroelectric, varistor, thermistor, and insulator fillers to be explored.

Porous Composites

Composite humidity sensors have been synthesized by loading lithium fluoride with alumina.¹⁷ Differential thermal contraction of the LiF matrix and Al_2O_3 filler causes internal microcracks to open within the composite making the electrical resistance of this material very sensitive to humidity (Figure 12). Moisture penetrates into the microcracks affecting the surface resistance. Conduction probably occurs by the Grotthuss mechanism ($\text{H}_3\text{O}^+ \rightleftharpoons \text{H}_2\text{O} + \text{H}^+$) at low humidity levels, and by Li^+ ion conduction in adsorbed water layers at high humidity. In any case, the ceramic alumina particles play an interesting role in the composite: their presence initiates the microcracking responsible for increased surface conduction.

Composite gas sensors have been constructed on similar principles.¹⁸ The addition of Al_2O_3 to ZnO ceramics stabilizes a porous microstructure ideal for adsorption-desorption type gas sensors. The porous texture enhances the electrical conductivity to such an extent that the sensitivity to flammable gases is adversely affected, but soaking the porous structure in a lithium-containing solution increases the resistivity, resulting in a reproducible gas sensor sensitive to methane, propane, and other hydrocarbon gases.

As pointed out by Yanagida,¹⁹ interactions between two different materials can give rise to very unusual phenomena. Dispersing a basic refractory (MgCr_2O_4) in an acid refractory (TiO_2) produces a composite humidity sensor suitable for monitoring cooking in electric ovens.

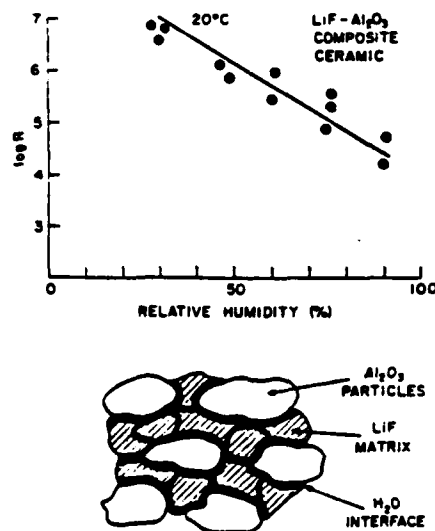


FIGURE 12 Electrical resistance of Al_2O_3 -LiF composites used as humidity sensors.

Contacts between *p*- and *n*-type ceramic grains are also sensitive to humidity.²⁰ The I-V characteristics of ZnO (*n*-type) and NiO (*p*-type) junctions change markedly with humidity and exposure to flammable gases.

Another interesting composite in which the ceramic filler plays an indirect role is the metal-ceramic contact used for high current switches (Stockel, 1975). In one type, cadmium oxide particles are embedded in a silver metal matrix. Large switching currents sometimes cause localized melting which welds the contact shut. When the silver grains melt in the composite, CdO grains are exposed, lowering the current flow and preventing welding. Cadmium oxide decomposes to prevent surface accumulation. This results in a blowing effect which quenches arc formation.

Polychromatic Percolation

Transport by percolation through two or more materials can be visualized in terms of colors. Black and white patterns (Figure 13) illustrate percolation in a diphasic solid. Three kinds of percolation are possible: (i) percolation through an all-white path, (ii) percolation through an all-black path, and (iii) percolation through a combined black-white path. From a composite point of view, the third possibility is the most interesting because it offers the possibility of discovering new phenomena which are not present in either phase individually. Foremost among these effects are the interfacial phenomena which arise by inserting a thin insulating layer between particles with high electrical conductivity. Varistors, PTC thermistors and boundary layer capacitors are examples. In ceramic varistors conducting ZnO grains are surrounded by thin layers of Bi_2O_3 insulation. The tunneling of electrons through this barrier gives rise to the varistor effect.

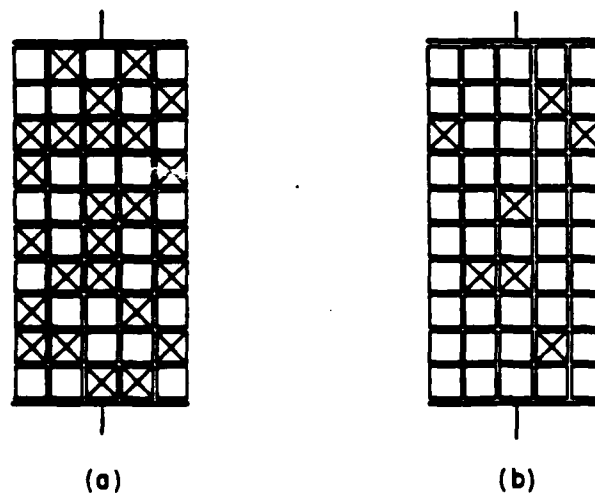


FIGURE 13 Black and white percolation patterns drawn for randomly mixed particles of equal size and shape. The black/white mixing ratios are 50/50 in (a), and 15/85 in (b).

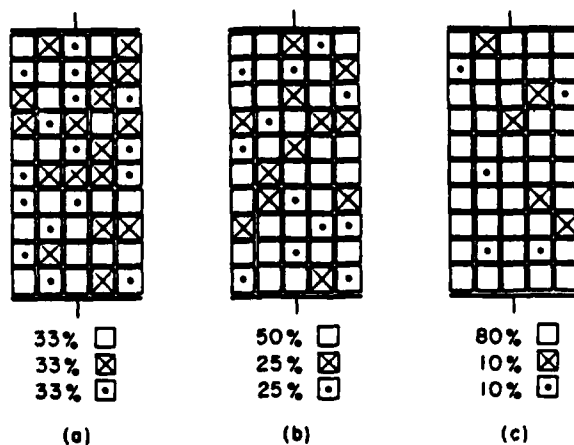


FIGURE 14 Tricolor percolation patterns drawn for randomly mixed particles of equal size and shape. Mixing ratios are 33/33/33 in (a), 50/25/25 in (b), and 80/10/10 in (c).

The two-color patterns in Figure 13 show how percolation depends on volume fraction for a random mix. As pointed out earlier, the percolation limit depends on connectivity. Highly connected segregated mixtures have lower percolation limits than random mixtures of low connectivity. Of the three kinds of transport paths, all three may occur in a diphasic composite with equal proportions of the two constituents. As pictured in Figure 13a, there are all-white paths, all-black paths, and black-white paths, with the latter predominating. When one color outnumbers the other (Figure 13b) the minority phase may lose its connectivity as its volume fraction drops below the percolation limit.

Three-color percolation is illustrated in Figure 14. Seven kinds of conduction paths are possible: three monicolor, three bicolor, and one tricolor. When all three are present in equal amounts (Figure 14a), it is possible that there will be no monicolor transport. In this case bicolor and tricolor paths become important. Monicolor conduction paths become increasingly important as the volume fractions become unbalanced (Figures 14b, c).

Ternary composition diagrams (Figure 15) are useful in determining which type of conduction paths are to be found in a composite. Figure 15a shows a symmetric three-phase composite with low connectivity. Only monicolor conduction composition regions are identified. Monicolor paths occur only when a high volume fraction of the color in question is present. No monicolor transport occurs for compositions near the center of the ternary system, although bicolor and tricolor paths are present.

The situation is very different for a tricolor system with high connectivity and easy percolation (Figure 15b). In this case, the percolating limits for monicolor transport overlap to give regions in the ternary where two or three monicolor conduction paths coexist. Bicolor and tricolor paths also exist in the system. Connectivity requirements for polychromatic percolation have been discussed from a theoretical viewpoint by Zallen.²²

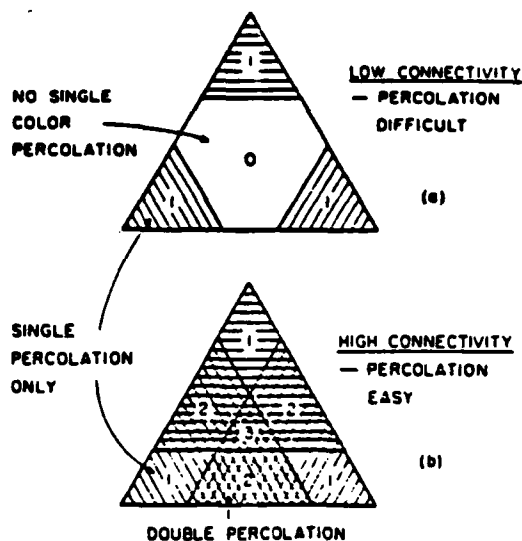


FIGURE 15 Ternary percolation diagrams for tricolor composites. (a) A composite with low connectivity shows single-color percolation only near end-member compositions. (b) High connectivity promotes percolation throughout the diagram. All three colors can percolate simultaneously near the center of the diagram.

An example of coupled bicolor percolation is shown in Figure 16. Consider the situation where an insulating polymer matrix is partially filled with two kinds of particles. If the particles are of low connectivity, percolation occurs only when filled to high levels. The conduction may be monocolor or bicolor depending on the relative proportions of the two fillers.

For high connectivity fillers, conduction is much easier and the ternary diagram possesses a region of overlap for monocolor conduction. At lower levels of filling there is also a region where only bicolor transport is possible.

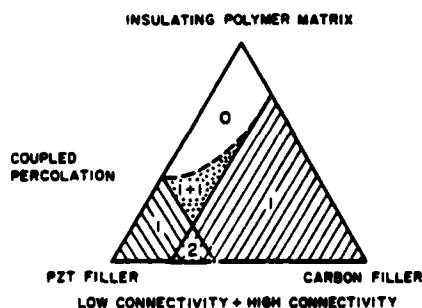


FIGURE 16 Ternary percolation diagram for polymer-PZT-carbon composite. Composites can be poled in the 1 + 1 coupled percolation region.

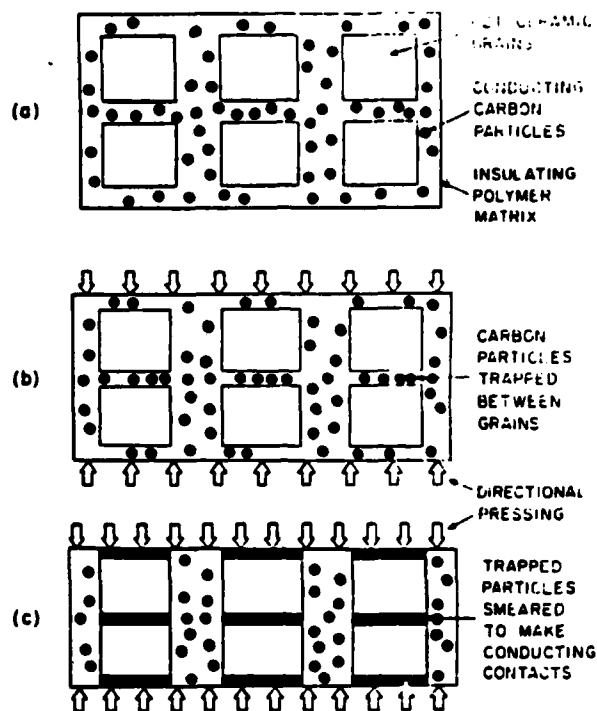


FIGURE 17 Pressed ternary composites made by mixing PZT and carbon particles in an epoxy matrix. (a) Carbon particles are small ($\sim 5 \mu\text{m}$) with low connectivity. When pressed, (b) the carbon particles are trapped between PZT grains to form conducting contacts in the poling direction (c).

An asymmetric percolation diagram is shown in Figure 16. Here one filler has high connectivity, the other low. The high connectivity phase might be a finely divided material such as carbon; the low connectivity phase could be of coarser grain size.

An example of such a system is an easy-poling piezoelectric composite made up of two kinds of particles mixed in an insulating polymer matrix.²³ The first kind of particulate phase in a piezoelectric composite is PZT (lead zirconate titanate), a ferroelectric ceramic phase which must be poled to make it piezoelectrically active. Poling is difficult because the PZT grains are not in good electrical contact; and when shielded by a polymer, only a small fraction of the poling field penetrates into the ferroelectric PZT particles. To aid in poling, a small amount of a second conductive filler material is added. When a conductor is added and the composite is stressed, electrical contact is established between the ferroelectric grains, making poling possible (Figure 17a-c). Pressure sensors of greater sensitivity can be obtained in this way.²³

Doubly filled composites are also used as backing materials for broadband piezoelectric transducers such as PZT. To efficiently couple the backing material to the transducer it is necessary to match the acoustic impedance of the backing to that

of the piezoelectric. The acoustic impedance of an isotropic solid is given by $z = \rho v$, where ρ is the density and v the acoustic wave velocity.

Two-phase mixtures consisting of a polymer matrix and a heavy metal filler provide the required high attenuation and a wide range of acoustic impedances. The filler particles scatter the acoustic waves efficiently and polymers generally have high absorption coefficients; together the two provide the required high attenuation. Acoustic impedances of about $30 \times 10^6 \text{ kg/m}^2\text{-sec}$ are required to match piezoelectric transducers made from PZT or LiNbO_3 , but it is not easy to obtain such values with normal composite materials. In principle an epoxy-tungsten composite can provide a wide range of acoustic impedances ($3\text{-}100 \times 10^6$), but in practice it is difficult to load the matrix to more than 70 volume percent tungsten. It is found that most of the change in impedance takes place at higher volume fractions. Metal-matrix backing materials avoid this problem. Using lead-indium based alloy as a matrix with copper and tungsten fillers gave impedance values closely matched to the transducers.²⁴ Three-phase backing materials such as this make excellent acoustic dampers with impedances in the range of $20\text{-}45 \times 10^6 \text{ kg/m}^2\text{-sec}$.

SYMMETRY OF COMPOSITE MATERIALS

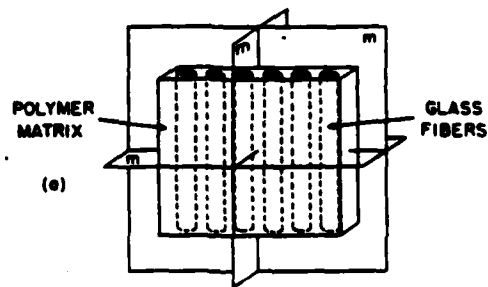
A wide variety of symmetries are found in composite materials. Examples of crystallographic groups, Curie groups, black-and-white groups, and color groups will be given, and the resulting effect on physical properties discussed.

In describing the symmetry of composite materials, the basic idea is Curie's principle of symmetry superposition: A composite material will exhibit only those symmetry elements that are common to its constituent phases and their geometrical arrangement.

The practical importance of Curie's principle rests upon the resulting influence on physical properties. Generalizing Neumann's law from crystal physics: The symmetry elements of any physical property of a composite must include the symmetry elements of the point group of the composite. Applications of Neumann's law to single crystal materials can be found in the book by Nye.²⁵ A discussion of more wide-ranging topics concerning the effects of symmetry has been given by Shubnikov and Koptsik.²⁶

Laminate Symmetry

The laminated composites pictured in Figures 18, 19, and 20 are good illustrations of composite symmetry. In a unidirectional laminate (Figure 18) the glass fibers are aligned parallel to one another, such that a laminate has orthorhombic symmetry (crystallographic point group mmm). Mirror planes are oriented perpendicular to the laminate normal, and perpendicular to an axis formed by the intersection of the other two mirrors. The physical properties of a unidirectional laminate must therefore include the symmetry elements of point group mmm . If the laminate is heated, it will change shape because of thermal expansion. Less expansion will take place parallel to the fiber axis because glass has a lower thermal expansion and greater stiffness than that of polymer. The laminate will therefore expand anisotropi-



THERMAL EXPANSION

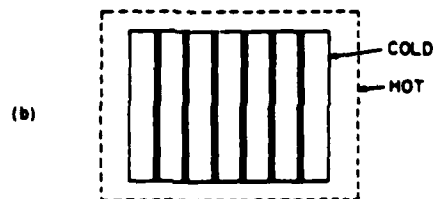


FIGURE 18 (a) Unidirectional laminate consisting of parallel glass fibers in an epoxy matrix. (b) The orthorhombic mmm symmetry of the composite is maintained on heating.

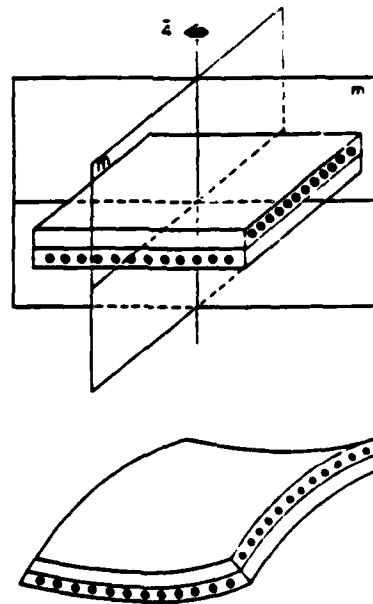


FIGURE 19 Cross-ply laminate containing orthogonal fibers in adjacent layers. (b) Double curvature occurs on heating, consistent with $42m$ symmetry.

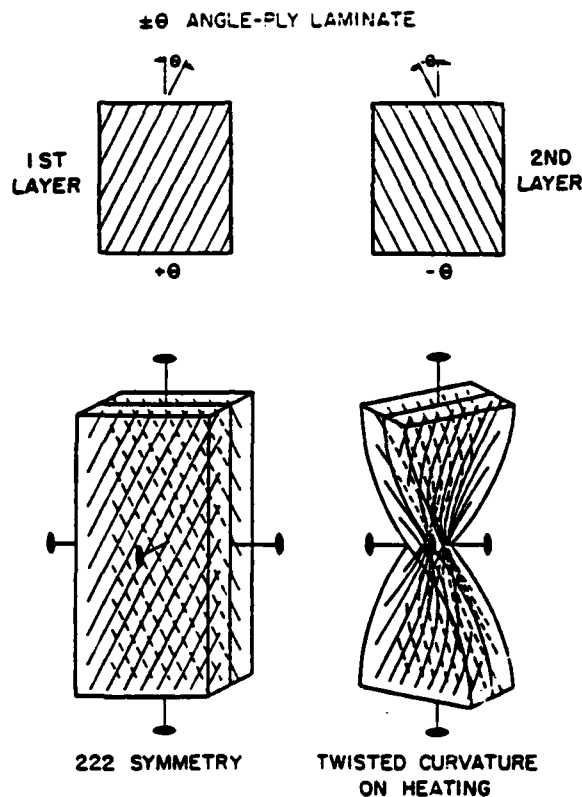


FIGURE 20 (a) $\pm\theta$ angle-ply laminate with 222 symmetry. (b) Twisted curvature develops when the temperature is raised.

cally but it will not change symmetry. The heated laminate continues to conform to point group mmm.

A cross-ply laminate (Figure 19) is made up of two unidirectional laminates bonded together with the fiber axes at 90° . Such a laminate belongs to tetragonal point group $\bar{4}2m$. The four-fold inversion axis is perpendicular to the laminated sheets and to both sets of glass fibers. Two-fold symmetry axes are oriented perpendicular to the $\bar{4}$ axis and at 45° to the fiber axes. The tetragonal symmetry is maintained on heating. A double curvature distortion occurs but the symmetry elements of point group $\bar{4}2m$ are not violated.

Laminated composites with $\pm\theta$ angle-ply alignment exhibit orthorhombic symmetry consistent with point group 222. In a $\pm\theta$ angle-ply laminate the fibers in the first layer are oriented at an angle of $+\theta$ with respect to the edge of the laminate. Fibers in the second layer form an angle of $-\theta$ with the edge, and an angle of 2θ with respect to the fibers in the first layer. Two two-fold symmetry axes bisect the fiber directions, with a third perpendicular to the laminated layers. When heated, the layers twist but the symmetry is unchanged (Figure 20).

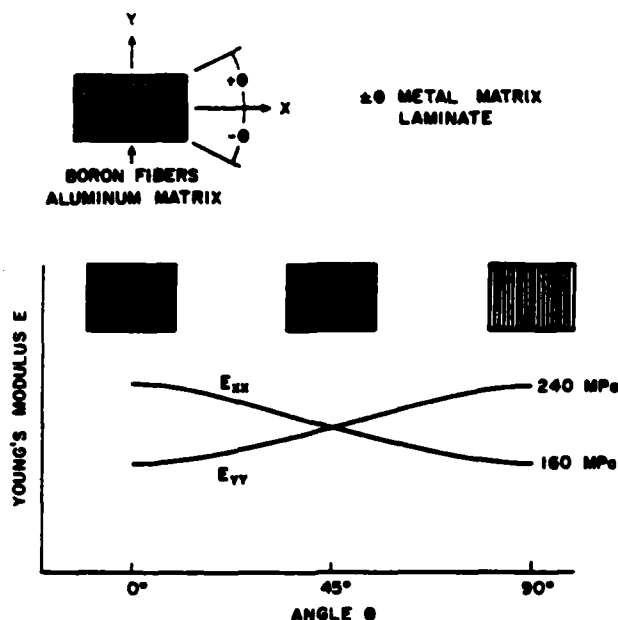


FIGURE 21 Elastic properties of a boron-fiber; aluminum matrix composite in $\pm\theta$ angle-ply configuration. Young's moduli (E_{xx} and E_{yy}) are plotted as a function of θ . The symmetry changes from orthorhombic ($E_{xx} \neq E_{yy}$) to tetragonal ($E_{xx} = E_{yy}$) at $\theta = 45^\circ$, corresponding to cross-ply lamination.

The thermal strain of the three laminated composites just discussed are excellent examples of Neumann's law. In all three cases the symmetry of the physical property includes that of the point group of the composite. Other properties of the composite obey Neumann's law as well. The elastic properties of an angle-ply metal matrix are graphed in Figure 21. Young's moduli are plotted as a function of the fiber angle θ . Maximum anisotropy in Young's modulus is observed when the fibers in the adjacent layers are parallel to one another ($\theta = 0^\circ$ or 90°). In this case the symmetry of the composite is clearly orthorhombic, but as θ approaches 45° , the anisotropy disappears until the symmetry becomes tetragonal at $\theta = 45^\circ$, corresponding to the cross-ply laminate situation.

The point groups for unidirectional laminates (mmm), cross-ply laminates ($\bar{4}2m$), and angle-ply laminates (222), are examples of crystallographic symmetry in composite materials. More complicated symmetry patterns have been incorporated in three-dimensional weaves. Woven carbon-carbon composites are made from carbon fibers infiltrated with pyrolytic carbon.²⁷ Aerospace engineers have found that weaves with cubic geometries show excellent ablation resistance. Cubic symmetry is obtained by weaving the fibers in directions corresponding to the important symmetry directions of a cube. In one such pattern, the fiber axes are aligned perpendicular to one another along three non-intersecting $\langle 100 \rangle$ directions. Another utilizes four non-intersecting $\langle 111 \rangle$ directions as fiber directions. An even more complex weave is obtained by combining the $\langle 100 \rangle$ and $\langle 111 \rangle$ patterns in a seven-directional weave

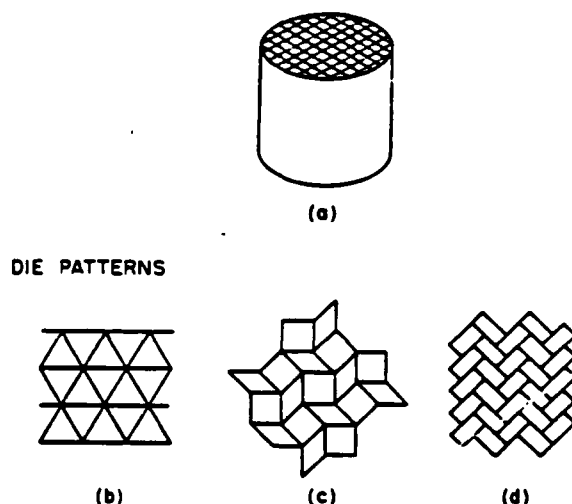


FIGURE 22 Electroceramic bodies can be extruded with many different symmetries. Monolithic honeycomb patterns with (b) hexagonal, (c) tetragonal, and (d) orthorhombic symmetries are illustrated.

with faceted strands. In the carbon-carbon composites, 60–75% of the volume is occupied by carbon fibers.

Extruded Geometries

Other types of symmetry elements can also be introduced during processing. The extruded honeycomb ceramic used as catalytic substrates is an interesting example.²⁸ By suitably altering the die used for extruding the ceramic slip, a large number of different symmetries can be incorporated into the composite body when the extruded form is filled with a second phase. Figure 22 illustrates three of the extruded geometries with hexagonal, tetragonal and orthorhombic symmetries. The orthorhombic pattern (Figure 22d) resembles the cellular structure of wood in which cell walls terminate on adjacent transverse walls. Such a structure has excellent resistance to mechanical and thermal shock.

Lead zirconate titanate (PZT) honeycomb ceramics have been transformed into piezoelectric transducers by electroding and poling. The symmetry of the honeycomb transducers depends on the symmetry of the extruded honeycomb and also on the poling direction. For a square honeycomb pattern, the symmetry of the unpoled ceramic is tetragonal (4/mmm) with four-fold axis parallel to the extrusion direction. When poled parallel to the same direction, the symmetry changes to 4mm. Longitudinally-poled PZT composites have been investigated by ShROUT and co-workers.²⁹ Transversely poled composites filled with epoxy are especially sensitive to hydrostatic pressure waves.³⁰ In this case the symmetry belongs to orthorhombic point group mm2 (Figure 23).

Not all composites have crystallographic symmetry. Some belong to the seven limiting groups of ∞ -fold symmetry axes (Figure 24). The best known of the Curie

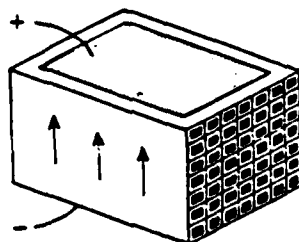


FIGURE 23 Honeycomb pressure sensor extruded with tetragonal $4/mmm$ symmetry and then transversely poled to give orthorhombic $mm2$ symmetry.

groups are those with spherical ($\infty\infty m$), cylindrical (∞/mm) and conical (∞m) symmetry.²⁶ The remaining four groups exhibit right- and left-handed characteristics which can best be illustrated with various types of liquids.

An ordinary liquid (water or benzene) has spherical symmetry. In such a liquid the molecules have no alignment or handedness, hence there are an infinite number of ∞ -fold axes and mirror planes, corresponding to Curie group $\infty\infty m$. All other limiting groups are subgroups of $\infty\infty m$, as indicated in Figure 24.

The mirror planes are lost when the liquid possesses handedness. Dissolving sugar in water is a simple way of imparting handedness to water. Though randomly

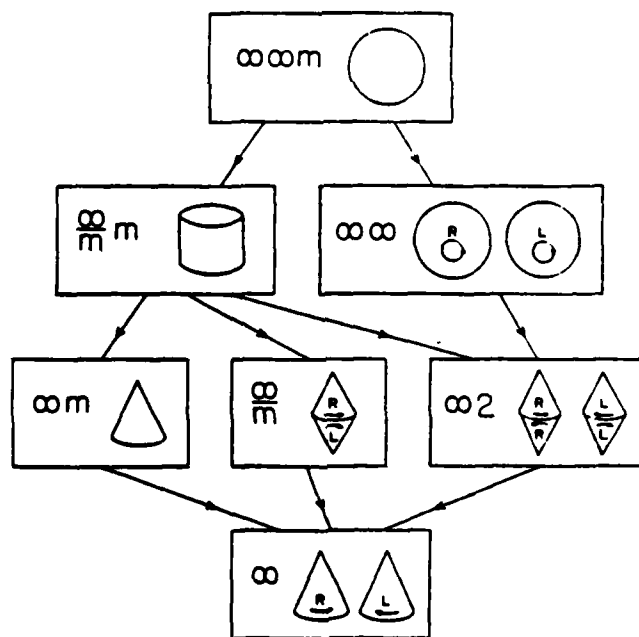


FIGURE 24 Curie groups showing subgroup-supergroup relationships.

oriented in water, the sucrose molecules are all of the same handedness, thereby making the solution optically active. When dissolved in water, dextrose and levose—the right- and left-handed forms of sugar—give rise to the enantiomorphic forms of point group $\infty\infty$. This symmetry can be imposed on a composite material by incorporating randomly-oriented molecules with a handedness within the body.

Point groups $\infty\infty m$ and $\infty\infty$ are consistent with random orientation of crystallites as well. A polycrystalline body of alumina (single crystal symmetry $\bar{3}m$) belongs to $\infty\infty m$. The symmetry group of polycrystalline quartz (enantiomorphic single crystal group 32) depends on the relative population of right- and left-handed grains. If the two were equal in population, as would normally be the case, the symmetry of a randomly-oriented polycrystalline body is $\infty\infty m$. If left-handed grains were systematically excluded, say by grinding up a right-handed crystal, the symmetry group would be $\infty\infty$.

Composite bodies with texture may belong to one of the five remaining Curie groups: ∞/mm , ∞m , ∞/m , $\infty 2$, or ∞ . All five groups have a special symmetry axis. Liquid crystals have orientational order which conforms to Curie group symmetry. In nematic liquid crystals, the molecules are parallel to one another, giving cylindrical symmetry ∞/mm . When the molecules are parallel and polar, conical symmetry (∞m) is achieved. And if the liquid crystal molecules have handedness, or are stacked in helical fashion as in cholesteric liquids, then the symmetry group is $\infty 2$. Group ∞/m occurs in the unlikely circumstance that right- and left-handed molecules align with opposite polarity. Certain ferroelectric crystals such as $Pb_5Ge_3O_{11}$ exhibit such ambidextrous behavior. The lowest symmetry Curie group, polar point group ∞ , occurs in ferroelectric liquid crystals with handedness.

Mixed liquids can lead to some interesting symmetry changes. Mixing an enantiomorphic liquid ($\infty\infty$) with a nematic liquid crystal (∞/mm) creates a "mixed drink" with symmetry $\infty 2$ in accordance with the principle of symmetry superposition.

Physical forces or fields can be assigned to certain symmetry groups. As an example consider a temperature gradient dT/dx . This is a vector which can be imposed on a composite material during processing, and if the material has a "memory," the vector nature of the temperature gradient will be retained after the temperature gradient is removed. The polar glass-ceramics developed at Penn State illustrate the idea.³¹ A glass is crystallized under a strong temperature gradient with polar crystals growing like icicles into the interior from the surface. Certain glass-ceramic systems such as $Ba_2TiSi_2O_3$ and $Li_2Si_2O_3$ show sizeable pyroelectric and piezoelectric effects when prepared in this manner. Polar glass-ceramics belong to the Curie point group ∞m , the point group of a polar vector. As the glass is crystallized in a temperature gradient, it changes symmetry from spherical ($\infty\infty m$) to conical (∞m), the same as that of a poled ferroelectric ceramic.

Magnetic Curie Groups

Other physical forces can also be classified into Curie group symmetries. The chart in Figure 25 is helpful in relating these symmetries. To describe the magnetic fields and properties it is necessary to introduce the black-and-white Curie groups.

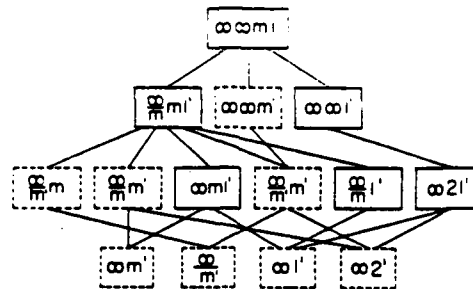


FIGURE 25 Curie groups (solid boxes) and their magnetic derivatives (dashed boxes).

Magnetic fields are represented by axial vectors with symmetry ∞/mm' . The symbol m' indicates that the mirror planes parallel to the magnetic field are accompanied by time reversal. The relationship between black-and-white Curie groups is shown in Figure 25. The symbol l' is added to the Curie group symbols to indicate that in normal Curie groups all symmetry elements occur twice, both with and without time reversal.

Polar vectors such as temperature gradient or an electric field belong to Curie group $\infty ml'$. Tensile stress is represented by a second rank tensor belonging to cylindrical group ∞/mm' .

The symmetry superposition principle applies to the point groups in Figure 25. In the magnetoelectric composites made from ferroelectric and ferromagnetic phases, the symmetry of the poling fields is retained through domain wall motion. If the electric and magnetic poling fields are applied in the same direction, the symmetry of the composite is $\infty m'$. When the poling fields are perpendicular to one another, the symmetry group is $2'mm'$. This point group also applies to the NiSb-InSb field plate described earlier.

To summarize the symmetry of diphasic composites, some belong to crystallographic point groups (cross-ply laminate $\bar{4}2m$), some to limiting groups (polar glass-ceramics ∞m), some to black-and-white limiting groups (magnetoelectric composite $\infty m'$) whilst those containing more than two phases can be described by color group symmetry.

The magnetoelectric composite described previously is an excellent illustration of the importance of symmetry in composite materials. Figure 26 shows the change in symmetry going from domain—single crystals of CoFe_2O_4 and BaTiO_3 through multidomain and polycrystalline states to a polycrystalline composite that has been poled and magnetized in parallel E- and H-fields. In combining a magnetized ceramic (symmetry group ∞/mm') with a poled ferroelectric ceramic (symmetry group $\infty ml'$), the symmetry of the composite is obtained by retaining the symmetry elements common to both groups: $\infty m'$.

An interesting feature of this symmetry description is its effect on physical properties. According to Neumann's law, the symmetry of a physical property of a material must include the symmetry elements of the point group. The symmetry of

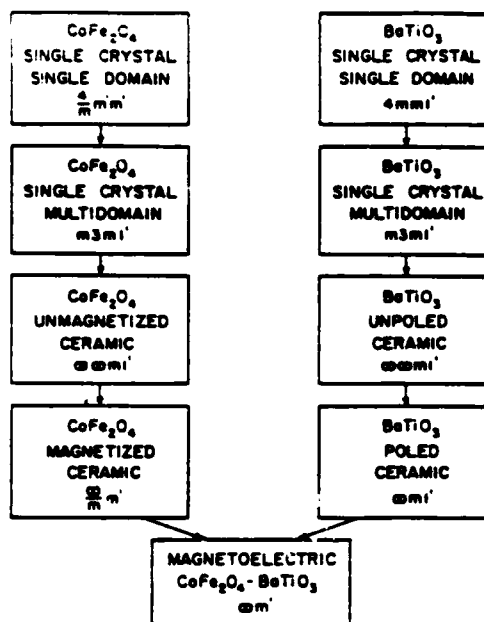


FIGURE 26 Symmetry derivation for a polycrystalline $\text{BaTiO}_3\text{-CoFe}_2\text{O}_4$ magnetoelectric composite poled and magnetized in parallel electric and magnetic fields.

this magnetized ceramic and the poled ferroelectric forbid the occurrence of magnetoelectricity, but their combined symmetry ($\infty m'$) allows it. By incorporating materials of suitable symmetry in a composite, new and interesting product properties can be expected to occur.

A listing of property coefficients for the Curie groups and their magnetic analogs is presented in Tables II and III.

TABLE II

The number of independent property coefficients for the seven Curie groups. Polar tensors of rank one through four are represented by pyroelectricity (p), permittivity (ϵ), piezoelectricity (d), and elastic compliance (s). Optical activity coefficients (g) constitute an axial second rank term

Curie Group	p	ϵ	d	s	g
$\infty \infty ml'$	0	1	0	2	0
$\infty \infty l'$	0	1	0	2	1
∞ / mml'	0	2	0	5	0
∞ / ml'	0	2	0	5	0
$\infty ml'$	1	2	3	5	0
$\infty 2l'$	0	2	1	5	2
$\infty l'$	1	2	4	5	2

TABLE III

Number of independent property coefficients for the fourteen magnetic Curie groups. Axial tensors of rank 1, 3, and 4 are represented by pyromagnetism (i), magnetoelectricity (α), and piezomagnetism (Q). Magnetic susceptibility coefficients behave as a polar second rank tensor

Magnetic Curie Group	i	χ	α	Q
$\infty\infty m$	0	1	0	0
$\infty\infty m'$	0	1	0	0
$\infty\infty$	0	1	0	0
∞/mm'	0	2	1	1
∞/mm	1	2	0	3
$\infty/m'm$	0	2	1	0
$\infty/m'm'$	0	2	2	0
∞/m	1	2	1	4
∞/m'	0	2	3	0
∞m	0	2	1	1
$\infty m'$	1	2	2	3
$\infty 2$	0	2	2	1
$\infty 2'$	1	2	1	3
∞	1	2	3	4

CONNECTIVITY

Connectivity³² is a key feature in property development in multiphase solids since physical properties can change by many orders of magnitude depending on the manner in which connections are made. Imagine, for instance, an electric wire in which the metallic conductor and its rubber insulation were connected in series rather than in parallel. Obviously its resistance would be far higher.

Each phase in a composite may be self-connected in zero, one, two or three dimensions. It is natural to confine attention to three perpendicular axes because all property tensors are referred to such systems. If we limit the discussion to diphasic composites,[†] there are ten connectivities:³² 0-0, 1-0, 2-0, 3-0, 1-1, 2-1, 3-1, 2-2, 2-3, and 3-3. The ten different connectivities are illustrated in Figure 27, using a cube as the basic building block. A 2-1 connectivity pattern, for example, has one phase self-connected in two-dimensional chains or fibers. The connectivity patterns are not generally unique. In the case of a 2-1 pattern, the fibers of the second phase might be perpendicular to the layers of the first phase, as in Figure 27, or they might be parallel to the layers.

During the past few years we have been developing processing techniques for making ceramic composites with different connectivities.³³ Extrusion, tape-casting and replamine methods have been especially successful. The 3-1 connectivity pattern in Figure 27 is ideally suited to extrusion processing. A ceramic slip is extruded

[†]Connectivity patterns for more than two phases are similar to the diphasic patterns, but more numerous. There are 20 three-phase patterns and 35 four-phase patterns compared to the 10 two-phase patterns in Figure 27. For n phases the number of connectivity patterns is $(n+3)!/3!n!$. Triphasic connectivity patterns are important when electrode patterns are incorporated in the diphasic ceramic structures discussed later.

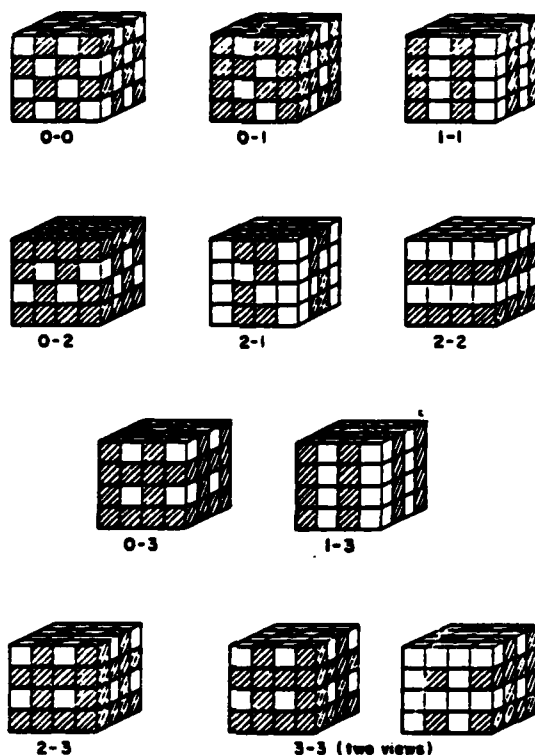


FIGURE 27 Ten connectivity patterns used to describe the tensor properties of diphasic composites.³²

through a die giving a three-dimensionally connected pattern with one-dimensional holes, which can later be filled with a second phase (see Figure 23).

Another type of connectivity well-suited to processing is the 2-2 pattern made up of alternating layers of the two phases. The tape-casting of multilayer capacitors with alternating layers of metal and ceramic is a way of producing 2-2 connectivity. In this arrangement both phases are self-connected in the lateral X and Y directions but not connected perpendicular to the layer along Z .

In 3-2 connectivity, one phase is three-dimensionally connected, the other is two. This pattern can be considered a modified multilayer pattern with 2-2 connectivity. If holes are left in the layers of one phase, layers of the second phase can connect through the holes giving three-dimensional connectivity.

The most complicated and in many ways the most interesting pattern is 3-3 connectivity in which the two phases form interpenetrating three-dimensional networks. Patterns of this type often occur in living systems such as coral where organic tissue and an inorganic skeleton interpenetrate one another. These structures can be replicated in other materials using the lost-wax method. The replamine process, as it is called, can also be used to duplicate the connectivity patterns found in foam, wood, and other porous materials.³⁴

Stress Concentration

The importance of stress concentration in composite materials is well known from structural studies but its relevance to electroceramics is not so obvious. Stress concentration is a key feature of many of the piezoelectric composites made from polymers and ferroelectric ceramics.³³ By focusing the stress on the piezoelectric phase, some of the piezoelectric coefficients can be enhanced and others reduced.³²

As an example, consider the piezoelectric voltage coefficient \bar{g}_{33} , relating electric field to applied stress. Both the tensile stress, σ_3 , and the resulting electric field, E_3 , are parallel to the poling direction.

If the two phases of the composite are arranged in parallel, the stress acting on the more compliant phase will be transferred to the stiffer phase. Under these circumstances, the voltage coefficient is

$$\bar{g}_{33} = \frac{E_3}{\sigma_3} = \frac{\bar{d}_{33}}{\epsilon_3} = \frac{{}^1V {}^1d_{33} {}^2s_{33} + {}^2V {}^2d_{33} {}^1s_{33}}{({}^1V {}^2s_{33} + {}^2V {}^1s_{33})({}^1V \epsilon_{33} + {}^2V \epsilon_{33})}.$$

In this expression the properties of the two are designated with superscripts 1 and 2. Symbols 1V , ${}^1d_{33}$, ${}^1\epsilon_{33}$, and ${}^1s_{33}$ represent the volume fraction of phase 1, and its piezoelectric charge coefficient, electric permittivity, and elastic compliance. The corresponding properties of the second phase are 2V , ${}^2d_{33}$, ${}^2\epsilon_{33}$, and ${}^2s_{33}$.

A composite of interest here is that of a ferroelectric ceramic (phase 1) in parallel with a compliant polymer (phase 2). In this case ${}^1d_{33} \gg {}^2d_{33}$, ${}^1s_{33} \ll {}^2s_{33}$, ${}^1\epsilon_{33} \gg {}^2\epsilon_{33}$, and

$$\bar{g}_{33} = \frac{{}^1d_{33}}{{}^1V \epsilon_{33}} = \frac{{}^1g_{33}}{{}^1V}$$

If 90% of the composite volume is polymer, then ${}^1V = 0.1$ and \bar{g}_{33} is ten times larger than the voltage coefficient of the ceramic, g_{33} . Excellent hydrophone designs are derived from such considerations.³³

Advantageous internal stress transfer can also be utilized in pyroelectric coefficients. If the two phases have different thermal expansion coefficients, there is stress transfer between the phases which generates the electric polarization through the piezoelectric effect. In this way it is possible to make a composite pyroelectric in which neither phase is pyroelectric.³²

Electric Field Concentration

The multilayer design used for ceramic capacitors is an effective configuration for concentrating electric fields. By interleaving metal electrodes and ceramic dielectrics, relatively modest voltages are capable of producing high electric fields.

Multilayer piezoelectric transducers are made in the same way as multilayer capacitors.³⁵ The oxide powder is mixed with an organic binder and tape-cast using a doctor blade configuration. After drying, the tape is stripped from the substrate and electrodes are applied with a screen printer and electrode ink. A number of pieces of tape are then stacked, pressed, and fired to produce a ceramic with internal

electrodes. After attaching leads, the multilayer transducer is packaged and poled. When compared to a simple piezoelectric transducer, the multilayer transducer offers a number of advantages. (1) The internal electrodes make it possible to generate larger fields for smaller voltages, eliminating the need for transformers for high-power transmitters. Ten volts produce a high driving field of 10^5 V/m across a tape-cast layer 100 microns thick produces an electric field of 10^5 V/m. (2) The higher capacitance inherent in a multilayer design may also help in impedance matching. (3) Many different electrode designs can be used to shape poling patterns which in turn controls the mode of vibration and the ultrasonic beam pattern. (4) Additional design flexibility by interleaving layers of different composition, eg alternate ferroelectric and antiferroelectric layers, increase the depoling field. (5) Grain-oriented piezoelectric ceramics can also be tape-cast into multilayer transducers which exhibit enhanced piezoelectric properties by aligning the crystallites parallel to the internal electrodes.³⁶ (6) The thin dielectric layers in a multilayer transducer have improved electric breakdown strength. Gerson and Marshal³⁷ measured the breakdown strength of PZT as a function of specimen thickness. The D.C. breakdown field for ceramics 1 cm thick were less than half that of 1 mm thick samples. It is likely that the trend will continue to even thinner specimens, leading to easier poling and more reliable transducers.

Perhaps even more important than these factors is the enhancement of electrostrictive effects. Electrostriction is a second order electromechanical coupling between strain and electric field. For small fields electrostrictive strains are small compared to piezoelectric strain, but this is not true for the high fields generated in multilayer transducers.

Multilayer electrostrictive transducers³⁸ made from relaxor ferroelectrics such as lead magnesium niobate (PMN) are capable of generating strains larger than PZT (Figure 28). Since there are no domains in PMN there are no "walk-off" effects in electrostrictive micropositioners. Moreover, poling is not required and there are no aging effects. The concentration of electric fields make nonlinear effects increasingly important.

Multilayer Thermistors

For many applications it is desirable to lower the room temperature resistance because the thermistor elements are often connected in series with the circuit elements they are designed to protect. It is possible, of course, to lower the resistivity of the composite by altering the components, but the resistivity cannot be lowered indefinitely without degrading the PTC thermistor effect.

The introduction of internal electrodes offers a way to reduce the resistance per unit volume without affecting the temperature characteristics. Thermistor devices are presently being fabricated as ceramic discs or as composite wafers. Recently we developed a way of making multilayer BaTiO_3 PTC thermistors³⁹ which greatly lowers the room temperature resistance. Barium titanate powder doped with rare-earth ions is mixed with an organic binder and tape cast on glass slides. Electrodes are then screen-printed on the tapes, followed by stacking, pressing, and firing. The internal electrode configuration is very similar to multilayer capacitors.

The basic idea involves comparison of a single layer disk thermistor with a multilayer thermistor of the same external dimensions. The multilayer device is

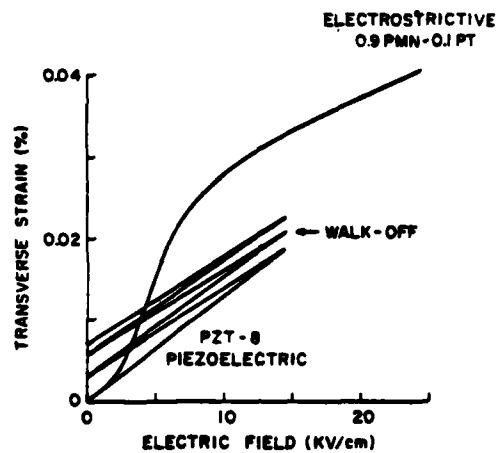


FIGURE 28 Comparison of electrostrictive and piezoelectric micropositioners. Nonlinear effects become important in multilayer composites where the electric fields are large.

assumed to have n ceramic layers and $n + 1$ electrodes. Let A represent the area of the single layer disk thermistor, t be its thickness, and ρ the resistivity. The resistance of the disk thermistor is

$$R_s = \rho t / A.$$

For the multilayer thermistor the total electroded area is nA (neglecting margins) and the thickness is t/n (neglecting the electrode thickness). The resistance of the multilayer device is

$$R_M = \rho(t/n) / nA = R_s / n^2.$$

The resistivity of the thermistor is lowered by a factor of $1/n^2$ with $n - 1$ internal electrodes.

We have demonstrated the feasibility of this idea with a multilayer device containing four tape-cast layers. As predicted, the resistance of the multilayer specimen is approximately $n^2 (= 16)$ times smaller with very little change in the temperature characteristic.

SUMMARY

Some of the basic ideas underlying composite electroceramics have been illustrated in this paper and are summarized as follows:

1. *Sum properties* involve the averaging of similar properties in the component phases, with the mixing rules bounded by the series and parallel models. For a simple sum property such as the dielectric constant, the dielectric constant of the composite lies between those of the individual phases. This is not true for

combination properties based on two or more properties. Acoustic velocity depends on stiffness and density, and since the mixing rules for these two properties are often different, the acoustic velocity of a composite can be smaller than those of its constituent phases.

2. *Product properties* are even more complex because three properties are involved: different properties in the constituent combine to yield a third property in the composite. In a magnetoelectric composite, the piezoelectric effect in barium titanate acts on the magnetostrictive effect of cobalt ferrite to produce a composite magnetoelectric effect.
3. *Connectivity patterns* are a key feature of composite electroceramics. The self-connectiveness of the phases determines whether series or parallel models apply, and thereby minimize or maximize the properties of the composite. The three-dimensional nature of the connectivity patterns makes it possible to minimize some tensor components while maximizing others. Piezoelectric composites made from parallel ferroelectric fibers have large d_{33} coefficients and small d_{31} values.
4. *Concentrated field and force patterns* are possible with carefully selected connectivities. Using internal electrodes, electrostrictive ceramics are capable of producing strains comparable to the best piezoelectrics. Stress concentration is achieved by combining stiff and compliant phases in parallel. A number of different hydrophone designs are based on this principle.
5. *Periodicity and scale* are important factors when composites are to be used at high frequencies where resonance and interference effects occur. When the wavelengths are on the same scale as the component dimension, the composite no longer behaves like a uniform solid. The colorful interference phenomena observed in opal and feldspar minerals are interesting examples of natural composites. Acoustic analogs occur in the PZT-polymer composites used as biomedical transducers.
6. *Symmetry* governs the physical properties of composites just as it does in single crystals. The Curie Principle of symmetry superposition and Neumann's Law can be generalized to cover fine-scale composites, thereby elucidating the nature of their tensor properties. As in the case of magnetoelectric composites, sometimes the composite belongs to a symmetry group which is lower than any of its constituent phases. Unexpected product properties occur under such circumstances.
7. *Interfacial effects* can lead to interesting barrier phenomena in composites. ZnO-Bi₂O₃ varistors and carbon-polymer PTC thermistors are important examples of Schottky barrier effects. Barrier layer capacitors made from conducting grains separated by thin insulating grain boundaries are another example.
8. *Polychromatic percolation* is an interesting concept which has yet to be fully explored. Composites fabricated from two or more conducting phases can have several kinds of transport paths, both single phase and mixed, depending on percolation limits and volume fractions. Carbon-PZT-polymer composites can be poled because polychromatic percolation establishes flux continuity through ferroelectric grains. The SiC-BeO composites under development as substrate ceramics are another example. These diphasic ceramics are excellent thermal conductors and poor electrical conductors at one and the same time. A thin

layer of BeO-rich carbide separates the SiC grains, insulating them from one another electrically, but providing a good acoustic impedance match ensuring phonon conduction.

9. *Coupled phase transformation* in polyphasic solids introduce additional possibilities. Recently discovered NTC-PTC composites made from V_2O_5 powder and embedded in polyethylene combine matrix and filler materials with complementary properties. At low temperatures the vanadium oxide particles are in a semiconducting state and in intimate contact with one another. On passing through a semiconductor-metal transition, the electrical conductivity increases by five orders of magnitude. Further heating brings the polymer to a phase transformation, causing a rapid expansion in volume, and pulling the V_2O_5 particles apart. As a consequence the electrical conductivity decreases dramatically by eight orders of magnitude. In addition to this "Window Material" with a controlled conductivity range, several other composites with coupled phase transformations were described in the text.
10. *Porosity and inner surfaces* play a special role in many electroceramic composites used as sensors. Humidity sensors made from Al_2O_3 and LiF have high inner surface area because of thermally induced fracture. The high surface area and hygroscopic nature of the salt, result in excellent moisture sensitivity of the electrical resistance. Chemical sensors based on similar principles can be constructed in the same way.

REFERENCES

1. J. Van Suchtelen, *Philips Res. Rep.*, **27**, 28 (1972).
2. G. Partridge, *Glass Technology*, **24**, 293 (1983).
3. David Payne, Ph.D. Dissertation in Solid State Science, Pennsylvania State University (1973).
4. Ross and Sierakowski, *Shock and Vibration Digest*, **7**, 1 (1975).
5. T. R. Gururaja, Ph. D. Thesis in Solid State Science, Pennsylvania State University, 1984.
6. H. Weis, *Met. Trans.*, **2**, 1513 (1971).
7. W. N. Lawless, Private Communication.
8. J. van den Boomgaard, D. R. Terrell, R. A. J. Born and H. F. J. I. Giller, *J. Math. Sci.*, **9**, 1705 (1974).
9. A. M. J. G. van Run, D. R. Terrell and J. H. Scholing, *J. Math. Sci.*, **9**, 1710 (1974).
10. L. P. M. Bracke and R. G. Van Vliet, *Int. J. Electronics*, **51**, 255 (1981).
11. G. Rajagopal and M. Satyam, *J. Appl. Physics*, **49**, 5536 (1978).
12. S. K. Bhattacharya and A. C. D. Chaklader, *Polym. Plast. Tech. Eng.*, **19**, 21 (1982).
13. F. A. Doljack, *Trans. I.E.E.E., CHMT-4*, 372 (1981).
14. D. P. H. Smith and J. C. Anderson, *Phil. Mag. B*, **43**, 811 (1981).
15. K. A. Hu, B. V. Hiremath, J. P. Runt and R. E. Newnham (in preparation).
16. F. J. Morin, *Phys. Rev. Lett.*, **3**, 34 (1959).
17. B. C. Tofield and D. E. Williams, *Solid State Ionics*, **83**, 1299 (1983).
18. Y. Takuma, M. Miyoyama, and H. Yanagida, *Chemistry Letters*, **1982**, 345 (1982).
19. H. Yanagida, "Materials Design in Functional Ceramics," *Bull. Am. Ceramics Soc.*, **63**, 1135 (1984).
20. Y. Toyoshima, Miyayama and H. Yanagida, *Japan J. Appl. Phys.*, **22**, 1933 (1983).
21. D. Stockel, Proc. A.I.M.E. Conference on Composites, p. 139 (1975).
22. R. Zallen, *Phys. Rev.*, **B16**, 1426 (1977).
23. R. Newnham, A. Safari, G. Sa-gong, and J. Giniewicz, *Trans. I.E.E.E.* (in press).
24. Y. Bar-Cohen, D. A. Stubbs and W. C. Hopps, "Multiphase Backing Materials for Piezoelectric Broadband Transducers," *J. Acoust. Soc. Amer.*, **75**, 1629-1633 (1984).
25. J. F. Nye, "Physical Properties of Crystals," (Oxford University Press, 1957).
26. A. V. Shubnikov and V. A. Koptsik, "Symmetry in Science and Art," (Plenum Press, N.Y., 1974).
27. J. J. Gebhardt, *A.C.S. Symposium Series*, **21**, 212 (1976).
28. I. M. Lachman, R. D. Bagley and R. M. Lewis, *Bull. Amer. Ceram. Soc.*, **60**, 202 (1981).

29. T. R. Shrout, L. J. Bowen, and W. A. Schulze, *Mat. Res. Bull.*, **15**, 1371 (1980).
30. A. Safari, A. Halliyal, R. E. Newnham and I. M. Lachman, *Math. Res. Bull.*, **17**, 302 (1982).
31. A. Halliyal, A. S. Bhalla and R. E. Newnham, *Mat. Res. Bull.*, **18**, 1007 (1983).
32. R. E. Newnham, D. P. Skinner and L. E. Cross, *Math. Res. Bull.*, **13**, 525 (1978).
33. R. E. Newnham, L. J. Bowen, K. A. Klicker and L. E. Cross, *Materials in Eng.*, **11**, 93 (1980).
34. R. A. White, J. N. Weber, and E. W. White, *Science*, **176**, 922 (1972).
35. G. O. Dayton, W. A. Schulze, R. T. Shrout, S. Swartz and J. V. Biggers, *Adv. in Ceramics*, **8**, 115 (1984).
36. M. Granahan, M. Holmes, W. A. Schulze and R. E. Newnham, *J. Amer. Ceram. Soc.*, **64**, C68 (1981).
37. R. Gerson and T. C. Marshal, *J. Appl. Phys.*, **30**, 1650 (1959).
38. K. Uchino, S. Nomura, L. E. Cross, R. E. Newnham and S. J. Jang, *J. Mater. Sci.*, **16**, 569 (1981).
39. B. V. Hiremath, K. A. Hu and R. E. Newnham (in preparation).

FERROELECTRIC COMPOSITES

R.E. Newnham

Ferroelectric Composites

R. E. NEWNHAM

Materials Research Laboratory The Pennsylvania State University University Park, Pennsylvania, 16802 U.S.A.

Some of the underlying ideas governing composite ferroelectrics and their applications are reviewed: sum and product properties, combination properties and the figure of merit, three-dimensional connectivity patterns leading to field and stress rearrangement, boundary conditions in composites, the symmetry of composite materials and its influence on physical properties, the importance of periodicity and scale in ferroelectric composites, the effect of ferroelectric phase transitions on interfacial phenomena, thermistor effects arising from coupled phase transformations, polyohromatic percolation and the poling of composites through the use of coupled flux paths, electrostriction and other non-linear phenomena, and the important role that porosity and inner surfaces play in many composites.

§1. Introduction

In modern usage, composite materials are made from a filler—usually in the form of particles, flakes, or fibers—embedded in a matrix made of polymer, metal or glass. According to the broadest definition of the word, however, almost any material consisting of two or more phases, is a composite. If we accept the latter definition, most—if not all—practical applications of ferroelectrics involve the use of composite materials. Many of these innovations have taken place here in Japan, where university scientists and industrial engineers lead the world in the development of new ferroelectric components and devices.

Space restrictions forbid the full development of the ideas presented in this talk, but by way of summary, we might state them as eight basic concepts. Further detail can be found in the references.

§2. Physical Properties

For polyphasic materials, the properties can be classified as sum properties, combination properties, and product properties.¹⁾

Sum properties involve the averaging of an analogous property coefficient in the constituent phases, with the mixing rules bounded by the series and parallel models. For a simple sum property such as the dielectric constant,²⁾ the dielectric constant of the composite lies between those of the individual phases. In multilayer capacitors made from ferroelectric ceramics, a grain boundary phase is sometimes used to depress the peaks in the dielectric constant, thereby improving the temperature coefficient.

A "figure of merit" involving two or more property coefficients is often used to determine the best material for a given application. For a composite material, **combination properties** require that two or more properties be averaged for the component phases. Acoustic velocity depends on stiffness and density, and since the mixing rules for these two properties are often different, the acoustic velocity of a composite can be smaller than those of its constituent phases.³⁾

Product properties are even more complex because three properties are involved: different properties in the constituent combine to yield a third property in the composite. In a magnetoelectric composite, the piezoelectric

effect in barium titanate acts on the magnetostrictive effect of cobalt ferrite to produce a composite magnetoelectric effect.^{4, 5)}

§3. **Connectivity patterns** are a key feature of composite electroceramics. The self-connectiveness of the phases determines whether series or parallel models apply, and thereby minimize or maximize the properties of the composite. The three-dimensional nature of the connectivity patterns makes it possible to minimize some tensor components while maximizing others.⁶⁾ Piezoelectric composites made from stiff ferroelectric fibers in a compliant matrix have large d_{33} coefficients and small d_{31} values.

Concentrated field and force patterns are possible with carefully selected connectivities. Using internal electrodes, electrostrictive ceramics⁷⁾ are capable of producing strains comparable to the best piezoelectrics. Stress concentration is achieved by combining stiff and compliant phases in parallel. A number of different hydrophone designs are based on this principle.⁸⁾

§4. **Periodicity and scale** are important factors when composites are to be used at high frequencies where resonance and interference effects occur. When the wavelengths are on the same scale as the component dimension, the composite no longer behaves like a uniform solid. Acoustic phase plates and biomedical transducers made from diced ceramics are under investigation at several laboratories.⁹⁾

§5. **Symmetry** governs the physical properties of composites just as it does in single crystals. The Curie Principle of symmetry superposition and Neumann's Law can be generalized to cover fine-scale composites, thereby elucidating the nature of their tensor properties.¹⁰⁾ As in the case of magnetoelectric composites, sometimes the composite belongs to a symmetry group ($\infty m'$) which is lower than any of its constituent phases. Unexpected product properties occur under such circumstances. Composite structures belong to many different symmetries: crystallographic groups, black-and-white groups, color groups, and Curie groups.

§6. **Interfacial effects** can lead to interesting barrier phenomena in composites. Varistors and PTC ther-

istors are important examples of Schottky barrier effects.⁽¹¹⁾ Barrier layer capacitors made from conducting grains separated by thin insulating grain boundaries are another example.

§7. Percolation is a well-known phenomenon in thick film components, but *polychromatic percolation*⁽¹²⁾ is an interesting concept which has yet to be fully explored. Composites fabricated from two or more conducting phases can have several kinds of transport paths, both single phase and mixed, depending on phase segregation, percolation limits, and volume fractions. Carbon-PZT-polymer composites can be poled because polychromatic percolation establishes flux continuity through ferroelectric grains.⁽¹³⁾

§8. Coupled phase transformations in polyphasic solids introduce additional possibilities. Recently discovered NTC-PTC composites made from V_2O_5 powder and embedded in polyethylene combine matrix and filler materials with complementary properties. At low temperatures the vanadium oxide particles are in a semiconducting state and in intimate contact with one another. On passing through a semiconductor-metal transition, the electrical conductivity increases by five orders of magnitude. Further heating brings the polymer to a phase transformation, causing a rapid expansion in volume, and pulling the V_2O_5 particles apart. As a consequence the electrical conductivity decreases dramatically by eight orders of magnitude.⁽¹⁴⁾

§9. Porosity plays a special role in some ferroelectric composites. Many kinds of porous ceramic sensors are under development for measuring humidity, methane gas concentration, temperature and pressure. Superb PTCR thermistors have been made from porous $BaTiO_3$ semiconductors doped with antimony.⁽¹⁵⁾ A maximum

step in resistivity of 10^4 times occurred for ceramics with about 20% connected porosity and very small grain size near $1 \mu m$. Oxygen diffusion is essential in of minor insulating Schottky barriers between the conducting ceramic grains, and porosity enhances the accessibility of grain boundaries to the atmosphere during the critical cooling process following sintering.

For many chemical sensors, the sensitivity is affected by catalytic coatings. Ferroelectric polarization is known to affect adsorptive and catalytic properties in certain systems. Studies of carbon monoxide oxidation over Pd deposited on $LiNbO_3$ crystals show that the positive polar surface interacts strongly with small Pd particles, and effectively reduces the CO adsorption bond.⁽¹⁶⁾

References

- 1) J. van Suchtelen: Philips Res. Repts. 27 (1972) 28.
- 2) L. K. H. van Beek: Prog. in Dielect. 7 (1965) 69.
- 3) C. A. Ross and R. L. Sierakowski: Shock and Vibration Digest 7 (1975) 1.
- 4) J. van den Boomgaard, D. R. Terrell, R. A. J. Born and H. F. J. I. Giller: J. Mat. Sci. 9 (1974) 1705.
- 5) A. M. J. G. van Run, D. R. Terrell and J. H. Scholing: J. Mat. Sci. 9 (1974) 1710.
- 6) R. E. Newnham, D. P. Skinner and L. E. Cross: Mat. Res. Bull. 13 (1978) 525.
- 7) K. Uchino, S. Nomura, L. E. Cross and R. E. Newnham: J. Mat. Sci. 16 (1981) 569.
- 8) R. E. Newnham, L. J. Bowen, K. A. Klicker and L. E. Cross: Mat. in Eng. II (1980) 93.
- 9) T. R. Gururaja, W. A. Schulze, L. E. Cross, B. A. Auld and J. Wang: Proc. IEEE Ultrasonic Symp. (1984) 533.
- 10) I. S. Zheludev: Solid State Phys. 29 (1974) 315.
- 11) B. M. Kulwicki: J. Phys. Chem. Solids. 45 (1984) 1015.
- 12) R. Zallen: Phys. Rev. B16 (1977) 1426.
- 13) A. Safari, G. Sa-gong, J. Giniewicz and R. E. Newnham (in press).
- 14) K. A. Hu, J. Runt, A. Safari and R. E. Newnham (in press).
- 15) M. Kuwabara: Sol. State Elec. 27 (1984) 929.
- 16) Y. Inoue, I. Yoshioka and K. Sato: J. Phys. Chem. 88 (1984) 1148.

NEW MATERIALS FOR HYDROPHONE APPLICATIONS-
SINGLE CRYSTALS AND POLAR GLASS-CERAMICS

R.Y. Ting, A. Halliyal, and A.S. Bhalla

New Materials for Hydrophone Applications- Single Crystals and Polar Glass-Ceramics

R. Y. TING, A. HALLIYAL*, and A. S. BHALLA*

*Underwater Sound Reference Division, Naval Research
 Laboratory, P.O. Box 8337, Orlando, FL 32856, USA*

**Materials Research Laboratory, The Pennsylvania
 State University, University Park, PA 16802, USA*

Hydrostatic piezoelectric strain coefficients d_h (~ 10 pC/N) and voltage coefficients g_h ($80-100 \times 10^{-1}$ V m/N) on single crystals of $\text{Ba}_2\text{TiSi}_2\text{O}_8$, $\text{Ba}_2\text{TiGe}_2\text{O}_8$ have been measured as a function of temperature, pressure, and frequency. The values are found to be comparable to those of the state of the art piezoelectric PVDF polymers.

Measurements are also made on the glass-ceramics in the compositions of $\text{BaO-TiO}_2\text{-SiO}_2$ and some isostructural materials compositions in the system $\text{BaO-TiO}_2\text{-GeO}_2$. The typical values of the piezoelectric constants of glass ceramics are almost on the order of those obtained on the respective single crystal samples. Glass-ceramics provide a promising way of achieving the larger area samples needed for various piezoelectric devices.

§1. Introduction

Glass ceramics containing the crystalline phases of Li_2SiO_3 , $\text{Li}_2\text{Si}_2\text{O}_5$, $\text{Ba}_2\text{TiSi}_2\text{O}_8$, $\text{Ba}_2\text{TiGe}_2\text{O}_8$, $\text{Li}_2\text{B}_4\text{O}_7$ have shown large pyroelectric, piezoelectric and electromechanical coupling comparable to those obtain on the respective single crystalline phases.¹⁻⁵⁾ In our earlier studies, glass ceramics with the fersnoite crystalline phase were studied⁵⁾ as a potential transduction materials for application in sonar transducers. Glass ceramic of fersnoite $\text{Ba}_2\text{TiSi}_2\text{O}_8$ compositions showed the large hydrostatic voltage sensitivity. Also the free field voltage sensitivity of glass ceramic prototype hydrophone was higher than the sensitivity measured on those fabricated from the commonly used lead zirconate titanate ceramic elements. Piezoelectric properties d_h and g_h were also independent of pressure.

In the present paper, we report the hydrostatic piezoelectric properties measured on various nonferroelectric piezoelectric materials which could be of interest (for sonar transducers). Piezoelectric constants of $\text{Ba}_2\text{TiSi}_2\text{O}_8$ (BTS), $\text{Ba}_2\text{TiGe}_2\text{O}_8$, $\text{Li}_2\text{B}_4\text{O}_7$ single crystals are determined in order to project the expected hydrostatic piezoelectric performance from the glass ceramics containing any of these crystalline phases.

Fersnoite is one of the unique materials in which both d_{33} and d_{31} are positive and thus $d_h > d_{33}$. It is expected that some other members in this family may also give similar results. $\text{Ba}_2\text{TiGe}_2\text{O}_8$ is a ferroelastic material with probable crystal symmetry mm2 at room temperature. $\text{Li}_2\text{B}_4\text{O}_7$ has interesting SAW, piezoelectric, and pyroelectric properties.^{6,7)}

§2. Experimental and Results

Single crystal samples of $\text{Ba}_2\text{TiGe}_2\text{O}_8$, BTS, $\text{Li}_2\text{B}_4\text{O}_7$ were grown by Czochralski technique. $\text{Li}_2\text{B}_4\text{O}_7$ crystals provided by Plessey, UK, were studied for comparative studies. Crystals were cut in the form of c-plates and polished to thicknesses 0.5-1 mm.

Glass ceramics with oriented crystallites were prepared by recrystallizing the glasses of corresponding compositions in a temperature gradient. Detailed procedure for the preparation of glass ceramic samples has been described

in earlier papers.¹⁻⁵⁾ After recrystallization, oriented plates were cut normal to the temperature gradient direction and then polished to the desired thickness ≈ 0.4 mm.

Plates were coated with the sputtered gold electrodes and also the silver paint electrodes were applied on both sides of the samples. Piezoelectric d_{33} and d_{31} were measured by the d_{33} -meter and K and $\tan \delta$ were measured by the computer assisted set up using the HP-capacitance bridge.

The hydrostatic piezoelectric constants were measured by using an acoustic reciprocity technique.⁸⁻⁹⁾ Temperature and pressure of the samples were controlled to within $\pm 0.1^\circ\text{C}$ and ± 0.02 MPa, respectively.

The hydrostatic characteristics of the single crystals and glass ceramic samples were evaluated in a prototype design using a standard NRL-USRD H23 oil filled hydrophone assembly. Free-field voltage sensitivity as a function of frequency was measured at the NRL-USRD lake facility. The results of the experiments are summarized in Tables I and II. The pressure dependence of the piezoelectric properties of glass ceramics along with the single crystal is shown in Figure 1.

PZT and PVF₂ samples showed a pressure dependence of d_h and g_h whereas hydrophone characteristics of single crystals of BTS, BTG, $\text{Li}_2\text{B}_4\text{O}_7$ and the glass ceramics were pressure and temperature independent. Also the pressure cycling didn't show any pressure hysteresis effects which is in general quite significant in many potential hydrophone materials.¹⁰⁾

Thus it is evident that $\text{Ba}_2\text{TiSi}_2\text{O}_8$, $\text{Ba}_2\text{TiGe}_2\text{O}_8$, $\text{Li}_2\text{B}_4\text{O}_7$ and their analogue are potential candidate materials for hydrostatic pressure sensing devices. The d_h and g_h responses in these materials are independent of temperature (0-50°C), pressure (0-35 MPa) and frequency.

Table I. Piezoelectric Characteristics of Single Crystal Materials and $\text{Ba}_2\text{TiSi}_2\text{O}_8$ Glass Ceramics.

Material	Crystal Class	d_{11} (pC/N)	d_{11} (pC/N)	d_h (pC/N)	g_h ($\times 10^{-1}$ V m/N)
$\text{Ba}_2\text{TiSi}_2\text{O}_8$	4mm	8	1.5	11-12	82
$\text{Ba}_2\text{TiGe}_2\text{O}_8$	mm2	9			80
$\text{Li}_2\text{B}_4\text{O}_7$	4mm	24	-4.5	15	250
Glass Ceramic	∞ mm	8-10		8-10	90-100

Table II. Comparison of Measured Hydrophone Materials Properties.

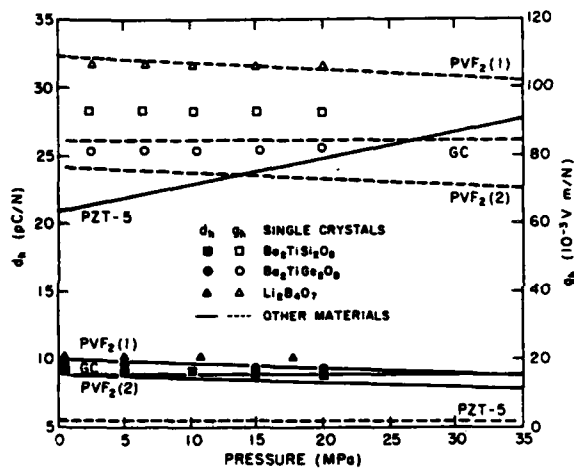
Material	K	Dielectric $\tan \delta$	d_r (pC/N)	Piezoelectric g_h 10^{-3} V m/N	dB re 1 V μPa	FFVS	Sample Thickness (mm)
PZT-4	1300	10^{-2}	45	4.0			
PZT-5	1600	10^{-2}	21	2	-222		6
Li_2SO_4	10	—	14	148	-187		6.4
PVF_2	13-10	10^{-2}	9-10	78-108	-207 to -202		0.7-0.56
$\text{Ba}_2\text{TiSi}_2\text{O}_8$ (SC)	11.5	$< 10^{-3}$	9-10	86-90	-210		0.4
BTS (GCI)	13	$< 10^{-3}$	8	82			
BTS (GCII)	12	$< 10^{-3}$	10	82			
$\text{Ba}_2\text{TiGe}_2\text{O}_8$ (SC)	12.5	10^{-3}	9	80			
$\text{Li}_2\text{B}_4\text{O}_7$ (SC)	10	10^{-2}	10	103			
	(0°C)	(0°C)					

GC-Glass ceramic

SC-Single crystal

BTS- $\text{Ba}_2\text{TiSi}_2\text{O}_8$

FFVS-Free field voltage sensitivity.

Fig. 1. Hydrostatic pressure dependence of piezoelectric d_h and g_h of single crystals of $\text{Ba}_2\text{TiGe}_2\text{O}_8$, $\text{Ba}_2\text{TiSi}_2\text{O}_8$, and $\text{Li}_2\text{B}_4\text{O}_7$, BTS glass ceramics (GC), PVF_2 and PZT-5 ceramics.

cy (0-50 kHz) and the free field voltage response is free of ageing and pressure hysteresis effects. The large area glass ceramic samples of these compositions can be prepared. Also the glass ceramics exhibit the hydrostatic piezoelectric properties equivalent to their respective single crystalline phases.

Acknowledgement

The authors are thankful to Dr. R. W. Whatmore and F. W. Ainger (Plessey, UK) for providing $\text{Li}_2\text{B}_4\text{O}_7$ single crystal. A. S. Bhalla and A. Halliyal acknowledge the support of the National Science Foundation (Grant No. DMR-8303906) and the Office of Naval Research (Contract No. N00014-82-K0339).

References

- 1) A. S. Bhalla, G. J. Gardopce: *Ferroelectrics* 27 (1980) 123.
- 2) G. J. Gardopce, R. E. Newnham, A. Halliyal and A. S. Bhalla: *Appl. Phys. Lett.* 36 (1980) 817.
- 3) G. J. Gardopce, R. E. Newnham and A. S. Bhalla: *Ferroelectrics* 33 (1981) 155.
- 4) A. Halliyal, A. S. Bhalla, R. E. Newnham and L. E. Cross: *J. Appl. Phys.* 53 (1982) 2871.
- 5) R. Y. Ting, A. Halliyal and A. S. Bhalla: *Appl. Phys. Lett.* 44 (1984) 852.
- 6) R. W. Whatmore, N. M. Shorrocks, F. W. Ainger and I. M. Young: *Electronics Lett.* 17 (1981) 11.
- 7) A. S. Bhalla and L. E. Cross: *IMF-6 Proceedings*.
- 8) R. J. Bobber: *Underwater Electroacoustic Measurements* GPO, Washington, DC (1970) 27-41.
- 9) C. C. Sims and T. A. Henriquez: *J. Acous. Soc. Amer.* 36 (1964) 1704.
- 10) R. Y. Ting: *Ferroelectrics* 49 (1983) 251.

POLING FLEXIBLE PIEZOELECTRIC COMPOSITES

G. Sa-Gong, A. Safari, S.J. Jang, and R.E. Newnham

POLING FLEXIBLE PIEZOELECTRIC COMPOSITES †

G. SA-GONG*, A. SAFARI, S.J. JANG AND R.E. NEWNHAM

Materials Research Laboratory, The Pennsylvania State
University, University Park, PA 16802

(Received for Publication December 17, 1985)

Abstract: Flexible piezoelectric composites made from PZT and polymer with 0-0-3 connectivity were fabricated using several types of Eccogel polymer. The conductivity of the composite is controlled by adding small amounts of a semiconductor filler such as carbon, germanium or silicon. By controlling conductivity, poling can be carried out very rapidly at low voltages, resulting in properties comparable to composites prepared without a conductive phase. For composites optimized for hydrophone performance, the hydrostatic voltage coefficient \bar{g}_h and hydrostatic figure of merit $\bar{g}_h \bar{d}_h$ are an order of magnitude larger than those of single phase PZT.

INTRODUCTION

Lead zirconate titanate (PZT) ceramics are used extensively as piezoelectric transducer materials despite several disadvantages. PZT has a large piezoelectric d_{33} coefficient

*Present address: Department of Electrical Engineering, Dong-A University, Pusan 600-02, South Korea

†Communicated by Dr. G. W. Taylor

but its hydrostatic piezoelectric coefficient $d_h (=d_{33}+2d_{31})$ is very low because d_{33} is positive and d_{31} is negative. Moreover, its high permittivity ($\epsilon=1800\epsilon_0$) lowers the voltage coefficient $g_h (=d_h/\epsilon)$ which is important to many devices. In addition, the high density of PZT (7.9g/cm^3) makes it difficult to obtain good impedance matching with water. PZT is a brittle ceramic and for some applications a more compliant material with better shock resistance is desirable.

One approach to these problems is with composite bodies made from piezoelectric ceramics and flexible polymers. The polymer phase lowers the density and permittivity and increases the elastic compliance. Over the past few years several investigators have examined PZT-polymer composite with different connectivity patterns. A summary can be found in references 1 and 2.

The simplest type of piezoelectric composite consists of a polymer matrix loaded with ceramic powder. In this type of composites, the particles are not in contact with each other and the polymer phase is self connected in all three dimensions, the so-called 0-3 connectivity³. In many ways the 0-3 composites are similar to polyvinylidene fluoride [$\text{PVF}_2=(\text{CH}_2-\text{CF}_2)_n$]. Both consist of a crystalline phase embedded in an amorphous matrix, and both are reasonably flexible.

The first flexible piezoelectric composites were made by embedding PZT particles 5-10 μm in size in polyurethane polymer^{4,5}. The \bar{d}_{33} coefficient of these composites were comparable with PVF_2 but the \bar{d}_h coefficient was lower than those of PZT and PVF_2 .

One difficulty with this type of composite is that the piezoelectric particles are smaller in diameter than the thickness of the composite. For fine-grain piezoelectric powder in a polymer matrix, very large poling fields are needed to achieve sufficient poling⁶. The reason for large fields

required for poling will be made clear from the following discussion.

For a 0-3 composite consisting of spherical grains embedded in a matrix, the electric field E_1 , acting on an isolated spherical grain is given by⁷

$$E_1 = \frac{3K_2}{K_1 + 3K_2} E_0$$

In this equation, K_1 and K_2 are the dielectric constants of the spherical piezoelectric grains and polymer matrix, respectively, and E_0 is the externally applied electric field. For a 0-3 composite of PZT powder and polymer, $K_1 \sim 1800$ and $K_2 \sim 5$. For such a composite with an external field of 100 KV/cm, the electric field acting on the piezoelectric particles is only about 1 KV/cm which is insufficient to pole PZT. According to the above equation, $E_1 \sim E_0$ only when the dielectric constant of the piezoelectric phase approaches that of the polymer phase. Most of the ferroelectric materials have very high dielectric constants and hence the above condition cannot be satisfied.

The importance of conductivity to poling can be assessed by applying the Maxwell-Wagner model to the 0-3 composites⁷. The model leads to a relationship between the electric field strength and the conductivities of the two phases.

After applying a DC poling field to the sample for a time long compared to the sample relaxation time, the field distribution in a two-layer capacitor is given by $\{E_1/E_2 = \sigma_2/\sigma_1\}$. The field acting on the ceramic is controlled by σ_2/σ_1 , the ratio of the electrical conductivity of the polymer to that of the ceramic.

One way to pole 0-3 composites is to create a continuous electric flux path between the PZT particles. To do this, we

added a small volume fraction of a conductive third phase to the PZT-polymer composite. Addition of a conductive phase to the composite raises the conductivity of the polymer matrix. This in turn increases the field on the high-K ferroelectric filler, making poling easier.

In the present study flexible piezoelectric composites of PZT and polymer were developed using small additions of carbon, germanium or silicon. This new piezoelectric composite has a 0-0-3 connectivity pattern, since the PZT and semiconductor phase are not self connected and the polymer phase is self connected in all three dimensions. These composites can be poled quickly at low voltages. The effect of the semiconductor phase on the poling condition and dielectric loss will be described in this paper.

SAMPLE PREPARATION

Commercial PZT-501A (Ultrasonic Powder, Inc.) and Eccogel polymer (an epoxy obtained from Emerson and Cuming) were used as piezoelectric filler and matrix respectively. The third semiconductor phase are fine-grained carbon, germanium and silicon (alpha product). To prepare the composites, PZT was mixed with one of the semiconductor phases and dry ball-milled for two hours. The polymer matrix was then added to the particulate phases and mixed by hand with spatula. The mixture was then placed in a mold and the composite formed under a pressure of 7500 PSI (50MPa). After curing, the composite was polished slightly to ensure that the faces of the composite were parallel. Electrodes of air-dried silver paste (Materials for Electronics, Inc., Jamaica, New York) were applied to the surfaces of the composite. The samples were poled at 100°C in a stirred oil bath. The effect of the magnitude of the poling field and its duration on the piezoelectric coefficients will be discussed later.

MEASUREMENTS

The capacitance and dissipation factor were measured at 1 kHz using a Hewlett-Packard 4270A Multi-Frequency LCR Meter. The \bar{d}_{33} coefficient was measured using a Berlincourt Piezo d_{33} -meter with the electromagnetic driver operating at a frequency of 100 Hz.

The \bar{g}_h coefficient was determined using the dynamic A.C. technique. An electromagnetic driver was used as an A.C. stress generator to apply pressure waves to the sample and a PZT standard, which were kept under a static pressure from the hydraulic press. The charge produced by the sample and standard were buffered with an impedance converter, and the voltages produced were measured on a Hewlett-Packard 3585A Spectrum Analyzer. The ratio of the voltages is proportional to the \bar{g}_h coefficients. Accounting for the geometries of the sample and PZT standard, and the stray capacitance of the holders, the \bar{g}_h coefficient of the sample was calculated. Using the measured values of \bar{g}_h , the hydrostatic piezoelectric coefficient, \bar{d}_h , was calculated from the relation, $\bar{d}_h = \epsilon_0 \bar{K} \bar{g}_h$.

The electrical resistivity of the composites was measured at poling temperature using a Keithly electrometer Model 616.

RESULTS AND DISCUSSION

Figure 1 shows the electrical resistivities of the germanium-polymer composite, carbon-polymer composite and PZT-polymer composites with and without conductive phase, all measured at the poling temperature (100°C). The resistivities of solid PZT and Eccogel polymer are also listed for comparison. The resistivity of the Eccogel polymer decreased by order of magnitude when a small amount of carbon or germanium was added. The resistivity of the PZT-polymer composite with carbon or germanium also decreased, as expected.

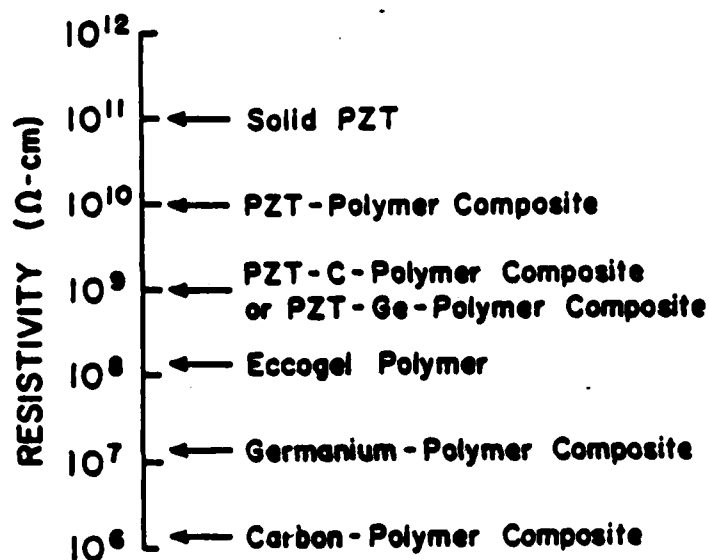


Figure 1. Resistivity of the PZT, the Eccogel polymer (1365-0) and several different composites measured at the poling temperature.

Table 1 summarizes the results of the dielectric and piezoelectric measurements on the PZT-polymer composites with different conductive phase additives. The corresponding values of solid PZT and PZT-polymer composites without a conductive phase additives are also listed for comparison.

The tangent δ of the composites containing a conductive phase are about twice that of a composite prepared without a conductive phase. Dielectric constant of the composites are similar but the \bar{d}_{33} , \bar{g}_h and \bar{d}_h coefficients of the composites with carbon, germanium or silicon are higher than those of composite without a conductive phase. Especially noteworthy are the \bar{g}_h and $\bar{g}_h \bar{d}_h$ values of PZT-polymer of composites prepared with carbon. The piezoelectric coefficients are an order of magnitude higher than the corresponding values of PZT-polymer composite prepared without carbon.

TABLE 1 Dielectric and Piezoelectric properties of PZT-polymer* composites with various conductive phase additions.

	$\tan\delta$	K_{33}	\bar{d}_{33}	\bar{g}_h	\bar{d}_h	$\bar{g}_h\bar{d}_h$
Solid PZT	0.015	1800	450	2	30	60
PZT(70)**-polymer (30)	0.030	100	45	10	10	100
PZT(68.7)·C(1.5)- Polymer (30)	0.078	120	50	30	30	900
PZT(66)·Ge(4)- Polymer (30)	0.081	90	44	22	17	375
PZT(68.5)-Si(1.5) Polymer (30)	0.075	85	44	23	18	415

*Polymer: Eccogel 1365-0

** (): Volume percent of polymer, piezoelectric ceramic filler or semiconductive phase.

Units for \bar{d}_{33} - pC/N; \bar{d}_h - pC/N; \bar{g}_h - 10^{-3} Vm/N; $\bar{g}_h\bar{d}_h$ - 10^{-15} m²/N

The dielectric and piezoelectric properties of PZT-carbon-polymer composites with different kinds of Eccogel polymer are summarized in Table 2. The volume percent PZT, carbon, and polymer in all the composites are identical. The chief differences between these Eccogel polymers are in their flexibility and conductivity. The Eccogel 1365-80 is mechanically the hardest and has the highest resistivity. The dielectric constant and the loss tangent of all the composites

Table 2 Dielectric and piezoelectric properties of PZT-C polymer Composites with different types of Eccogel polymer matrix.

	$\tan\delta$	K_{33}	\bar{d}_{33}	\bar{g}_h	\bar{d}_h	$\bar{g}_h\bar{d}_h$
PZT-C-Eccogel (1365-80)	0.062	130	43	12	14	168
PZT-C-Eccogel (1365-45)	0.067	135	45	12	14	168
PZT-C-Eccogel (1365-25)	0.077	130	48	20	23	460
PZT-C-Eccogel (1365-0)	0.078	120	50	30	30	900

Units for \bar{d}_{33} - pC/N; \bar{d}_h - pC/N; \bar{g}_h - 10^{-3} Vm/N; $\bar{g}_h\bar{d}_h$ - 10^{-15} m²/N

are similar but the \bar{d}_{33} , \bar{g}_h and \bar{d}_h coefficients of the composites increase with flexibility and conductivity of the polymer. The $\bar{g}_h\bar{d}_h$ product of the composite made with Eccogel (1365-0) is about ten times larger than that of composite made from Eccogel (1365-80).

The change in \bar{d}_{33} coefficient is plotted in Figure 2 as a function of the poling voltage for a composite containing 68.5 vol% PZT, 1.5 vol% carbon and 30 vol% Eccogel 1365-0. All the composites were poled at 100°C for different times. \bar{d}_{33} increases with increasing poling voltage and saturates at about 35 Kv/cm. It is observed that a duration of five minutes is

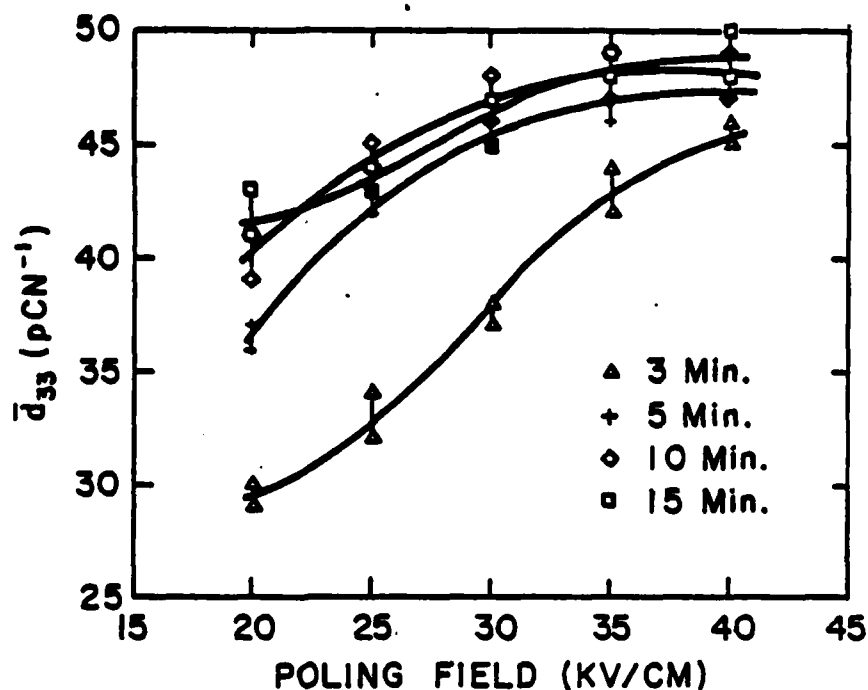


Figure 2 Variation of piezoelectric \bar{d}_{33} coefficient of PZT-carbon-Eccogel/composite with poling field.

sufficient for full poling of the composites.

Figure 3 shows the variation of the \bar{d}_{33} coefficient and $\bar{d}_h \bar{g}_h$ product with the pressure applied to the composite during the formation and curing. The \bar{d}_{33} and $\bar{d}_h \bar{g}_h$ product increases with pressure and show a maximum at 7500 PSI (50MPa). It appears that at this pressure the carbon particles were trapped between the PZT grains and created continuous electric flux path between the PZT particles leading to full poling of the composite.

Figures 4 and 5 show the variation of dielectric constant, loss tangent, \bar{d}_{33} , and \bar{g}_h coefficients with volume percent carbon in the PZT-Eccogel composite. Dielectric constant and loss tangent remain almost unchanged up to 1.5 vol% carbon but for larger amounts both dielectric constant and $\tan \delta$

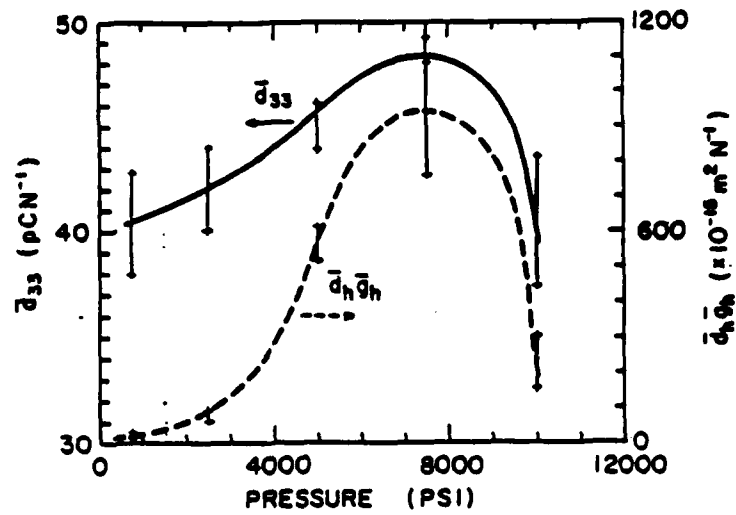


Figure 3 Variation of \bar{d}_{33} and figure of merit $\bar{d}_{33}^2/\bar{g}_{33}$ with pressure applied to the composite during formation and curing of the composite.

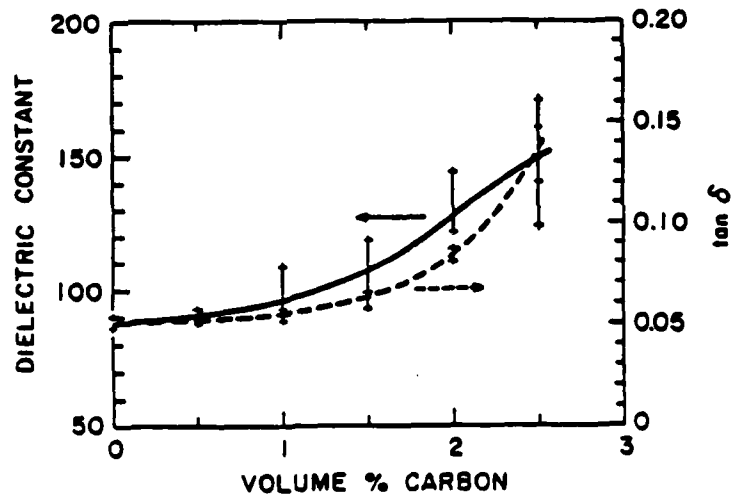


Figure 4 The change in the dielectric constant and dissipation factor with volume percent of carbon in PZT-polymer composite.

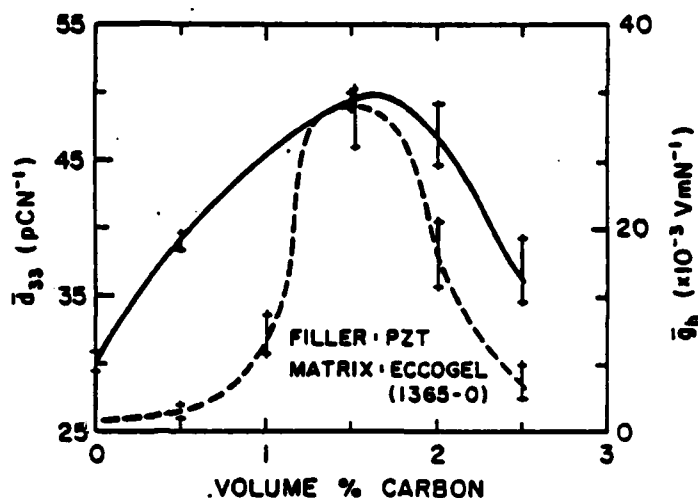


Figure 5 The \bar{d}_{33} and \bar{g}_h coefficients plotted as a function of volume percent carbon in PZT-polymer composite.

increase sharply. Both the \bar{d}_{33} and \bar{g}_h coefficients increase with increase in carbon content and show a maximum at about 1.5 volume percent. When the amount of the carbon in the composite exceeds 1.5 vol% the loss tangent rises dramatically making it difficult to apply the large voltages required for poling.

SUMMARY

Easily poled piezoelectric 0-3 composites have been made by adding a second filler such as carbon. A small amount of the carbon or germanium decreases the resistivity of the Eccogel polymer matrix and reduces the poling field to 35 Kv/cm. Only a few minutes are required for poling. This is a big improvement over normal poling conditions (100 Kv/cm, 1 hour). The hydrostatic voltage coefficient \bar{g}_h and figure of merit $\bar{g}_h \bar{d}_h$ of

PZT-carbon-Eccogel composites are an order of magnitude higher than the corresponding values of solid PZT and PZT-polymer composite prepared without a conductive phase.

ACKNOWLEDGEMENT

The authors are grateful for financial support received from the Office of Naval Research and the Celanese Research Company.

REFERENCES

1. R.E. Newnham, L.J. Bowen, K.A. Klicker and L.E. Cross, *Mater. Eng.*, 2, pp. 93-106 (1980).
2. R.E. Newnham, A. Safari, J. Giniewicz, and B.H. Fox, *Ferroelectrics*, 60, 15-21 (1984).
3. R.E. Newnham, D.P. Skinner and L.E. Cross, *Mat. Res. Bull.*, 13, p. 525 (1978).
4. L.A. Power, *IEEE Int. Conf. Rec.* pp. 1-5 (1973).
5. W.B. Harrison, *Proc., Workshop on Sonar Transducer Materials*, Naval Res. Labs. p. 257 (1975).
6. H. Banno, *Ferroelectrics* 50, 329-338 (1983).
7. A.R. Von Hippel, *Dielectrics and Waves*, John Wiley and Sons (1954).

THE INFLUENCE OF INTERFACIAL ADHESION ON THE PIEZOELECTRIC
RESPONSE OF ELECTROCERAMIC/POLYMER COMPOSITES

J. Runt, A. Safari, E.C. Galgoci and R.E. Newnham

THE INFLUENCE OF INTERFACIAL ADHESION ON THE PIEZOELECTRIC RESPONSE OF ELECTROCERAMIC/POLYMER COMPOSITES

J. RUNT, A. SAFARI, E. C. GALGOCI AND R. E. NEWNHAM
Materials Research Laboratory
The Pennsylvania State University
University Park, PA 16802

Abstract - The nature of the interfacial adhesion in composites of electroceramics and polymers was found to exert a profound influence on the piezoelectric activity of PZT-polymer composites with 1-3 connectivity and perforated PZT-polymer composites with 3-1 and 3-2 connectivity patterns. Treatment of the electroceramic surface with coupling agents (e.g. organosilanes or organostitanates) apparently improves the interfacial adhesion sufficiently to provide more efficient stress transfer from the polymer to the PZT. The $\bar{\epsilon}_h$ and d_h coefficients of the composites with coupling agents are from 20 to 35% higher than those prepared without coupling agent.

INTRODUCTION

In recent years there has been considerable interest in combining the desirable properties of electroceramics and polymers to form advanced sensing materials (1-4). Piezoelectric composites have particularly been the center of much attention because of their advantages over single phase piezoelectric materials (e.g. poly(vinylidene fluoride) and lead zirconate-titanate (PZT) ceramics) for hydrophone applications.

In all treatments to date it has been assumed that adequate interfacial adhesion exists between the electroceramic and polymer. However, we have recently shown that the strength of the interfacial bond between untreated PZT and a typical epoxy used in the manufacture of such composites is far from optimum (5). In fact, surface treatment of the ceramic is required to force fracture to occur in the polymer phase rather than at the interface. The nature of the ceramic-polymer adhesion should affect local stress fields in the composite and exert a significant influence on the piezoelectric response. In this note we report some of our initial findings on the influence of ceramic surface treatment on the dielectric and piezoelectric properties of several PZT-epoxy composites.

EXPERIMENTAL

A rigid epoxy ('Spurr' epoxy, obtained from Polysciences, Inc.) and PZT 501A (Ultrasonic Powders, Inc.) were used as the matrix and filler phase respectively for all composites. The formulation of the epoxy is as follows:

- 10 gm vinylcyclohexene dioxide
- 4 gm diglycidyl ether of polypropylene glycol
- 26 gm nonenyl succinic anhydride
- 0.4 gm dimethylaminoethanol

Several different designs (formulated on the basis of the concept of phase connectivity (6)) have been particularly effective in enhancing the hydrostatic piezoelectric sensitivity of the composites over single phase PZT. So-called 1-3

PZT-epoxy composites were prepared by immersing a rack of aligned, sintered PZT rods in the epoxy precursors and curing at 70°C for 8 hours. Final composites were 4 mm thick and contained 4 volume percent PZT. Further details on 1-3 composite fabrication can be found in references 7 and 8. Air-dry silver electrodes were applied to the two faces perpendicular to the rods and the composite poled at 75°C in an oil bath with a field of 22 kV/cm for 5 minutes.

Based on our previous studies (5), we found one of the most effective surface treatments to be the application of an organosilane coupling agent: γ -glycidoxypyrrolyltrimethoxysilane (Union Carbide A-187). Surface-treated PZT composites were prepared in a manner similar to those described above except that the PZT rods were dipped in a 1% solution of A-187 in acetone and dried at 70°C for 1 hour under vacuum before backfilling with epoxy. In addition, to mimic the worst case of poor interfacial adhesion, a mold release (Histoprep Mold Releasing Agent; obtained from Polysciences, Inc.) was applied to the PZT surfaces in a manner similar to the coupling agent.

Perforated PZT-polymer composites with 3-1 and 3-2 connectivity patterns were prepared by drilling one or two holes in a prepoled block of PZT in the directions perpendicular to the poling direction (electrode surfaces) with an ultrasonic cutter (9). The holes were then backfilled with the epoxy precursors and cured at 70°C for 8 hours. The exterior of the perforated blocks was also coated with epoxy. After curing, the composites were lightly polished along the poling direction to remove excess epoxy from the rigid PZT surface, thereby exposing the PZT and ensuring that the faces of the composites were parallel. Electrodes of air-dried silver paste were applied and composites were aged at least three days prior to measurement. Prepoling was carried out in an oil bath at 120°C by applying a field of 20 kV/cm for three minutes. The 3-1 composites evaluated in this study were 3.5 mm x 4 mm x 4 mm thick and contained a circular hole of 2.9 mm diameter. The 3-2 composites were 5 mm x 5 mm x 6 mm thick; the holes were 3 mm in diameter.

Surface treated 3-1 and 3-2 composites were prepared by the method just described; except that the PZT surfaces were treated with an organotitanate coupling agent; isopropyl tri(N ethylamino-ethylamino) titanate (Kenrich Petrochemicals, Inc., KR-44). Prior to backfilling, the perforated PZT was dipped into a solution of the coupling agent in isopropyl alcohol, dried at 70°C overnight and then backfilled with epoxy.

Dielectric measurements were performed with a Hewlett-Packard 4270A Automatic Capacitance Bridge at 1 kHz and 1V. The composite piezoelectric strain coefficient in the poling direction (\bar{d}_{33}) was measured using a Berlincourt Piezo \bar{d}_{33} -Meter with rounded rams. The \bar{d}_{33} value was computed from the average of 20 random measurements (10 on each electroded surface of the composite) at a ram pressure of approximately 55 psi. The hydrostatic piezoelectric voltage coefficient (\bar{g}_h) was measured by a dynamic method at a frequency of 50 Hz and 0.7 MPa pressure (10). From the measured value of \bar{g}_h , the hydrostatic piezoelectric strain coefficient (\bar{d}_h) was calculated from the equation $\bar{d}_h = \epsilon_0 \bar{g}_h \bar{K}_{33}$ where ϵ_0 is the permittivity of free space and \bar{K}_{33} the dielectric permittivity measured along the poling direction. For a hydrostatic transducer material, the $\bar{g}_h \bar{d}_h$ product is considered to be a useful "figure of merit".

RESULTS AND DISCUSSION

Table 1 summarizes the results of the dielectric and piezoelectric measurements on all composites. The reported values are an average of at least four samples of each type of composite. For the 1-3 composites, \bar{d}_{33} and \bar{d}_h are enhanced significantly on comparing poor (mold release) to good (coupling agent) interfacial adhesion. The organosilane surface treatment apparently improved the interfacial

TABLE 1 Effect of Ceramic Surface Treatment on the Piezoelectric Properties of PZT-Epoxy Composites

Connectivity	Coupling Agent mold release	\bar{K}	\bar{d}_{33} (μCN^{-1})	\bar{g}_h^c (mVmN^{-1})	\bar{d}_h^c (pCN^{-1})	$\bar{g}_h \bar{d}_h^c$ ($10^{-15} \text{ m}^2 \text{ N}^{-1}$)
1-3	release	116	155 ^a	30	31	930
1-3	no	110	170 ^a	36	35	1260
1-3	yes	101	195 ^a	47	42	1970
3-1	no	710	340 ^b	25	159	3900
3-1	yes	660	410 ^b	34	200	6800
3-2	no	580	260 ^b	40	200	8000
3-2	yes	550	350 ^b	50	245	12200

a Standard deviation is $\pm 12\%$

b Standard deviation is $\pm 3\%$

c Estimated errors are $\bar{g}_h \pm 16\%$, $\bar{d}_h \pm 12\%$ and $\bar{d}_h \bar{g}_h \pm 20\%$

coupling sufficiently to provide more efficient stress transfer from the epoxy to the PZT rods. The dielectric constant of the 1-3 composites decreased by ~10-15% upon improving the interfacial adhesion although the reason for this decrease is not clear at this time. Since $\bar{g}_h = \bar{d}_h \epsilon^{-1} \bar{K}_{33}^{-1}$, \bar{g}_h is also larger for the surface treated composites. Consequently the hydrostatic figure of merit, g_{hd} , is enhanced by up to 100% over composites with poor interphase coupling. Clearly, substantial improvements in piezoelectricity sensitivity can be realized in these composites by simply optimizing the interfacial bonding.

For the 3-1 and 3-2 composites prepared with coupling agents, the dielectric constants were again found to be lower than composites with untreated ceramic surfaces. In addition the \bar{d}_{33} , \bar{g}_h , \bar{d}_h and \bar{d}_{hg} coefficients of the treated composites are considerably larger than the untreated samples (from 20-40% higher) presumably due to improved stress transfer from the epoxy to PZT.

ACKNOWLEDGMENTS

The authors would like to express their appreciation to the Office of Naval Research for their support of this work through Contract N00014-82-K-0339. The authors would also like to thank Mr. Michael Farr for preparing many of the 1-3 composites.

REFERENCES

1. R. E. Newnham, L. J. Bowen, K. A. Klicker and L. E. Cross, Mater. Eng. 2, 93 (1980).
2. R. E. Newnham, A. Safari, J. Giniewicz and B. H. Fox, Ferroelectrics 60, 15 (1984).
3. R. E. Newnham, A. Safari, G. Sa-gong and J. Giniewicz IEEE Ultrasonic Symp. Proc. 1, 501 (1984).
4. R. E. Newnham and J. Runt, Polymer News 10, 132 (1984).
5. E. C. Galgoci and J. Runt, Manuscript in Preparation.
6. D. P. Skinner, R. E. Newnham and L. E. Cross, Mater. Res. Bull. 13, 599 (1978).
7. K. A. Klicker, J. V. Biggers and R. E. Newnham, J. Amer. Cer. Soc. 64, 5 (1982).
8. J. Runt and E. C. Galgoci, J. Appl. Polym. Sci. 29, 611 (1984).
9. A. Safari, R. E. Newnham, L. E. Cross and W. A. Schulze, Ferroelectrics 41, 197 (1982).
10. A. Safari, Ph.D. Thesis, The Pennsylvania State University, 1983.

FINITE ELEMENT/DIFFERENT MODELING OF ELECTROCERAMICS

S. DaVanzo, W. Carlson, R.E. Newnham and A. Safari

FINITE ELEMENT/DIFFERENT MODELING OF ELECTRO CERAMICS

S. DaVanzo, W. Carlson, R.E. Newnham and A. Safari

Materials Research Laboratory
The Pennsylvania State University
University Park, PA 16802 U.S.A.

ABSTRACT

The hydrostatic piezoelectric response of PZT composites and the electric field distribution around flaws in capacitor materials have been modeled using the Finite Element and Finite Different methods respectively. This paper reviews the work done at The Pennsylvania State University on these two models.

INTRODUCTION

Lead zirconate titanate (PZT) and barium titanate (BaTiO_3) are two of the most widely used materials in the electroceramics industry. PZT is used mainly for piezoelectric applications, while BaTiO_3 is used primarily as a capacitor dielectric.

This paper reviews the ongoing research efforts at the Materials Research Laboratory of The Pennsylvania State University on the modeling of electroceramic materials. It is divided into two parts, the first describes the Finite Element Method (FEM) modeling of PZT composites for hydrophone materials, while the second outlines the work on modeling the effects of flaws on the electric field distributions within capacitor materials using the Method of Finite Differences (FD).

HYDROPHONE MATERIALS

Numerous PZT composites have been fabricated for use as hydrophone materials. Although PZT has a strong uniaxial piezoelectric response, the hydrostatic piezoelectric response, d_h ($d_h = d_{33} + d_{31} + d_{32}$), is only approximately 10% of the uniaxial response due to the fact that $d_{31} = d_{32} = -(1/2)d_{33}$. A number of workers¹⁻⁵ have incorporated PZT into composites in order to improve upon the limitations of single phase PZT. Composites have been characterized by their connectivity patterns as described by Newnham⁵. The connectivity pattern refers to the number of orthogonal directions each phase within a composite is continuous. A 3-1 composite is one in which PZT is continuous in three directions and the the second phase (polymer in this case) is continuous in one.

Two types of composites, perforated 3-1 composites and 3-0 macrovoid composites will be discussed in this review. The 3-1 perforated composites were fabricated, by Safari³, by drilling holes perpendicular to the poling direction in prepoled PZT blocks. 3-0 macrovoid composites were fabricated by Kahn⁶ at the Naval Research Laboratory. In macrovoid composites ordered arrays of voids are introduced into PZT by screening a fugitive ion between layers of green PZT tapes in the desired void pattern. The parts were then constructed by stacking the ink tape combination to form a block. When the fugitive ink was burned out of the structure and the part fired the result was an ordered array of voids.

All of the composites fabricated for hydrophone applications were designed such that when a hydrostatic load is applied to the material the distribution of stress within the composite results in a larger component of the stress in the direction of poling than in the two orthogonal directions. The effect of this stress distribution is to reduce the effect of the hydrostatic response of the negative d_{31} and d_{32} piezoelectric coefficients thus enhancing the hydrostatic piezoelectric change coefficient d_h . In order to understand the enhancement of the hydrostatic response, as well as guide future research efforts, the FEM was employed to calculate the electric field distribution within the composites as parts of a model for the hydrostatic piezoelectric large coefficient d_h .

Finite Element Calculations

The FEM has been used by DaVanzo^{7,8} to model the hydrostatic response of 3-1 perforated and 3-0 macrovoid composites. The modeling of the composites follows the same procedure with one exception; modeling of the 3-0 composites requires calculations of the electric field distribution during poling. 3-1 composites are fabricated from prepoled PZT blocks whereas 3-0 composites are poled after fabrication. In the 3-1 composites poling of the ceramic phase is uniform in both direction and magnitude while in the 3-0 composites the voids distort the direction and magnitude of the electric field leading to non-uniform poling of the ceramic phase. The non-uniformity in the poling of the ceramic must be accounted for in the model. In this paper the method used for the modeling of the 3-1 composites will be outlined, the reader is referred to the references^{7,8} for a complete description of the model which includes poling effects.

The FEM is a method for solving boundary value problems in which the differential equation governing the behavior of the region of interest is expanded on a set of simple basis functions called 'shape' functions. The result of this expansion is a set of algebraic equations in which the generalized displacements (displacement, rotation, potential, etc.) of a finite number of points within the region, called 'nodes', become the independent variables. In practice the region is broken into a large number of small subregions called 'elements'. Figure 1 shows a typical FEM grid for a 3-1 perforated composite. The grid consists of cubic elements 0.25mm on a side. The above mentioned

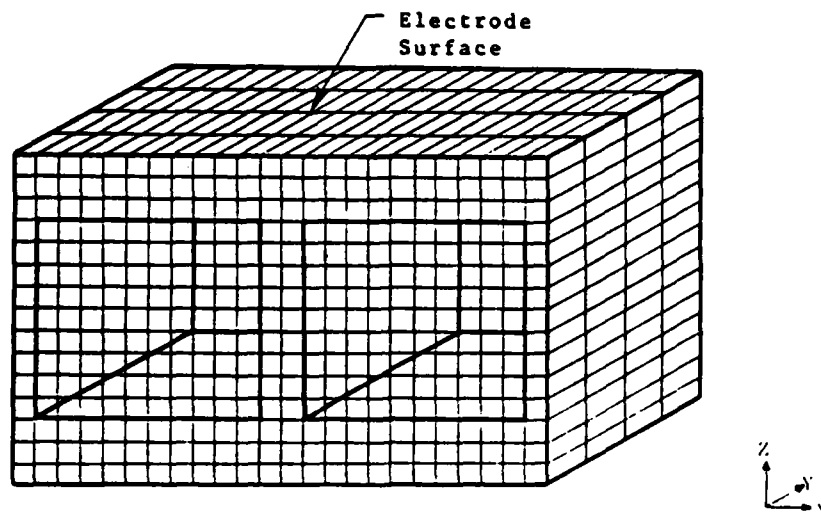


Fig. 1. A typical Finite Element grid for a 3-1 composite.

nodes are, in this case, the corners of the cubes. In order to use the FEM the model must be described to the FEM routine. The description included a number for each node, the location of each node, the node numbers which comprise each element, the material constants for each element and any loads on the nodes or elements. The first step in the model is to set up the FEM grid and supply the model information to the routine. For the 3-1 perforated composites the load was a hydrostatic load of 0.7MPa. The FEM routine calculates the displacement of each node and the six components of the stress at the centroid of each element. The next step in the model was to calculate a stress induced polarization for each element. The polarization was calculated for each element using the stress at the center of the element and the relation $P_i = d_{ijk} \sigma_{jk}$, where d_{ijk} is the piezoelectric tensor for PZT and σ_{jk} is the stress at the element centroid. These stress induced element polarizations were then summed using a series parallel model to obtain an induced polarization for the composite. The series parallel model treats each element as a parallel plate capacitor with a charge defined by $Q = P_3 A$ where P_3 is the component of the polarization in the direct of poling and A is the area of the element face normal to the poling direction. The element charges were then added using the procedure prescribed for summing capacitor networks. From the induced polarization for the composite the hydrostatic piezoelectric charge coefficient was then calculated using the relation $P_3 = d_{hp} p$ where p is the hydrostatic load applied to the composite.

Results and Discussion

Figure 2 shows a plot of d_h versus the hole center to center distance (X) for 3-1 perforated composites with a constant hole size of 2.5cm. The plot shows good agreement between experimental and FEM results. Figures 3-5 show contour plots of the σ_{11} , σ_{22} , and σ_{33} components of the stress on a plane, perpendicular to the y axis, 0.125mm into the composite. The relative intensity of the three

components of the stress at points between the holes should be noted. The σ_{33} component of the stress in this region is higher than the two orthogonal directions. Figure 6 shows a contour diagram of the stress induced polarization for the same plane. From either the stress diagrams or the stress induced polarization it can be seen that the major contribution to the hydrostatic piezoelectric response comes from the pillar regions.

Figure 7 shows an isometric view of a 3-0 macrovoid composite. In Table 1 the ratio of d_p/d_{33} where d_{33} is the piezoelectric coefficient in the direction of poling for single phase PZT, is listed for four 3-0 macrovoid composite configurations. The first two configurations contain voids which are approximately 6×10^{-4} cm in diameter while the second two are for voids 2.5×10^{-4} cm in diameter. In all four configurations the void patterns are designed to cover 50% of the void plane. For each diameter of voids two spacings, parallel to the void planes, were fabricated. The spacings were 3.8×10^{-3} and 7.6×10^{-3} cm respectively with the narrower spacing listed first. The Table shows good agreement between experimental and the FEM results for the ratios.

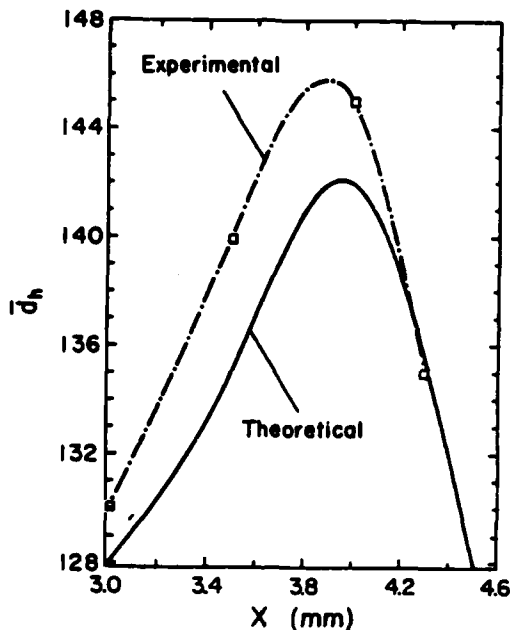


Fig. 2. Variation of the hydrostatic charge coefficient d_h as a function of X (the center to center distance for adjacent holes).

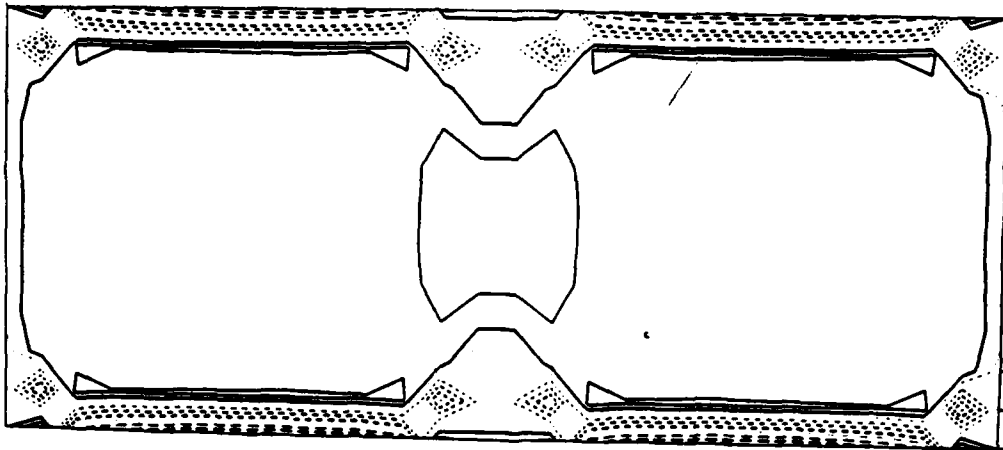


Fig. 3. A contour map of the 11 component of the stress tensor in a 3-1 composite.

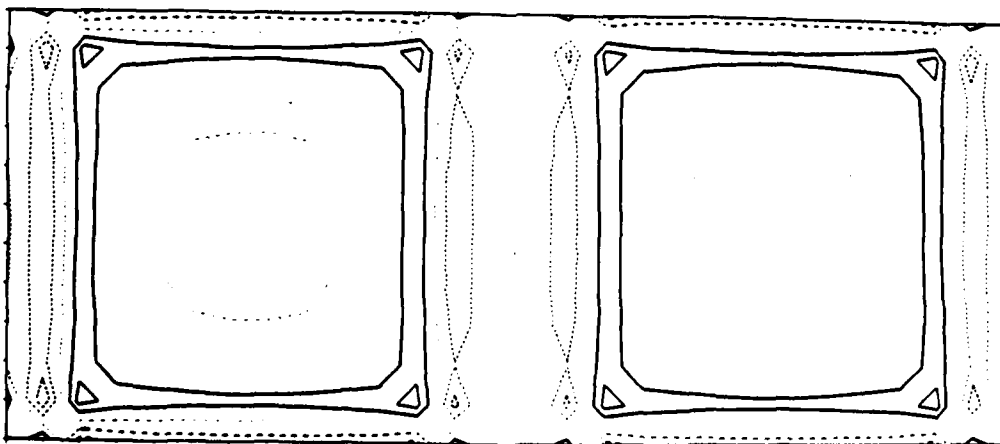


Fig. 4. A contour map of the 22 component of the stress tensor in a 3-1 composite.

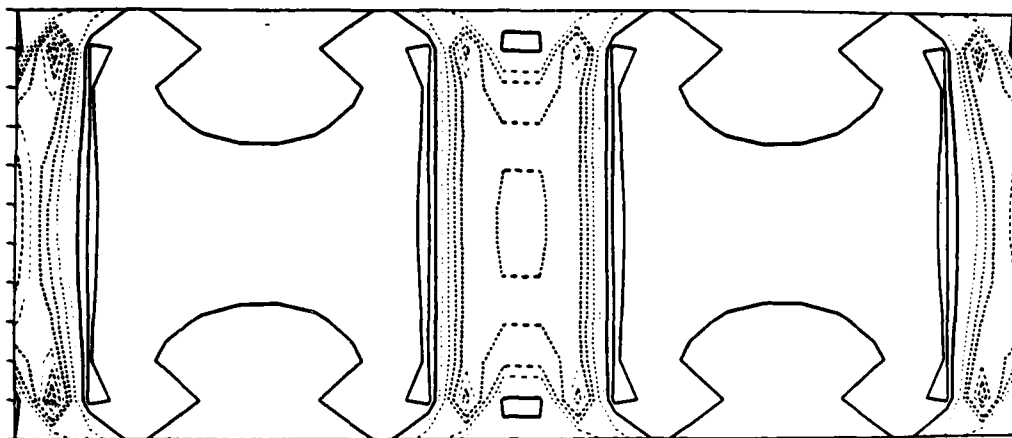


Fig. 5. A countour map of the 33 component of the stress tensor in a 3-1 composite.

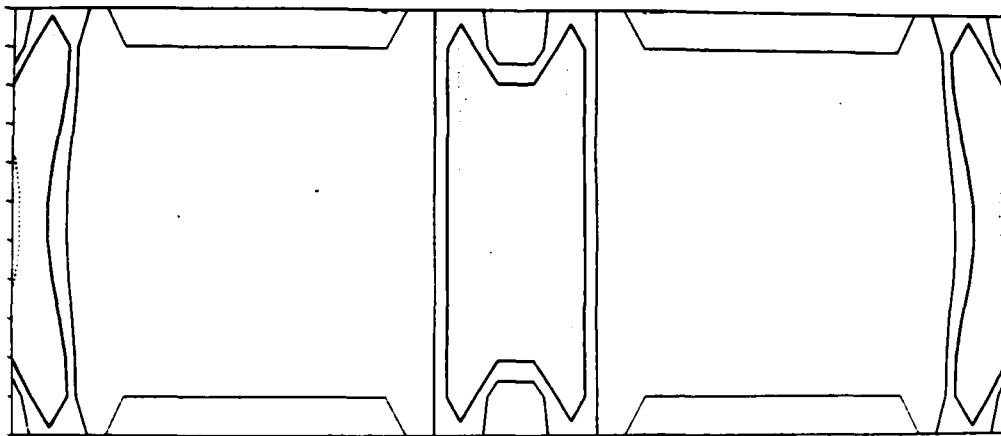


Fig. 6. A countour map of the 33 component of the stress induced polarization P_3 in a 3-1 composite.

Table 1. d_h/d_{33} Ratios for Macrovoid Composites with Circular Voids

Configuration	d_h/d_{33}	
	Exp.	FEM
Large Circles 1 layer	47%	48%
Large Circles 3 layers	42%	45%
Small Circles 1 layer	44%	49%
Small Circles 3 layers	40%	48%

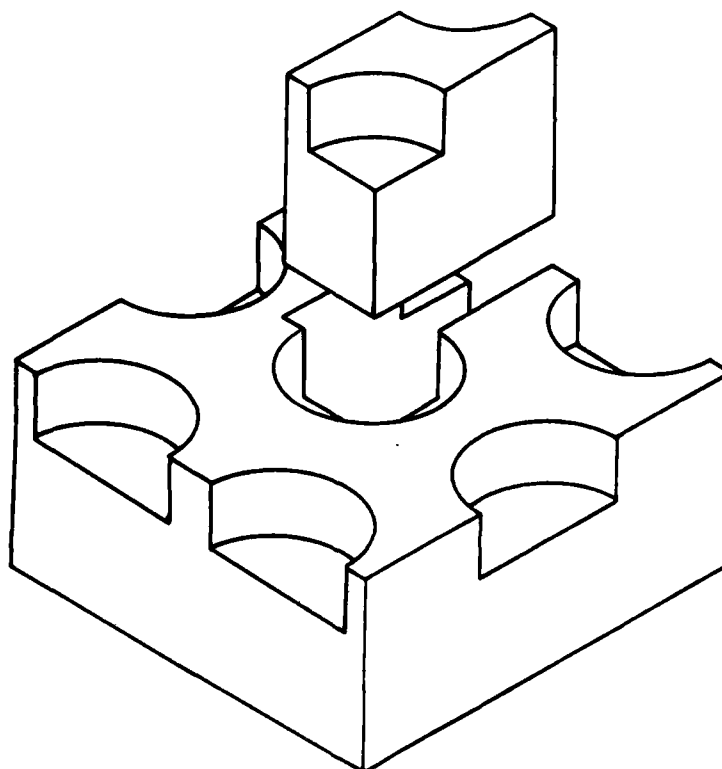


Fig. 7. An isometric view of a 3-0 macrovoid composite.

The FEM has been employed in a model for the hydrostatic response of PZT composites with very good reliability. The calculated stress fields within the composites make it possible to identify the parameters for each composite configuration which have the greatest influence on the hydrostatic response. The hydrostatic response for a number of new configurations of 3-0 macrovoid composites has been predicted and will be presented elsewhere⁹.

CAPACITOR MATERIALS

Because of its high dielectric constant BaTiO_3 is used widely in the capacitor industry, but the use of any dielectric material is limited by the dielectric breakdown of the material. A ceramic, although traditionally considered to be a single phase homogeneous material, can be considered to be a multiphase material where manufacturing flaws (pores, delamination of electrodes, etc.), as a second phase severely limit the breakdown voltage of the material.

A FD (Finite Different) computer model has been used to analyze non-conductive parallel plate capacitors. This model applies to which can be represented in two dimensions with an embedded second phase of either voids or conductive material of different geometries. Results of the analysis are presented as local potential or electrical field concentrations within the capacitor. Electrostrictive and piezoelectric strains can then be calculated knowing the material properties. These studies are intended to delineate the field-induced internal stress leading to mechanical fracture and electrical breakdown in BaTiO_3 materials. Identification of the stress field may result in alternate manufacturing techniques and improved quality control, by identifying and eliminating harmful flaws.

The FD technique is applied to a continuum that may be divided into a finite number of discrete nodes with each node representing an unknown value. Discretized equations at the nodes points are then used to replace the continuum differential equations. Solution of the set of these linear equations may then be found via direct or iterative linear procedures. The precision of the FD technique will be dependent on the manner of discretization of the domain, the computing machine, and the method of solution. The technique applied here depends on a regular rectilinear mesh, however, polar discretization has also been used by other investigators.

The FD method has been used to carry out two investigations. The first investigation has led to the electrical field distribution within a homogeneous ceramic with imbedded flaws. The second investigation uses the field study results together with the elastic parameters to predict stress and strain distributions which may lead to mechanical breakdown.

Calculations of Electric Potential

For field problems analyzed in this work the Laplace equation was treated by the method of central differences. This is a 'divided difference' scheme and is commonly used to analyze field problems⁹. The simultaneous solution of all nodes Laplacians as in a direct method will yield the potential at all points in the field. Boundary conditions are specified for both the perimeter of the field and the inclusions.

Symmetry conditions are applied where feasible but other conditions may occur where the potentials must be assumed. One such condition is the potential at a conductor interface. In this analysis the conductors are treated as constant potential surfaces. Another boundary condition is the far field condition which is defined as the undisturbed field far from an included object. The accuracy of this assumption is dependent on both the distance from the inclusion and the boundary conditions at the inclusion. In some cases the boundary condition at the inclusion may be approximated if the ratio of the permittivities between the two phases is very large. In addition to assumptions in the numerical calculations, there are further restrictions on the geometrical resolution. The continuum under study is assumed homogeneous in each phase, but the grain size limitations will alter the potential distribution and thereby place a lower limit on the validity of the numerical results. The node size is therefore limited by the physical nature of the material.

This code has been applied to flaws in uniform and non-uniform fields where the permittivity of the flaw is much lower than that of the surrounding ferroelectric. The code was used to determine local fields around spherical and elliptical flaws. Further checks have been made with closed-form solutions of spherically flawed geometries. The closed-form solutions have been derived for flaw geometries in uniform D.C. fields only. Geometries studied include spherical voids and spherical conductors about which the Laplacian differential equations have been solved electrostatic potential external to the void. Some elliptical solutions have also been derived. The local electric fields around and within flaws are easily determined from the potential derivative in the appropriate coordinate system and the particular flaw geometry. The coordinate geometry used in both cases depend on the shape of the inclusion: for the case of spherical flaws polar coordinates were used. The chief purpose of the closed form solutions are to check the field concentration around flaws in the capacitors by assuming that the far field is uniform. The check may also be useful for numerical results where acute geometries are encountered in the vicinity of cracks and delaminations.

Manufacturers have used numerical methods to predict electric field levels in various multilayer geometries, both with and without embedded flaws (delaminations, large voids, etc.). The FD model developed here is for the study of local potential concentrations around singular inclusions and is also applicable to multiple flawed ceramics. Principal assumptions of the analysis include a constant D.C. voltage, two-dimensional geometries, and the use of a square FD solution technique with Laplacian differential equations. Other features include a semi-automatic node generator requiring some user inputs, and a graphical output of electric potential values. The code is in operation on an IBM mainframe computer and requires the International Mathematics and Statistics Library software package. A summary of the case studies is shown in Table 2.

AD-A173 185

PIEZOELECTRIC AND ELECTROSTRICTIVE MATERIALS FOR
TRANSDUCER APPLICATIONS(U) PENNSYLVANIA STATE UNIV
UNIVERSITY PARK MATERIALS RESEARCH LAB

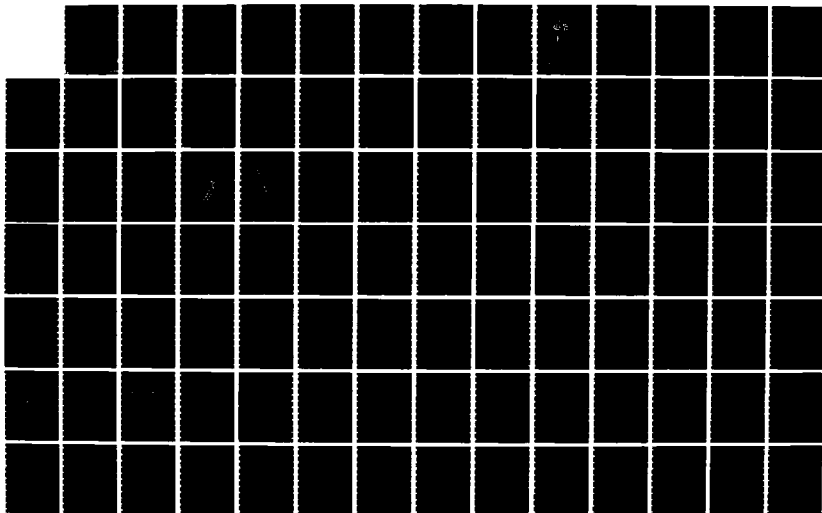
2/4

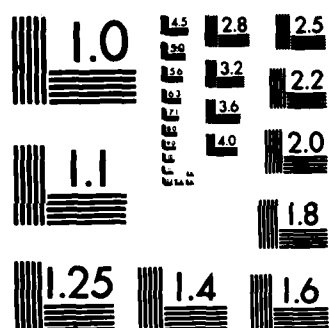
UNCLASSIFIED

L E CROSS ET AL JUL 86 N00014-82-K-0339

F/G 9/1

NL





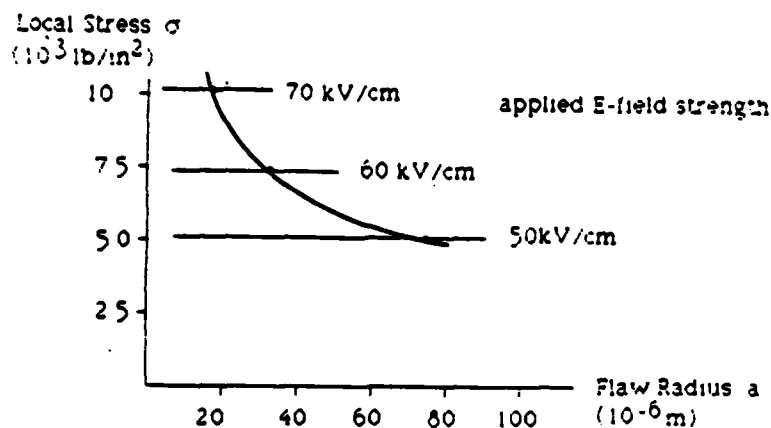
MICROCOPY RESOLUTION TEST CHART
NATIONAL BUREAU OF STANDARDS-1963-A

Table 2. Summary of Maximum Local Electrical Fields

Flaw Type	Electric Field inside of flaw	Electric Field exterior of flaw
Spherical Voids		
· closed-form	1.5	1.5
· roughened	2.3	2.2
· roughened w/protruding voids	5.1	2.8
Diamond void	3.2	2.9
Square void	2.7	1.9
Delamination 6% thickness	13	3.6
End of Conductors	-	1.2
Delamination on conductor 10% delam thickness	9.2	2.8
Misplaced Conductor	-	2.24
w/Protruding Conductor	-	3.51

Elastic Analysis

The second area of research requires both the elastic material parameters and the electrical field solutions. The goal is to describe stress and strain configurations in the ceramic under steady state and fatigue limitations of the material. In particular, interesting phenomena in the void formation, crack propagation, and fatigue from electrical loading are being investigated. Electrical field patterns are used to calculate the polarization and dielectric constants as well as to analyze local strains. The isotropic forms of electric polarization $P_i = \epsilon_0 X_{ij} E_j$ and electrostrictive strain $\epsilon_{ij} = Q_{ijkl} P_k P_l$ are utilized to evaluate the particular strains. Mechanical breakdown in the material for various flaw geometries is being treated with fracture mechanics theory to check stress intensity factors and to predict ultimate fracture strength. Principal assumptions are that permittivity, susceptibility, and electrostriction are constant for a given field strength and polarization. If only the maximum tensile and compressive stresses need to be determined, the electric potential data may be studied for the maximum gradients and these gradients used to calculate strain. Electrical field data resulting in a given strain may be compared to mechanical fracture strength via stress intensity factors and assumed flaw size for the particular material. Data from recent calculations is presented in Figure 8 showing fracture strength under various D.C. fields. This data show an approximate upper bound on the mechanical strength for various crack lengths in the ceramic.



$$\text{where } a = \frac{1}{\pi} \left[\frac{K_{Ic}}{1.12\sigma} \right]^2$$

$$K_{Ic} = 0.6 \text{ MN/m}^{3/2}$$

Fig. 8. Local stress vs. flaw radius for a local field of 1.5 times the applied field.

Conclusions

Some planar numerical studies have been conducted to determine local fields within BaTiO_3 ceramics with embedded second phase flaws. It has been determined through these studies that local electrostriction strains may approach and exceed fracture limitation criteria as defined by fracture mechanics theory. Further study will be undertaken to determine if local electrostriction strain and electrical fields are detrimental to the dielectric behavior of layered capacitors.

REFERENCES

1. K. Rittenmyer, T. Shrout, W.A. Schulze and R.E. Newnham. Piezoelectric 3-3 Composites. Ferroelectrics 41, 189-195 (1982).
2. D.P. Skinner, R.E. Newnham and L.E. Cross. Flexible Composite Transducers. Mat. Res. Bull. 13, 599 (1978).
3. A. Safari, R.E. Newnham, L.E. Cross and W.A. Schulze. Perforated PZT-polymer Composites for Piezoelectric Transducer Applications. Ferroelectrics 41, 197 (1982).
4. R.E. Newnham, L.J. Bowen, K.A. Klicker and L.E. Cross. Composite Piezoelectric Transducers. Mat. in Engr. 112, 93 (1980).
5. R.E. Newnham, D.P. Skinner and L.E. Cross. Connectivity and Piezoelectric-Pyroelectric Composites. Mat. Res. Bull. 13, 525 (1978).

6. M. Kahn. Ordered Macrovoid Composites. (to be published).
7. S. DaVanzo, A. Safari, R.E. Newnham. Finite Element Modeling of Perforated PZT-Polymer Composites. Ferroelectric Letters 3, 109-121 (1985).
8. S. DaVanzo and M. Kahn. Finite Element Modeling of Macrovoid Composites. (to be published).

COMPOSITE PIEZOELECTRIC SENSORS

A. Safari, G. Sa-Gong, J. Giniewicz and R.E. Newnham

COMPOSITE PIEZOELECTRIC SENSORS

A. Safari, G. Sa-gong, J. Giniewicz and R.E. Newnham

Materials Research Laboratory
The Pennsylvania State University
University Park, PA 16802 USA

INTRODUCTION

A hydrophone is an underwater microphone or transducer used to detect underwater sound. The sensitivity of a hydrophone is determined by the voltage that is produced by a hydrostatic pressure wave. The hydrostatic voltage coefficient, g_h , relates the electric field appearing across a transducer to the applied hydrostatic stress, and is therefore a useful parameter for evaluating piezoelectric materials for use in hydrophones. Another piezoelectric coefficient frequently used is the hydrostatic strain coefficient, d_h , which describes the polarization resulting from a change in hydrostatic stress. The g_h coefficient is related to the d_h coefficient by the relative permittivity (K): $g_h = d_h/\epsilon_0 K$, where ϵ_0 is the permittivity of free space.

A useful 'figure of merit' for hydrophone materials is the product of hydrostatic strain coefficient d_h and hydrostatic voltage coefficient g_h . The product $d_h g_h$ has the units of $m^2 N^{-1}$. Other desirable properties for a hydrophone transducer include (i) low density for better acoustical matching with water, (ii) little or no variation of the g_h and d_h coefficients with pressure, temperature and frequency, and (iii) high compliance and flexibility so that the transducer can conform to any surface and withstand mechanical shock. Compliance also leads to large damping coefficients which prevent 'ringing' in a passive transducer.

Lead zirconate titanate (PZT) is widely used as a transducer material because of its high piezoelectric coefficients. However, for hydrophones, PZT is a poor choice for several reasons. PZT has a large piezoelectric d_{33} coefficient, but its hydrostatic strain coefficient d_h ($=d_{33} + 2d_{31}$) is small because d_{33} and $2d_{31}$ are opposite in sign, and almost cancel one another. Moreover, the high permittivity of PZT ($K \approx 1800$) lowers the voltage coefficient g_h to miniscule values. In addition, the density of PZT (7.9 g/cm^3) makes it difficult to obtain good impedance matching with water. PZT is also a brittle ceramic and for some applications a more compliant material with better shock resistance is desirable.

Other materials used for hydrophone applications are lead metaniobate $PbNb_2O_6$ ⁽¹⁾ and $PbTiO_3$ ⁽²⁾. Their d_h values are slightly higher than that of PZT (Table 1) and the g_h values are an order of magnitude better because of their modest dielectric constants. Unfortunately, $PbNb_2O_6$ and $PbTiO_3$ are also

Table 1. Dielectric and Piezoelectric Properties of Single Phase and Selected Composite Materials

	K_{33}	d_{33} pC/N	g_h (10^{-3} Vm/N)	d_h pC/N	$g_h d_h$ 10^{-15} m ² /N
PZT (501)	1800	450	2.5	40	100
PbTiO ₃	230	53	23	47	1080
PbNb ₂ O ₆	225	85	33	67	2200
PVF ₂ =(CH ₂ -CF ₂) _n	12	35	100	10	1000
0-3 PZT-Polyurethane	26	10	8	2	10
0-3 PZT-Silicone (large particle)	100	340	32	28	900
0-3 PbTiO ₃ -Chloroprene	40	60	100	35	3500
0-3 0.5 PbTiO ₃ -0.5 BiFeO ₃	40	45	65	25	1625
0-3 0.5 PbTiO ₃ -0.5 Bi[Fe _{0.98} Mn _{0.02}]O ₃	40	55	90	30	2700
0-0-3 PZT-Carbon-Polymer Composite	120	50	30	30	900
1-3 PZT-Epoxy	54	150	56	27	1536
1-3 Glass-Ceramics	10	10	100	10	1000
1-3 Diced Copper Encapsulated Composite	400	400	75	265	20000
1-3-0 PZT-Epoxy + glass sphere	78	180	60	41	2460
1-3-0 Foamed Polyurethane	41	180	210	73	14600
3-1 Perforated PZT-Epoxy	650	410	30	170	5000
3-2 Perforated PZT-Epoxy	375	350	60	200	12000
3-3 PZT-Silicon Rubber	45	200	45	180	8100
3-3 PZT-Epoxy	-	-	50	90	4500

dense, brittle ceramics, which undergo a large volume change at the Curie temperature, often causing fracture during preparation.

Polyvinylidene fluoride [PVF₂ = (CH₂-CF₂)_n] offers several advantages over PZT and other piezoelectric ceramics³. It has low density, high flexibility, and although PVF₂ has low d_{33} and d_h , the piezoelectric voltage coefficient g_h is large because of its low relative permittivity.

There are, however, problems associated with the use of PVF₂. The major problem is the difficulty in poling PVF₂. A very high field is necessary to pole PVF₂ (1.2 MV/cm), and this limits the thickness that can be poled. Pyroelectric phenomena in PVF₂ also produce undesirable polarization fluctuations with temperature.

It is clear that none of the single-phase materials are ideal for hydrophones and there is need for better piezoelectric materials.

One approach to the problem is to develop composite materials in which the desired properties can be incorporated through use of a combination of materials with different properties. In designing composite materials for hydrophone applications, a logical choice would be a piezoelectric ceramic and a compliant polymer. In such a composite, the ceramic produces a large piezoelectric effect, while the polymer phase lowers the density and permittivity and increases the elastic compliance.

In a composite the electric flux pattern and the mechanical stress distribution, and hence the resulting physical and electromechanical properties, depend strongly on the manner in which the individual phases are interconnected. In this regard the connectivity of a composite, defined as

the number of dimensions in which each component phase is continuous⁴, is of crucial importance. When referred to in an orthogonal axis system, each phase in a composite may be self-connected in zero, one, two, or three directions. For diphasic composites, there are ten connectivity patterns designated as 0-0, 0-1, 0-2, 0-3, 1-1, 1-2, 1-3, 2-2, 2-3, and 3-3. In the notation used here, the piezoelectric phase appears first.

During the past few years, a number of investigators have examined piezoelectric ceramic-polymer composites with different connectivity patterns. The method of preparation of these composites covers a wide spectrum of ceramic fabrication processes, and the piezoelectric properties of the composites depend to a large extent, on the connectivity pattern. In this paper, a brief summary of the piezoelectric properties of composite transducers with different connectivity is presented. A more extensive description of the work on other PZT-polymer composites can be found in recent review papers^{5,6}. A schematic diagram of various types of composites with different connectivity is shown in Fig. 1.

COMPOSITES WITH 0-3 CONNECTIVITY

The simplest type of piezoelectric composite consists of a polymer matrix loaded with ceramic powder. In a composite with 0-3 connectivity, the ceramic particles are not in contact with each other while the polymer phase is self-connected in all three dimensions. In many ways the 0-3 composite is similar to polyvinylidene fluoride (PVF₂). Both consists of a crystalline phase embedded in an amorphous matrix, and both are reasonably flexible.

Early attempts to fabricate flexible composites of piezoelectric ceramic particles and polymers were made by Kitayama⁷, Pauer⁸ and Harrison⁹. The d_{33} coefficient of these composites were comparable with PVF₂, but the d_h value was lower than those of solid PZT and PVF₂ polymer (Table 1). To improve the properties of these composites Harrison⁹ fabricated a composite with much larger PZT particles up to 2.4 mm. Here the particle size approaches the thickness of the composite, and since the PZT particles extend from electrode to electrode, near saturation poling can be achieved. The large rigid PZT particles can also transmit applied stress extremely well, leading to high d_{33} values when measurements are taken across the particles. Permittivity in this composite is lower than that of homogeneous PZT, resulting in an improved voltage coefficient.

An improved version of the 0-3 composite was synthesized by Banno^{10,11}. Rather than using PZT as the ceramic filler, pure or modified lead titanate was employed because of its greater piezoelectric anisotropy. The lead titanate filler is produced by water-quenching the ceramic, thereby exploiting the high strain present in the material in order to produce fine powders. The average particle size was about 5 μ m. To fabricate composite bodies, the piezoelectric powders and chloroprene rubber were mixed and rolled into 0.5mm thick sheets at 40°C using a hot roller, and then heated at 190°C for 20 minutes under a pressure of 13 kg/cm². The composites were poled in a field of 100-150 kV/cm field for 30 minutes.

As shown in Table 1, the hydrostatic voltage coefficient g_h of pure PbTiO₃ composites is comparable to that of PVF₂ polymer. The d_h value of 35 pC/N was independent of pressure and g_h values was reduced only about 2% when pressure was increased to 40MPa¹².

Recently we have fabricated flexible composites with a more active piezoelectric material¹³. The piezoelectric ceramic used in these composites are Pb_{1-x}Bi_xTi_{1-x}Fe_xO₃ (PT-BF) and 0.5 PbTiO₃-0.5 Bi[Fe_yMn_{1-y}]O₃ (Mn doped PT-BF) which has a very large spontaneous strain.

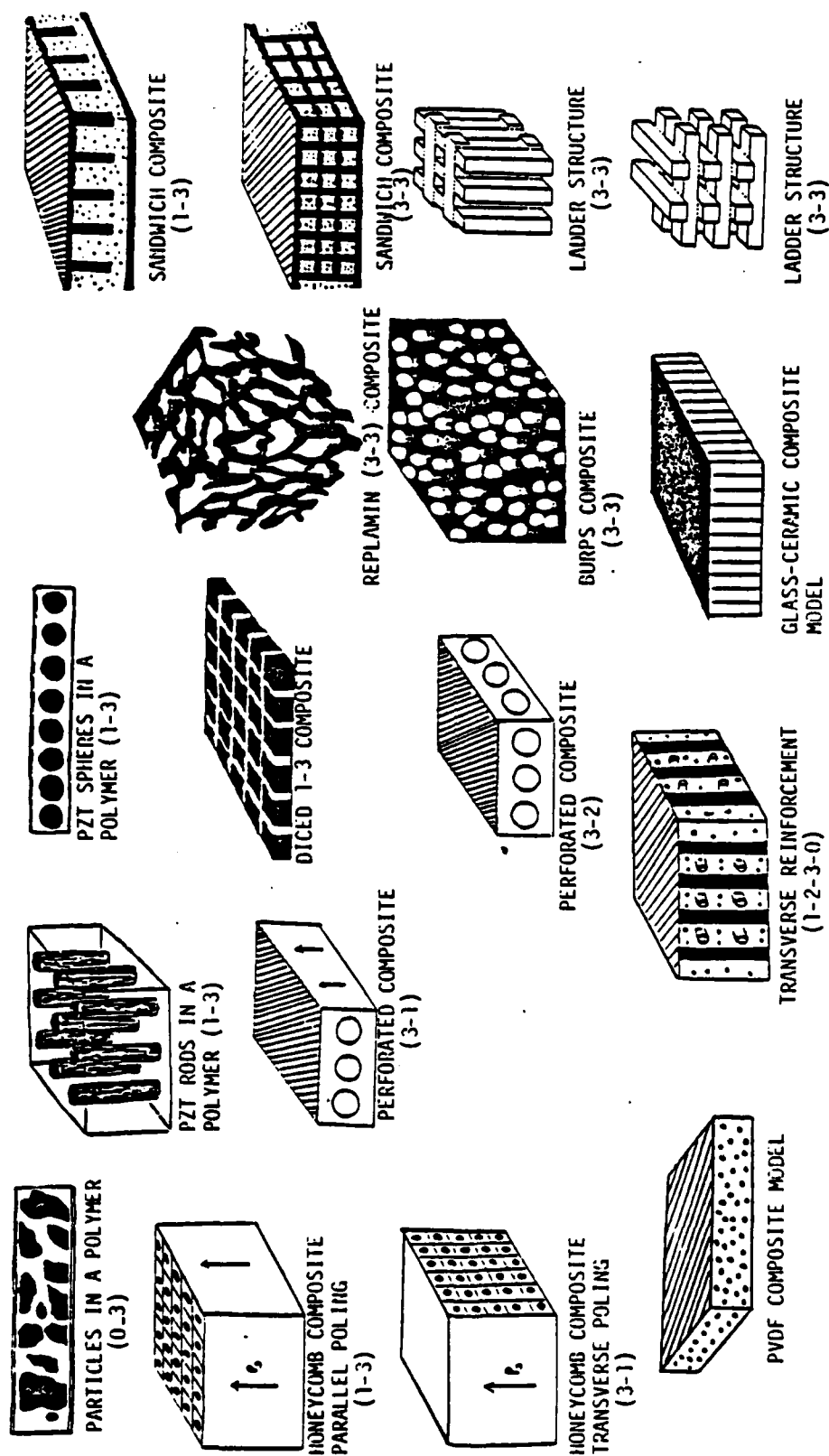


Figure 1. Schematic diagram of various types of composites with different connectivity.

The spontaneous strain in PbTiO_3 is about 6%. In PZT compositions near the morphotropic boundary, it is about 2%. And since in BF-PT, the spontaneous strain is as large as 18%, we were not surprised to find a substantial increase in the hydrostatic voltage coefficients of the composites.

To fabricate the composites, the filler powder is synthesized from the system $\text{Pb}_{1-x}\text{Bi}_x\text{Ti}_{1-y}\text{Fe}_y\text{O}_3$ for which there is a continuous solid solution across the entire composition range. The composition of the powders synthesized in this study lie in the range $x = 0.5-0.7$ and $y = 0.005-.1$. To prepare the filler powder, PbO , TiO_2 , Bi_2O_3 , Fe_2O_3 and MnO_2 were mixed and ball-milled with zirconia media. The oxides were subjected to a low temperature ($700^\circ\text{C}-800^\circ\text{C}$) primary calcination for 1.5 hours, followed by a second high temperature firing ($950^\circ\text{C}-1050^\circ\text{C}$). Water quenching produces an average particle size of $5\mu\text{m}$. To fabricate the composites, piezoelectric ceramic powders and eccogel polymer¹⁴ were mixed and calendered at 40°C . The calendered material is then cured at 80° under slight pressure. Composites were poled in an 80°C silicone oil bath by applying a field $100-120\text{ kV/cm}$ for 20 minutes. The poled composites exhibit outstanding hydrostatic sensitivity attaining values of g_h and $d_h g_h$ well in excess of the values reported for pure PbTiO_3 composites (Table 1). the g_h and d_h values of these composites¹² remain virtually constant over a broad pressure range (Fig. 2).

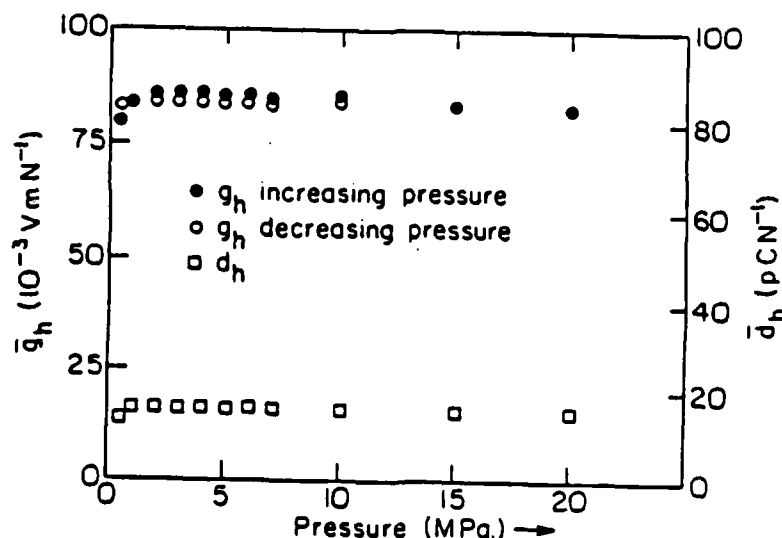


Fig. 2. Variation of g_h and d_h with pressure for $\text{Pb}_{0.5}\text{Bi}_{0.5}\text{Ti}_{0.5}\text{Fe}_{0.5}\text{O}_3$ -polymer composite.

Flexible 0-3 composite have also been developed at Bell Laboratories by Zipfel¹⁵. In this composite a polyurethane matrix material is mixed with 30-40 volume percent of a non-ferroelectric filler such as tartaric acid or lithium sulfate monohydrate. The liquid mixture is injected into an evacuated 3 inch diameter steel mold having two broad faces approximately 1.27mm apart. While the polymer is undergoing polymerization, the composite is polarized by applying hydrostatic pressure and an electric field. In this way the piezoelectric crystals suspended in the liquid copolymer rotate until they are electrically aligned. After polymerization, the resulting rubbery matrix holds the oriented particles in polar alignment for maximum sensitivity. The dielectric constant of this cable hydrophone is typically 4.2 and the piezoelectric sensitivity is stated to be 'comparable with most of the other piezoelectric materials.'

Poling Method of 0-3 Composites

As mentioned earlier, 0-3 composites prepared from PZT, PbTiO_3 and $(\text{Pb,Bi})(\text{Ti,Fe})\text{O}_3$ powders are poled at very large field strength (100-150 kV/cm) in order to achieve sufficient poling. The reason for the necessity of such large fields will be clear from the following discussion.

For a 0-3 composite consisting of spherical grains embedded in a matrix, the electric field E_1 , acting on an isolated spherical grain is given by:

$$E_1 = \frac{3K_2}{K_1 + 2K_2} E_0.$$

In this equation, K_1 and K_2 are the dielectric constants of the spherical piezoelectric grains and the polymer matrix, respectively, and E_0 is an externally applied electric field. For a 0-3 composite of PZT powder and polymer, K_1 is about 2000 and K_2 about 5. In such a composite with an external field of 100 kV/cm, the electric field acting on the piezoelectric particles is only about 1 kV/cm which is insufficient to pole the composite. According to the above equation $E_1 \sim E_0$ only when the dielectric constant of the piezoelectric phase approaches that of the polymer phase. Most of the ferroelectric mat. have very high dielectric constants and hence the above condition cannot be satisfied.

A different way to control the poling of 0-3 composites is to create a continuous electric flux path between the PZT particles. To do this, we have added a small volume fraction of a conductive third phase such as carbon, germanium, silver and silicon to the PZT-polymer composite. In preparing these composites, 68.5 volume percent PZT 501 and 1.5 volume percent carbon were mixed and dry ball-milled. After ball milling, the fillers were mixed with eccogel polymer and placed in a mold under pressure. It is found that the PZT-polymer composite with a small addition of a conducting phase can be poled in about five minutes under a field of 35-40 kV/cm at about 100°C. Fig. 3 shows the effect of the poling voltage on the d_{33} values of the composite. It is observed that a duration of 5 minutes is sufficient for full poling of the composites. Similar composites were made using a powder of pure PbTiO_3 as a filler. It is found that in PbTiO_3 composites, the poling results of composites with germanium additives were better than carbon additives. Dielectric and piezoelectric properties of PZT and PbTiO_3 composites with conductive additives are shown in Table 1. The g_h d_h values of these composites are comparable with those of PVF₂, further details of the poling method will be reported elsewhere¹⁶.

COMPOSITES BASED ON 1-3 CONNECTIVITY

Composites in which the piezoelectric ceramic is self connected one dimensionally and the polymer phase is self-connected three dimensionally were developed by Klicker¹⁷. In a 1-3 composite, PZT rods are embedded in a continuous polymer matrix. Under the idealized saturation in which the polymer phase is far more compliant than PZT, the stress on the polymer will be transferred to the PZT rods. The stress amplification on the PZT phase along with the reduced permittivity greatly enhances the piezoelectric voltage coefficient. To provide a better understanding of the composites, the piezoelectric properties were studied as a function of volume fraction PZT, rod diameter, and sample thickness.

The magnitude of the $d_h g_h$ product of 1-3 composites with PZT rods in polymer matrix is large, but far less than the theoretical value. Part of the reason is that the Poisson ratio of the polymer used is fairly high thus an

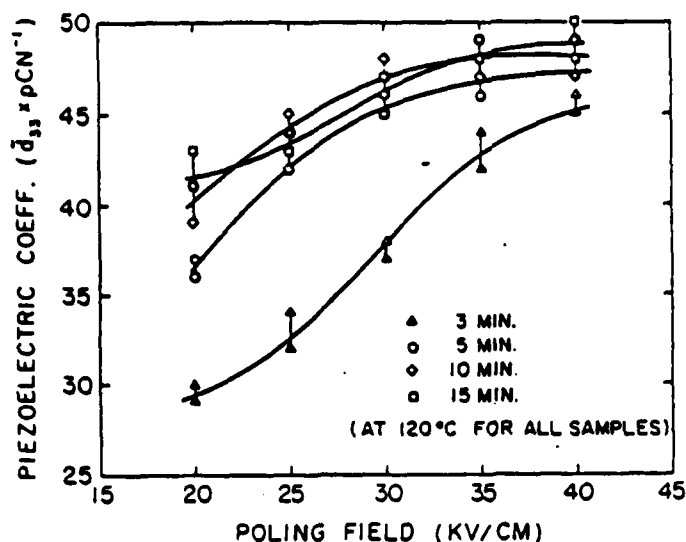


Fig. 3. Variation of piezoelectric d_{33} coefficient of PZT-carbon-eccogel composite with poling field.

internal stress exists which opposes the applied stress, and the stress amplification of a 1-3 connectivity model is greatly reduced. One way to reduce the Poisson ratio of a polymer is to introduce porosity into it. The fabrication of 1-3-0 composites with porous polyurethanes was developed by Klicker¹⁸ who showed that porosity in the polyurethane matrix has a dramatic effect on d_h and g_h . Other types of 1-3-0 composites were studied by Lynn¹⁹. Porosity was introduced into different types of polymer matrices either by adding a foaming agent or by mixing commercial hollow glass spheres with the polymer. Using a foamed REN epoxy, composites with 4 volume % of 280 μ m diameter rods showed a three-fold increase in d_h above the unfoamed REN Epoxy. When hollow glass spheres of an average diameter of 80 μ m and 2 μ m wall thickness were mixed in REN and Spurr's epoxy, d_h increased about twice that of the ordinary epoxy composites. For all the composites with glass spheres, no pressure dependences were found, while in foamed REN epoxy composites, the pressure dependence remains a problem.

Transverse reinforcement is another technique used to enhance the hydrostatic piezoelectric coefficient^{20,21}. These composites were made by mounting two types of fibers in the polymer matrix: PZT rods parallel to the poling direction and stiff glass fibers in the two transverse directions. The glass fibers carry most of the transverse stress thereby decreasing d_{31} without appreciable reduction in d_{33} . Transversely reinforced composites have 1-2-3 connectivity, or 1-2-3-0 connectivity if the polymer matrix is foamed. In many of these polymer ceramic composites a coupling agent is required to achieve good stress transfer.

Savakus²² developed a simplified preparation technique for making composites with 1-3 connectivity. Composite piezoelectric transducers have been constructed by partially dicing PZT ceramics and back-filling with epoxy. Composites containing 10 to 70 volume percent PZT were prepared with several different rod diameters. Measured dielectric constants ranged from 200 to 1000, longitudinal piezoelectric coefficients d_{33} from 200 to 350 pC/N, and hydrostatic piezoelectric coefficients d_h from 40 to 80 pC/N. When diced

PZT ceramic capped with 2mm thick brass or stainless steel and encapsulated with alumina, d_h and g_h increased dramatically²³. The g_h and d_h of this type of composite are 75×10^{-3} Vm/N and 265 pC/N respectively.

Recently extensive study has been made of the dielectric and piezoelectric properties of a new family of polar glass ceramics^{24,25}. Grain oriented glass-ceramics of $Li_2Si_2O_5$ and $Ba_2TiSi_2O_8$ are prepared by crystallization of the glasses in a temperature gradient. They may be regarded as diphasic composites composed of a glassy phase and one or more crystalline phases, wherein needle-like crystals nucleate from the surface and grow into the bulk of the sample in the direction of the temperature gradient. g_h and $g_h d_h$ of these tested sample are comparable with those of PVF₂ polymer. The usual problems of depoling and aging encountered in PVF₂ and most ceramics are avoided with the glass-ceramics which are non-ferroelectric and hence do not require poling.

Composites with 3-1 and 3-2 Connectivity

Composites of PZT and polymer with 3-1 and 3-2 connectivity patterns have been fabricated²⁶ by drilling holes in sintered PZT blocks and filling the holes with epoxy. The influence of hole size and volume fraction PZT on the hydrostatic properties of the composite was evaluated. By decoupling the piezoelectric d_{33} and d_{31} coefficients in the composite, the hydrostatic coefficients are greatly enhanced. On samples optimized for hydrophone performance, the dielectric constants of 3-1 and 3-2 composites are 600 and 300 respectively. For two typical composites, the piezoelectric coefficients d_h , g_h , and $g_h d_h$ for 3-1 composites are 170 (pC/N), 30 ($\times 10^{-3}$ Vm/N), and 5000 (10^{-15} m²/N) respectively, and the corresponding values for 3-2 composites are 200 (pC/N), 60 ($\times 10^{-3}$ Vm/N), and 12000 (10^{-15} m²/N).

The composites are extremely rugged and show no pressure dependence up to 7MPa (1000 PSI). Recently perforated PZT blocks were fabricated by injection molding of the ceramic²⁷ and backfilled with polymer. g_h and $g_h d_h$ of these composites fifteen and fifty times larger than those of PZT ceramics respectively. Similar composites can be made²⁸ by extruding the ceramic rather than drilling. Composites with 3-1 connectivity were fabricated by impregnating an extruded, sintered honeycomb configuration of PZT with epoxy. The composites had lower density (≈ 3000 Kg/m³) and lower dielectric constant (≈ 400) than that of solid PZT. The maximum piezoelectric d_{33} coefficient of the composites was 350 pC/N. g_h and $d_h g_h$ values of the composites were an order of magnitude higher than those of solid PZT.

The study of the 3-1 composites was carried one step further by developing a small hydrophone containing a number of perforated 3-1 elements²⁹. Sixteen cubic elements were prepared measuring each being 0.4 x 0.4 x 0.4cm with a 0.2mm diameter hole filled with epoxy, the elements were encapsulated in a flexane polyurethane which was modified by foaming with nitrogen gas and mixing with 55% glass microballoons. The specimen exhibited a g_h value of 34×10^{-3} Vm/N which is comparable with that of single element composite.

COMPOSITES WITH 3-3 CONNECTIVITY

In a 3-3 composite each of the constituent phases is continuously self-connected in three dimensions to give two interlocking skeletons in intimate contact with one another. This type of structure is exhibited by certain polymer foams, by some phase-separated metals and glasses, by three-dimensional waves, and by natural substances such as wood and coral. The piezoelectric and pyroelectric properties of 3-3 composites have been investigated with some rather remarkable results. For certain coefficients,

dramatic improvements can be made over the best single-phase piezoelectrics.

Piezoelectric ceramic-polymer composites with 3-3 connectivity were first made by Skinner³⁰ using a lost-wax method with coral as a starting material. Among the advantages of these composites are high hydrostatic sensitivity, low dielectric constant, low density for improved acoustic impedance matching with water, high compliance to provide damping, and the mechanical flexibility needed to develop conformable transducers. Shrout³¹ developed a simpler method for fabricating a three-dimensionally interconnected lead zirconate-titanate (PZT) and polymer composite with properties similar to the coral-based composites. The simplified preparation method involves mixing plastic spheres and PZT powder in an organic binder. When carefully sintered, a porous PZT skeleton is formed, and later back-filled with polymer to form a 3-3 composite. This technique is commonly referred to as the BURPS process, an acronym for burned-out plastic spheres. Since the process involves the generation and emission of gaseous hydrocarbons, the name BURPS is highly appropriate. Scientists at Mitsubishi Mining and Cement have developed several techniques for introducing connected porosity in PZT ceramics: reactive sintering, foaming agents, organic additives, and careful control of particle size and firing conditions³². The porosity of the samples tested for hydrophone performance was about 50%. The average pore/size was about 100 μ m. g_h and d_{hg} coefficient of this sample was about 50×10^{-3} Vm/N and 90 xpc/N respectively³³. The g_h showed very slight decrease when the applied pressure was increased up to 70MPa and upon releasing the pressure, the g_h values were recovered.

SUMMARY

The dielectric and piezoelectric properties of several different types of composites are described and their figures of merit for hydrophone applications (d_{hg}) are discussed. Hydrophones are used at low frequencies where the acoustic signal has a wavelength much larger than the scale of the macrostructure of the composite. It is shown that the hydrostatic voltage coefficient g_h and figure of merit $g_h d_h$ of ceramic-polymer composites are an order of magnitude higher than those of single phase materials.

REFERENCES

1. G. Goodman, 'Ferroelectric Properties of Lead Metaniobate,' J. Am. Ceram. Soc. 36:368 (1953).
2. T.-Y. Tien and W.G. Carlson, 'Effect of Additives on Properties of Lead Titanate,' J. Am. Ceram. Soc. 45:567 (1962).
3. Y. Wada and R. Hayakawa, 'Piezoelectricity and Pyroelectricity of Polymers,' Japan J. Appl. Phys. 15:2041 (1976).
4. R.E. Newnham, D.P. Skinner and L.E. Cross, 'Connectivity and Piezoelectric-Pyroelectric Composites,' Mat. Res. Bull. 13:525 (1978).
5. R.E. Newnham, A. Safari, J. Giniewicz and B.H. Fox, 'Piezoelectric Sensors,' Ferroelectrics 60:15 (1984).
6. R.E. Newnham, A. Safari, G. Sa-gong and J. Giniewicz, 'Flexible Composite Piezoelectric Sensors,' IEEE Ultrasonic Symposium Proceedings, 501 (1984).
7. T. Kitayama and Sugawara, 'Flexible Piezoelectric Materials,' Rep. Proc. Gr. Inst. Elec. Comm. Eng. Japan, CPM27-17 (1972).
8. L.A. Pauer, 'Flexible Piezoelectric Materials,' IEEE Int. Conf. Res., p. 1-5 (1973).
9. W.B. Harrison, 'Flexible Piezoelectric Organic Composites,' Proc. of the Workshop on Sonar Transducer Materials, Naval Research Labs., (Feb. 1976).
10. H. Banno and S. Saito, 'Piezoelectric and Dielectric Properties of

- Composites of Synthetic Rubbers and PbTiO_3 and PZT,' Japan. J. Appl. Phys. 22: supp. 22-2, 67 (1983).
11. H. Banno, 'Recent Developments of Piezoelectric Ceramic Products and Composites of Synthetic Rubber and Piezoelectric Ceramic Particles,' *Ferroelectrics*, 5 (1983).
 12. R.Y. Ting, 'Evaluation of New Piezoelectric Composite Materials for Hydrophone Applications,' *Ferroelectrics* (to be published).
 13. J. Giniewicz, '(Pb,Bi)(Ti,Fe) O_3 -Polymer Composite Materials for Hydrophone Applications,' M.S. Thesis, The Pennsylvania State University (1985).
 14. Eccogel 1365 Series (Emerson and Cumming, Densey and Almy Chemical Division, W.R. Grace and Co.).
 15. G.G. Zipfel, '0-3 Piezocomposite,' *Bell Labs. Record.*, April. 1983, p. 11-13.
 16. G. So-gong, A. Safari, R.E. Newnham, 'Easily poled 0-3 composites,' *Ferroelectrics* (to be published).
 17. K.A. Klicker, 'Piezoelectric Composite with 3-1 Connectivity for Transducer Applications,' Ph.D. Thesis, The Pennsylvania State University (1980).
 18. K.A. Klicker, J.V. Biggers and R.E. Newnham, 'Composites of PZT and Epoxy for Hydrostatic Transducer Applications,' *J. Am. Ceram. Soc.* 64:5 (1982).
 19. S.Y. Lynn, 'Polymer-Piezoelectric Ceramic Composites with 3-1-0 Connectivity for Hydrophone Applications,' M.S. Thesis, The Pennsylvania State University (1982).
 20. M. Haun, 'Transverse Reinforcement of 1-3 and 1-3-0 PZT-Polymer Piezoelectric Composites with Glass Fibers,' M.S. Thesis, The Pennsylvania State University (1983).
 21. M. Haun, P. Moses, T.R. Gururaja and W.A. Schulze, 'Transversely Reinforced 1-3 and 1-3-0 Piezoelectric Composites,' *Ferroelectrics* 49:259 (1983).
 22. H.P. Savakus, K.A. Klicker and R.E. Newnham, 'PZT-Epoxy Piezoelectric Transducers: A Simplified Fabrication Procedure,' *Mat. Res. Bull.* 16:677 (1981).
 23. A. Safari, R.E. Newnham and L.E. Cross, 'Diced, Capped and Encapsulated PZT Composite,' (applied for patent).
 24. A. Halliyal, A. Safari, A.S. Bhalla, R.E. Newnham and L.E. Cross, 'Grain-Oriented Glass-Ceramic for Piezoelectric Devices,' *J. Am. Ceram. Soc.* 67:331 (1984).
 25. R.Y. Ting, A. Halliyal and A.S. Bhalla, 'Polar Glass Ceramic For Sonar Transducers,' *J. Appl. Phys. Lett.* 44:9 (1984).
 26. A. Safari, 'Perforated PZT-Polymer Composites with 3-1 and 3-2 Connectivity for Hydrophone Applications,' Ph.D. Thesis, The Pennsylvania State University (1983).
 27. I. Kalnin and R. Hughes, 'Preparation of Perforated PZT by Injection Molding,' (applied for patent).
 28. A. Safari, A. Halliyal, R.E. Newnham and I.M. Lachman, 'Transverse Honeycomb Composite Transducers,' *Mat. Res. Bull.* 17:301 (1982).
 29. R.Y. Ting, 'Evaluation of New Piezoelectric Composite Materials for Hydrophone Applications,' *Ferroelectrics* (to be published).
 30. D.P. Skinner, R.E. Newnham and L.E. Cross, 'Flexible Composite Transducers,' *Mat. Res. Bull.* 13:599 (1978).
 31. K.R. Rittenmyer, T.R. Shrout and R.E. Newnham, 'Piezoelectric 3-3 Composites,' *Ferroelectrics* 41:189 (1982).
 32. R.Y. Ting, 'Evaluation of New Piezoelectric Composite Materials for Hydrophone Applications,' *Ferroelectrics* (to be published).

PIEZOELECTRIC CERAMIC-POLYMER COMPOSITES AS
TRANSDUCER AND VIBRATION ABSORBERS

S. Pilgrim, R.E. Newnham, T.R. Gururaja and A. Safari

PIEZOELECTRIC CERAMIC-POLYMER COMPOSITES AS TRANSDUCERS AND VIBRATION ABSORBERS

S. Pilgrim, R.E. Newnham, T.R. Gururaja and A. Safari

Materials Research Laboratory, The Pennsylvania State University,
University Park, PA 16802

ABSTRACT

Diphasic composite materials are fabricated by embedding piezoelectric ceramics in the form of filler powders, elongated fibers, multilayer and more complex three-dimensional structures in a polymer matrix. The concept of phase connectivity, the manner in which the individual phases are interconnected, has been used to optimize the electric flux pattern and mechanical stress distributions in attaining remarkable improvements in the hydrostatic strain coefficient (d_h) and the hydrostatic voltage coefficient (g_h) over the corresponding values of single phase materials. Recent results on simple 0-3 and 0-0-3 composites are presented, and their utilization as passive and active vibration absorbers discussed. Possible loss mechanisms in 0-3 composites include mechanical, electrical, electromechanical, magnetic and interfacial losses.

INTRODUCTION

The design and fabrication of composite materials optimized for special application has been the subject of extensive research, ranging from mechanical structures to electronic devices. In designing composite materials, primary importance is given to the proper choice of component phases and to the way in which they are interconnected to maximize a predefined figure of merit for the envisaged application. There has been a major effort at the Materials Research Laboratory to develop piezoelectric composite materials with large hydrostatic pressure sensitivity. These

materials are intended to be used as underwater sound detectors (hydrophones) in the low frequency range (<40 kHz). Many different composite structures have been fabricated from piezoelectrically active ceramics such as lead zirconate titanate (PZT) or lead titanate (PT) and piezoelectrically inactive polymers¹⁻⁴. The hydrostatic sensitivity of some of these composites was orders of magnitude larger than that of the piezoelectric phase used in the composite. The composites also have a relatively low density with a good acoustic impedance match to water. The composite materials have also shown excellent performance in the low megahertz frequency range for use in biomedical imaging applications^{5,6}.

In this paper, the principles used to design and fabricate piezoelectric composites for hydrophone applications are discussed briefly, and recent results on composites made from piezoelectric ceramic powders embedded in a polymer matrix are presented. This type of composite is being presently explored for utilization as passive and active vibration absorbers. Possible loss mechanisms including mechanical, electrical, electromechanical and interfacial losses are to be examined.

PIEZOELECTRIC COMPOSITES

Lead zirconate titanate (PZT) is widely used as a transducer material because of its high piezoelectric coefficients. However for hydrophones, PZT is a poor choice for several reasons. PZT has a large piezoelectric d_{33} coefficient, but its hydrostatic strain coefficient $d_h (= d_{33} + 2d_{31})$ is small because d_{33} and $2d_{31}$ are opposite in sign, and almost cancel one another. Moreover, the high permittivity of PZT ($K \approx 1800$) lowers the voltage coefficient g_h to miniscule values. In addition, the density of PZT (7.9 g/cm^3) makes it difficult to obtain good acoustic matching with water. PZT is also a brittle ceramic and for some applications a more compliant material

with better shock resistance is desirable. With these requirements in consideration, we have fabricated a number of different diphasic composites made from polymers and PZT. In a composite the electric flux pattern and the mechanical stress distribution, and hence the resulting physical and electromechanical properties, depend strongly on the manner in which the individual phases are interconnected. In this regard the connectivity of a composite, defined as the number of dimensions in which each component phase is continuous¹, is of crucial importance. When referred to in an orthogonal axis system, each phase in a composite may be self-connected in zero, one, two, or three directions. For diphasic composites, there are ten connectivity patterns designated as 0-0, 0-1, 0-2, 0-3, 1-1, 1-2, 1-3, 2-2, 2-3, and 3-3. In the notation used here, the piezoelectric phase appears first. Thus a 1-3 composite consists of PZT fibers embedded in a polymer matrix, and a 3-1 composite is a solid piece of PZT with parallel holes filled with polymer. During the past few years, a number of investigators have examined piezoelectric ceramic-polymer composites with different connectivity patterns^{1,2,7}. The method of preparation of these composites covers a wide spectrum of ceramic fabrication processes, including extrusion, tape-casting, and injection-molding.

In this paper, a brief summary of the piezoelectric properties of flexible composites with 0-3 connectivity is presented. A 0-3 composite consists of polycrystalline grains of a piezoelectric ceramic embedded in a polymer matrix. The product of \bar{d}_h and \bar{g}_h is used as the figure of merit to evaluate the composites. A more extensive description of the work on the PZT-polymer composites can be found in recent review papers^{2,3}.

Flexible 0-3 and 0-0-3 Composites for Hydrophone Applications

The simplest type of piezoelectric composite consists of a polymer matrix loaded with ceramic powder. In a composite with 0-3 connectivity, the ceramic particles are not in contact with each other while the polymer phase is self-connected in all three dimensions. This type of composite does not have the desirable stress concentration factor found in some other connectivity patterns^{2,4,5}, so the hydrostatic figure of merit $\bar{d}_h \bar{g}_h$ is not large. However, this type of composite is easy to fabricate and amenable for mass production. In many ways the 0-3 composite is similar to poly(vinylidene fluoride) (PVF₂). Both consist of a crystalline phase embedded in an amorphous matrix, and both are reasonably flexible.

The first successful 0-3 composite with large hydrostatic pressure sensitivity was developed by Banno⁷. Rather than using PZT as the ceramic filler, pure or modified lead titanate was employed because of its greater piezoelectric anisotropy. The piezoelectric ceramic fillers used in these composites are PbTiO₃, Bi₂O₃-modified PbTiO₃ and WO₃-modified PZT. Fine-grained (~ 5 μ m) particles of pure PbTiO₃ were made by water quenching sintered ceramics. To fabricate the composite bodies, the piezoelectric powders and chloroprene rubber were mixed and rolled into 0.5 mm thick sheets at 40°C using a hot roller, and then heat treated at 190°C for 20 minutes under a pressure of 13 kg/cm². The composites were poled in an electric field of 100-150 kV/cm for 30 minutes. As shown in Table 1, the hydrostatic voltage coefficient \bar{g}_h of pure PbTiO₃ composite is comparable to that of poly(vinylidene fluoride).

Recently we have fabricated flexible composites with a more active piezoelectric material. The piezoelectric ceramic filler used in these composites is Pb_{1-x}Bi_xTi_{1-x}-Fe_xO₃ (BF-PT) which has a very large spontaneous strain.

There are two reasons why large spontaneous strain is advantageous. First, it makes it easy to obtain a loose ceramic powder of extremely fine-grain size. On cooling from high temperature, the BF-PT ceramic undergoes brittle fracture at the Curie point as it transforms from a cubic state to a tetragonal phase with c/a ratio as large as 1.18⁸. Water-quenching accelerates the fracture process, further reducing the particle size, and making it possible to fabricate very thin piezo-films. The second reason is that a large spontaneous strain promotes greater piezoelectric anisotropy. This increases the hydrostatic sensitivity by reducing the cancellation between piezoelectric coefficients d_{33} and d_{31} . Banno⁷ found that in 0-3 composite ferroelectrics, pure PbTiO_3 has a larger hydrostatic piezoelectric effect than $\text{Pb}(\text{Zr,Ti})\text{O}_3$.

The spontaneous strain in PbTiO_3 is about 6%. In PZT compositions near the morphotropic boundary, it is about 2%. And since in BF-PT, the spontaneous strain is as large as 18%, we expected to find a substantial increase in the hydrostatic voltage coefficients of the composites.

To fabricate the composite, piezoelectric ceramic powders with composition $x = 0.5$ and eccogel polymer* were mixed and calendered at 40°C. The calendered material is then cured at 80° under slight pressure. Composites were poled in an 80°C silicone oil bath by applying a field 100-120 kV/cm for 20 minutes. The poled composites exhibit outstanding hydrostatic sensitivity attaining values of k_h and $d_h g_h$ well in excess of the values reported for pure PbTiO_3 composites³ (Table 1).

As mentioned earlier, 0-3 composites prepared from PZT, PbTiO_3 and $(\text{Pb,Bi})(\text{Ti,Fe})\text{O}_3$ powders were poled at very large field strength (100-150

*Emerson and Cuming, W.R. Grace and Co., Canton, MA.

kV/cm) in order to achieve sufficient poling. The reason for the necessity of such large fields will be clear from the following discussion.

For a 0-3 composite consisting of spherical grains embedded in a matrix, the electric field E_1 , acting on an isolated spherical grain is given by

$$E_1 = \frac{3K_2}{K_1 + 3K_2} E_0$$

In this equation, K_1 and K_2 are the dielectric constants of the spherical piezoelectric grains and polymer matrix, respectively, and E_0 is externally applied electric field. For a 0-3 composite of PbTiO_3 powder and polymer, $K_1 \sim 300$ and $K_2 \sim 5$. For such a composite with an external field of 100 kV/cm, the electric field acting on the piezoelectric particles is only about 5 kV/cm which is insufficient to pole the composite. According to the above equation $E_1 \approx E_0$ only when the dielectric constant of the piezoelectric phase approaches that of the polymer phase. Most of the ferroelectric materials have very high dielectric constants and hence the above condition cannot be satisfied.

One way to increase poling is to increase the polymer conductivity to below that of the PZT filler. To do this, we have added a conducting third phase such as carbon to the PZT-polymer composite. In preparing these composites, 68.5 volume percent PZT 501 and 1.5 volume percent carbon were mixed and dry ball-milled. After ball-milling, the fillers were hand-mixed with eccogel polymer, and placed in a mold under pressure. It is found that the PZT-polymer composite with small amount of carbon additive can be poled in about five minutes under a field of 35-40 kV/cm at 100°C (Table 1). Further details of the poling method will be reported elsewhere⁹.

Composites for Vibration Absorbers

The basic property of a vibration absorber is high damping in the frequency range of interest. Most applications also require a good impedance matching to the exterior medium. The standard vibration absorbers are based on a rubber matrix with various fillers to form 0-3 composites. The major loss mechanisms in such composite are the viscoelastic loss of the matrix along with interfacial and scattering loss by the filler materials. For most polymers, the loss factor attains its maximum value within the glass transition zone and drops rapidly to low values on either side of the zone. Efforts have been made to increase the peak loss factor and to shift and broaden the peak to cover the desired frequency and temperature range.

Changes in loss factor have been achieved by incorporating carbon black in elastomers. Carbon black has an advantage over many other fillers because of their high surface area, their topological complexity and their chemical reactivity, all of which contributes to strong bonding with the polymer matrix. It is not clear, however, whether this is an advantage or a disadvantage in regard to loss factor. Juve¹⁰ reports increased elastic hysteresis in the rubbery domain below the transition zone, but Lee¹¹ was unable to confirm this trend with other carbon-loaded polymers.

If de-wetting of the filler by the polymer matrix is important, then other fillers might be more effective than carbon black in raising the loss factor. Francis¹² has shown that dispersed solids with smooth fracture surfaces permit de-wetting at very low strain levels. It is with precisely such 'feature-less' fillers that Cramer and Silver¹³ were able to achieve maximum $\tan \delta$ values at 5 kHz in their experiments on nitrobutadiene rubber. Glass spheres¹⁴, and heavy metals¹⁵ have also been investigated as fillers in anechoic coatings. The friction between filler particles has been suggested as another loss mechanism.

A dynamic loss mechanism suggested by several authors is that of a liquid moving through a solid network, for example, a plasticizer in a polymer matrix¹⁶. Viscous losses associated with the motion of a liquid through an immobile reticulated structure can lead to acoustic attenuation.

In summary, the effects of dispersed solid or liquid fillers are not simple, but a number of different loss mechanisms seem possible. To clarify the role of fillers it is necessary to characterize particle size, surface area, density, and other physical properties of the composite components.

The research in our laboratory is aimed mainly to determine what useful sound absorption characteristics are exhibited by composites containing one or more active filler materials. We are examining a variety of ferroic materials with movable twins or domains: ferroelectric, ferromagnetics, and ferroelastics. Recent work in Japan indicates that this might be a fruitful line of research.

A composite containing magnetic ferrite particles is now being marketed by the Nippon Electric Co. (NEC) as an efficient absorber of vibrations and noise¹⁷. It is a 0-3 composite composed of 0.1-10 μm ferrite powder embedded in a polyester resin. The loss mechanism is believed to be magneto-mechanical in nature: the ferrite particles are much denser than the polymer matrix, and resonate well with the elastic resin. These vibrations are damped with much greater efficiency than is possible with only pure ferrite or pure plastic because of the magnetic interactions between particles. The NEC material is expected to find applications in fields where the control of vibration and noise is essential: high magnification microscopes, VLSI processing, casings for audio equipment, and vibration-free benches for precision engineering.

The NEC ferrite-polyester resin composite has a number of very attractive features: excellent corrosion resistance and machinability, less expensive

than iron and with a damping factor 100 times higher; thermal expansion coefficients of $1-4 \times 10^{-5}/K$, capable of matching many metals; and compressive strengths of 150 MN/m^2 , sufficient to support heavy loads.

The principal goal of our research has been to identify the loss mechanisms inherent to ferroic fillers. Some of these will be electric, magnetic, or mechanical in nature. Therefore, we are investigating composites in which we control the electrical conductivity, piezoelectric activity, the coercive force controlling domain wall motion, and the particle size and shape. By carrying out a series of experiments in which each factor is varied systematically, we hope to identify the major loss mechanisms.

Experimental evaluation of anechoic materials involves applying an acoustic sine wave to the material positioned in a water-filled tube. Comparison of the incident and reflected wave pressures gives the reflection coefficient, which is calibrated with a perfect reflector to provide a measure of the materials effectiveness in echo reduction. This pulse tube method can also be used to measure the phase shift of the reflected wave, thereby giving the loss angle. Attenuation measurements are generally performed with somewhat thicker samples.

Active Absorber Experiments

We have been successful in constructing active absorbers in which the phase cancellation effect between the incoming wave and the resonant vibration of the composite reduces the reflection coefficient markedly. The concept is elaborated in the following paragraphs with a summary of the results.

The composite material consisted of thin PZT rods (diameter 0.45 mm) arranged in a periodic square lattice in a polymer matrix (Spurrs epoxy). The composite is cut perpendicular to the length of the PZT rods. The volume fraction of PZT in the composite is varied from 10 to 30%. In such a

composite, complex resonance are observed because of the periodicity in the lateral direction. The lowest frequency resonance in the lateral direction occurs when the wavelength of the shear wave in epoxy is equal to the lattice periodicity. Measurement of the surface displacements of the composite showed that the epoxy at the center of the unit cell of the periodic lattice vibrates with a much larger amplitude than that of the PZT and with 180° out of phase¹⁸.

An acoustic wave incident on the sample at this frequency sets up a standing wave pattern in the composite structure. The cancellation effects between the incident wave and the large amplitude of the epoxy with a phase difference of 180° causes a substantial decrease in the reflected echo. Figure 1 is a plot of reflection coefficient of acoustic waves at the water to composite interface. Calculations of the reflection coefficient were made assuming steel as a near-perfect reflector. It is seen in the figure that the reflection coefficient of the composites go much below that of the single phase epoxy used in the composite. The minima for 10, 20 and 30 vol% PZT composites occur at 0.45, 0.825 and 1.125 MHz respectively. The frequencies have an inverse relationship with the lateral periodicity of the corresponding composite. The frequency corresponding to the minima in each composite matches with the lateral resonance frequency measured by resonance technique. These results demonstrated that by knowing the elastic properties of the component phases, a composite resonant absorber can be designed with a very low reflection coefficient.

We have also been experimenting with 0-3 composites for active absorbers using piezoelectric ceramic powders PZT and lead metaniobate as filler materials. Commercially available PZT powder (particle size = $1\text{-}5\mu\text{m}$) is mixed with polyethylene to form composites with up to 70 vol% PZT. The attenuation in this composite comes mainly from interfacial and scattering losses by the

filler material. When the composite is polarized by applying large electric field, it becomes piezoelectric and consequently an additional loss mechanism. Measurements of acoustic impedance and attenuation are being made on unpoled and poled composites to delineate the contribution due to the piezoelectric phase. Lead metaniobate powders prepared from molten salt technique are needle shaped with an aspect ratio of 10 to 1. The evaluation of the composites made from acicular lead metaniobate powder will be beneficial to separate out the effect of the shape of the filler particles on the acoustic damping. Preliminary results on the acoustic impedance of PZT-polyethylene composite are given in Figure 2. The data agrees well with calculations based on logarithmic mixing rule.

REFERENCES

1. R.E. Newnham, L.J. Bowen, K.A. Klicker and L.E. Cross, *Materials in Engineering* 2, 93-106 (1980).
2. R.E. Newnham, A. Safari, J. Giniewicz and B.H. Fox, *Ferroelectrics* 60, 15-22 (1984).
3. R.E. Newnham, A. Safari, G. Sa-gong and J. Giniewicz, *Proc. 1984 IEEE Ultrasonic Symposium*, 501-506.
4. A. Safari, Ph.D. Dissertation, The Pennsylvania State University (1984).
5. T.R. Gururaja, W.A. Schulze, L.E. Cross and R.E. Newnham, *Proc. 1984 IEEE Ultrasonic Symposium*, 523-527.
6. T.R. Gururaja, W.A. Schulze, L.E. Cross and R.E. Newnham, *Proc. 1984 IEEE Ultrasonic Symposium*, 533-538.
7. H. Banno, *Ferroelectrics* 50, 329-338 (1983).
8. S.A. Fedulov, Yu. N. Venevtsev, G.S. Zhdanov, E.G. Smazhevskaya and I.S. Rez, *Soviet Physics. Cryst.*, Vol. 7, No. 1 (1962).
9. G. Sa-gong, A. Safari and R.E. Newnham (to be published).
10. A.E. Juve, *Rubber Chem. and Tech.* 37, 434 (1964).
11. G. Lee, W.M. Madigosky and J.J. Erynck, 'Dynamic Viscoelastic Properties of Materials for Underwater Applications,' N.S.W.C. Report TR-78-138, July, 197.
12. E.C. Francis and C.H. Carlton, *J. Spacecraft Rockets* 6, 65 (1969).
13. W.S. Cramer, *Nav Ord Report (NOL/Whiteoak) No. 1778*, February, 1951.
14. I. Galperin and T.K. Kwe, *J. Appl. Polymer Sci.* 10, 673 (1966).
15. R.E. Peterson, 'Vibration and Mechanical Wave Damping,' U.S. Patent 3,130,700, April, 1964.
16. V.J. Keenan and M.W. Keenan, 'Polymer for Anechoic Coating,' N.S.S.C. Report No. N00024-81-C-5313, May 15, 1982.
17. W.S. Cramer, *U.S. Navy J. of Underwater Acoustics*, 10 (1), 75 (1960).

18. B.A. Auld, H.A. Kunkel, Y.A. Shui and Y. Wang, Proc. 1984 IEEE Ultrasonic Symposium.

Table 1. Dielectric and Piezoelectric Properties of Single Phase and Composite Materials.

Description	Dielectric		$\bar{\epsilon}_{33}$		$\bar{\epsilon}_h$		\bar{d}_h		$\bar{d}_h \bar{\epsilon}_h$	
	Constant	\bar{d}_{33}	pCm^{-1}	$(\times 10^{-3} \text{Vm}^{-1})$	$(\times 10^{-3} \text{Vm}^{-1})$	(pCm^{-1})	$(\times 10^{-15} \text{m}^2 \text{N}^{-1})$			
PZT 501 Ceramic	1800	450	28	2.5	40	100				
PbTiO ₃ Ceramic	230	53	26	23	47	1080				
PVF ₂ -(CH ₂ -CF ₂) _n	12	35	329	100	10	1000				
Pure PbTiO ₃ -Chloroprene Composite	54	60	125	47	22	1000				
PZT-Ecoogel Composite	100	43	51	9	10	90				
Carbon Added PZT-Ecoogel Composite	120	50	47	32	24	800				
0.5PbTiO ₃ -0.5BiFeO ₃ -Ecoogel Polymer Composite	20	40	225	85	16	1300				

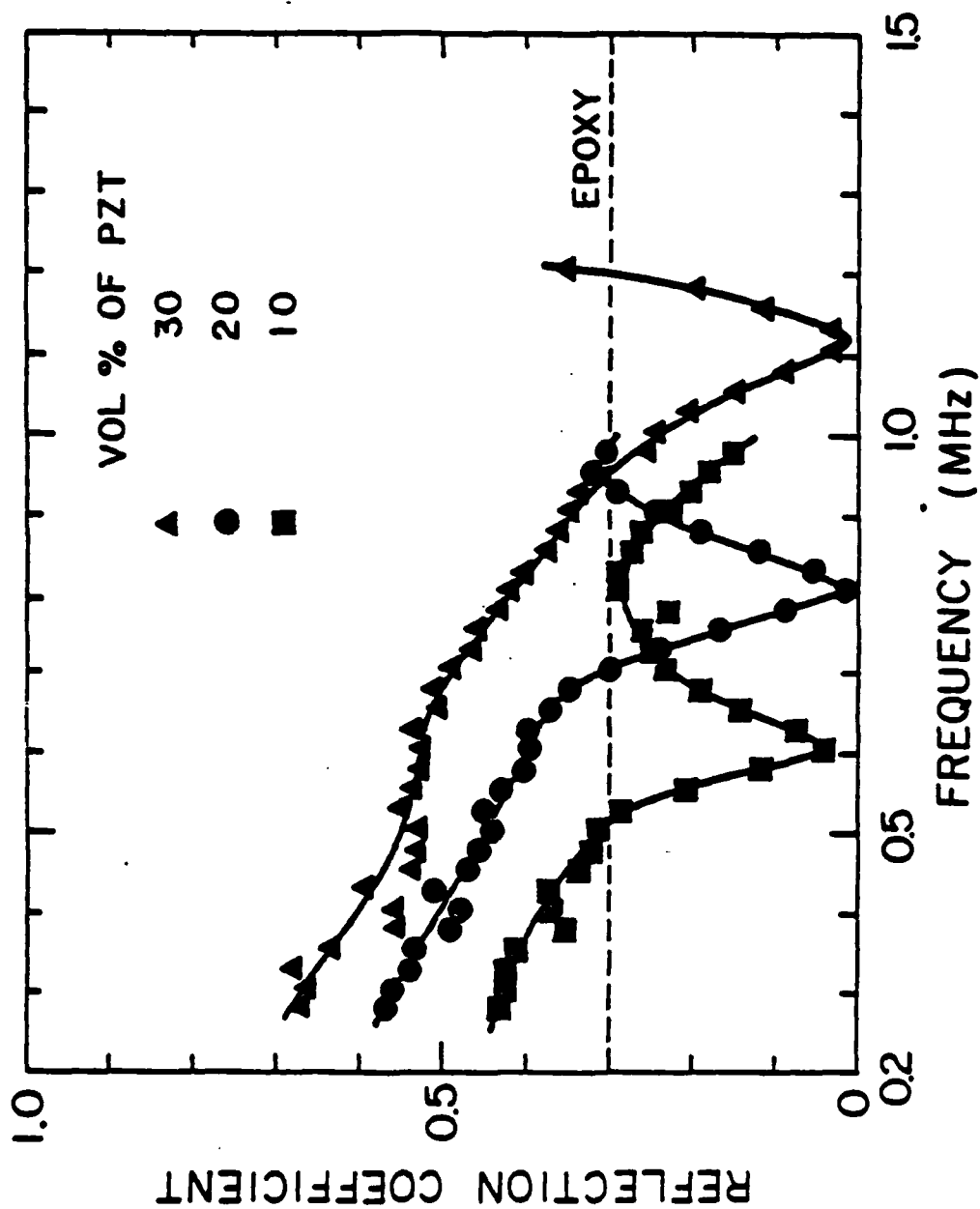


Figure 1. Reflection coefficient as a function of frequency for 1-3 PZT rod-polymer composites.

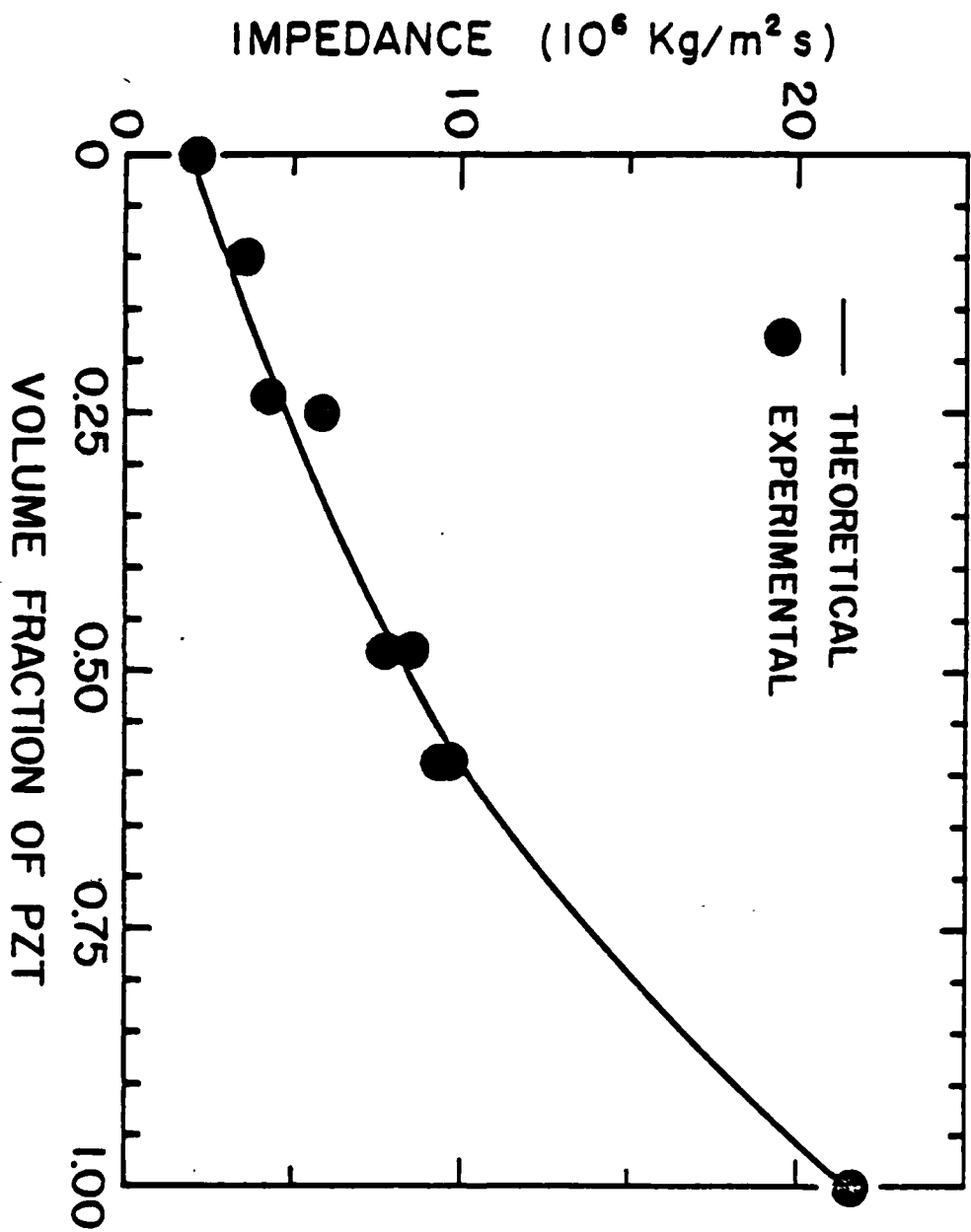


Figure 2. Acoustic impedance as a function of volume fraction PZT in 0-3 PZT powder-polymer composite.

AN EXPERIMENTAL AND THEORETICAL STUDY OF 1-3 and 1-3-0
PIEZOELECTRIC PZT-POLYMER COMPOSITES FOR HYDROPHONE APPLICATIONS

M.J. Haun and R.E. Newnham

AN EXPERIMENTAL AND THEORETICAL STUDY OF 1-3 AND 1-3-0 PIEZOELECTRIC PZT-POLYMER COMPOSITES FOR HYDROPHONE APPLICATIONS

M. J. HAUN and R. E. NEWNHAM

*Materials Research Laboratory, Pennsylvania State University,
University Park, PA 16802 USA*

(Received January 7, 1986)

A new type of piezoelectric PZT-polymer 1-3-0 composite was fabricated with a single large void present in the center of the composite. Experimentally and theoretically the addition of this type of void to a 1-3 composite significantly enhances the hydrostatic piezoelectric d_h and g_h coefficients.

A comparison of the experimental results and theoretical predictions was made. The pressure and frequency dependences of the properties of the 1-3 and 1-3-0 composites were measured, along with the effect of hydrostatic pressure cycling. The 1-3-0 composites partially depoled from pressure cycling to 600 psi (4.1 MPa), indicating that the limit of hydrostatic sensitivity, physically possible for the soft PZT used, was exceeded.

1. INTRODUCTION

Many different types of piezoelectric composites composed of lead zirconate titanate (PZT) and polymer have been fabricated for possible use in hydrophone applications.¹ Based on the idea of decoupling the piezoelectric d_{33} and d_{31} coefficients and lowering the permittivity, these composites have produced some remarkable improvements in the hydrostatic d_h and g_h coefficients.

One type of composite that has been particularly successful is the 1-3 composite with PZT rods aligned in the poling direction (x_3) and held together by a polymer matrix.²⁻⁵ In the notation 1-3 the one refers to the one-dimensionally connected PZT phase, and the three refers to the three-dimensionally connected polymer phase.

Porosity has been added to the polymer matrix of a 1-3 composite to further enhance the hydrostatic sensitivity.³⁻⁵ 1-3-0 connectivity notation is used to describe a 1-3 composite with a porous polymer matrix. The 0 refers to the polymer porosity, which is not connected through the composite.

The porous matrices previously used in 1-3-0 composites were fabricated by foaming the polymer, which produced many small pores throughout the matrix. This paper deals with a different type of 1-3-0 composite where a single large void was used to isolate a region of the PZT rods from the polymer.

In Section 2 a theoretical model for 1-3 and 1-3-0 composites will be presented. The experimental procedure used to fabricate and test these composites will be described in Section 3. A comparison between the experimental results and theoretical predictions will be made in Section 4. The effect of hydrostatic pressure cycling

on the properties of the composites will be discussed in Section 5, along with the pressure and frequency dependences of the \bar{g}_k coefficient. Finally in Section 6, the conclusions of this study will be given.

2. THEORETICAL MODEL FOR 1-3 AND 1-3-0 COMPOSITES

In this section equations for the piezoelectric \bar{d}_{33} and \bar{d}_{31} coefficients for a 1-3-0 composite will be derived from the volume fractions and material constants of the constituent phases. The porosity of the polymer matrix will be assumed to be composed of one large void in the center of the composite, as shown in Figure 1. Thickness ($t = c/d$) and width ($w = a/b$) ratios of the dimensions of the void to the composite dimensions will be included in the derivation to demonstrate the effects of the shape of the void on the properties.

The polarization of the composite arises from the piezoelectric material: PZT, in this case, assuming the polymer to be non-piezoelectric. The composite d_{33} coefficient is given by

$$\bar{d}_{33} = \frac{\bar{P}_3}{\bar{\sigma}_3} = \frac{{}^zV d_{33}^z \sigma_3}{\bar{\sigma}_3}, \quad (1)$$

where P_3 and σ_3 are the polarization and stress in the poling direction, the superscript z refers to the PZT phase, a bar over a symbol refers to the total composite, and zV is the volume fraction of PZT in the composite. Transverse effects in the x_1 and x_2 directions were neglected in Equation (1), because the composite was assumed to be free to expand or contract in these directions.

In the x_3 direction the PZT rods are connected in parallel to the polymer, and the phases were assumed to be bonded together perfectly. All parallel connections were assumed to strain uniformly, and therefore the transverse effects cannot be neglected when determining the \bar{d}_{31} coefficient.

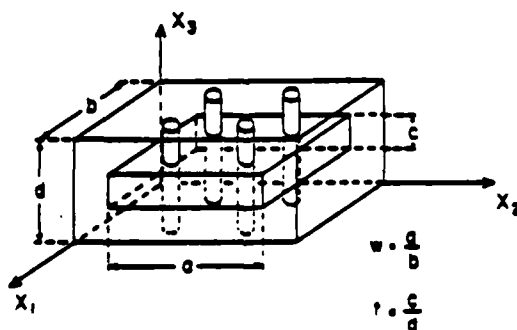


FIGURE 1 A 1-3-0 composite with PZT rods aligned in the x_3 direction and a single large void in the center of the composite. The x_1 and x_2 axes are symmetric.

When a stress is applied in the x_1 direction, an internal stress develops in the x_3 direction at the PZT-polymer interface due to the mismatch in the transverse compliance s_{13} coefficients ($= -\nu_{13}s_{11}$) of the two phases. An additional term was used to account for the internal stress, as shown in the following \bar{d}_{31} relation:

$$\bar{d}_{31} = \frac{\bar{P}_3}{\bar{\sigma}_1} = \frac{z_V}{\bar{\sigma}_1} ({}^i d_{31} \sigma_1 + {}^i d_{33} \sigma_3) \quad (2)$$

The first term in Equation (2) represents the polarization in the x_3 direction that results from an applied stress in the x_1 direction. The second term is the contribution to the \bar{d}_{31} coefficient from the stress on the PZT in the x_3 direction, due to the mismatch in s_{13} coefficients. This stress produces a polarization through the d_{33} coefficient of PZT.

The stress ratios in Equation (1) and (2) were related to the compliances and volume fractions of the phases through simple series and parallel models. A uniform stress state and a uniform strain state were assumed across series and parallel connections, respectively.

To model the composite, it was divided into parallel sections that were either single phase or a series connection of two or more phases. After determining the compliance of the individual sections with a series model, the sections were then combined with a parallel model.

Replacing the stress ratios with compliance relations as described above, the following equations were derived for a 1-3 composite without porosity:

$$\bar{d}_{33} = \frac{{}^i V {}^i d_{33} {}^p s_{33}}{{}^i V {}^p s_{33} + (1 - {}^i V) {}^i s_{33}}, \quad (3)$$

and

$$\bar{d}_{31} = \frac{{}^i V {}^i d_{31} {}^p s_{11}}{\alpha} + \frac{{}^i d_{33} \beta}{\gamma}, \quad (4)$$

where

$$\alpha = \left[1 - \frac{1}{2} (\Pi {}^i V)^{1/2} + {}^i V \right] {}^p s_{11} + \left[\frac{1}{2} (\Pi {}^i V)^{1/2} - {}^i V \right] {}^i s_{11}$$

$$\beta = {}^i \nu_{13} {}^i s_{11} - {}^p \nu_{13} {}^p s_{11},$$

and

$$\gamma = \frac{{}^i s_{33}}{{}^i V} + \frac{{}^p s_{33}}{1 - {}^i V}.$$

The superscript p refers to the polymer phase, and ν_{13} is Poisson's ratio.

For the 1-3-0 composite shown in Figure 1, the following relation resulted:

$$\bar{d}_{33} = \frac{{}^2V^2 d_{33}^p s_{33}}{{}^2V^2 s_{33} + (1 - w^2){}^2s_{33}} \quad (5)$$

and

$$\bar{d}_{31} = \frac{1}{\delta} \left[{}^2V^2 d_{31}^p s_{11} (1 - t) + {}^2d_{33} \alpha \beta \left(\frac{1}{\gamma} - \frac{1}{\zeta} \right) \right] \quad (6)$$

where

$$\delta = \left[\left(1 - \frac{1}{2} (\Pi^2 V)^{1/2} \right) \left(\frac{1 - tw}{1 - t} \right) + {}^2V \right] s_{11} + \left[\frac{1}{2} (\Pi^2 V)^{1/2} \left(\frac{1 - tw}{1 - t} \right) - {}^2V \right] s_{11},$$

and

$$\zeta = \frac{{}^2s_{11}}{{}^2V} + \frac{{}^2s_{33}}{w^2 - {}^2V}.$$

t is the thickness ratio, and w is the width ratio as described in Figure 1. α , β , and γ are equal to the same relations used for the 1-3 composite.

The volume fraction of porosity is equal to $t(w^2 - {}^2V)$. When t and w^2 are equal to zero and 2V , respectively; the volume fraction of the void is zero, and Equations (5) and (6) for a 1-3-0 composite simplify to Equations (3) and (4) for a 1-3 composite.

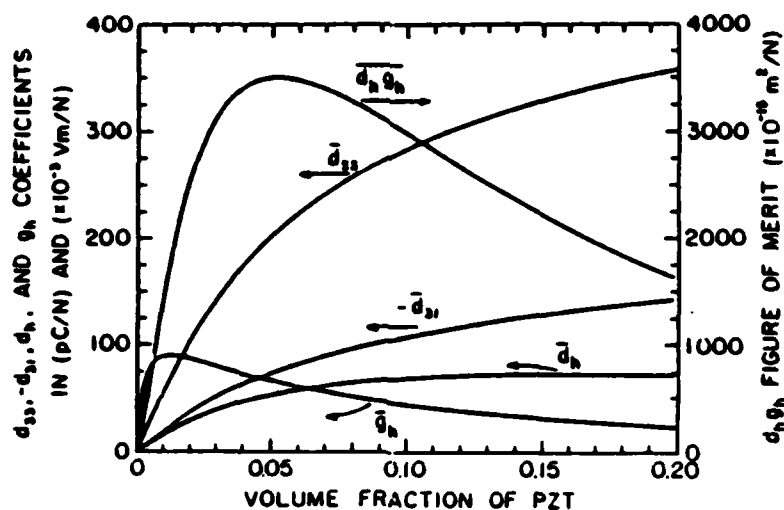


FIGURE 2 Theoretical piezoelectric coefficients of a 1-3 composite plotted versus the volume fraction of PZT.

TABLE I

Piezoelectric and elastic coefficients used in the theoretical calculations

Constant	Value	Reference
\bar{d}_{33}	450 pC/N	Experimentally determined on PZT-501
\bar{d}_{31}	204 pC/N	Experimentally determined on PZT-501
s_{33}	$1.88 \times 10^{-11} \text{ m}^2/\text{N}$	Jaffe, <i>et al.</i> ⁶
s_{11}	$1.64 \times 10^{-11} \text{ m}^2/\text{N}$	Jaffe, <i>et al.</i> ⁶
ν_{13}	0.44 ($= -s_{13}/s_{11}$)	Jaffe, <i>et al.</i> ⁶
ρ_{33}	$29 \times 10^{-11} \text{ m}^2/\text{N}$	Parratt ⁷
ρ_{13}	0.35	Parkyn ⁸

The \bar{d}_{33} and \bar{d}_{31} coefficients for a 1-3 composite calculated from Equations (3) and (4) are plotted versus the volume fraction of PZT in Figure 2. The hydrostatic \bar{d}_h ($= \bar{d}_{33} + 2\bar{d}_{31}$) and \bar{g}_h ($= \bar{d}_h/\epsilon_0 \bar{K}_{33}$) coefficients, and the $\bar{d}_h \bar{g}_h$ product used as the figure of merit are also plotted in this figure.

The dielectric constant \bar{K}_{33} for the 1-3 composite was calculated using the following parallel mixing rule:

$$\bar{K}_{33} = V^* K_{33} + V' K_{33} \quad (7)$$

The dielectric constants of PZT (K_{33}) and polymer (K_{33}) used in the calculations were 1760 and 4, respectively. These values were experimentally determined for PZT 501 and for Spurr's epoxy; the components used to fabricate the composites discussed later in this paper.

Table I gives the values of the other material constants used in the calculations. The constants given for the polymer are for a typical epoxy.

According to the theoretical calculations for a 1-3 composite shown in Figure 2, the optimum percentage of PZT to maximize the $\bar{d}_h \bar{g}_h$ figure of merit should be four to six percent PZT. In the following theoretical calculations, and in the experimental composites fabricated in this study, six percent PZT was used.

The \bar{d}_{33} coefficient of a 1-3-0 composite, as defined by Equation (5), is independent of the thickness ratio of the porosity, but is dependent on the width ratio. In Figure 3 the change in the \bar{d}_{33} coefficient was plotted against the volume fraction of porosity. The thickness ratio was kept constant for each curve, and the volume fraction of porosity was varied by changing w .

In Figure 4 the change in the \bar{d}_{31} and \bar{d}_h ($= \bar{d}_{33} + 2\bar{d}_{31}$) coefficients are plotted on a log scale versus the volume fraction of porosity. In Figure 4a the width ratio was held constant for each curve and the thickness ratio was varied, while in Figure 4b the thickness ratio was held constant and the width ratio varied. The thickness ratio has a greater effect than the width ratio on the \bar{d}_{31} coefficient, but less of an effect on the \bar{d}_h coefficient, because the \bar{d}_{33} coefficient is independent of the thickness ratio.

In Figure 5 the thickness and width ratios were set equal and the change in the \bar{d}_{33} , \bar{d}_{31} , \bar{d}_h and \bar{g}_h coefficients, and the $\bar{d}_h \bar{g}_h$ figure of merit were plotted on a log scale versus the volume fraction of porosity. The values of these coefficients and the dielectric constant for twenty and forty percent porous 1-3-0 composites are com-

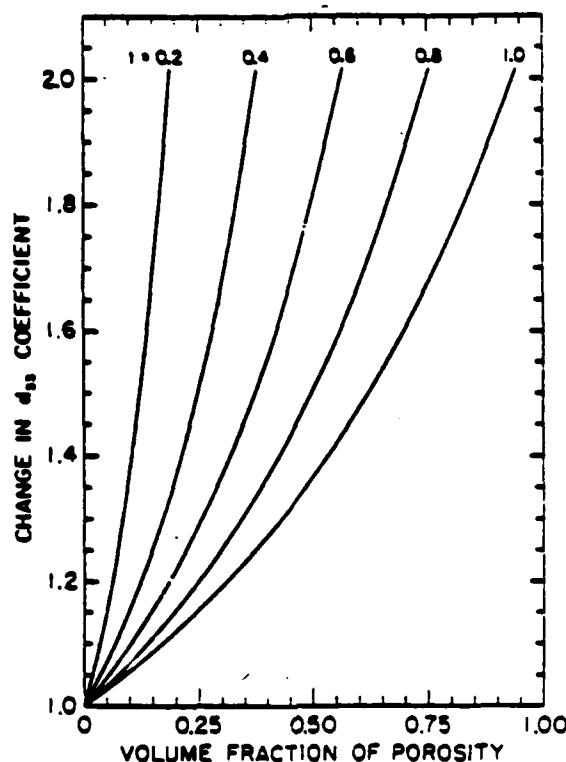


FIGURE 3 Predicted change in \bar{d}_{33} coefficient plotted versus the volume fraction porosity for a 1-3-0 composite with six percent PZT. The thickness ratio (t) was held constant, and the width ratio (w) varied from $(0.06)^{1/2}$ to 1.0 for each curve.

pared with a non-porous 1-3 composite and with single-phase PZT ceramic in Table II.

The dielectric constant \bar{K}_{33} for the 1-3 composite was calculated using Equation (7). The addition of porosity connected in series with the polymer only slightly effects the dielectric constant. Thus the dielectric constants of the 1-3-0 composites are approximately equal to the value calculated for the 1-3 composite.

The theoretical values of the coefficients shown in Table II demonstrate the possible enhancement in the hydrostatic sensitivity that can be achieved through the use of 1-3 or 1-3-0 composites as compared to single-phase PZT. The basic idea of a 1-3 composite is to reduce the \bar{d}_{31} coefficient relative to the \bar{d}_{33} coefficient, while also decreasing the dielectric constant.

Adding porosity to a 1-3 composite allows the PZT rods to support a greater fraction of the applied stress in the x_3 direction, thereby increasing the \bar{d}_{33} coefficient. The addition of porosity decreases the \bar{d}_{31} coefficient because of two effects: the area of PZT exposed to an applied stress in the x_1 direction is reduced, and the internal stress on the PZT in the x_3 direction caused by the mismatch in s_{13} compliance coefficients of the PZT and polymer is decreased. Thus the hydrostatic

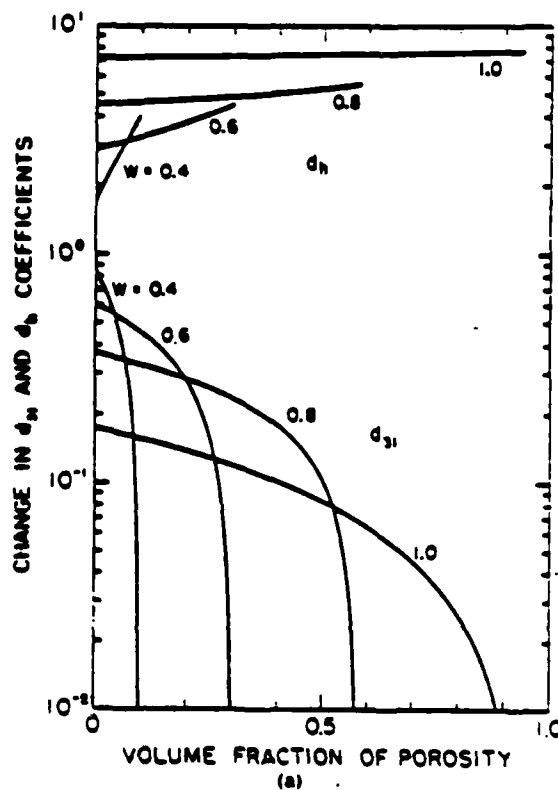


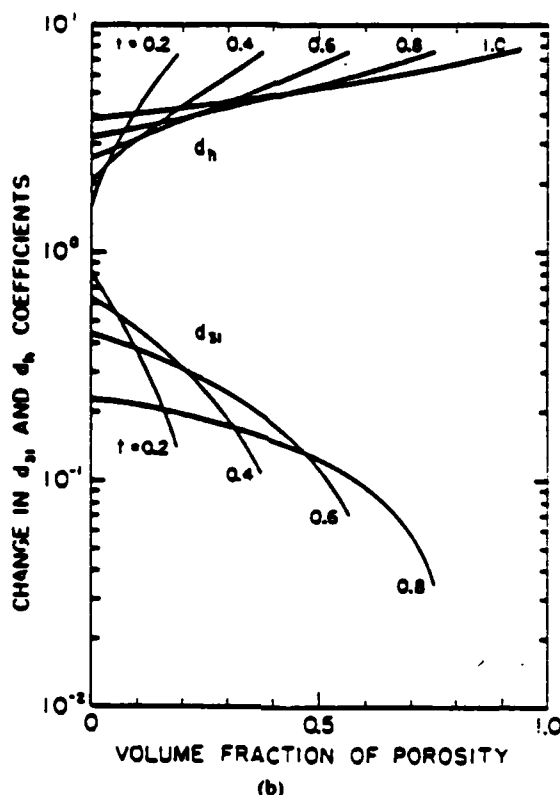
FIGURE 4 The theoretical change in \bar{d}_{31} and \bar{d}_h coefficients plotted against the volume fraction porosity for a 1-3-0 composite with six percent PZT. In (a) the width ratio (w) was held constant and the thickness ratio (t) varied from 0 to 1.0 for each curve. In (b) the thickness ratio was held constant, and the width ratio varied from $(0.06)^{1/2}$ to 1.0 for each curve.

piezoelectric sensitivity should be enhanced through the addition of porosity (in the form of a void as shown in Figure 1) to a 1-3 composite.

In this section the \bar{d}_{31} coefficient of a 1-3-0 composite was shown to be dependent on the thickness ratio of the void, and independent of the width ratio. The \bar{d}_{31} coefficient depends more on the thickness ratio than on the width ratio. The opposite is true for the \bar{d}_h coefficient, which depends more on the width ratio than on the thickness ratio. Thus a void elongated in the x_1 direction would be more advantageous in enhancing the hydrostatic sensitivity.

3. PROCEDURE FOR PROCESSING AND EVALUATING 1-3-0 PIEZOELECTRIC COMPOSITES

A fabrication procedure for PZT-polymer composites with 1-3 connectivity has been reported earlier.² Additional steps were added to the procedure to introduce a void into the composite as shown in Figure 1.



Alignment racks were made from two 1.8 cm diameter brass discs with a square array of holes drilled in each. The two discs were bolted together so that PZT rods could be passed through corresponding holes aligning the rods in place. The alignment racks were suspended over molds, which were filled with Spurr's epoxy and cured. The epoxy served as a base to hold the PZT rods in place so that the brass racks could be removed.

Five additional steps were used to form the void in the center of the composite. The epoxy base described above was used as one of the six sides surrounding the void. The next side was formed by suspending the epoxy base perpendicular to a mold with the PZT rods parallel to the mold. The mold was then filled with epoxy and cured. The remaining sides were made in four similar steps by rotating the structure ninety degrees to the previous orientation and again suspending the structure over a mold, which was then filled with epoxy and cured.

After forming the six sides around the void, a diamond saw was used to cut a 1-3-0 composite sample out of the section containing the void. A 1-3 composite for comparison was then cut out of the remaining polymer and PZT. This allowed a direct comparison between 1-3 and 1-3-0 composites composed of the same PZT rods. The samples were then polished and air-dry silver was applied to the faces perpendicular to the x_3 direction to act as electrodes.

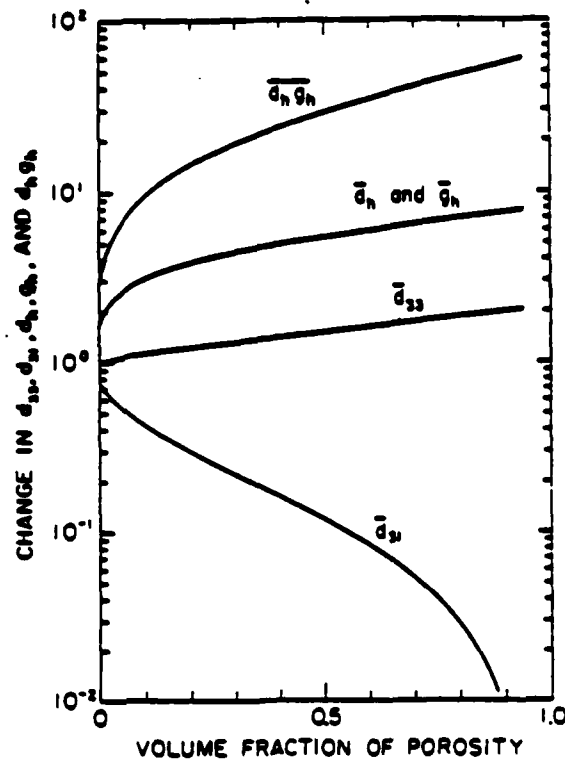


FIGURE 5 The theoretical change in piezoelectric coefficients plotted versus the volume fraction of porosity for a 1-3-0 composite with six percent PZT. The thickness (t) and width (w) ratios were set equal, and both varied from $(0.06)^{1/2}$ to 1.0.

TABLE II

Comparison between the properties of single-phase PZT and the theoretical predictions for 1-3 and 1-3-0 composites containing six percent PZT

Coefficient	Single-phase PZT	1-3	1-3-0 ^a (20% porosity)	1-3-0 ^b (40% porosity)
\bar{K}_{33}	1760	109	≈ 109	≈ 109
\bar{d}_{33} (pC/N)	450	223	270	310
\bar{d}_{31} (pC/N)	-204	-83	-25	-13
\bar{d}_h (pC/N)	42	57	220	284
\bar{g}_h ($\times 10^{-3}$ Vm/N)	2.7	59	228	294
$\bar{d}_h \bar{g}_h$ ($\times 10^{-15}$ m ² /N)	113	3400	50,200	83,500

^a $t = w = 0.619$

^b $t = w = 0.764$

Nine pairs of 1-3 and 1-3-0 composites were fabricated by the procedure just described. Due to the high degree of wetting of the uncured epoxy on cured epoxy and on PZT, it was difficult to form a completely uniform void through the PZT rod section in many of the 1-3-0 composites.

The samples were poled in a 70°C oil bath with a field of 14 KV/cm applied for five minutes. After aging for at least 24 hours, the dielectric and piezoelectric properties were measured.

The capacitance and dissipation factor were measured at 1 kHz using a Hewlett-Packard 427A Multi-Frequency LCR Meter. The d_{33} coefficient was measured dynamically using a Berlincourt Piezo d_{33} -meter with the electromagnetic driver operating at a frequency of 100 Hz. Twenty five d_{33} measurements were made on each sample using single-point probes, and the average was used as the d_{33} coefficient of the composite.

The \bar{g}_h coefficient was determined using the dynamic A.C. technique illustrated in Figure 6. An electromagnetic driver was used as an A.C. stress generator to apply pressure waves to the sample and a PZT standard, which were also under a static pressure from the hydraulic press. The charges produced from the sample and standard were buffered with an impedance convertor, and the voltages produced were measured on a Hewlett-Packard 3585A Spectrum Analyzer. The ratio of the

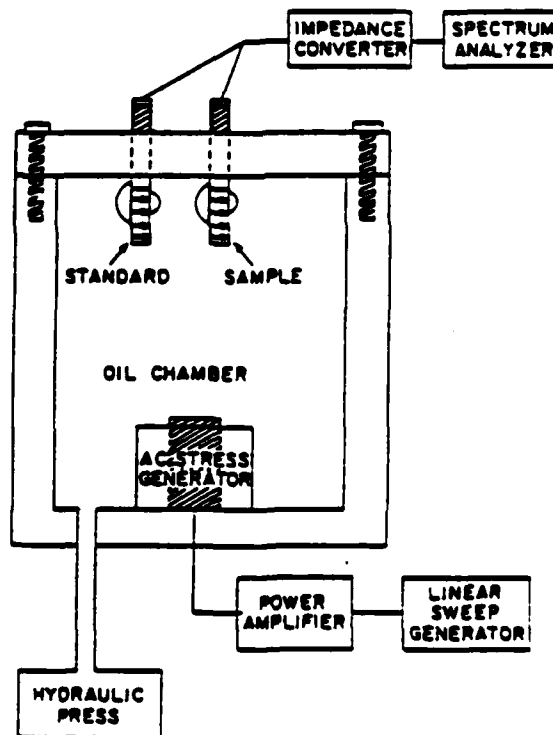


FIGURE 6 Apparatus used to measure \bar{g}_h by the dynamic A. C. method.

voltages produced is proportional to the \bar{g}_h coefficients. By accounting for the sample geometries and the stray capacitance of the holders, the \bar{g}_h coefficient of the sample was calculated.

Using the Spectrum Analyzer the frequency dependence of the samples was measured from 50 Hz to 1 KHz from the harmonics of the fundamental peak. The pressure dependence was measured by applying static pressures of up to 1000 psi (6.9 MPa) from the hydraulic press.

4. COMPARISON BETWEEN EXPERIMENTAL RESULTS AND THEORETICAL PREDICTIONS

As mentioned in the previous section, many of the 1-3-0 composites did not have a uniform void through the PZT rod section. However all of these composites showed significant enhancements in the hydrostatic coefficients compared to the corresponding 1-3 composites cut from the same sets of PZT rods. The $\bar{d}_h \bar{g}_h$ figures of merit of these composites increased by factors of 6 to 80 times with the addition of the void.

The results for a 1-3-0 composite with a complete uniform void covering the PZT rod section are shown in Table III, along with the results of the 1-3 composite cut from the same set of PZT rods. Also listed in Table III are the theoretical predictions for the 1-3 and 1-3-0 composites.

The experimental results shown in the first and third columns labeled MRL were measured at the Materials Research Laboratory, The Pennsylvania State University, according to the procedure described in the previous section. The results shown in the fourth column labeled NRL were measured independently at the Underwater Sound Reference Detachment, Naval Research Laboratory, Orlando, Florida.¹¹

The PZT rods in the composites were aligned in a square array with PZT occupying six percent of the volume in this section of the composite. However, when fabricating the 1-3-0 composite the void covered a larger area than the PZT rod section. This extra area of polymer and void lowered the percentage of PZT in the total composite to approximately one percent. Both composites were fabricated with the same dimensions; the thickness 7.5 mm, and the areas 3.2 cm².

As would be expected, the \bar{d}_{33} coefficient measured over the PZT rod section varied greatly from the \bar{d}_{33} of the outer portion of the samples. It was therefore

TABLE III
Comparison between the experimental results and theoretical predictions for 1-3 and 1-3-0 composites

Coefficient	1-3 Composite		1-3-0 Composite (29% Void)		
	MRL	Theoretical	MRL	NRL	Theoretical
\bar{K}_{33}	22	22	24	25	22
\bar{d}_{33} (pC/N)	217	223	225	—	288
\bar{d}_h (pC/N)	10	17	63	100	95
\bar{g}_h ($\times 10^{-3}$ Vm/N)	52 ^a	87	295 ^a	446 ^b	488
$\bar{d}_h \bar{g}_h$ ($\times 10^{-15}$ m ² /N)	520	1480	18,600	44,600	46,400

^a Measured at 100 psi (0.69 MPa) and 50 Hz.

^b Measured at 72 psi (0.5 MPa) and 1 KHz.

difficult to determine a \bar{d}_{33} coefficient for the total area of the composites.

In Table III the experimental \bar{d}_{33} coefficients represent averages of d_{33} measurements made only over the PZT rod section of the samples. Thus six percent PZT was assumed for the theoretical calculations of the \bar{d}_{33} coefficients. For the \bar{d}_{33} of the 1-3-0 composite the thickness and width ratios of the void were both assumed to be equal to 0.6921, corresponding to 29 percent porosity.

The values of the dielectric constant, \bar{d}_h and \bar{g}_h coefficients, and $\bar{d}_h\bar{g}_h$ figure of merit in Table III were determined for the total area of the samples. In the theoretical calculations of these coefficients one percent PZT was assumed, and for the 1-3-0 composite the thickness and width ratios were assumed to be equal to 0.677, corresponding to 29 percent porosity.

The agreement between the experimental and theoretical dielectric constants shows that the simple parallel model works quite well. The experimental and theoretical \bar{d}_{33} coefficients were also in good agreement. The experimental \bar{d}_{33} coefficients would be expected to be less than the theoretical values, because the phase do not actually strain equally across parallel connections as assumed in the theory, and thus less stress would be transferred to the PZT from the polymer.

As was shown in Table III the \bar{g}_h coefficients of the 1-3-0 composite measured at MRL and NRL were different. The difference in measuring pressures and frequencies used should not account for this difference in \bar{g}_h coefficients, as will be shown in the next section by the pressure and frequency dependences.

The electrical impedance was low due to the small percentage of PZT present in these composites. Samples with low impedance were difficult to measure using the equipment at MRL, and thus conservative values were reported in Table III. The measurements made at NRL using the reciprocity method (see reference 9 for a description of the method), probably give more accurate results for low impedance samples.

The conservative values of the measurements made at MRL were low compared to the theory. However, the measurements made at NRL agree remarkably well with the theoretical calculations.

The addition of a 29 percent void to a 1-3 composite significantly enhanced the hydrostatic properties of the composite. By improving the procedure of fabricating 1-3-0 composites to reduce the excess area around the PZT rod sections, the \bar{d}_h coefficient could conceivably be further increased by a factor of four to five.

5. EFFECT OF CYCLES OF HYDROSTATIC PRESSURE AND PRESSURE AND FREQUENCY DEPENDENCES

The \bar{g}_h coefficient of the composites was measured as a function of pressure up to 1000 psi (6.9 MPa). With repeated pressure cycles it was found that the \bar{g}_h coefficients of the 1-3-0 composites continually decreased after each cycle of pressure.

Krueger and Berlincourt¹⁰ have shown that for soft PZT, such as that used in this study, cycles of longitudinal compressive stress up to 10,000 psi (69 MPa) continually decreased the \bar{d}_{33} coefficient, and slightly increased the dielectric constant. After approximately 30 to 40 cycles of pressure, the \bar{d}_{33} coefficient had decreased to less

than half the original value, but additional pressure cycles had no significant effect. When applying lateral stress cycles only a small decrease in the d_{33} coefficient was found. It was also observed that the time of exposure to the longitudinal or lateral stress had little effect on the \bar{d}_{33} coefficient or dielectric constant of soft PZT.

When a hydrostatic stress is applied to a 1-3 composite, the stiff PZT rods support most of the stress in the x_3 direction. This results in a large longitudinal stress on the PZT, substantially greater than the applied stress. In a 1-3-0 composite the stress is even further amplified.

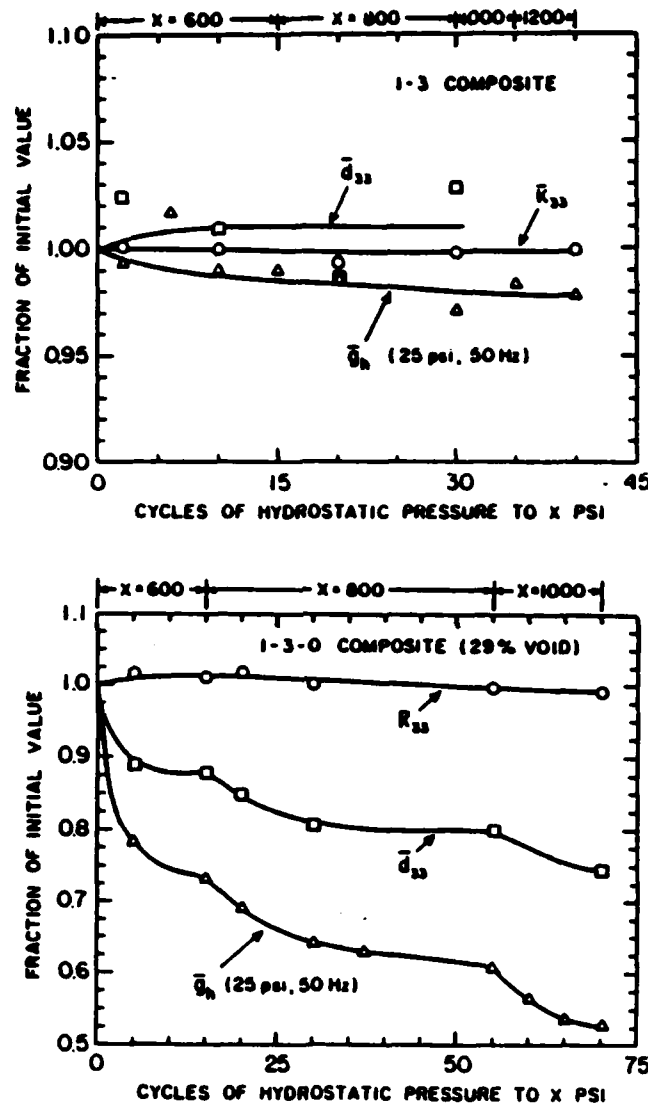


FIGURE 7 The change in the initial values of dielectric constant (\bar{K}_{33}), and \bar{d}_{33} and \bar{g}_h coefficients plotted versus cycles of pressure to x psi: (a) For a 1-3 composite, and (b) For a 1-3-0 composite with twenty-nine percent porosity.

The change in the dielectric and piezoelectric properties are plotted in Figure 7 as a function of the number of hydrostatic pressure cycles for the same 1-3 and 1-3-0 composites in Table III. The maximum pressures of the cycles were held for only a few seconds, and are shown at the top of both figures. The first fifteen cycles went up to 6000 psi (4.1 MPa), the next set of cycles to 800 psi (5.5 MPa), etc.

The 1-3 composite showed no significant change in properties with pressure cycling, even up to 1200 psi (8.3 MPa). The dielectric constant \bar{K}_{33} of the 1-3-0 composite increased slightly during the first pressure cycle, and then gradually decreased with additional cycles. Krueger and Berlincourt¹⁰ observed a similar change in the dielectric constant of soft PZT.

The \bar{d}_{33} and \bar{g}_h coefficients of the 1-3-0 composites both decreased with cycles of pressure. After many cycles up to the same pressure, the decrease in piezoelectric coefficients began to level off. The maximum pressure was then increased, and the same trend was seen again.

After pressure cycling these samples as described above, the pressure and frequency dependences of the \bar{g}_h coefficients were measured, and are shown in Figures 8 and 9. The 1-3 composite showed no significant pressure or frequency dependence. The \bar{g}_h coefficient of the 1-3-0 composite decreased with pressure, but no significant frequency dependence was observed.

After determining the pressure and frequency dependences, both samples were repoled and remeasured. The initial values of the dielectric constant, and \bar{d}_{33} and \bar{g}_h coefficients were reproduced, indicating that the cycles of pressure had not degraded the 1-3-0 composite, but instead had partially depoled it.

The 1-3-0 composite was tested at NRL, after it was pressure cycled and repoled as described above. Figure 10 shows the dielectric and piezoelectric properties plotted versus hydrostatic pressure. The $\bar{d}_h \bar{g}_h$ figure of merit is more than two orders

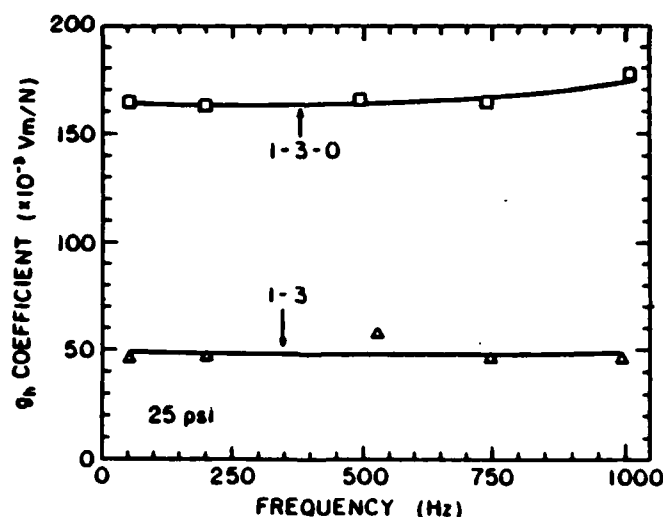


FIGURE 8 The \bar{g}_h coefficient plotted as a function of hydrostatic pressure. Measurements were carried out at 50 Hz for a 1-3 composite and a 1-3-0 composite with twenty-nine percent porosity.

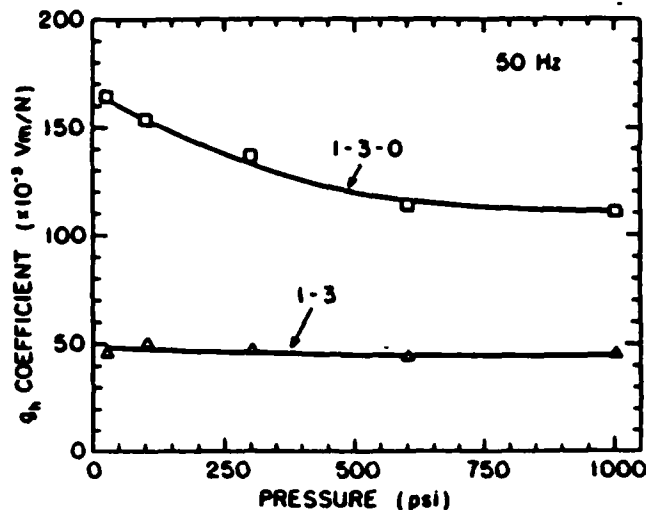


FIGURE 9 The frequency dependence of the \bar{g}_h coefficient measured at 25 psi for a 1-3 composite and a 1-3-0 composite containing twenty-nine percent porosity.

of magnitude greater than the d_{33} of single-phase PZT, even at 1000 psi (6.9 MPa). The free-field voltage sensitivity is also very high, with a value of $-169 \text{ dB re } 1 \text{ V}/\mu\text{Pa}$ at 145 psi (1 MPa).

These results demonstrate the enhancement that is possible with a 1-3-0 composite. However, the stress amplification on the PZT rods becomes so large that depoling occurred from pressure cycling at only 600 psi (4.1 MPa). This indicates that the limit of hydrostatic sensitivity, physically possible for the soft PZT used, was exceeded.

Krueger and Berlincourt¹⁰ showed that hard PZT did not depole even after 200 longitudinal stress cycles to 10,000 psi (69 MPa). Hard PZT has a considerably lower d_{33} coefficient than soft PZT, and thus is not normally used in PZT-polymer composites for hydrophone applications. Nevertheless, if the depoling limit of soft PZT is exceeded, the use of hard PZT may result in greater hydrostatic sensitivity for applications involving pressure cycling.

6. CONCLUSIONS

The addition of a large single void to a 1-3 composite was shown to enhance the hydrostatic piezoelectric \bar{d}_h and \bar{g}_h coefficients. The experimental results and theoretical predictions were in good agreement, but not enough samples were fabricated to test all the variables.

Cycling the hydrostatic pressure up to 1200 psi (8.3 MPa) had no significant effect on the dielectric and piezoelectric properties of the 1-3 composites. Pressure cycles up to 600 psi (4.1 MPa) caused depoling and a degradation in the \bar{d}_{33} and \bar{g}_h coefficients of the 1-3-0 composites.

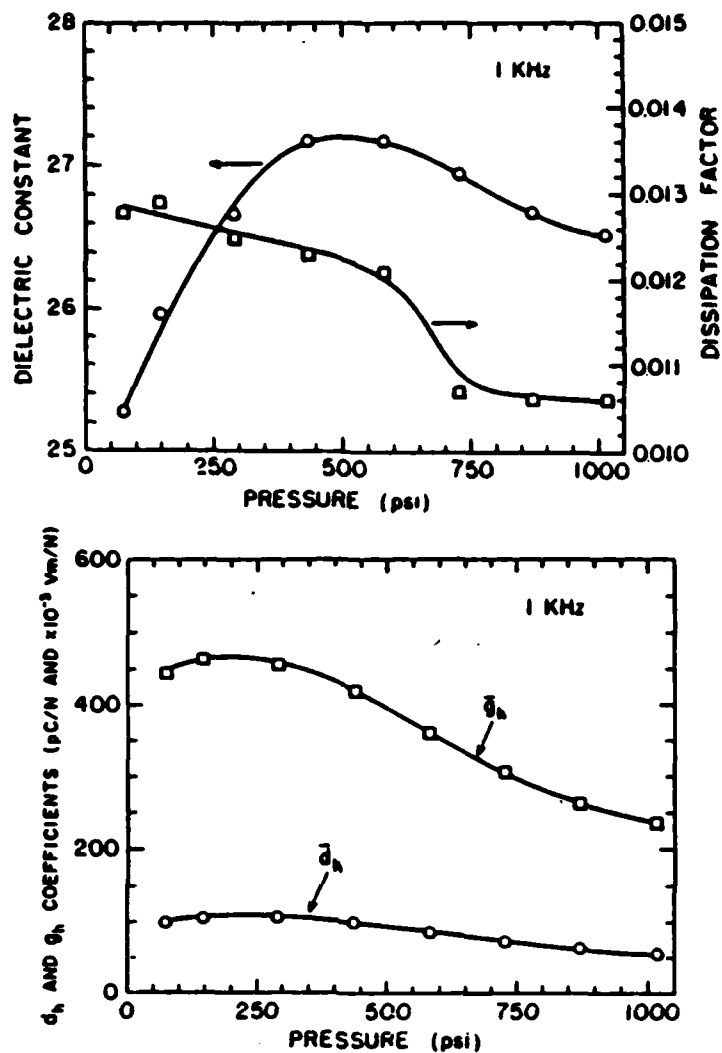
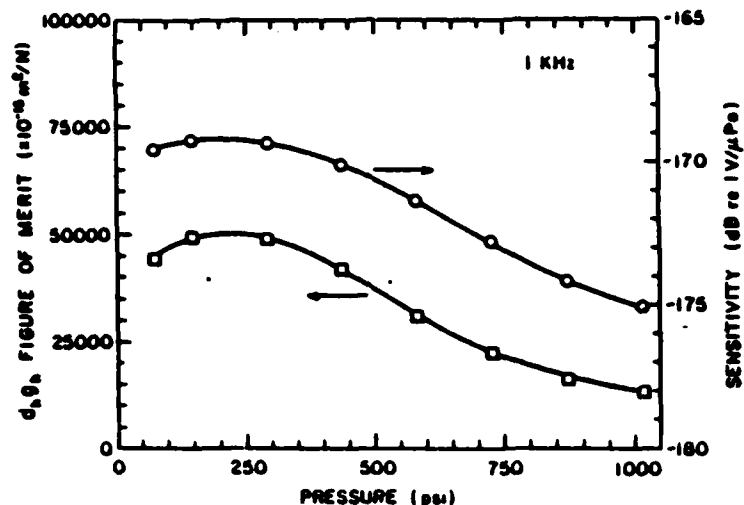


FIGURE 10 Dielectric and piezoelectric properties plotted versus pressure for a 1-3-0 composite with twenty-nine percent porosity. The measurements were made at the Underwater Sound Reference Detachment, Naval Research Laboratory, Orlando, Florida: (a) dielectric constant and dissipation factor, (b) d_h and g_h coefficients, and (c) $\bar{d}g_h$, figure of merit and free-field voltage sensitivity.



The \bar{g}_d coefficients of the 1-3 composites showed no pressure dependence up to 1000 psi (6.9 MaPa), and no frequency dependence from 50 Hz to 1 KHz. After pressure cycling the 1-3-0 composites, the \bar{g}_d coefficient decreased with pressure up to 1000 psi, but no significant frequency dependence was measured.

ACKNOWLEDGMENT

The authors wish to thank Bridget Chadwick for assisting in the fabrication and testing of samples, and K. Rittenmyer and R. Y. Ting for measurements conducted at the Underwater Sound Reference Division, Naval Research Laboratory, Orlando, Florida. This research was sponsored by the Office of Naval Research through Contract No. N00014-82-K-0339.

REFERENCES

1. R. E. Newnham, L. J. Bowen, K. A. Klinker and L. E. Cross, *Mat. in Engr.*, 2, 93, December (1980).
2. K. A. Klinker, J. V. Biggers and R. E. Newnham, *J. Am. Ceram. Soc.*, 64, 5 (1981).
3. S. Y. Lynn, R. E. Newnham, K. A. Klinker, K. Rittenmyer, A. Safari and W. A. Schulze, *Ferroelectrics*, 38, 955 (1981).
4. K. A. Klinker, W. A. Schulze and J. V. Biggers, *J. Am. Ceram. Soc.*, 65 C208 (1982).
5. M. J. Haun, P. Moses, T. R. Gururaja, W. A. Schulze and R. E. Newnham, *Ferroelectrics*, 49, 259 (1983).
6. B. Jaffe, W. R. Cook and H. Jaffe, *Piezoelectric Ceramics*, Academic Press, New York (1971), p. 146.
7. M. J. Parratt, *Fibre Reinforced Materials Technology*, Van Nostrand Reinhold Company, London (1972), p. 18.
8. B. Parkyn, Editor, *Glass Reinforced Plastics*, C. R. C. Press, Cleveland (1970), pp. 206-219.
9. R. Y. Ting, *Ferroelectrics*, 49, 251 (1983).
10. H. H. Krueger and D. Berlincourt, *J. Acoust. Soc. Am.*, 33, 10 (1961).
11. K. Rittenmyer, Personal communication, Underwater Sound Reference Detachment, Naval Research Laboratory, Orlando, Florida.

1-2-3 AND 1-2-3-0 PIEZOELECTRIC COMPOSITES
FOR HYDROPHONE APPLICATIONS

M.J. Haun, W.A. Schulze, and R.E. Newnham

1-2-3 and 1-2-3-0 Piezoelectric Composites
for Hydrophone Applications

M.J. Haun,* W.A. Schulze,** and R.E. Newnham*

*Materials Research Laboratory
The Pennsylvania State University
University Park, PA 16802

**McMahon Building
New York State College of Ceramics at
Alfred University
Alfred, NY 14802

Abstract

Piezoelectric PZT-polymer 1-3 and 1-3-0 composites were transversely reinforced with glass fibers to increase the hydrostatic piezoelectric charge and voltage coefficients (\bar{d}_h and \bar{g}_h) for possible use in hydrophone applications. These composites consisted of a foamed or non-foamed polymer matrix with PZT rods aligned parallel to the poling direction and glass fibers in the two transverse directions. The addition of glass fibers greatly decreased the transverse piezoelectric charge coefficient (\bar{d}_{31}) by supporting most of the lateral stresses, while also reducing the adverse internal stresses that develop at the PZT-polymer interface. The longitudinal piezoelectric charge coefficient (\bar{d}_{33}) is relatively unaffected because the PZT rods carry most of the stress in the poling direction. This decoupling of the \bar{d}_{31} and \bar{d}_{33} coefficients enhances the hydrostatic piezoelectric charge coefficient (\bar{d}_h). Because of the small percentage of PZT required, these composites have densities near that of water, and much lower dielectric constants than solid PZT, resulting in large increases in the hydrostatic piezoelectric voltage coefficient (\bar{g}_h). By increasing the \bar{d}_h and \bar{g}_h coefficients, the $\bar{d}_h \bar{g}_h$ product, used as the figure of merit, is greatly enhanced.

I. Introduction

Hydrophone devices use piezoelectric materials to act as passive listening devices for low frequency acoustic waves [1]. The wavelengths are much greater than the dimensions of the device, thus the stress is effectively hydrostatic. The sensitivity of a hydrophone is determined by the voltage that is produced from this hydrostatic pressure. The hydrostatic piezoelectric voltage coefficient (g_h) relates the electric field (= voltage/thickness) of a piezoelectric material to the applied hydrostatic stress, and hence is a useful parameter for evaluating a material for use as a hydrophone.

The g_h coefficient can be determined from the following equation:

$$g_h = \frac{d_h}{K_{33}\epsilon_0},$$

where d_h is the hydrostatic piezoelectric charge coefficient, K_{33} is the dielectric constant in the x_3 direction (the poling direction), and ϵ_0 is the permittivity of free space. The d_h coefficient relates the polarization (= charge/area) produced from an applied hydrostatic stress. A large d_h coefficient and low dielectric constant are desired for hydrophones to have a large g_h coefficient, and thus high sensitivity. The product of the d_h and g_h coefficients is often used as the figure of merit of a material for use in hydrophone applications.

In addition to large d_h and g_h coefficients, hydrophones have other requirements. The piezoelectric element within the device should be acoustically impedance matched to water. The hydrophone should also be rugged enough to withstand mechanical shock from pressure fluctuations. Finally, if the device is to be mounted on the hull of a ship, at least limited flexibility is required.

Lead zirconate titanate (PZT) has traditionally been used for hydrophone devices, but has several disadvantages. Even though the magnitudes of the piezoelectric charge coefficients d_{33} and d_{31} are large, the hydrostatic coefficient d_h ($= d_{33} + 2d_{31}$) is low, because the d_{33} and d_{31} coefficients are opposite in sign. The hydrostatic g_h coefficient is also low, due to the high dielectric constant of PZT. To increase the hydrostatic sensitivity, thin-walled cylinders and spheres of PZT have been used to convert the hydrostatic stress into an axial stress [2]. Physical stability of these devices is a problem, because the cylinders and spheres are easily broken by mechanical shock or by failure of the seals under pressure [3]. The stiff dense PZT also has the disadvantage of not acoustically matching well to water. Matching layers are presently used to improve the acoustical coupling between PZT and water. Due to the stiffness of PZT, the devices do not conform easily to the hull of a ship. These disadvantages of PZT show that a definite need exists for the development of improved materials for hydrophone devices.

The properties of single-phase materials conflict with the desired properties for hydrophone applications. To obtain a high g_h coefficient, the d_h coefficient must be large accompanied by a low dielectric constant. The problem with single-phase materials, such as PZT, is that by increasing the d_{ij} coefficients, normally the dielectric constant also increases. The materials with the highest d_{ij} coefficients are piezoelectric ceramics that are brittle, dense and stiff. Thus all the desired properties of a hydrophone device cannot be accomplished by using single-phase ceramic materials.

To solve the conflicting requirements of hydrophone devices, piezoelectric composites of PZT and polymer have been fabricated with the desirable

properties of each phase [4]. The PZT supplies the piezoelectric activity of the composite, while the polymer lowers the dielectric constant and density, and adds flexibility. Through the proper selection of the connectivity and properties of the phases, the d_{33} and d_{31} coefficients can be decoupled, resulting in the enhancement of the d_h coefficient compared to single-phase PZT. By replacing most of the PZT (high K_{33}) with polymer (low K_{33}), the dielectric constant can be significantly reduced, resulting in an enhanced g_h coefficient.

One type of connectivity pattern that has been particularly successful is the 1-3 composite with PZT rods aligned in the poling direction (x_3) held together by a polymer matrix [5]. In the notation 1-3 the one refers to the one-dimensionally connected PZT phase, and the three refers to the three-dimensionally connected polymer phase. The stiffer PZT rods support most of an applied stress in the x_3 direction, because of the parallel connection with the more compliant polymer phase. In the x_1 and x_2 directions of the composite (using an orthogonal axes system) the PZT rods are connected in series with the more compliant polymer matrix, causing the stress to be shared more evenly between the two phases. With the proper selection of the elastic properties of the polymer phase, the \bar{d}_{31} coefficient can be reduced to a greater extent than the reduction of the \bar{d}_{33} coefficient. Hence, the \bar{d}_h coefficient for a 1-3 composite can be increased compared to single-phase PZT.

The \bar{d}_{33} coefficient of a 1-3 composite can be improved by increasing the longitudinal compliance of the polymer. The most compliant polymers usually have high Poisson's ratios. A large longitudinal compliance coefficient (s_{11}) and a high Poisson's ratio (ν_{13}), result in a large s_{13} ($= -\nu_{13}s_{11}$) transverse compliance coefficient. Polymers generally have much

greater s_{13} coefficients than ceramics, such as PZT. In a 1-3 composite adverse internal stresses develop at the PZT-polymer interface due to the difference in the s_{13} compliance coefficients of the phases, resulting in a contribution to the \bar{d}_{31} coefficient [6]. 1-3 composites fabricated with an epoxy (relatively low s_{11} and ν_{13}) matrix were shown to have larger \bar{d}_h coefficients than when a polyurethane (relatively high s_{11} and ν_{13}) matrix was used [7]. The composites with a polyurethane matrix had larger \bar{d}_{33} coefficients, but also had larger \bar{d}_{31} coefficients compared to the epoxy matrix composites. The high Poisson's ratio of polyurethane (~ 0.5) causes the material to be hydrostatically incompressible, resulting in a low \bar{d}_h coefficient.

Porosity has been added to polyurethane to allow the matrix to be compressible [2,6,7]. 1-3-0 connectivity notation is used to describe a 1-3 composite with a porous polymer matrix. The 0 refers to the polymer porosity, which is not connected in any orthogonal direction through the composite. With the addition of porosity the Poisson's ratio decreases more than the increase of the s_{11} coefficient, resulting in a lower s_{13} coefficient. Thus the internal stresses are decreased, reducing the \bar{d}_{31} coefficient. This enhances the \bar{d}_h coefficient, but only at low hydrostatic pressures. As the pressure is increased the pores collapse, and the \bar{d}_h coefficient is reduced.

The addition of hollow glass spheres to the polymer matrix has also been used to reduce the s_{13} compliance coefficient of the polymer, without the severe pressure dependence found with the addition of porosity [6]. However, due to the stiffness of the glass spheres, only a small enhancement in the \bar{d}_h coefficient was obtained.

This paper deals with another method of reducing the internal stresses without the severe pressure dependence. This method involves the addition of

glass fibers aligned in the x_1 and x_2 directions [8,9]. These directions will be referred to as the transverse directions to the aligned PZT rods. Using the connectivity notation, a 2 will be used to represent the glass fibers connected through the composite in two directions. Thus 1-2-3 and 1-2-3-0 connectivity patterns represent transversely reinforced 1-3 and 1-3-0 composites, respectively. Figure 1 shows a schematic drawing of a 1-2-3 composite.

The glass fibers reduce both the s_{11} coefficient and Poisson's ratio of the polymer without a significant reduction in the s_{33} coefficient, thus reducing the internal stresses. The glass fibers also support most of the longitudinal stresses in the x_1 and x_2 directions, but allow the PZT rods to support most of the stress in the x_3 direction. Hence the \bar{d}_{31} coefficient is reduced more than the reduction of the \bar{d}_{33} coefficient, resulting in an enhanced \bar{d}_h coefficient. The experimental procedure used to fabricate transversely reinforced 1-3 piezoelectric composites, the optimum results obtained, and the conclusions of the study will be presented in the following sections.

II. Procedure for Processing and Evaluating Piezoelectric Composites

A fabrication procedure for PZT-polymer composites with 1-3 and 1-3-0 connectivity has been reported earlier [7]. This procedure was modified with additional steps used to align E-glass fibers in the transverse directions to the PZT rods.

Alignment racks were made from two 1.8 cm diameter brass discs with a square array of holes drilled in each. The two discs were bolted together so that PZT rods or glass fibers could be passed through corresponding holes aligning the rods or fibers in place. The alignment racks were suspended over molds, which were filled with Spurr's epoxy and cured. The epoxy served as a base to hold the PZT rods or glass fibers in place so that the brass racks could be removed. Two glass fiber arrays were interposed in the x_1 and x_2 directions through a PZT array. This arrangement provided the basic structure of a 1-2-3 composite.

The PZT-rod glass-fiber structures were placed in a mold and vacuum impregnated in either Spurr's epoxy, Devcon polyurethane, or ten volume percent foamed Devcon polyurethane. After curing the polymer, samples were cut to a thickness of 4.5 mm along the x_3 direction. A diamond saw was used to cut the stiff epoxy matrix composites, but could not be used for the compliant polyurethane matrix composites. Instead, an electric belt sander was used, which may have caused some PZT rods to fracture. To prevent the penetration of oil, the foamed polyurethane composites were encapsulated in Spurr's epoxy. This encapsulation also provided additional transverse reinforcement to the composite. Air-dry silver was used to electrode the epoxy and polyurethane matrix composites, and silver epoxy was used for the foamed polyurethane matrix composites. For comparison, 1-3 composite samples without transverse reinforcement were also fabricated.

The samples were poled in a 70°C oil bath with a field of 22 KV/cm applied for five minutes. After aging for at least 24 hours, the dielectric and piezoelectric properties were measured. The capacitance and dissipation factor were measured using a Hewlett-Packard 427A Multi-Frequency LCR Meter at 1 KHz under atmospheric pressure, and also under hydrostatic pressure for use in \bar{d}_h and \bar{g}_h calculations at higher pressures. The d_{33} coefficient was measured dynamically using a Berlincourt Piezo d_{33} -meter, with the electromagnetic driver operating at a frequency of 100 Hz. Two techniques were used to determine the hydrostatic piezoelectric coefficients: a static Ramp method and a dynamic A.C. method. The Ramp method was used to measure all the samples fabricated in this study, and the A.C. method was used to measure selected samples for comparison.

Figure 2 shows a schematic drawing of the static Ramp method apparatus used. The hydrostatic pressure in the oil chamber was hydraulically increased at approximately 50 psi/sec (345 KPa/sec), and measured with a Teledyne pressure transducer. The charge released from the sample was collected with a Keithly 616 digital electrometer. The voltage outputs from the pressure transducer and the electrometer were plotted on an x-y recorder. After cycling the samples several times, the \bar{d}_h coefficient was calculated from the slope of the charge versus pressure curve.

A dynamic A.C. method was also used to determine the hydrostatic piezoelectric coefficients of selected samples. This technique is more directly related to hydrophone applications than the Ramp method because various frequency pressure waves can be applied to the samples while under a static pressure. Figure 3 shows the apparatus used for this method. The A.C. stress generator was driven at frequencies from 50 to 200 Hz producing

effectively hydrostatic pressure on the sample and standard. The charges produced from the sample and standard were buffered with an impedance convertor, and the voltages produced were measured on an oscilloscope. The ratio of these voltages is proportional to the ratio of the \bar{g}_h coefficients of the sample and the standard. By accounting for the sample geometries and the stray capacitance of the holders, the \bar{g}_h coefficients of the samples were calculated using the following relation:

$$\frac{1}{\bar{g}_h} = \frac{(c_1 + 40)^2 c_2^2 t^2 v^2 \bar{g}_h}{(c_2 + 40)^2 c_1^2 t^2 v^2}$$

where 1 and 2 refer to the sample and standard, respectively, c is the capacitance (pF), t is the thickness, v is the voltage, and 40 pF is the stray capacitance of the holders.

III. Experimental Results and Discussion

Composite samples with 1-3, 1-3-0, 1-2-3, and 1-2-3-0 connectivity were fabricated and tested according to the experimental procedure described in the previous section. The dielectric and piezoelectric properties are plotted as a function of the volume percentage of glass fibers in Figures 4a, 4b, and 4c for epoxy, polyurethane, and encapsulated ten-percent-foamed polyurethane matrix composites, respectively.

The dielectric constant increased slightly with the addition of glass fibers for the epoxy matrix composites with five percent PZT, as shown in Figure 4a. During the curing of the polymer, thermal expansion differences create compressive stresses that may effectively clamp the PZT rods, and thus reduce the dielectric constant. If the glass fibers support some of this compressive stress, then the dielectric constant would increase due to less clamping.

The \bar{d}_{33} coefficient of the epoxy matrix composites decreased as the percentage of glass fibers was increased because the glass supported part of the stress in the x_3 direction, decreasing the stress on the PZT. The magnitude of the \bar{d}_{31} coefficient, calculated from the measured \bar{d}_{33} and \bar{d}_h coefficients, also decreased with the addition of glass fibers. As described in the Introduction, the glass fibers theoretically should decrease both the shear stresses at the interface (due to the mismatch in s_{13} compliance coefficients) and the longitudinal stresses on the PZT in the x_1 and x_2 directions, and thus reduce the magnitude of the \bar{d}_{31} coefficient. The hydrostatic coefficients \bar{d}_h and \bar{g}_h and the $\bar{d}_h \bar{g}_h$ figure of merit initially increased with the addition of glass fibers, but then decreased when the composite was significantly stiffened in the x_3 direction causing a large reduction of the \bar{d}_{33} coefficient.

Figure 4b shows the properties of polyurethane matrix composites with five percent PZT. The dielectric constant of these composites did not significantly change with the addition of glass fibers, but the magnitudes were lower than that of the epoxy matrix composites, which had the same volume fraction of PZT. The high compliance of polyurethane may have allowed some PZT rods to be broken during the fabrication of these composites, thus giving lower dielectric constants. Without transverse reinforcement the \bar{d}_h coefficient was lower for the polyurethane matrix composites than for the epoxy matrix composites, even though the compliance of polyurethane is more than an order of magnitude greater than the epoxy compliance. This is due to the incompressible nature of polyurethane (high Poisson's ratio), as discussed in the Introduction. With the addition of glass fibers the \bar{d}_{33} coefficient remained large due to the high compliance of the polyurethane, but the magnitude of the \bar{d}_{31} coefficient was significantly reduced, resulting in an enhanced \bar{d}_h coefficient. The \bar{g}_h coefficient was also increased with the addition of glass fibers, and the $\bar{d}_h \bar{g}_h$ figure of merit was increased by almost an order of magnitude with the addition of 14 percent glass fibers.

Figure 4c shows the properties of encapsulated foamed polyurethane matrix composites with 13 volume percent PZT rods. The dielectric constant decreased with the addition of glass fibers, possibly due to an additional breakage of PZT during fabrication. The breakage would also contribute to the decrease of the \bar{d}_{33} coefficient. The hydrostatic piezoelectric coefficients were determined using both the Ramp (curve 1) and the A.C. (curve 2) techniques. Even though the \bar{d}_{33} coefficient decreased with the addition of glass fibers, the \bar{d}_h coefficient increased, due to the large reduction in the magnitude of the \bar{d}_{31} coefficient. Thus the \bar{g}_h coefficient and $\bar{d}_h \bar{g}_h$ figure of merit were significantly enhanced with the addition of glass fibers.

The \bar{d}_h coefficient determined from the Ramp method gave higher results than from the A.C. method, due to the viscoelasticity of the polyurethane. Using the Ramp method the full viscoelastic deformation did not have time to occur, due to the fast increase in pressure. A static pressure was applied using the A.C. method allowing the polymer to deform completely, and thus a lower \bar{d}_h coefficient resulted. The difference in \bar{d}_h coefficients using the two techniques was previously shown to be much less for epoxy matrix composites, because epoxy is less viscoelastic than polyurethane [8].

The \bar{d}_{31} coefficient determined from the Ramp method becomes positive with the addition of twenty percent glass fibers. Theoretically, a positive \bar{d}_{31} coefficient should not be possible in a 1-3 type composite when the matrix is more compliant than the one-dimensionally connected phase [8]. Thus the \bar{d}_h coefficients determined from the Ramp method are probably higher than the true values. However, using the A.C. method more realistic values were obtained.

Table 1 shows a comparison of the densities, and dielectric and piezoelectric properties of single-phase PZT and a 1-2-3-0 composite. The density of the composite is much closer to the density of sea-water, resulting in a better acoustical match with water than that of PZT. In the composite most of the PZT has been replaced with polymer. Thus the dielectric constant was reduced by more than an order of magnitude. The PZT rods in the composite support most of the stress in the x_3 direction, while the glass fibers support most of the stress in the x_1 and x_2 directions and also decrease the adverse internal stresses. This results in a reduction of the \bar{d}_{31} coefficient by a factor of forty, but the \bar{d}_{33} coefficient by only a factor of two. Hence, the \bar{d}_h coefficient was increased by almost a factor of five. The increase of the \bar{d}_h coefficient and decrease of the dielectric constant, caused the \bar{g}_h

coefficient to increase by nearly two orders of magnitude, and the $\overline{d_h g_h}$ figure of merit to increase by more than a factor of 400.

IV. Conclusions

Transverse reinforcement of 1-3 and 1-3-0 piezoelectric composites with glass fibers was experimentally shown to significantly improve the hydrostatic piezoelectric coefficients and figure of merit. The effectiveness of the glass fibers depends on the volume fractions of PZT rods, glass fibers, and polymer porosity, and on the Poisson's ratio and compliance of the polymer. Due to the stiffness of the epoxy matrix composites only a slight increase in the $\overline{d_h g_h}$ figure of merit was obtained with the addition of glass fibers. However, the $\overline{d_h g_h}$ figure of merit was significantly enhanced with the addition of glass fibers to the polyurethane and encapsulated foamed polyurethane matrix composites. This research has shown that 1-2-3 and 1-2-3-0 connectivity piezoelectric composites are promising candidates for use in hydrophone applications.

References

1. B. Jaffe, W.R. Cook, and H. Jaffe, Piezoelectric Ceramics, Academics, London, 1971.
2. K.A. Klicker, W.A. Schulze, and J.V. Biggers, J. Am. Ceram. Soc., 65[2] C208-C210 (1982).
3. D.P. Skinner Jr., Ph.D. Thesis in Solid State Science, The Pennsylvania State University.
4. R.E. Newnham, L.J. Bowen, K.A. Klicker, and L.E. Cross, Mat. in Engr., Vol. 2, December (1980).
5. K.A. Klicker, J.V. Biggers, and R.E. Newnham, J. Am. Ceram. Soc., 64[1] 5-9 (1981).
6. S.Y. Lynn, M.S. Thesis in Solid State Science, The Pennsylvania State University (1982).
7. K.A. Klicker, Ph.D. Thesis in Solid State Science, The Pennsylvania State University (1980).
8. M.J. Haun, M.S. Thesis in Ceramic Science, The Pennsylvania State University (1983).
9. M.J. Haun, P. Moses, T.R. Gururaja, W.A. Schulze, and R.E. Newnham, Ferroelectrics, Vol. 49, 259-264 (1983).

Table I. Comparison of Single-Phase PZT and a 1-2-3-0 PZT-Polymer Composite

	SINGLE-PHASE PZT	1-2-3-0 COMPOSITE*
Density (g/cc)	7.90	1.25
Dielectric constant \bar{K}_{33}	1760	104
Piezoelectric coefficient \bar{d}_{33} (pC/N)	450	213
Piezoelectric coefficient \bar{d}_{31} (pC/N)	-204	-5
Piezoelectric coefficient \bar{d}_h (pC/N)**	42	203
Piezoelectric coefficient \bar{g}_h ($\times 10^{-3}$ Vm/N)**	2.7	220
Figure of merit $\bar{d}_h \bar{g}_h$ ($\times 10^{-15}$ m ² /N)**	110	44,700

*Encapsulated ten-percent-foamed polyurethane matrix composite with 13 percent PZT and 20 percent glass fibers.

**Determined using the A.C. technique at 25 psi and 50 Hz.

Figure 1. Schematic drawing of a 1-2-3 composite. PZT rods are aligned in the x_3 direction and glass fibers in the x_1 and x_2 directions.

Figure 2. Apparatus used for the static Ramp method measurements [7].

Figure 3. Apparatus used for the dynamic A.C. method measurements [6].

Figure 4. The dielectric and piezoelectric properties plotted versus the volume percentage of glass fibers for (a) epoxy matrix composites with five volume percent PZT, (b) polyurethane matrix composites with five volume percent PZT, and (c) encapsulated ten-percent-foamed polyurethane matrix composites with thirteen volume percent PZT. The hydrostatic properties for the epoxy, polyurethane, and encapsulated composites (curves labeled 1) were determined at 100 psi (0.7 MPa) using the static Ramp method. The curves labeled 2 for the encapsulated composites were determined at 25 psi (0.17 MPa) and 50 Hz using the dynamic A.C. method.

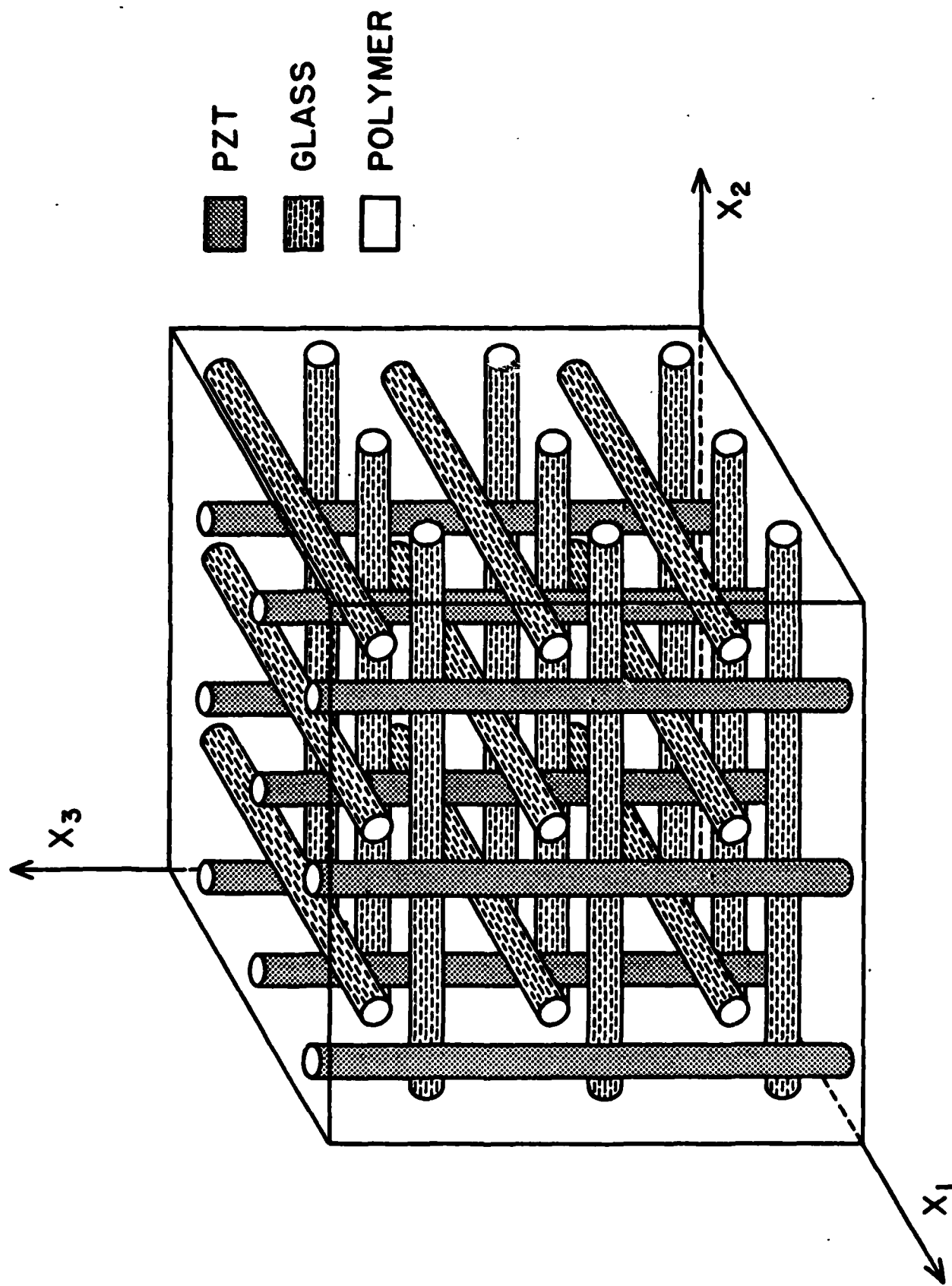


Figure 1

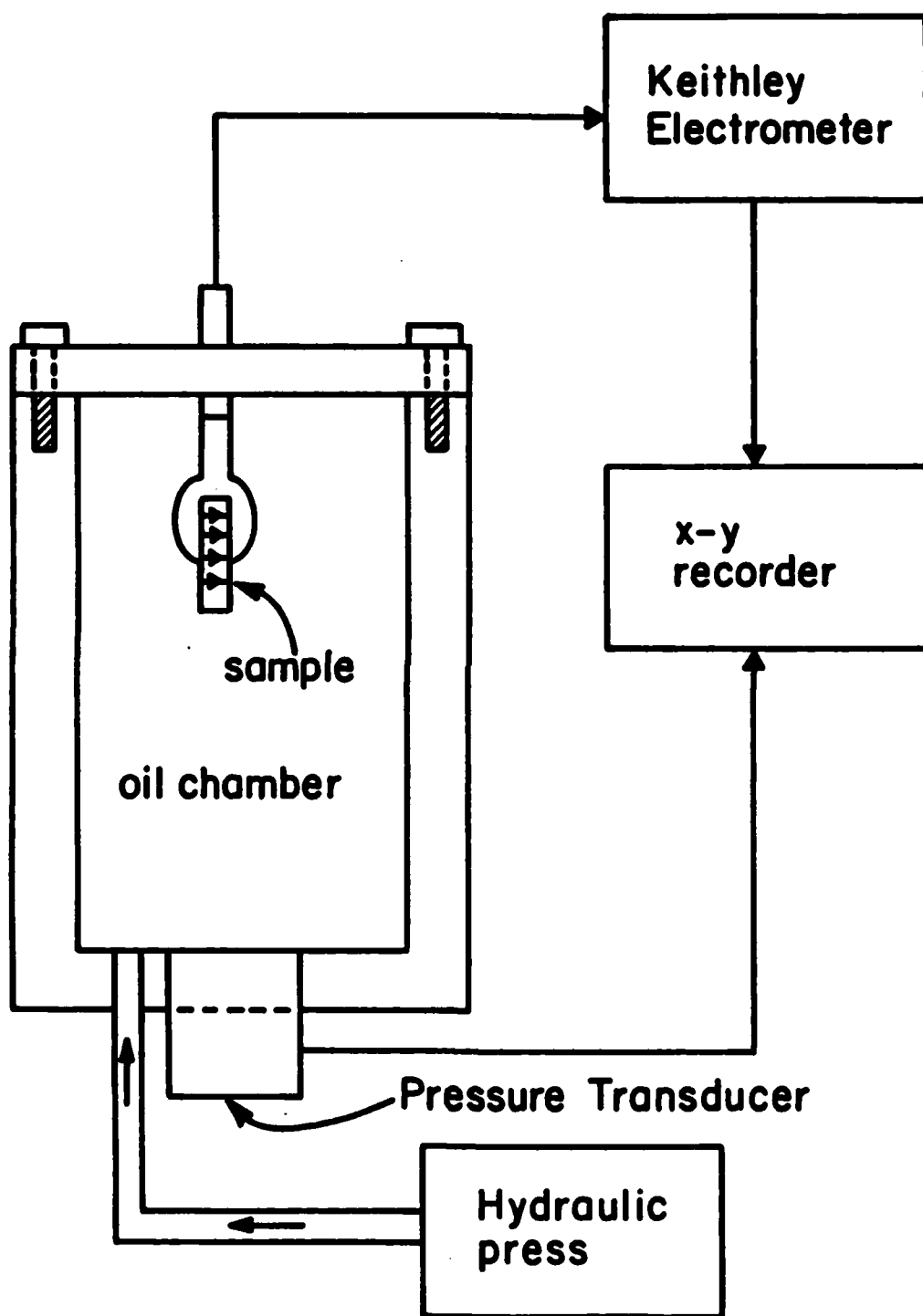


Figure 2

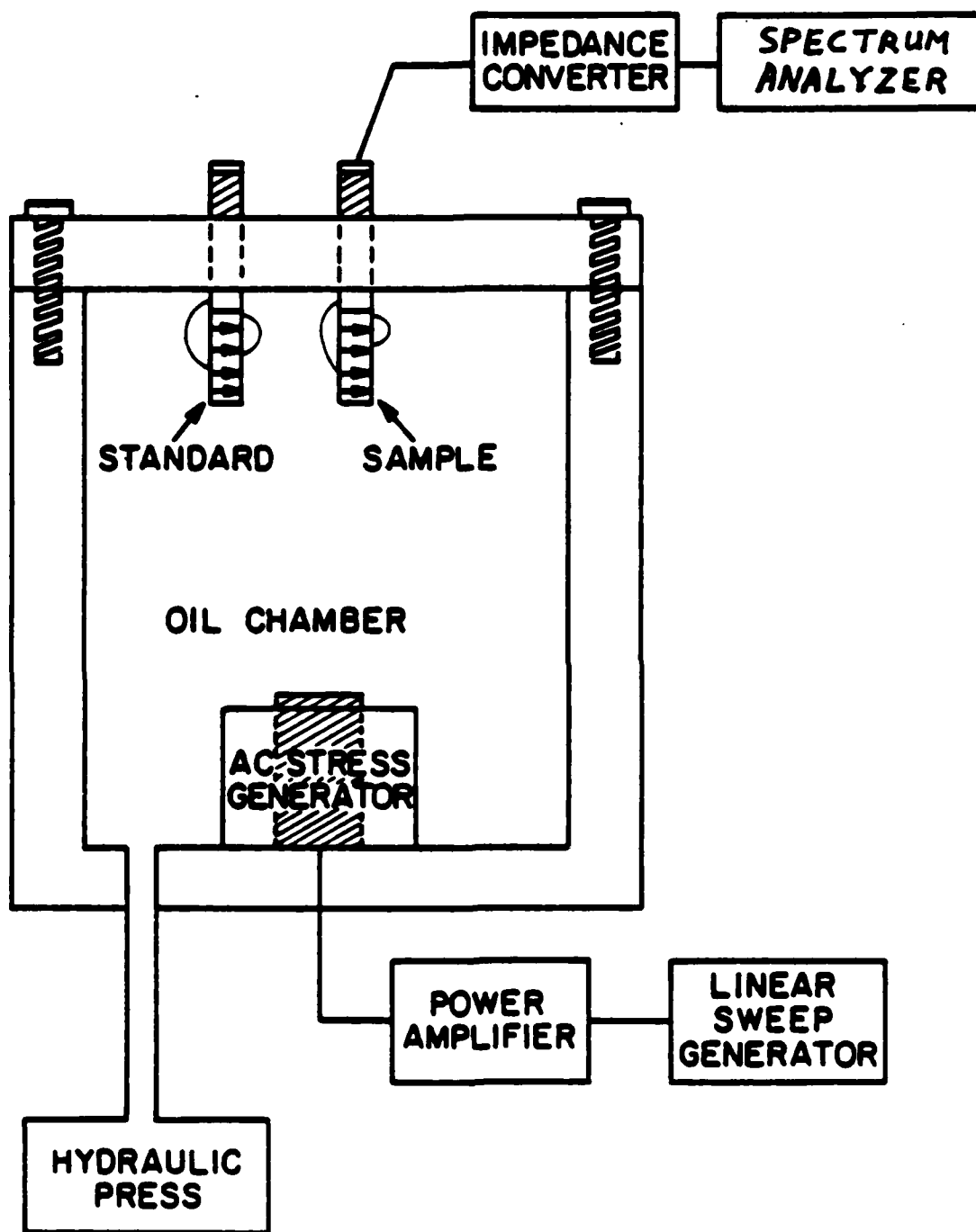


Figure 3

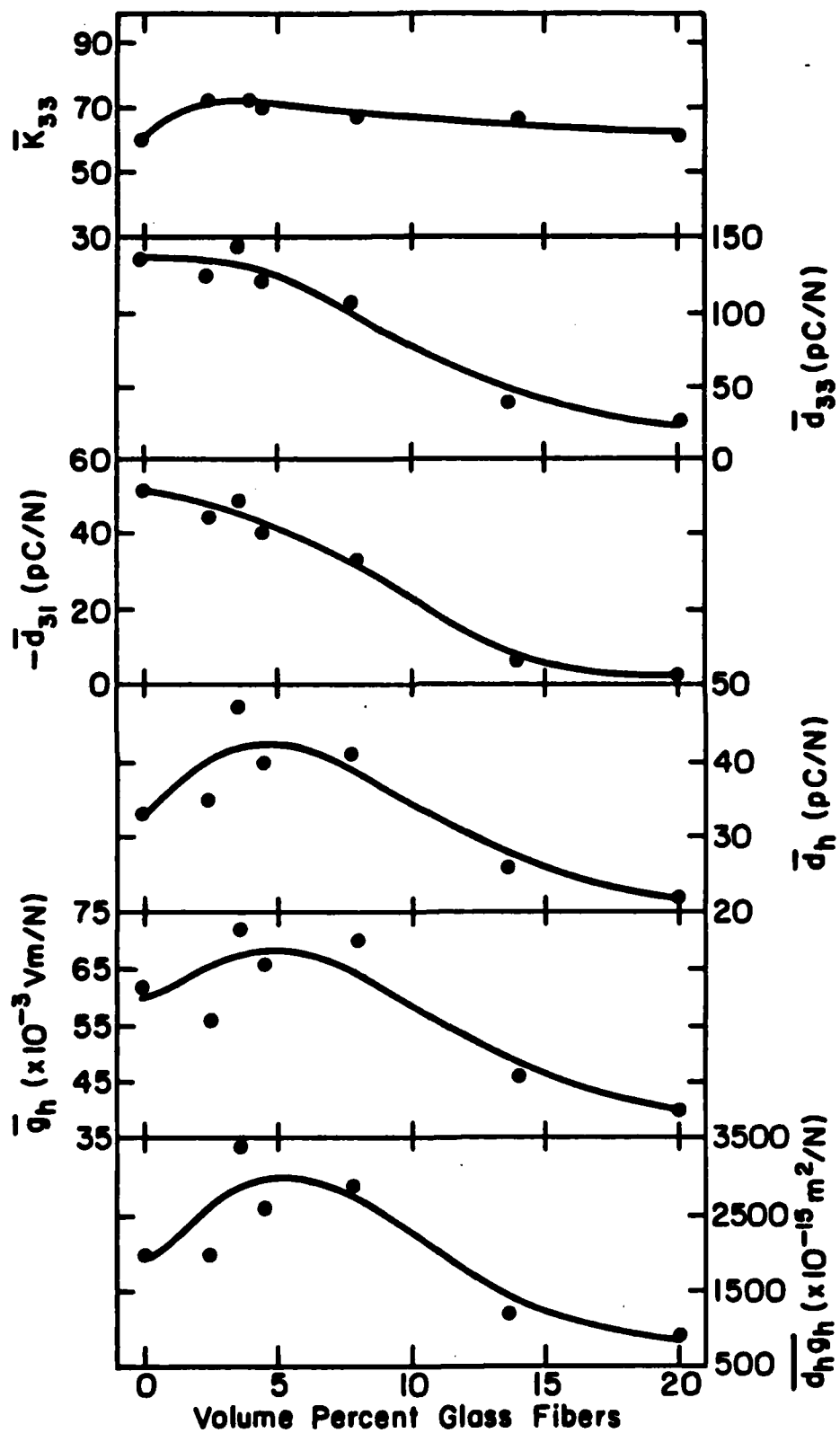


Figure 4

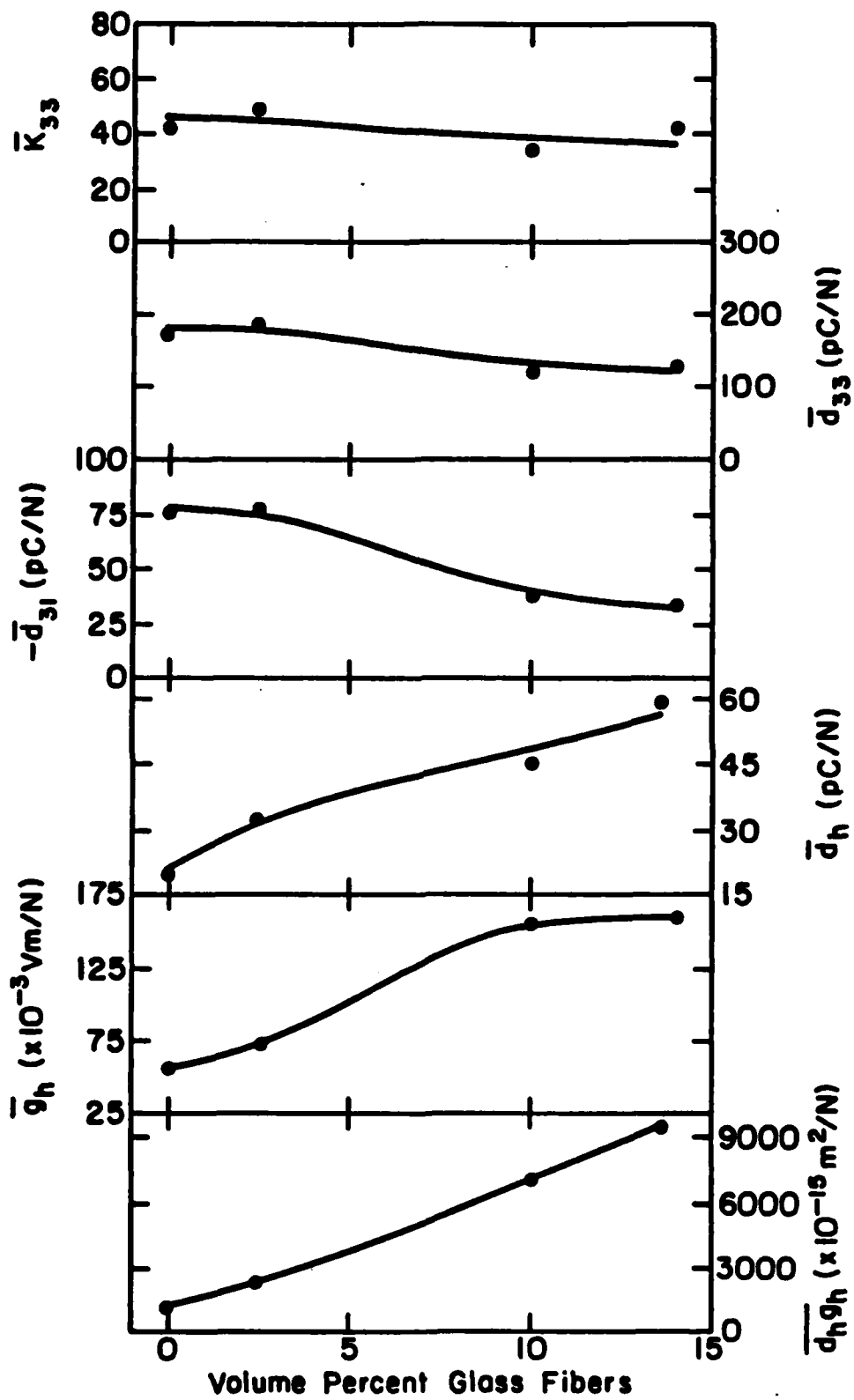


Figure 5

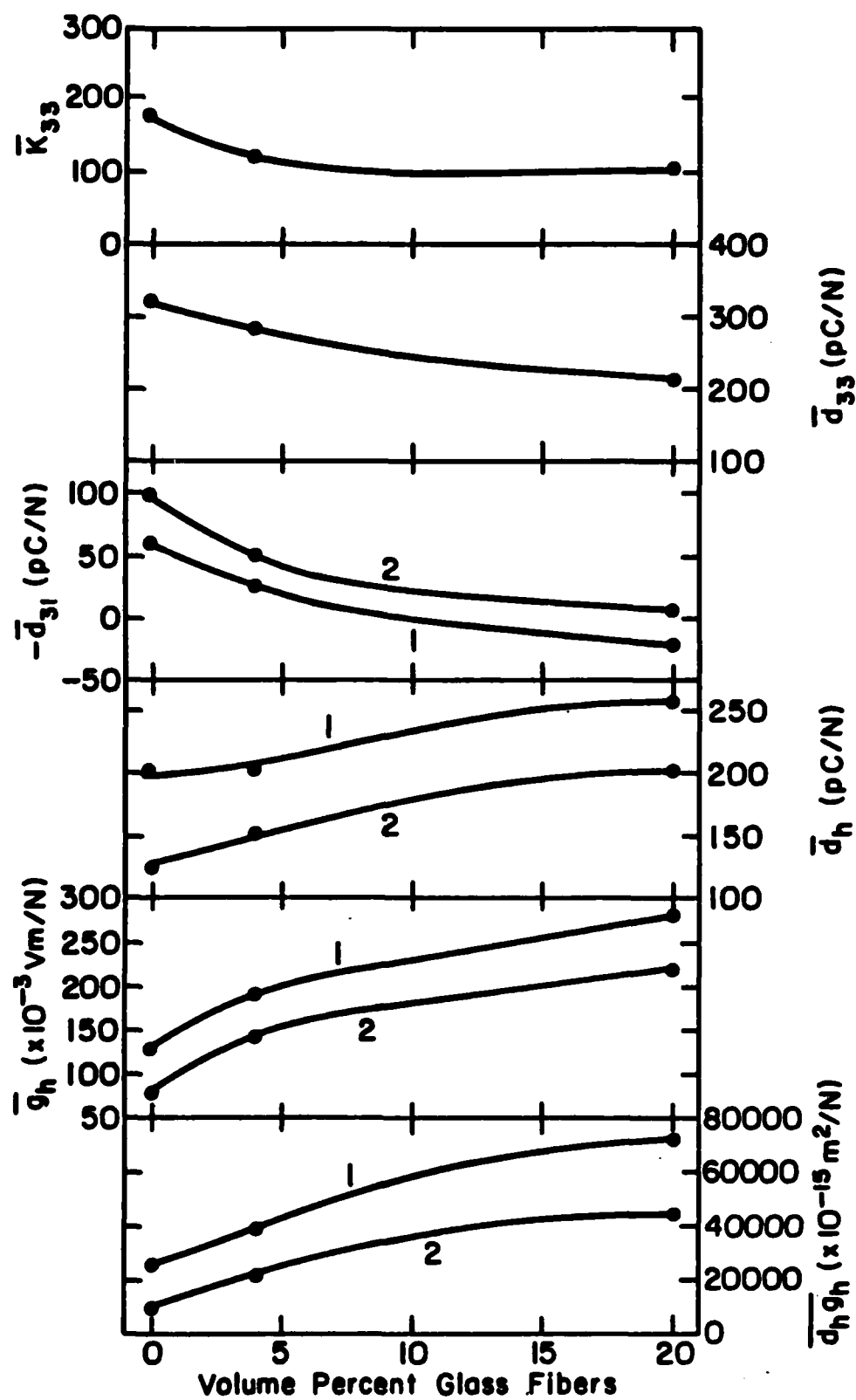


Figure 6

PYROELECTRICITY IN 1-3 PZT/POLYMER COMPOSITES

E.C. Galgoci, D.G. Schreffler, B.P. Devlin and J. Runt

PYROELECTRICITY IN 1-3 PZT/POLYMER COMPOSITES

E. C. GALGOCI, D. G. SCHREFFLER, B. P. DEVLIN AND J. RUNT*
Materials Research Laboratory and Polymer Science Program
The Pennsylvania State University
University Park, PA 16802 U.S.A.

Abstract - Measurements of the pyroelectric coefficients (\bar{p}) and the pyroelectric figures of merit ($\bar{p}/\bar{\epsilon}$) for PZT/polymer composites consisting of slender PZT rods embedded in various polymer matrices have been performed. The pyroelectric response was found to decrease with increasing temperature as qualitatively predicted by theory. At room temperature, the absolute values of $\bar{p}/\bar{\epsilon}$ for most composites were lower than that of PZT, while at higher temperatures modest enhancement of $\bar{p}/\bar{\epsilon}$ was observed. The effects of mechanical coupling between the polymer and PZT on the composite pyroelectric properties are discussed.

I. INTRODUCTION

Polymer/ferroelectric ceramic composites have received much attention¹ as new piezoelectric materials for applications such as hydrophones and medical ultrasound. Designs with continuous lead zirconate titanate (PZT) rods aligned normal to two electrode surfaces and embedded in a polymer matrix can possess relatively large hydrostatic piezoelectric sensitivities²⁻⁶ because saturation poling can be attained and because composite dielectric permittivities (ϵ) can be very much lower than homogeneous PZT. However, the pyroelectric properties of these composites have rarely been evaluated. In this paper, the temperature dependence of the pyroelectric coefficients (p) and the dielectric permittivities of 1-3 composites of PZT and several polymers will be discussed.

II. THEORY

Pyroelectric materials respond to a change in temperature (T) with a change in polarization (P) given by

$$dP = p dT \quad (1)$$

where p is the pyroelectric coefficient. Thermodynamic analysis of the pyroelectric effect yields the expression:

$$p_i^\sigma = p_i^\epsilon + d_{ijk}^T C_{jklm}^{T,E} \alpha_{lm}^E \quad (2)$$

*To whom correspondence should be addressed

Here p_i^σ is the net pyroelectric coefficient at constant stress (σ), and p_i^ϵ is the primary effect at constant strain (ϵ). The secondary effect, which develops through piezoelectricity as a result of thermal expansion (or contraction), is given by the second term in Equation 2, where d , C , and α are the piezoelectric, elastic stiffness, and thermal expansion coefficients, respectively. For homogeneous ferroelectrics (e.g., PZT) p_i^ϵ is large and negative, while the secondary effect is smaller and of opposite sign to the primary effect.

In most polymer/PZT composites one would expect an additional secondary contribution which arises as a consequence of the great disparity in thermal expansion-contraction between the polymer and ceramic phases. Making the following assumptions:

- 1) the polymer is not piezoelectric or pyroelectric (or that the effects are negligible).
- 2) the polymer has a much larger thermal expansion than PZT.
- 3) PZT is much stiffer than the polymer.
- 4) the polymer properties are isotropic.

the expression derived for the pyroelectric coefficient (\bar{p}_3) for a 1-3 composite^{7,8} reduces to

$$\bar{p}_3 = {}^1V {}^1p_3 + {}^2C {}^2\alpha ({}^2V {}^1d_{33} + 2 {}^1V {}^1d_{31}) \quad (3)$$

where V is the volume fraction and superscripts 1 and 2 represent PZT and polymer, respectively. ${}^2\alpha$ would be expected to remain roughly constant above and below the glass transition temperature (T_g) of the polymer, while 2C decreases slightly as temperature is increased. At T_g , however, ${}^2\alpha$ will increase by a factor of three or four, but 2C decreases drastically (by several orders of magnitude) for non-crystalline polymers. Therefore, Equation 3 predicts that \bar{p}_3 should decrease as the temperature increases, and the effect of temperature should be most pronounced near the matrix T_g .

For many pyroelectric applications, a materials' "figure of merit", p/ϵ , can be defined. For 1-3 PZT/polymer composites, p/ϵ can be written as:

$$\frac{\bar{p}_3}{\bar{\epsilon}_3} = \frac{{}^1V {}^1p_3 + {}^2C {}^2\alpha ({}^2V {}^1d_{33} + 2 {}^1V {}^1d_{31})}{{}^1V {}^1\epsilon_3} \quad (4)$$

Like \bar{p}_3 , $\bar{p}_3/\bar{\epsilon}_3$ would be expected to decrease with increasing temperature.

III. EXPERIMENTAL

Because more extensive descriptions of the composite fabrication process are presented elsewhere^{3,5,6}, only a brief summary will be given here. Extruded and sintered PZT 501A rods (305 μ m in diameter) were aligned in racks so that all composites contained 4% PZT by volume. Polymer matrices were prepared by either in situ polymerization of monomers (styrene to polystyrene (PS), methyl methacrylate to poly(methyl methacrylate) (PMMA) and 11-aminoundecanoic acid to nylon 11) or by melting pellets of poly(butylene terephthalate) (PBT) and Hytrel copolymers in glass molds which contained filled racks of PZT rods. These fabrication techniques were found to be the most suitable methods because of the fragility of the PZT rods.

Once the polymers solidified and cooled to room temperature, the molds were broken. The composites were cut perpendicular to the rod axis with an electric diamond saw and then sanded with 60-grit garnet paper followed by polishing with 200-grit garnet paper. All composites were 1 mm thick in the fiber direction.

Air-dry silver electrodes were applied to the two faces perpendicular to the rods, and the composites were poled at 75°C in an oil bath with a field of 22 kV/cm for 5 min. After the composites were removed from the bath, they were allowed to cool in air under a field of 7.5 kV/cm for 10 min. to prevent depoling during cooling. The poled composites were aged for at least 24 hr. prior to pyroelectric and dielectric measurements.

Pyroelectric coefficients were measured by use of the Byer-Roundy method⁹ at heating rates of either 2 or 4°/min. Dielectric constant as a function of temperature was monitored using a Hewlett-Packard 4274A LCR meter at 100kHz. All pyroelectric samples were temperature cycled to avoid anomalous, thermally-stimulated currents. The pyroelectric coefficients were considered reproducible when heating and cooling curves coincided. The reported plots of \bar{p} vs. T are for cooling runs.

IV. RESULTS AND DISCUSSION

Results of the pyroelectric and dielectric are presented in Table 1 for temperatures of 20°C and 70°C (or 100°C). As predicted by Equations 3 and 4, \bar{p}_3 and $\bar{p}_3/\bar{\epsilon}_T$ were found to decrease with increasing temperature (Figures 1 and 2). At 20°C PS, PMMA, PBT and nylon 11 are below their respective T_g 's and are consequently rather stiff. The relatively high modulus polymers act as mechanical clamps on the PZT rods and produce a significant change in polarization through the piezoelectric effect. Composite, secondary pyroelectricity is opposite in sign to the primary response, so that the combined effect is a rather low absolute value for \bar{p}_3 . In fact, the secondary response for PMMA/PZT composites is large enough to effect a sign change in \bar{p}_3 . At even lower temperatures than studied here, the pyroelectric coefficients of all the composites may change sign due to secondary pyroelectricity. As the temperature is raised, the clamping relaxes, so that less coupling occurs between the matrix and PZT. For temperatures above T_g (especially significant for PS and PMMA) where the polymers are compliant, the measured \bar{p}_3 values are due primarily to PZT pyroelectricity. So, for PS/PZT we observe \bar{p}_3 to level off at a relatively constant value above the T_g (~100°C) of PS (Figure 1). It also appears that \bar{p}_3 for PMMA/PZT is beginning to plateau above ~100°C (T_g for PMMA is ~100°C).

As mentioned previously, α and C in Equations 3 and 4 are a function of temperature. How these parameters vary with respect to temperature will determine how \bar{p} and $\bar{p}/\bar{\epsilon}_T$ behave as the temperature changes. Furthermore, differences which exist in the relative values of α and C among the various polymer matrices will alter the effect of composite secondary pyroelectricity. In addition, interfacial adhesion, composite aging and internal stresses (developed as a result of polymerization, polymer crystallization, cutting, polishing, and poling) complicate composite pyroelectricity even more. Therefore, it is not surprising that no two composites have the same pyroelectric response as a function of temperature. Generally, however, $\bar{p}/\bar{\epsilon}_T$ for the composites falls into two categories at 20°C. The composites with stiffer matrices (PS, PMMA, nylon 11 and PBT) tend to have lower absolute values than composites with more compliant polymers (the Hytrels). This may in large part be due to secondary pyroelectricity as discussed previously. Although the $\bar{\epsilon}_T$ are much lower than that of PZT at 20°C, most of the composites have absolute $\bar{p}/\bar{\epsilon}_T$ values lower than that of PZT. However, at higher temperatures $\bar{p}/\bar{\epsilon}_T$ for the composites is significant higher, so that most exceed that of PZT.

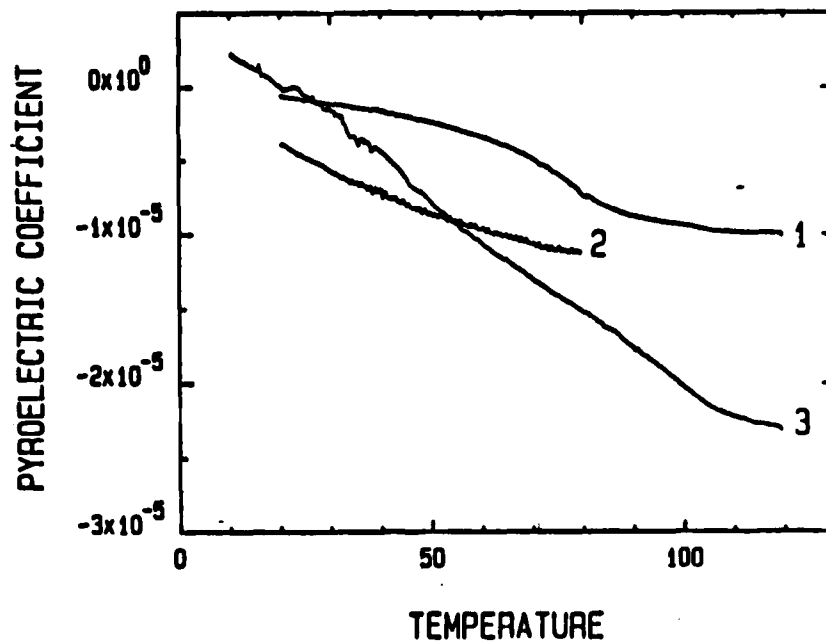


Figure 1. Pyroelectric coefficient vs. temperature (°C) for composites with 1-PS, 2-PBT, and 3-PMMA matrices.

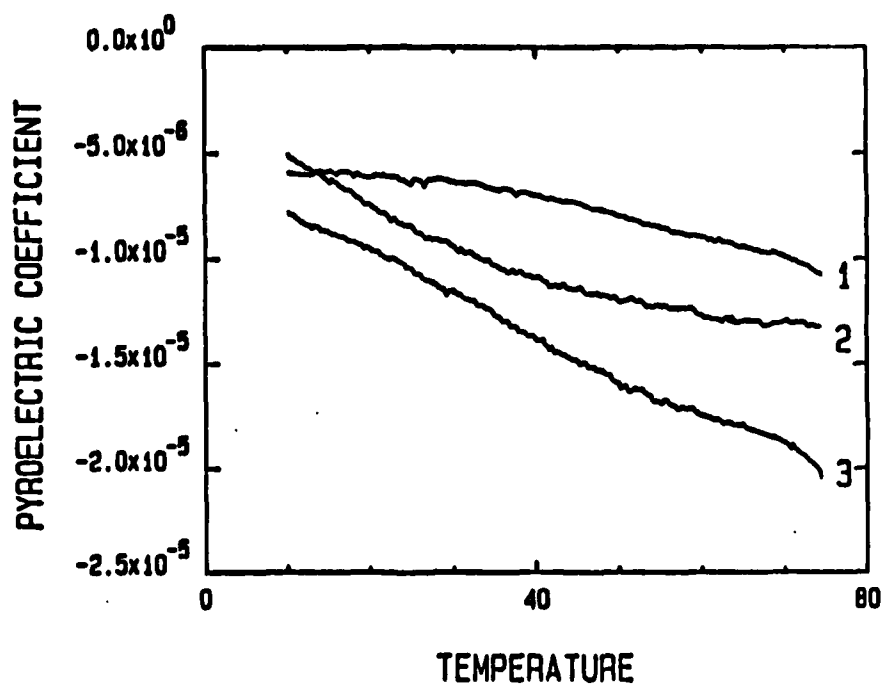


Figure 2. Pyroelectric coefficient vs. temperature (°C) for composites with 1-Hytrel 4056, 2-Hytrel 995, and 3-nylon 11 matrices.

TABLE 1 Composite Pyroelectric and Dielectric Properties

T = 20°C

Sample	$\bar{\epsilon}_r$	$\bar{p}(10^{-5} \text{ C/m}^2\text{-}^\circ\text{C})$	$\bar{p}/\bar{\epsilon}_r (10^{-7} \text{ C/m}^2\text{-}^\circ\text{C})$
PS	35	0	0
PMMA	43	0.1	0.2
Nylon 11	41	-1.0	-0.2
PBT	47	-0.4	-0.9
4056	17	-0.6	-3.5
995	35	-0.8	-2.3

T = 70°C

Sample	$\bar{\epsilon}_r$	$\bar{p}(10^{-5} \text{ C/m}^2\text{-}^\circ\text{C})$	$\bar{p}/\bar{\epsilon}_r (10^{-7} \text{ C/m}^2\text{-}^\circ\text{C})$
PS	43 (100°C)	-0.9	-2.1
PMMA	58 (100°C)	-2.0	-3.4
Nylon 11	51	-1.9	-3.7
PBT	53	-1.1	-2.1
4056	17	-1.0	-5.9
995	39	-1.3	-3.3
Pure PZT	1800	-50	-2.8

V. CONCLUSIONS

The measured pyroelectric response of 1-3 composites of several polymers and PZT agrees qualitatively with that predicted by theory. At low temperatures composite secondary pyroelectricity can dominate, while at elevated temperatures PZT pyroelectricity is the primary influence. At a temperature of 70 to 100°C the pyroelectric figure of merit for most of the composites is enhanced relative to PZT.

ACKNOWLEDGMENTS

The authors would like to express their appreciation to the Office of Naval Research for their support of this work through contract N00014-82-K-0339 and to Dr. Amar Bhalla of the Materials Research Laboratory at The Pennsylvania State University for helpful discussions.

REFERENCES

1. R. E. Newnham, L. J. Bowen, K. A. Klickner and L. E. Cross, Mat. Eng., 2, 93 (1980).
2. R. E. Newnham and J. P. Runt, Polymer News, 10, 132, (1984).
3. K. A. Klickner, J. V. Biggers and R. E. Newnham, J. Amer. Ceram. Soc., 64, 5 (1981).
4. K. A. Klicker, W. A. Schulze and J. V. Biggers, Comm. Amer. Ceram. Soc., 65, 208 (1982).
5. J. Runt and E. C. Galgoci, J. Appl. Poly. Sci., 29, 611 (1984).
6. J. Runt and E. C. Galgoci, Mat. Res. Bull., 19, 253 (1984).
7. A. S. Bhalla, R. E. Newnham, L. E. Cross, W. A. Schulze, J. P. Dougherty, and W. A. Smith, Ferroelectrics, 33, 139 (1981).
8. R. E. Newnham, D. P. Skinner and L. E. Cross, Mat. Res. Bull., 13, 525 (1978).
9. R. L. Byer and C. B. Roundy, Ferroelectrics, 3, 333 (1972).

ELECTROCERAMIC-POLYMER COMPOSITE THERMISTORS

K.A. Hu, J. Runt, A. Safari and R.E. Newnham

ELECTROCERAMIC-POLYMER COMPOSITE THERMISTORS

K.A. Hu, J. Runt, A. Safari and R.E. Newnham
Materials Research Laboratory, The Pennsylvania State
University, University Park, PA 16802

Abstract Transition metal oxide fillers such as VO_2 , V_2O_3 and Ti_2O_3 were incorporated in polymeric matrices to give composite materials with low room temperature resistivities and sizable thermistor effects. Percolation limits were determined by mixing ceramic powders in different proportions with both rigid and flexible epoxies. These composites exhibited unusually large PTC effects with resistance increases as high as nine orders of magnitude.

INTRODUCTION

Doped BaTiO_3 ceramics exhibiting a positive temperature coefficient (PTC) effect have been known for quite some time and have been widely used as temperature-dependent resistors (thermistors). However, BaTiO_3 PTC materials are limited by their relatively high resistivity at room temperature, and high material and fabrication costs. Much effort has been devoted to overcoming these difficulties. Probably the most successful alternative materials have been based on composites of carbon black with a semi-crystalline polymer (often polyethylene) or a paraffin¹⁻⁷. PTC effects similar to BaTiO_3 ceramics are observed when crystalline polymers are loaded near the percolation threshold with carbon black. At room temperature the carbon black particles are in contact giving resistivities of approximately 1 ohm-cm. Upon heating, a large volume change occurs at the polymer melting point; the polymer expands much more rapidly than the carbon black in this temperature range, separating the carbon grains and raising the resistivity.

A rapid increase in resistivity of between typically 1.5 and 8 orders of magnitude around the polymer or paraffin melting point has been reported⁴⁻⁷. It is interesting to note that only very small PTC effects have been reported for conductive composites in which amorphous polymers are used as matrices⁴.

In this paper we report some of our initial findings on a new class of thermistor materials which exhibit low room temperature resistivities and very large PTC anomalies. These materials are based on conductive ceramics and amorphous polymers. Several of the transition metal oxide fillers used in the study undergo a negative temperature coefficient (NTC) transformation changing from semiconductor to metal. In combination with the appropriate polymer, interesting NTC-PTC composites can be produced, and will be described in a later paper.

EXPERIMENTAL

Two polymers were used in our studies: a flexible and rigid epoxy. The rigid epoxy ('Spurr' epoxy) was obtained from Polysciences, Inc., and has a glass transition temperature (T_g), when cured, of approximately 65°C. The flexible epoxy (Eccogel 1365-80) was obtained from Emerson Cuming. The conductive fillers VO_2 , V_2O_3 , VO , Ti_2O_3 ⁸ and NbO_2 were obtained from Alfa Products.

Resistivity versus temperature curves (Fig. 1) for most of the fillers exhibit a rather sharp transition to a more metallic state. For instance in VO_2 there is a transition at 60°C which results in a large change in resistance. Above 60°C it exhibits metallic behavior and below 60°C it shows semiconductor behavior. The critical temperature can be modified somewhat by changes in chemical composition.

Composites were fabricated by mixing the polymer and ceramic fillers in the desired proportions and curing at 70°C for 8 hours. All concentrations stated in this paper refer to volume percent ceramic. The resistivity of the composites was measured as a

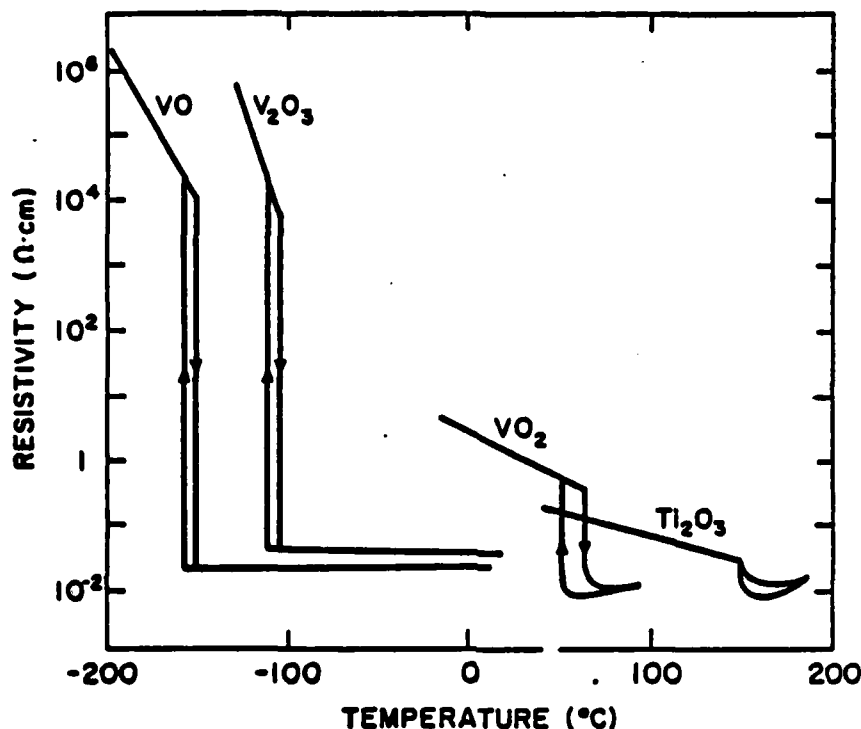


FIGURE 1 Semiconductor-metal transformations in V_2O_3 , VO_2 , VO and Ti_2O_3 single crystals (Morin, 1959).

function of temperature with a Keithley digital electrometer Model 616. Resistance measurements on thinned samples confirmed the overall specimen uniformity.

RESULTS AND DISCUSSION

The relationship between resistivity (ρ) and temperature for several VO_2 composites with the rigid Spurrs epoxy is shown in Fig. 2. As evidence by the relatively low values for the room temperature resistivity, the compositions shown in this figure are above the percolation threshold. The room temperature resistivities for Spurrs composites with various volume percent of VO_2 are plotted in Fig. 3. Composites with greater than about 60

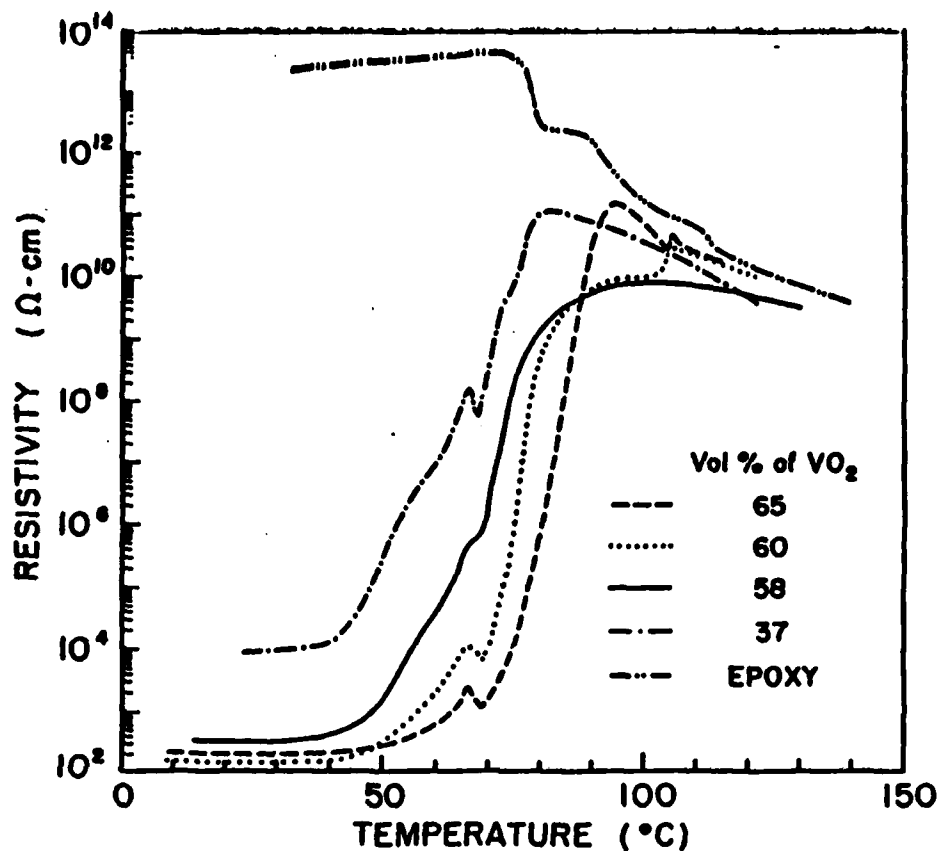


FIGURE 2 Temperature dependence of the electrical resistivity of VO_2 -Spurrs epoxy composites made with different volume percent fillers.

volume percent VO_2 exhibit resistivities on the order of 100-200 ohm-cm, somewhat greater than that of pure VO_2 . In the composition range between 37% (our lowest concentration due to filler settling problems) and 65%, a dramatic increase in resistivity of up to nine orders of magnitude is observed in the vicinity of 60-80°C. The relatively small negative temperature dependence of resistivity above the PTC anomaly is caused by the temperature dependence of the polymer resistivity, as illustrated in Fig. 2. Examining the curves in Fig. 2 closely, a shoulder near 65°C is observed which is attributed to the phase transition of VO_2 .

The magnitude of this transition is nearly obscured by the large PTC effect in the composite, and appears to be significantly smaller than in the pure oxide.

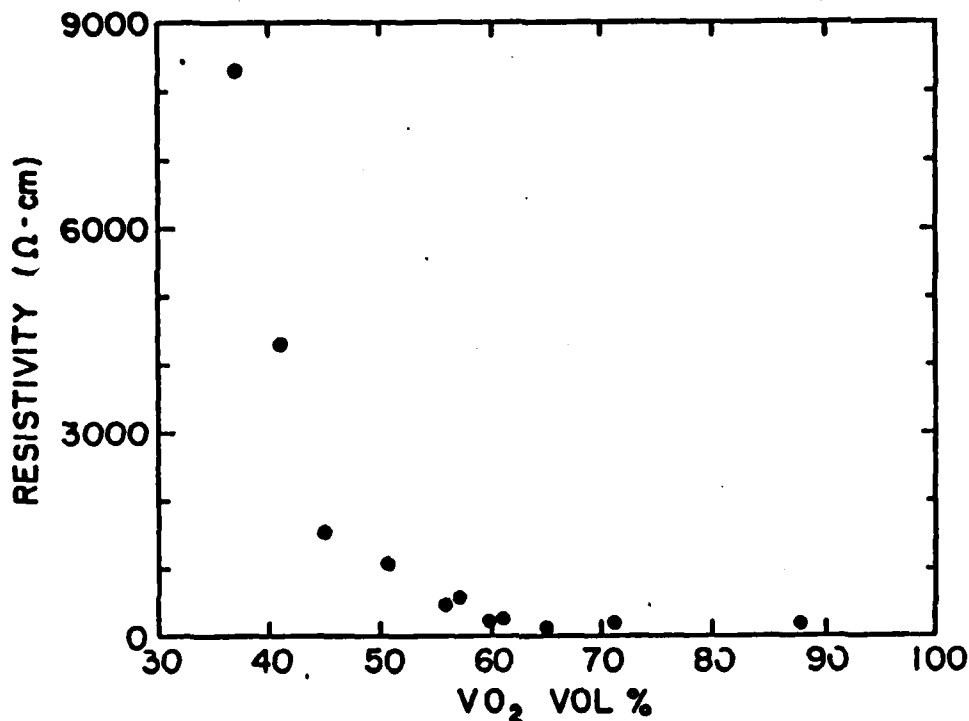


FIGURE 3 Dependence of the room temperature resistivity of VO_2 -Spurrs epoxy composites on the volume percent filler.

The VO_2 -Spurrs polymer composites exhibit excellent reproducibility. For the VO_2 -Spurrs composite with 60 volume percent of VO_2 , the room temperature resistivity increases by a small amount from the first to second run, but remains constant (as does the magnitude of the PTC anomaly) upon further temperature cycling (Fig. 4). The position of the PTC phenomenon moves to slightly lower temperatures upon cycling.

Similar behavior has been observed for composites made with Spurr's epoxy and V_2O_3 , VO , Ti_2O_3 as conductive fillers. Resist-

ivity versus temperature curves for Spurr's epoxy composites with several different fillers are illustrated in Fig. 5. The volume fraction filler in these composites are above the percolation threshold and so have quite low room temperature resistivities, although somewhat larger than the conductive filler alone. VO-Spurr's composites appear to exhibit the lowest room temperature values (on the order of 30 ohm-cm). The position of the PTC phenomenon is remarkably constant for high loadings of VO_2 , VO and Ti_2O_3 ; the mid point of the PTC is about 20°C lower for V_2O_3 composites. Composites prepared from NbO_2 (a semiconductor over the temperature range of interest) also exhibit an effect in the same temperature range as the other composites (Fig. 5). Since the ultimate room temperature resistivity of NbO_2 is considerably larger than that of the metallic fillers, the magnitude of the anomaly is much smaller (~five orders of magnitude).

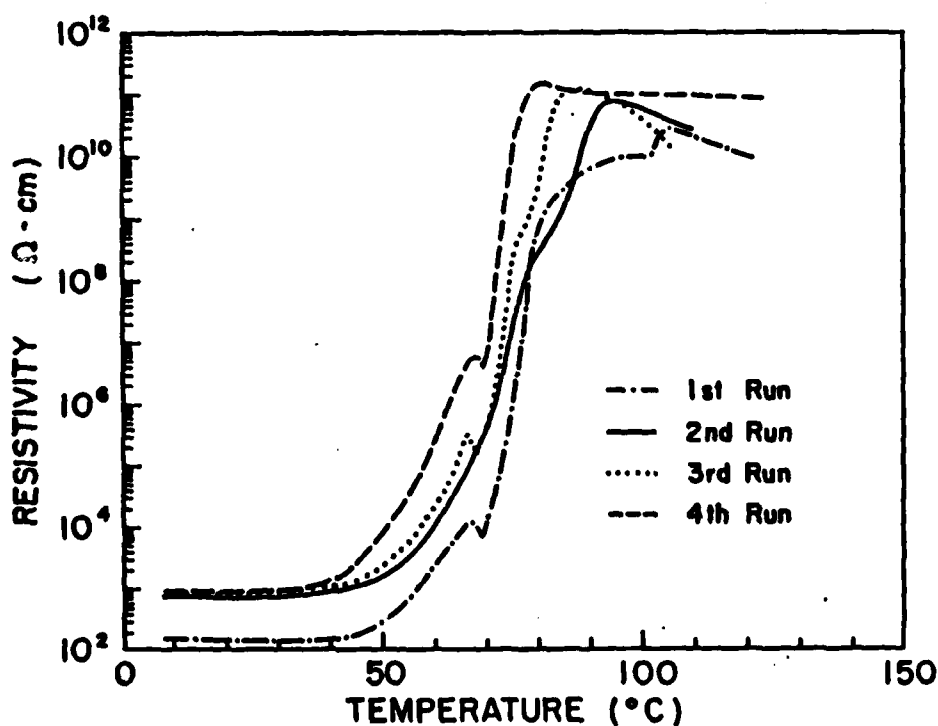


FIGURE 4 Reproducibility of the PTC anomaly in a composite made from Spurr's epoxy and 60 volume percent VO_2 filler.

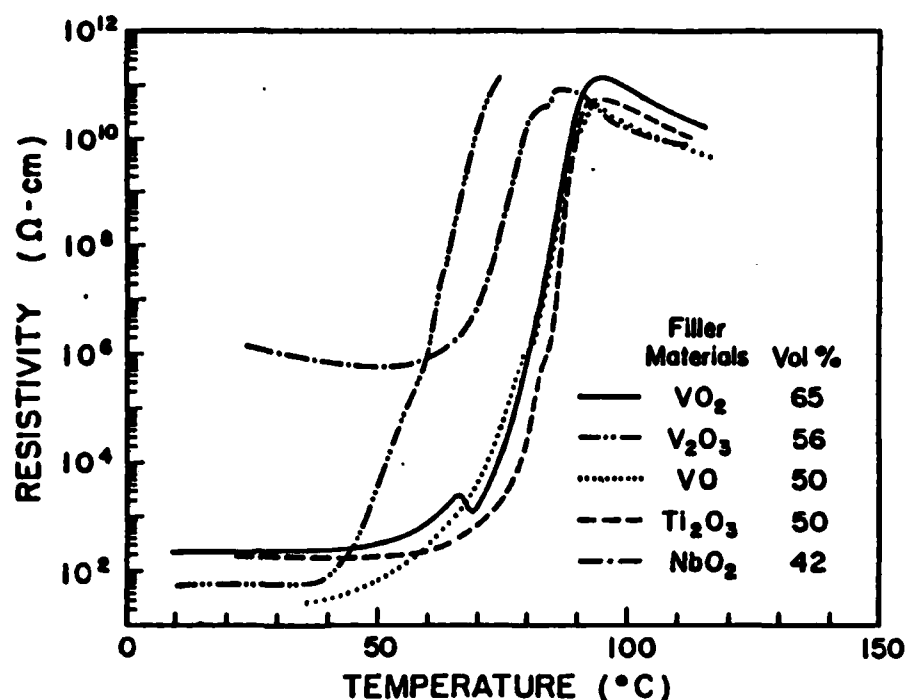


FIGURE 5 Temperature dependence of the electrical resistivity of Spurr's epoxy composites with different filler materials.

One of the most important questions that arises from this work is why do we observe a very sizable and reproducible PTC effect with an amorphous polymer matrix? One might speculate that in the case of Spurr's epoxy composites, ~~that~~ the differential thermal expansion is such that the oxide particles are forced far enough apart to cause the observed transition. However, we do not observe a sizable volume expansion of the Spurr's epoxy at temperatures near the PTC transition, as is normally observed in semicrystalline polymer composites at the melting point⁴. The T_g of the Spurr's epoxy is about 65°C as measured by differential scanning calorimetry and thermal mechanical analysis and it is tempting to correlate the temperature of the PTC phenomenon with T_g . However, composites prepared with the

elastometric Eccogel 1365-80 epoxy (T_g less than room temperature) exhibit a large PTC effect at approximately the same temperature (although the transition is not as sharp) as the Spurr's-based composite (Fig. 6). Further experimental work is in progress to understand more clearly the nature of the PTC transition in amorphous polymer-conductor composites.

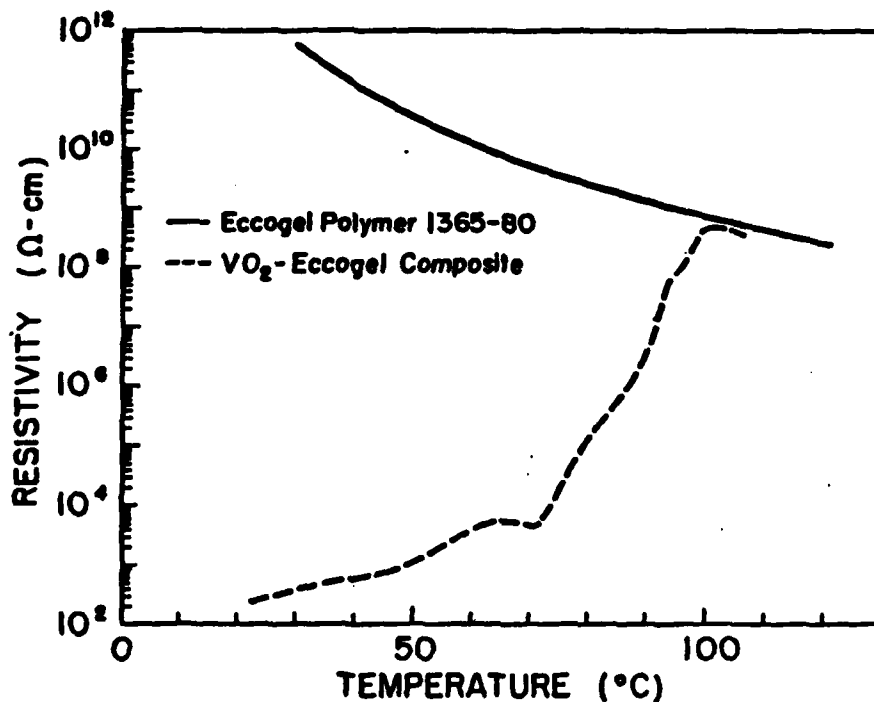


FIGURE 6 Temperature dependence of the electrical resistivity of Eccogel epoxy and VO₂-Eccogel composite containing 60 vol% of filler.

The results of the study are summarized in Fig. 7 where the maximum resistivity and the room temperature resistivity ρ_{RT} are shown for the composites of Fig. 5. The VO and V₂O₃ composites show the lowest room temperature resistivities as expected from the pure filler properties (Fig. 1). All conductor-filled composites exhibit very large PTC intensities of approximately

the same magnitude, except for NbO_2 . Interesting NTC-PTC behavior is seen in several of the composites. This will be discussed in more detail in a forthcoming publication.

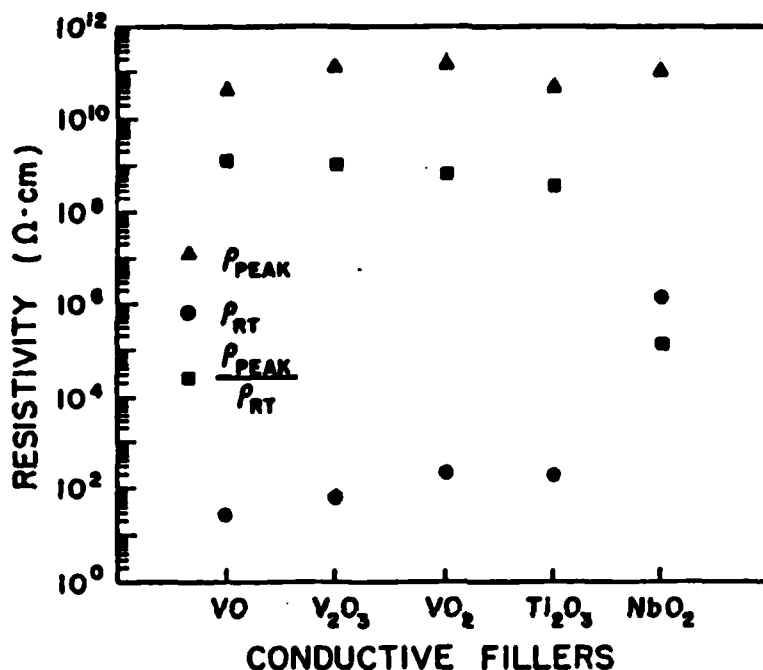


FIGURE 7 The maximum resistivity (ρ_{peak}), room temperature resistivity (ρ_{RT}) and magnitude of PTC effect $\left(\frac{\rho_{\text{peak}}}{\rho_{\text{RT}}}\right)$ of spurrs epoxy composite with various filler materials.

ACKNOWLEDGEMENTS

The authors would like to thank Mr. D. Murphy of the Perkin Elmer Corporation for performing the thermal mechanical analysis experiments.

REFERENCES

1. K. Ohe and Y. Naito, Jap. J. Appl. Phys. 10, 99 (1971).
2. F. Beuche, J. Appl. Phys. 44, 532 (1973).
3. F. Beuche, J. Polym. Sci. Polym. Phys. Ed. 11, 1319 (1973).
4. J. Meyer, Polym. Eng. Sci. 13, 42 (1973).
5. J. Meyer, Polym. Eng. Sci. 14, 706 (1974).
6. M. Narkis, A. Ram and F. Flashner, Polym. Eng. Sci. 18, 459 (1978).
7. M. Narkis, A. Ram and Z. Stein, J. Appl. Polym. Sci. 15, 1515 (1980).
8. F.J. Morin, Phys. Rev. Lett. 3, 34 (1959).

$(\text{Pb,Bi})(\text{Ti,Fe})\text{O}_3$ /POLYMER 0-3 COMPOSITE MATERIALS
FOR HYDROPHONE APPLICATIONS

M.S. Thesis

Jayne R. Giniewicz

The Pennsylvania State University

The Graduate School

**(Pb, Bi)(Ti, Fe)O₃ / Polymer 0-3 Composite Materials
for Hydrophone Applications**

A Thesis in

Solid State Science

by

Jayne R. Giniewicz

**Submitted in Partial Fulfillment
of the Requirements
for the Degree of**

Master of Science

August 1985

I grant The Pennsylvania State University the nonexclusive right to use this work for the University's own purposes and to make single copies of the work available to the public on a not-for-profit basis if copies are not otherwise available.

Jayne R. Giniewicz

ABSTRACT

The $(1-x)\text{PbTiO}_3 - (x)\text{BiFeO}_3$ solid solution system was investigated as the piezoelectric component of a 0-3 composite sheet material. The study involved: (1) a general study of the solid solution system within the range $0.5 \leq x \leq 0.8$, (2) the optimization of the powder preparation conditions for a conventional processing method to produce single phase fine-grained powders from the highly anisotropic tetragonal phase region, (3) the development of a practical and reproducible 0-3 composite processing procedure for preparing test samples, and, finally, (4) a systematic survey of samples incorporating the most highly anisotropic tetragonal compositions of the solid solution near the morphotropic phase boundary.

The optimum conditions for the preparation of single phase tetragonal $(\text{Pb}_{1-x}\text{Bi}_x)(\text{Ti}_{1-x}\text{Fe}_x)\text{O}_3$ compositions by a conventional processing method were established and a preliminary investigation of the morphotropic phase boundary region was conducted. The tetragonal modification of the solid solution was produced for compositions in the range $0.5 \leq x \leq 0.7$ by a double roasting procedure consisting of a preliminary low temperature firing at 800°C for 1.5 hours followed by a second high temperature firing at 1000°C for 1.5 hours. Fine crystallites of the single phase tetragonal $(\text{Pb}_{1-x}\text{Bi}_x)(\text{Ti}_{1-x}\text{Fe}_x)\text{O}_3$ compositions were produced by water quenching from the firing temperature to room temperature directly after the soak period. A two-phase region was observed across the composition range $0.7 < x < 0.8$. The breadth of the region and the relative amounts of each phase were found to be dependent upon the composition, the firing conditions, and the cooling schedule imposed.

The dependence of particle size distribution on composition, firing conditions, quench rate, and quench temperature was examined. Fracture of the ceramic upon cooling through the transition temperature, T_C , occurs primarily at grain boundaries producing, under optimum conditions, fine, nearly spherical crystallites. It was observed that ceramics prepared closer to the phase boundary are more completely disrupted upon quenching than those prepared at compositions for which the structural anisotropy is less. In addition, samples prepared at higher temperatures and for longer soak periods also undergo greater disruption and achieve smaller particle sizes due to more complete reaction and enhanced crystallinity. Thermal shock was also found to play a role in the disruption of the microstructure and the ultimate particle size distribution.

A prototype 0-3 composite sheet design was developed composed of the $(\text{Pb,Bi})(\text{Ti,Fe})\text{O}_3$ filler and an epoxy (Eccogel) matrix. This basic design was optimized on the laboratory scale to consistently produce samples with adequate integrity to withstand routine polarization and measurement so as to best represent the hydrostatic capabilities of the material.

The hydrostatic piezoelectric response of composite materials representing $(\text{Pb}_{1-x}\text{Bi}_x)(\text{Ti}_{1-x}\text{Fe}_x)\text{O}_3$ compositions from the highly anisotropic tetragonal region in the vicinity of the morphotropic phase boundary were measured and compared. The considerable difficulty in poling encountered and, hence, the diminished piezoelectric response encountered as the composition of the filler is shifted closer to the phase boundary was determined to be largely due to the high conductivity of the BiFeO_3 - rich compositions. The ceramic was modified with Mn in an attempt to lower its conductivity. Composites incorporating the Mn-doped filler poled more rapidly and easily than the undoped material and ultimately achieved a hydrostatic piezoelectric figure of merit 40% better than that observed

AD-A173 185

PIEZOELECTRIC AND ELECTROSTRICTIVE MATERIALS FOR
TRANSDUCER APPLICATIONS(U) PENNSYLVANIA STATE UNIV
UNIVERSITY PARK MATERIALS RESEARCH LAB

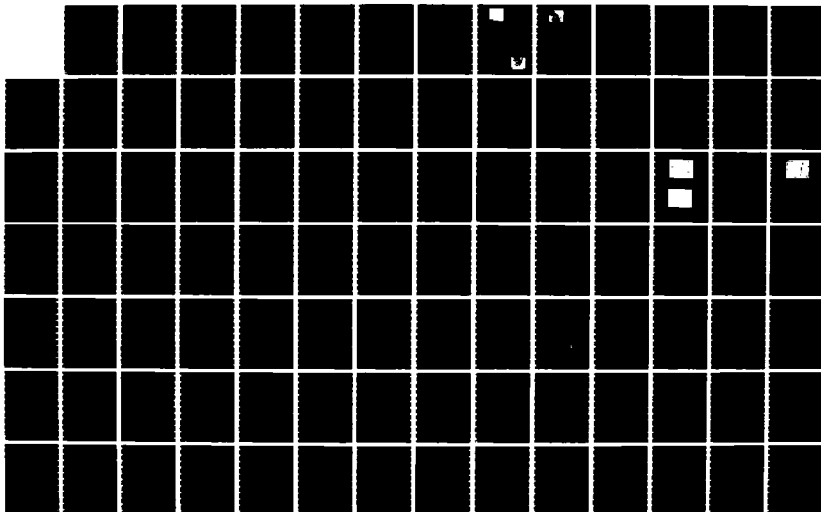
3/4

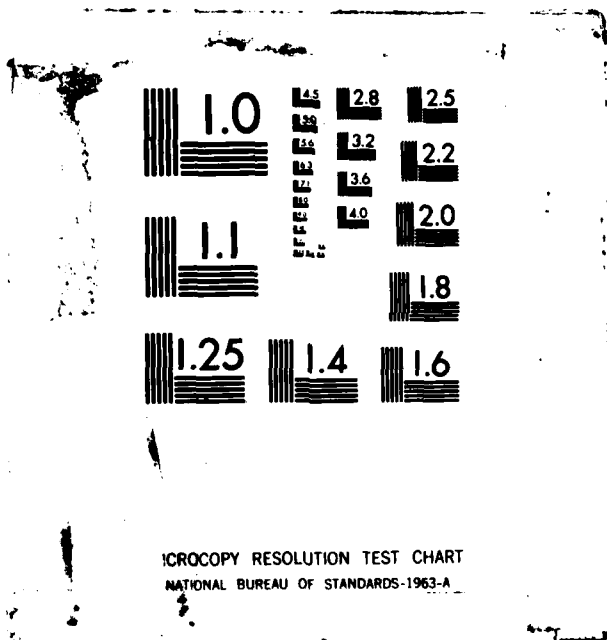
UNCLASSIFIED

L E CROSS ET AL JUL 86 N00014-82-K-0339

F/G 9/1

NL





for the undoped samples. The hydrostatic response remains stable over a broad pressure range. Among the samples investigated, the highest hydrostatic figures of merit were exhibited by samples containing the doped and undoped $x=0.5$ fillers.

ELECTROSTRICTION PROPERTIES OF OXYGEN OCTAHEDRON FERROELECTRICS

P. Asadipour, U. Kumar, S.J. Jang, A.S. Bhalla and L.E. Cross

Electrostriction Properties of Oxygen Octahedron Ferroelectrics

P. ASADIPOUR, U. KUMAR, S. J. JANG, A. S. BHALLA and L. E. CROSS

Materials Research Laboratory
 The Pennsylvania State University
 University Park, PA 16802 USA

For the materials with diffuse phase transitions it is suspected that the long-range coupling may be weakened by local composition fluctuations and thus near T_c strong local fluctuations could develop in P_i . In the case of $\text{Sr}_{0.61}\text{Ba}_{0.39}\text{Nb}_2\text{O}_6$ (SBN) measurements of the electric polarization P_i , thermal strain x_i and x_{ij} , dielectric constant, K_i , and optical birefringence are used to confirm that the polarization P_i^2 is not zero for a range of temperature above T_c . The values of P_i^2 deduced from x_i vs T and birefringence vs T , the two independent methods are in good agreement indicating substantial polarization fluctuations which decay slowly above the mean Curie temperature, T_c .

§1. Introduction

In the congruently melting $\text{Sr}_{0.61}\text{Ba}_{0.39}\text{Nb}_2\text{O}_6$ (SBN, tetragonal ferroelectric species 4/mmm(1)D4F4mm) measurements of the electrostriction constants Q_{33} and Q_{31} ¹⁾ have shown a strong anomalous decrease for temperatures above but close to the Curie point T_c . Earlier measurements by Shrout²⁾ on the elastic stiffness of the same crystal also showed an anomalous softening in the Curie range near T_c which could not be accounted for on the Landau-Ginsburg-Devonshire (LGD) phenomenology. For both measurements the coupling between polarization and elastic response is quadratic and depends upon P^2 .

For most ferroelectric crystals, it has become customary to neglect the effect of fluctuations in the order parameter P near T_c as the long range nature of the dipole-dipole coupling would militate against large amplitude fluctuations. Thus in triglycine sulphate, for example, the Curie-Weiss behavior of dielectric constant, K_0 , appears to hold within millidegrees of the transition. In crystals like SBN, however, it is well known that the Curie Weiss law does not hold for temperatures close to T_c and it could be that local variations in the site occupancy of Ba and Sr cations gives a distribution of local Curie points, a distribution of transition temperatures T_c and a low radio frequency dependence of the relative permittivity K_1 (relaxor effect) for temperatures near but below T_c .

In this system then, one may suspect that the long-range coupling may be weakened by local composition fluctuations and thus near T_c strong local fluctuations could develop in P_i . For the tetragonal ferroelectric form in SBN, the Curie-Weiss temperature θ_i is very much higher than θ_1 and thus P_i should be the strongly fluctuating component, i.e. near T_c we may expect $\sqrt{P_i^2}$ to be non-zero. Thus any property tensor coupled quadratically to the polarization e.g. thermal expansion, optical refractive index, elastic compliances might be expected to begin to change above T_c as P_i^2 increases.

By measuring a number of the property tensors which are coupled quadratically to P_i , we can get several independent checks of the magnitude and temperature dependence of $\sqrt{P_i^2}$. In this paper we report the measurements of thermal strains and birefringence and

polarization $\sqrt{P_i^2}$ and compare it with the measured values of P_i obtained from the integration of the pyroelectric currents vs temperature data.

§2. Experimental and Results

a) Thermal Expansion Measurements: Since the elastic strains x_{11} and x_{33} are coupled to the polarization P_i by the electrostriction constants so that

$$x_{kl} = Q_{3kl} P_i^2 \quad (1)$$

$$x_{11} = Q_{311} P_i^2 \text{ or } x_1 = Q_{31} P_i^2 \quad (2)$$

and

$$x_{33} = Q_{333} P_i^2 \text{ or } x_3 = Q_{33} P_i^2 \quad (3)$$

For decreasing temperature T above T_c , it may be expected that the thermal contraction could begin to be moderated as P_i^2 increases.

Using a thick plate of SBN cut normal to the c axis and carefully annealed at 600°C to remove internal stress and bias effects, the thermal contraction measured on a high sensitivity LVDT dilatometer is shown in Fig. 1. It is interesting to note that the sample begins to depart from linear contraction at close to 300°C, even though the permittivity maximum (taken to be T_c) in this composition does not occur until 80°C.

Earlier measurements had shown that remote from T_c , Q_{333} is positive and thus an escalation of $\sqrt{P_i^2}$ would be expected to produce increasing dilatation along the c axis

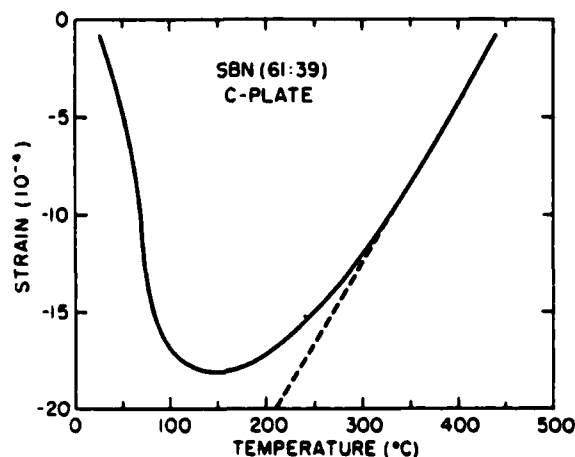


Fig. 1. Temperature dependence of strain along the c -axis of a 61:39-

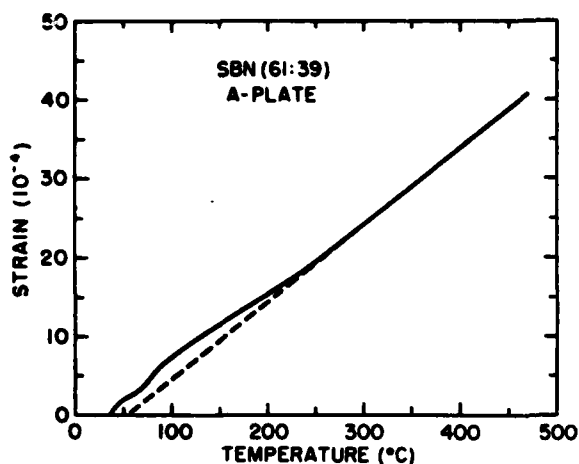


Fig. 2. Temperature dependence of strain x_1 vs T for 61: 39-SBN crystal.

counteracting and apparently overriding the normal thermal contraction as the sample cooled towards the ferroelectric state.

Measurements of thermal contraction on cooling a thick a -cut plate gives similar results. Again there is evidence of a break in the normal contraction at a temperature near 300°C as shown in Fig. 2.

b) Birefringence Measurements

Clearly if the strain behaves in this anomalous manner above T_c , the optical impermeability (ΔB_{ij}), must also reflect the fluctuations, through the quadratic electro-optic coefficients (g_{ijk}), i.e.,

$$\Delta B_{ij} = g_{ij33} P_3^2 \quad (4)$$

$$\therefore \Delta B_1 = g_{133} P_3^2 \quad (5)$$

and

$$\Delta B_3 = g_{333} P_3^2 \quad (6)$$

From Eq. (5) and (6)

$$\Delta n_{31} = -\frac{1}{2} n_0^3 (g_{33} - g_{13}) P_3^2 \quad (7)$$

From the bulk crystals 'a' cut plates were prepared into

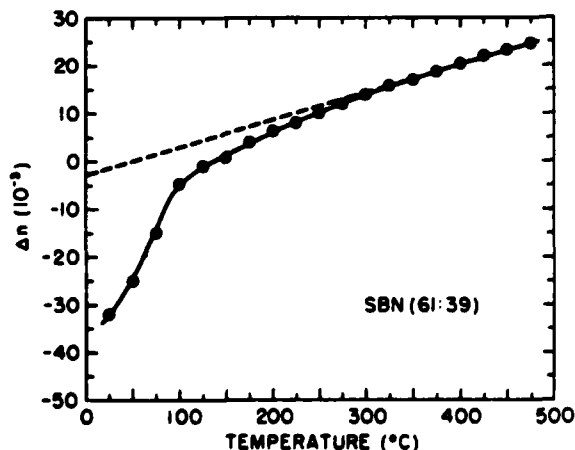


Fig. 3. Birefringence vs temperature for a 61: 39 SBN single crystal.

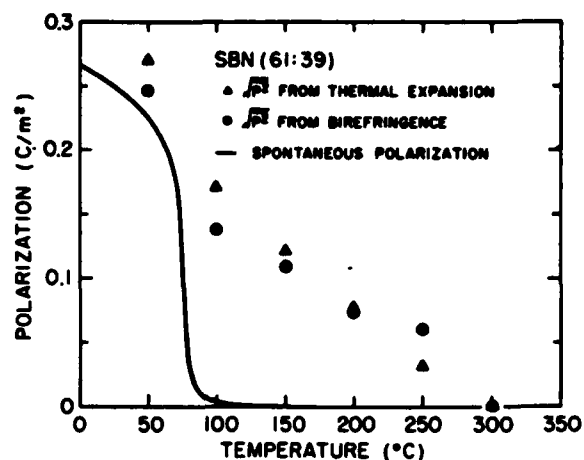


Fig. 4. Calculated $\sqrt{P_3^2}$ from thermal expansion and optical birefringence data. Also shown is a measured polarization for SBN single crystal.

wedge shapes with a known angle (typically 7°). Using a polarizing microscope in conjunction with a hot stage, the birefringence Δn_{31} was determined as a function of temperature. A sodium lamp was used for the source of monochromatic light. The birefringence was calculated from the following equation:

$$\Delta n_{31} = \frac{\lambda}{d \sin \theta} \quad (8)$$

where λ is the wavelength of sodium light (5893 Å), d the width of interference fringes resulting from the varying thickness of the wedge, and θ the angle of the wedge.

The birefringence values as a function of temperature are shown in Fig. 3. Δn_{31} passed through zero above T_c with a corresponding change in slope.

Taking the measured values Q_{33} and Q_{31} vs temperature¹⁾ the values of $\sqrt{P_3^2}$ at various temperatures were deduced and plotted in Fig. 4. Using the values of $n_0 = 2.3$ and $(g_{33} - g_{13}) = 0.068 \text{ m}^4/\text{C}^2$, P_3^2 were calculated from the birefringence data at various temperatures (Fig. 4). It is evident from Fig. 4 that agreement is quite good in the $\sqrt{P_3^2}$ values calculated from two independent methods. The fluctuating polarization is smaller at the lower temperature and are of much larger values than the polarization deduced from a simple Byer-Roundy thermal depolarization, also shown in Fig. 4, showing quantitatively the slow decay of $\sqrt{P_3^2}$ above Curie temperature.

References

- 1) C. Sundius, "Direct Measurement of the Temperature Dependence of Electrostrictive Coefficients in Strontium Barium Niobate," M. S. Thesis in Solid State Science, The Pennsylvania State University (1984).
- 2) T. Shrout, "A Phenomenological Theory for Predicting the Temperature Dependence of Elastic Constants in Simple Proper Ferroelectric Tungsten Bronzes," Ph. D. Thesis in Solid State Science, The Pennsylvania State University (1981).

TEMPERATURE DEPENDENCE OF THE RELAXOR MATERIAL $\text{Pb}(\text{Sc}_{0.5}\text{Ta}_{0.5})\text{O}_3$

H.M. Chan, M.P. Harmer, A. Bhalla and L.E. Cross

TEM of the Relaxor Material $\text{Pb}(\text{Sc}_{0.5}\text{Ta}_{0.5})\text{O}_3$

H. M. CHAN, M. P. HARMER, A. BHALLA*
 and L. E. CROSS*

Lehigh University, Bethlehem, PA 18015

*Pennsylvania State University, University Park, PA 16802

The transmission electron microscope (TEM) was used to directly observe ordered microdomains in $\text{Pb}(\text{Sc}_{0.5}\text{Ta}_{0.5})\text{O}_3$ (PST). The microstructure of both single crystal and polycrystalline PST was studied as a function of S , the degree of order (which was controlled by thermal treatment). The observed domain sizes were in good agreement with the results of prior X-ray studies. It was found that the domain coarsening kinetics are much slower for the single crystal than the polycrystalline material. Also evidence was obtained for the presence of short range order within PST.

§1. Introduction

Lead scandium tantalate $\text{Pb}(\text{Sc}_{0.5}\text{Ta}_{0.5})\text{O}_3$ is one of a number of ferroelectric compounds which exhibit so-called "relaxor behavior" i.e., these materials show a broad dielectric permittivity versus temperature peak, and dielectric dispersion at low frequencies. It has been postulated¹⁻³⁾ that this type of behavior is due to the presence of microscopic regions within the material which are of slightly differing compositions (and hence Curie temperatures).

Setter and Cross investigated this model by studying the behavior of lead scandium tantalate (PST).^{4,5)} This material is particularly suited to this type of study because the degree of order of the B-site cations (Sc^{3+} and Ta^{5+}) can be controlled by thermal treatment. The structure of fully ordered PST is shown in Fig. 1; it can be seen that the Sc^{3+} and Ta^{5+} ions adopt a NaCl type structure on the B-site sublattice. Setter and Cross showed that in the disordered state, PST exhibited classic relaxor behavior. On ordering however, a pronounced sharpening of the permittivity versus temperature curves took place, thus supporting the model that the relaxor behavior is caused by chemical inhomogeneity on a nanoscopic scale.

Until very recently, evidence for the existence of ordered microdomains within PST has been indirect.⁴⁾ Harmer *et al.*⁶⁾ were the first workers to directly observe ordered microdomains in PST using the transmission electron microscope (TEM). The scale of the ordered structures was found to be of the order of 35–120 nm, which was in good agreement with the earlier X-ray results. A particularly interesting result from the study of Setter and Cross⁵⁾ was the difference in domain coarsening behavior exhibited by the single crystal and polycrystalline PST. On annealing the polycrystalline (ceramic) PST, the degree of order increased, and there was a corresponding increase in the size of the ordered domains (as determined by X-ray line broadening measurements). For the single crystal however, even for relatively high degrees of order (~80%), the domain size was determined to be <100 Å. The purpose of this study, therefore, was to use the TEM to directly examine the ordered domain configurations for both single crystal and ceramic PST, as a function of annealing conditions. In this way, it was hoped to gain a better understanding

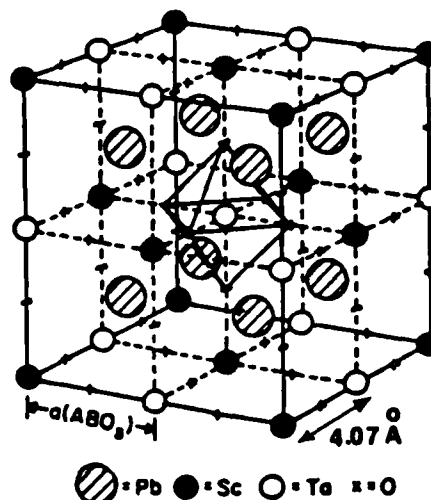


Fig. 1. Structure of ordered perovskite $\text{Pb}(\text{Sc}_{0.5}\text{Ta}_{0.5})\text{O}_3$ (after Galasso¹¹⁾).

Table I

PST	Heat Treatment	Degree of Order
Single Crystal	a) As-grown	0.8
	b) Annealed 24 hrs. 1000°C	0.8
	c) 1 hr. 1400°C air quenched	0.35
Polycrystal	a) As sintered	0.37
	b) 2 hrs. 1000°C	0.86
	c) 30 hrs. 1000°C	0.86

system.

§2. Experimental

The techniques used to prepare the PST single crystals⁴⁾ and polycrystalline sintered pellets⁵⁾ have been described in detail elsewhere. The samples studied, together with the corresponding heat-treatments are summarized in Table I. Lead loss during the annealing treatments was minimized by surrounding the specimens with a PbZrO_3 -20 wt% PbO mixture. Thin foil TEM specimens were prepared by polishing down to ~30 μm , and argon-ion-beam thinning using 6 kV argon ions incident 15° to the foil plane. To prevent lead evaporation during ion-beam milling, a liquid- N_2 cooled cold stage was used.



Fig. 2. Single crystal, as grown. Centered dark-field micrograph, bright regions are ordered microdomains.

Table II

Disordered			Ordered (NaCl structure)*			d-spacing (Å)	
<i>h</i>	<i>k</i>	<i>l</i>		<i>h</i>	<i>k</i>		<i>l</i>
—			F	1	0	0	8.14
—			F	1	1	0	5.76
—				1	1	1	4.70
1	0	0		2	0	0	4.07
1	1	0		2	2	0	2.88

F=forbidden reflection

doubling of the unit cell parameters when PST goes from the disordered to the ordered state. The effect of this on the observed reflections in the electron diffraction pattern is shown in Table II. The (100), and (110), superlattice reflections are forbidden due to structure factor considerations, however the (111), is allowed. It is this reflection therefore which can be used to image the ordered domains in dark field.

§3. Results

3.1 Single Crystal

i) As grown ($S=0.8$)

Figure 2 shows a centered dark-field micrograph of the as grown single crystal taken using the (111), reflection. The bright regions are the ordered microdomains; the matrix (dark contrast) is disordered. The domain size was of the order 100–600 Å. When this structure was annealed for 24 hrs. at 1000°C, no coarsening of the domains was observed, and the microstructure remained for the most part unchanged. This is in direct contrast to the behavior of the polycrystal which is discussed in a later section. Figure 2 is representative of the structure observed in the majority of the areas studied. In some isolated regions of the sample however, domains more resembling those reported by Harmer *et al.*⁶⁾ were observed. The reason for this variation in structure is unclear. It may be related to local variations in the degree of order occurring during the growth process.

ii) $S=0.35$

The degree of order of the as grown single crystal was relatively high. Disorder can be achieved however by annealing for 1 hr. at 1400°C, and air quenching. The resulting structure was very similar to that shown in Fig.

2. Despite the lower degree of order, ordered microdomains are still visible, the scale of the domains being similar to those of the "as grown" state.

3.2 Polycrystal

i) As sintered ($S=0.34$)

In the as sintered state, the degree of order is relatively low. Ordered microdomains ~200 Å in diameter were observed, and the overall microstructure resembled that of the single crystal.

ii) Annealed at 1000°C ($S=0.86$)

After annealing for 30 hrs. at 1000°C, the structure underwent considerable coarsening as can be seen in Fig. 3. The wavy boundaries seen separating the domains are anti-phase domain boundaries (APB's). An APB is characterized by a disruption in the correct ordering sequence, and separates two fully ordered regions.⁶⁾ The observed domain size varied widely from ~200 Å to over 4000 Å. A similar structure was observed after annealing for only 2 hrs. at 1000°C, except in this case the maximum observed domain size was ~2000 Å. This result confirms that coarsening of the domain structure occurs much more rapidly in the polycrystal than in the single crystal, and possible reasons for this will be discussed later.

3.3 Anomalous (110), Reflection

As discussed previously, for the ordered NaCl structure, the (110), superlattice reflection is forbidden due to structure factor considerations. Faint (100), reflections were observed, however, for both single crystal and ceramic PST (Fig. 4). The possible origin of this anomalous (110), reflection will be discussed more fully in the next section.

§4. Discussion

4.1 Single Crystal

For both the disordered ($S=0.35$) and ordered ($S=0.8$) single crystal, dark field imaging showed the structure to consist of ordered microdomains (200–600 Å) within a disordered matrix. At first sight, the lack of dependence of the ordered domain size or density on the overall degree of order is difficult to understand. It should be remembered however that S (the degree of order) was estimated by ratioing the intensity of the (111), X-ray reflection to that of the (200),. The value of



Fig. 3. Polycrystal, annealed 30 hrs. at 1000°C.

*Indexed using the ordered unit cell.

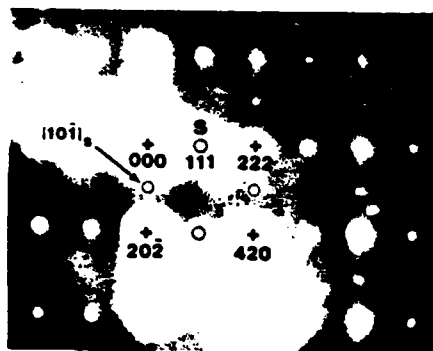


Fig. 4. [121] diffraction pattern, note diffuse (110) reflections.

S obtained is thus an average for the whole specimen. The dark field imaging technique however only detects those volumes of material where the intensity of the (111), is sufficient to produce an image in reasonable exposure times. Thus the X-ray and TEM techniques are measuring slightly different quantities, and in general one would expect the X-ray technique to give the higher value of S. Another factor which must be taken into consideration is the possibility of partial, short-range ordering (SRO). This is intermediate between disordered and fully ordered, and represents the stage where there is a marked preference for the B-site ions to have unlike neighbors, but the ordering extends over several unit cells only. This could account for the speckled contrast observed within the ordered domains.⁹⁾

4.2 Polycrystalline PST

The ordered domain structure for the polycrystal (annealed 30 hrs. at 1000°C) is similar to that observed by Chang and Chen¹⁰⁾, however these workers did not state whether they were studying single or polycrystalline material, or the nature of the heat treatments carried out (if any). For the type of order occurring in PST, there is one unique type of APB whose anti-phase vector can be defined as $1/2 [001]$. For this reason, no APB triple points can occur, and it is impossible to form a stable foam-like structure. Coarsening usually occurs readily for this type of APB configuration, and this was observed to be the case for the ceramic PST.

The reason for the lack of domain coarsening in the single crystal is not clear. One possibility is that it is related to differences in chemistry between the two samples, since the preparation techniques for the single crystal and polycrystal were completely distinct. If there is an excess of one of the B-site cations for example, this may have a stabilizing influence on a particular domain configuration.¹²⁾

4.3 Anomalous (110), Reflection

A series of experiments were carried out in order to determine the origin of the anomalous reflection (110). The results were as follows:

- a) It was determined that the (110), reflection was not a thinning artefact, as the reflection was observed in thin specimens produced by crushing, as well as in ion-beam thinned samples.
- b) It was shown to be unlikely that the (110), reflection was the result of beam damage, because the d-spacing did not correspond to any reflections previously obtained from heavily damaged areas.
- c) The (110), reflection was determined not to originate from the APB's, since the reflection was observed even for selected area diffraction patterns taken from within a single domain.

Taking into account the above evidence, it is postulated that the observed (110), reflections are the result of small regions within the crystal which have a type of order different from the NaCl structure. These regions could occur in either conventionally ordered or disordered regions of the crystal. Unfortunately this model is difficult to test because the diffuseness of these reflections made dark-field imaging of these regions impractical.

§5. Summary

Dark field imaging has been used to directly observe ordered microdomains in $\text{Pb}(\text{Sc}_{0.5}\text{Ta}_{0.5})\text{O}_3$. The size of the microdomains was in good agreement with the results of earlier X-ray determinations. The domain coarsening kinetics were much slower for the single crystal. Evidence has been obtained for the presence of short range order within PST. This study has focussed on the microstructural features of the ordered domains. These results will be presented more fully, together with the corresponding dielectric data, in a separate paper.

Acknowledgement

Financial support from the National Science Foundation and the Office of Naval Research is gratefully acknowledged.

References

- 1) V. A. Isupov: *Sov. Phys.-Tech. Phys.* 1 (1956) 1846.
- 2) B. N. Rolov: *Sov. Phys. Solid State* 6 (1965) 1676.
- 3) V. V. Kirillov and V. A. Isupov: *Ferroelectrics* 5 (1973) 3.
- 4) N. Setter and L. E. Cross: *J. Mat. Sci.* 15 (1980) 2478.
- 5) N. Setter and L. E. Cross: *J. Appl. Phys.* 51 (1980) 4356.
- 6) M. P. Harmer, A. Bhalla, B. Fox and L. E. Cross: *Mat. Letters* 2 (1984) 278.
- 7) N. Setter and L. E. Cross: *J. Crystal Growth* 50 (1980) 555.
- 8) D. A. Porter and K. E. Easterling: *Phase Transformations in Metals and Alloys* (Van Nostrand Reinhold (UK) Co. Ltd., 1982) 3rd ed. p. 358.
- 9) J-P. A. A. Chevalier and W. M. Stobbs: *Proc. 6th Eur. Congr. on Electron Micros., Jerusalem, 1976.*
- 10) Y. J. Chang and Z. L. Chen: *Ferroelectrics Letters* 4 (1985) 13.
- 11) F. S. Galasso: *Structure, Properties and Preparation of Perovskite-type Compounds* (Pergamon, New York, 1969).
- 12) C. L. Rase and D. E. Mikkola: *Met. Trans.* 6A (1975) 2267.

**DIELECTRIC AGEING EFFECTS IN DOPED LEAD MAGNESIUM NIOBATE:
LEAD TITANATE RELAXOR FERROELECTRIC CERAMICS**

Wuyi Pan, E. Furman, G.O. Dayton and L.E. Cross

Dielectric ageing effects in doped lead magnesium niobate: lead titanate relaxor ferroelectric ceramics

WUYI PAN, E. FURMAN, G. O. DAYTON, L. E. CROSS

Materials Research Laboratory, The Pennsylvania State University, University Park, Pennsylvania 16802, USA

Earlier studies in the laboratory [1] have shown no evidence of dielectric ageing phenomena in lead magnesium niobate $\text{Pb}(\text{Mg}_{1/3}\text{Nb}_{2/3})\text{O}_3$ (PMN) or in lead magnesium niobate: lead titanate solid solutions $(\text{PbMg}_{1/3}\text{Nb}_{2/3}\text{O}_3:\text{PbTiO}_3)$ (PMN:PT) although all compositions up to 13 mol % PbTiO_3 addition show ferroelectric relaxor character. Studies of the PLZT relaxor compositions [2], however, and also strontium barium niobate (SBM) materials [3] show significant ageing phenomena. In seeking the difference between these two families of relaxors, it may be noted that the PLZT and SBN are intrinsically "defective" in the sense that in the stoichiometric composition not all sites for the cations are occupied while in the PMN derived compositions the structure is fully "stuffed" and has all lattice sites occupied.

To explore further the role of defects in the ageing phenomena in relaxors, PMN:10 mol % PT compositions have been fabricated with a 0.1 mol % doping of MnO. The work reported here shows that these doped ceramics show ageing effects similar in many respects to the PLZT relaxor compositions.

Ceramic samples of PMN:10% PT for use in this study were prepared using the pre-reaction of MgO and Nb_2O_5 to form first the columbite structure precursor in the manner discussed in earlier papers [4, 5]. For the doping studies, MnO was introduced using a dilute $\text{Mn}(\text{NO}_3)_2$ solution, added to the calcine. Final sintered samples were all above 97% theoretical density and were shown by X-ray diffraction to be free of pyrochlore phase contamination.

For ageing studies, disk-shaped samples were equipped with chrome:gold electrodes on the major faces. Ageing was accomplished by first heating the sample above 150°C to relieve all earlier ageing, then bringing the sample down to a fixed temperature and starting the measuring clock. Room-temperature ageing was carried out in a dessicator in the air-conditioned laboratory space (22 to 28°C). The 40°C ageing runs were carried through in a heated plexol oil bath with temperature fluctuation less than $\pm 0.5^\circ\text{C}$. The -15°C runs were carried out in a commercial freezer with a measured temperature variation of $\pm 2^\circ\text{C}$. All runs were carried out with the sample under open circuit conditions, connection being made at intervals to establish the capacitance and loss but then relieved for the ageing time.

The permittivity-temperature runs were made in a computer-controlled environment chamber (Delta Design Model 2300) using liquid nitrogen as the coolant. The sample was put into the chamber at a

temperature below the ageing temperature, the temperatures were then lowered to -70°C and the dielectric properties were measured during heating at 4°C min^{-1} . For cooling runs, the samples were heated to 170°C, kept at that temperature for $\frac{1}{2}$ h, then measured as the temperature was lowered at 4°C min^{-1} down to -70°C . Dielectric properties were measured using the Hewlett packard LCR meter (model 4274A) under computer control covering a frequency range from 100 Hz to 100 kHz with field strength less than 100 V cm^{-1} .

Hysteresis loops were measured with a Sawyer and Tower system [6] under 0.1 Hz frequency driving field. The aged sample was measured without any prior heating above the ageing temperature. The a.c. de-aged sample was measured by applying a 10 Hz field of 20 kV cm^{-1} for 20 min and measuring with 0.1 Hz field. The thermally de-aged sample was measured after heating the sample above the Curie range and measuring as soon as the temperature reached room temperature.

Fig. 1a shows the variation of frequency dispersion with temperature. The curves may be divided into four regions. (i) A low-temperature region (below 10°C) where the frequency dispersions for both aged and deaged samples are similar. (ii) A region of decreasing dispersion (10 to 25°C) ending at the ageing temperature. (iii) A region of very markedly reduced dispersion for the aged samples (25 to 60°C) between the ageing temperature and a temperature above that of the permittivity peaks. The dispersion reduction due to ageing in this region is more pronounced than that observed by Schulze *et al.* [1] in PLZT. (iv) A paraelectric region (about 60°C) with no apparent ageing or dispersion.

In Fig. 1b, the loss tangents against temperature may be divided into three regions. (i) A region where the $\tan \delta$ of the aged sample are slightly greater than those of the de-aged samples but with similar frequency dispersion. (ii) A region where the $\tan \delta$ of the aged sample are markedly less than those of de-aged samples especially at the ageing temperature. (iii) A region (above 55°C) where the $\tan \delta$ for aged and de-aged samples are the same.

Fig. 2 shows the variation of the frequency dispersion with temperature for a PMN + 10% PT relaxor ceramics without MnO doping, which is typical for all undoped samples which do not show ageing.

Fig. 3 shows the effect of ageing time on the dielectric constants. In the vicinity of the ageing temperature, a decrease of the dielectric permittivity with

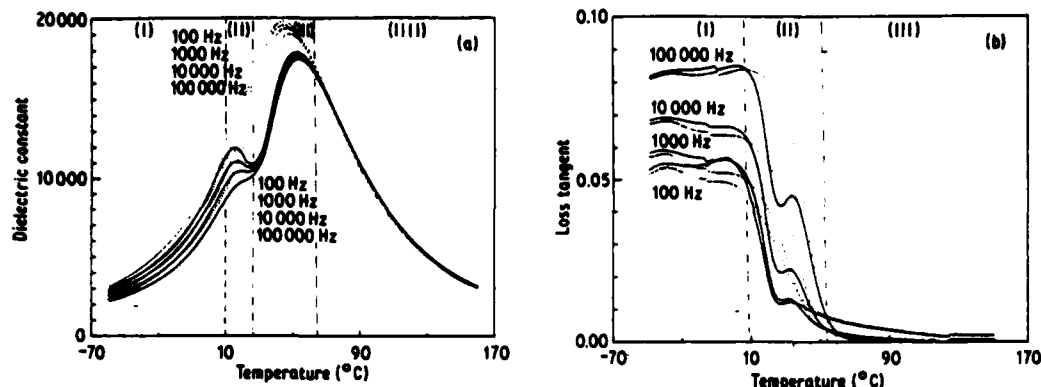


Figure 1 (a) Dielectric permittivity and (b) dielectric loss tangent against temperature for $(\text{PbMg}_{1-x}\text{Nb}_{2-x}\text{O}_{3-y})(\text{PbTiO}_{1-y})$ ceramic doped with 0.1 mol % MnO. Solid curves show the data obtained after ageing for 1000 h at 23 °C. Dotted curves show data for a sample freshly de-aged at 160 °C for 30 min. Frequencies of measurement are as illustrated.

increasing ageing time was observed. Below and above this region, the variation of dielectric constant with ageing time is reduced.

Fig. 4 shows the effects of ageing temperature on the dielectric constant against temperature curves. The saddle point occurring at the ageing temperature shifts as the ageing temperature is changed. Low-temperature ageing was observed to have less effect on the dielectric constant as observed in Curve C (Fig. 4) probably because of the much reduced ageing rate at the lower temperature. As observed in Fig. 4, Curve C, a minimum of dielectric constant in the ageing temperature observed for the higher temperatures was not obvious in the curve for the lowest temperature.

Fig. 5a shows the loop of an aged sample. A double loop with a slim portion in the low-field region was observed. Fig. 5b shows the loop of the above aged sample after 20 min under a 10 Hz field of 20 kV cm^{-1} . The slim portion gradually disappears. Fig. 5c shows the loop for the thermally de-aged sample. The absence of the waisted loop character is obvious. Fig. 5d shows the loop for a sample which was free from MnO doping. Again a loop with no waisted character was evident immediately upon first application of the field.

The data presented in Fig. 2 confirm that as indicated by earlier measurements there is no obvious ageing effect in a PMN:PT composition. However, in the samples of PMN doped with 0.1 mol % MnO there

is now an obvious ageing effect which is in many respects similar to that observed earlier in the relaxor ferroelectric PLZT compositions [2].

It has been suggested that for both normal and relaxor ferroelectrics an essential ingredient of the ageing process is a lattice defect which has polar character [7]. The suggested model is that the polar defect couples to the P_r vector in the domain or microdomain and readjusts its orientation slowly so as to minimize the energy of the system [8]. If defect orientation is thermally activated, ageing proceeds much more slowly at low temperature than at high. Clearly if the energy is minimized for an existing domain orientation, switching from that orientation will be inhibited. Thus if the bulk sample is unpoled, a balanced array of domains will stabilize and the nonpolar state will be preferred, leading to a well defined waist in the hysteresis loop. If, however, the sample is cycled over a saturated loop, the domain vectors will spend almost as much time away from the aged-in polar defect direction as they do in this direction; and thus, slowly the waist of the loop will be lost as the defects randomize.

The suggestion for PMN is that in the stoichiometric composition there is a very low concentration of defects, and thus no obvious ageing. In the MnO doped composition, however, the aliovalent manganese is presumably compensated by oxygen

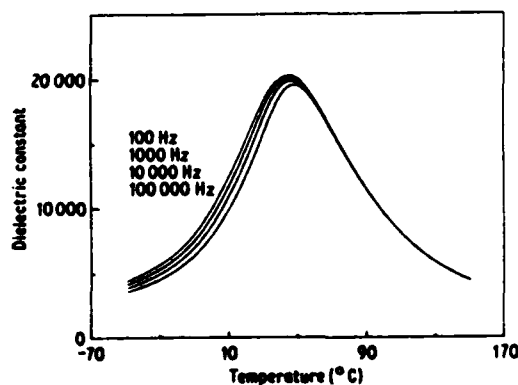


Figure 2 Dielectric permittivity against temperature for a pure $(\text{PbMg}_{1-x}\text{Nb}_{2-x}\text{O}_{3-y})(\text{PbTiO}_{1-y})$ ceramic after ageing for 1000 h at 23 °C.

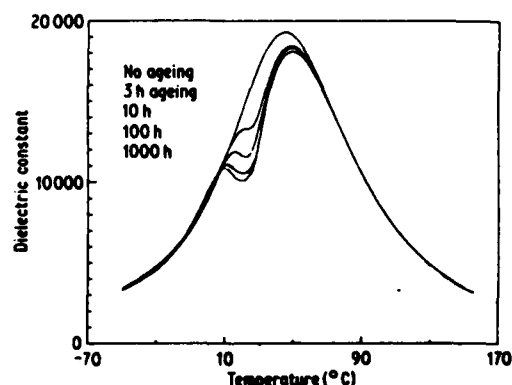


Figure 3 Effects of ageing time on the 100 Hz dielectric permittivity against temperature curves on $(\text{PbMg}_{1-x}\text{Nb}_{2-x}\text{O}_{3-y})(\text{PbTiO}_{1-y})$ ceramic doped with 0.1 mol % MnO.

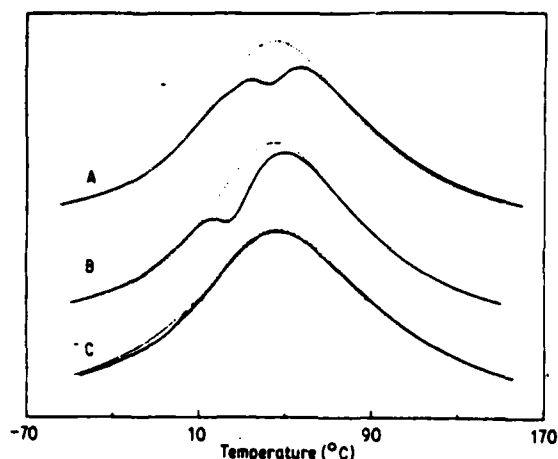


Figure 4 Effect of ageing temperature on the 100 Hz dielectric permittivity against temperature in 0.1 mol % MnO doped PMN:10% PT. Solid curves are for aged samples: Curve A 70 h at 40 °C; Curve B 10 h at 23 °C; Curve C 100 h at -15 °C. Dashed curves are for freshly de-aged samples.

vacancies providing the thermally activated defect dipole pair which is the essential component for ageing.

Both PMN and PMN:PT are relaxor ferroelectrics, and here as in the PLZT relaxors, there is a very obvious preferential ageing of the dispersive component of the permittivity. In PLZT, because of the valence of lanthanum in the solid solution, all samples are necessarily "defective" with lead vacancies the most probable defect species. Thus it is certainly not unexpected that all PLZT relaxors exhibit ageing.

For PMN: +10% PT 0.1% MnO, the asymmetry of the elimination of the dispersive component for temperatures above that of the ageing temperature, and

the re-emergence of ageing below that temperature is extreme and strongly suggests that the polar micro-regions responsible for the superparaelectric dispersion are stabilized by a volume distribution of defect dipoles. Thus on heating when one is emerging into the paraelectric phase, all material in the polar regions is still aged; on cooling, however, new unaged material will be falling into the polar phase and will therefore be able to reorient under field and re-establish the dispersive component of permittivity.

From the dielectric hysteresis data, it is evident that the high field can effect an amalgamation of micro-regions into macrodomains which switch with the field, thus eliminating the preferred orientation and effectively de-ageing the sample as in a normal ferroelectric.

References

1. W. A. SCHULZE, J. V. BIGGERS and L. E. CROSS, *J. Am. Ceram. Soc.* **61** (1978) 46.
2. G. BORCHHARDT, J. VON CIEMINSKI and G. SCHMIDT, *Phys. Status Solidi (a)* **59** (1980) 749.
3. G. A. SMOLENSKII, V. A. ISUPOV, A. I. AGRANOVSKA and N. POPOV, *Sov. Phys. Solid State* **2** (1961) 2584.
4. S. L. SWARTZ and T. R. SHROUT, *Mater. Res. Bull.* **17** (1982) 1245.
5. S. L. SWARTZ, T. R. SHROUT, W. A. SCHULZE and L. E. CROSS, *J. Am. Ceram. Soc.* **67** (1984) 311.
6. H. DIAMANT, K. DRENCK and R. PEPINSKY, *Sci. Instrum.* **28** (1) (1957) 30.
7. K. CARL and K. H. HARDTL, *Ferroelectrics* **17** (1978) 473.
8. K. CARL and K. GEISEN, *Proc. IEEE* **61** (7) (1973).

Received 25 November
and accepted 4 December 1985

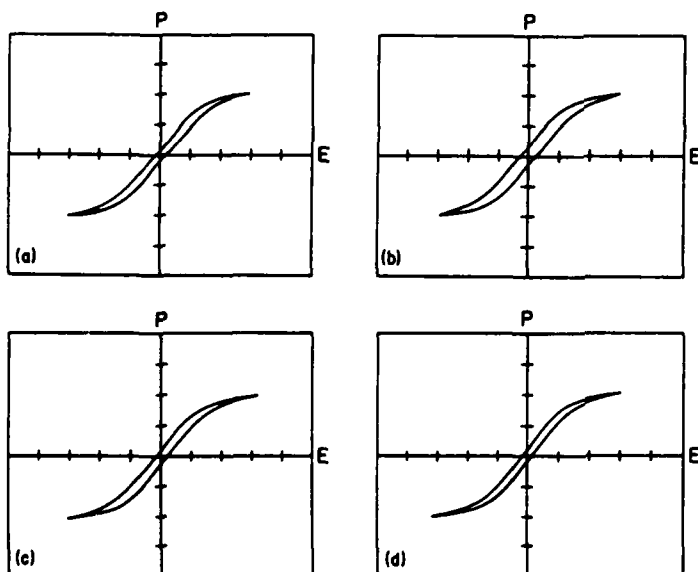


Figure 5 (a) Dielectric hysteresis loop of a 0.1 mol % MnO PMN:10% PT sample aged at 23 °C for 100 h. (b) Hysteresis loop of a.c. de-aged sample driven for 20 min. (c) Hysteresis loop for a sample freshly thermally de-aged by heating to 160 °C for 30 min. (d) Hysteresis in an undoped PMN:10% PT sample.

DIRECT AND CONVERSE ELECTROSTRICTIVE EFFECTS
IN $\text{Pb}(\text{Mg}_{1/2}\text{Nb}_{2/3})\text{O}_3$ CERAMICS

Wuyi Pan and L.E. Cross

DIRECT AND CONVERSE ELECTROSTRICTIVE EFFECTS IN $\text{Pb}(\text{Mg}_{1/2}\text{Nb}_{2/3})\text{O}_3$ CERAMICS

Wuyi Pan and L.E. Cross

Materials Research Laboratory
The Pennsylvania State University
University Park, PA 16802

ABSTRACT

Polarization related electrostrictive coefficients \bar{Q}_{11} and \bar{Q}_{12} for $\text{Pb}(\text{Mg}_{1/2}\text{Nb}_{2/3})\text{O}_3$ ceramics have been measured over the relaxation temperature range by the direct electrostrictive effect. Both coefficients are observed to be independent of temperature. The Q_{11} coefficient has also been measured over a 50°C temperature range above room temperature by the converse electrostrictive effect. A slight increase of the \bar{Q}_{11} coefficient with increasing temperature is observed. Reasonable agreement between the magnitudes of \bar{Q}_{11} coefficients from both methods is achieved, and comparison with earlier single crystal data also shows very good accord.

1.0 INTRODUCTION

The paper by Meng and Cross¹ shows that the converse electrostrictive measurement by means of a compressometer can be successfully applied in determining the electrostrictive effect in normal crystals such as calcium fluoride. The papers of Uchino et al.² and Kuwata et al.³ presented the magnitudes and the temperature dependence of electrostrictive coefficients Q_{11} , Q_{12} for single crystal lead magnesium niobate and \bar{Q}_{11} , \bar{Q}_{12} for ceramics respectively measured by the direct method, but no effort appears to have been made to utilize the converse electrostrictive effect to determine the longitudinal electrostrictive coefficients in typical ferroelectric relaxor ceramics such as $\text{Pb}(\text{Mg}_{1/2}\text{Nb}_{2/3})\text{O}_3$. The goal of this paper is to compare the magnitudes and temperature dependence of electrostrictive coefficients measured by both direct and converse electrostrictive effects.

2.0 SAMPLE PREPARATION

The procedure for preparing ceramic samples used in this study may be found in an earlier paper⁴. The samples for different measurements were prepared in one batch to obtain uniform properties. X-ray powder diffraction and dielectric measurement indicated that a pure perovskite phase was obtained.

3.0 EXPERIMENTAL RESULTS

3.1 Direct Electrostrictive Measurement

The polarization related electrostrictive coefficients of a ceramics are defined by the following equations:

$$\bar{Q}_{11} = 1/2 \frac{\partial^2 x_1}{\partial P_1^2} \quad (1)$$

and

$$\bar{Q}_{12} = 1/2 \frac{\partial^2 x_2}{\partial P_1^2} \quad (2)$$

where x_1 and x_2 are the longitudinal and transverse induced strains respectively. By plotting the strains as a function of the square of the electric polarization P_1^2 , the values of \bar{Q} can be calculated from the slopes.

Gold electrodes were sputtered onto the faces of the samples and polyimide foil strain gauges (KYOWA, KFR-02-C1-11) were bonded with cement (KYOWA, PC-6) on the appropriate faces of the samples. The electrostrictive strains x_1 and x_2 were measured as a function of electric field (.064 Hz) at temperatures ranging from -60°C to 100°C. The longitudinal electrostrictive strain as a function of electric field for five selected temperatures is shown in Figure 1. The induced electric polarization was measured at .064 Hz using a Sawyer-Tower circuit. The polarization as a function of electric field at five selected temperatures is shown in Figure 2. For a precise determination

of Q coefficients, the strain signal from strain amplifier and polarization signal from a Sawyer-Tower circuit were simultaneously recorded and read by a digital oscilloscope (Nicolet 240A). A plot of strain as a function polarization is shown in Figure 3 for five selected temperatures. It is evident that the quadratic relationship between strain and polarization is excellent. The \bar{Q}_{11} and \bar{Q}_{12} values were calculated by a least square "line fitting" computer program. The \bar{Q}_{11} and \bar{Q}_{12} coefficients as a function of temperature are shown in Figure 4. It is evident that the electrostrictive coefficients do not change significantly through the relaxation temperature $\bar{Q}_{11} = 1.90 \pm .10 \cdot 10^{-2} \text{ m}^4/\text{C}^2$, $\bar{Q}_{12} = .61 \pm .03 \cdot 10^{-2} \text{ m}^4/\text{C}^2$.

3.2 Converse Electrostrictive Measurement

By using the Maxwell relationship, equation (1) is transformed as follows:

$$Q_{11} = -1/2 \frac{\partial X_1}{\partial X_1} \quad (3)$$

where X_1 is the uniaxial stress and X_1 is the reciprocal dielectric susceptibility. If the reciprocal susceptibility X_1 is plotted against the uniaxial stress X_1 , the Q_{11} can be calculated from the slope of the linear relationship between X_1 and X_1 .

To measure the uniaxial pressure dependence of permittivity, the dc compressometer¹ was used to apply uniaxial pressure. A general radio 1621 capacitance bridge was used to measure capacitance change at room temperature. Temperature was varied by a powerstat and monitored by a digital thermometer. An automatic capacitance bridge (HP 4270A) was used to measure capacitance change above room temperature. A disk-shaped sample ($D = 2.30 \text{ cm}$, $T = 0.5510 \pm .0003 \text{ cm}$) was used for our investigation. The stress transmitting ram extenders were made of $\text{Pb}(\text{Mg}_{1/2}\text{Nb}_{2/3})\text{O}_3$ to establish true uniaxial pressure at the sample. The uniaxial pressure dependence of dielectric stiffness change

measured under an AC frequency of 1000 Hz at various temperatures is shown in Figure 5. A linear relationship between dielectric stiffness and uniaxial pressure is evident. The \bar{Q}_{11} values can be, therefore, calculated directly from the slopes. The Q_{11} values thus obtained as a function of temperature are shown in Figure 6. An increase of Q_{11} values with increasing temperature can be observed. The \bar{Q}_{11} values increases from $1.77 \pm 0.03 \cdot 10^{-2} \text{ m}^4/\text{C}^2$ at room temperature to $2.15 \pm 0.05 \cdot 10^{-2} \text{ m}^4/\text{C}^2$ at 70°C . The frequency dependence of the \bar{Q}_{11} value at room temperature is shown in Figure 7, an increase of Q_{11} value with decreasing frequency is present but is not pronounced. These effects will be discussed in the next section.

4.0 DISCUSSION

It is evident from the data presented that in ceramic samples of $\text{PbMg}_{1/3}\text{Nb}_{2/3}\text{O}_3$ prepared so as to avoid pyrochlore contamination \bar{Q}_{11} measured by the direct method agrees closely with \bar{Q}_{11} measured by the converse method, i.e.

by the direct method

$$\bar{Q}_{11} = 1.90 \pm 0.1 \cdot 10^{-2} \text{ m}^4/\text{C}^2 \quad \bar{Q}_{12} = 0.61 \pm 0.03 \cdot 10^{-2} \text{ m}^4/\text{C}^2$$

and by the converse method

$$\bar{Q}_{11} = 1.77 \pm 0.03 \cdot 10^{-2} \text{ m}^4/\text{C}^2$$

Single crystal values for the Q constants have been given by Uchino

$$Q_{11} = 2.50 \pm 0.14 \cdot 10^{-2} \text{ m}^4/\text{C}^2$$

$$Q_{12} = -0.96 \pm 0.02 \cdot 10^{-2} \text{ m}^4/\text{C}^2$$

and

$$Q_h = 0.60 \pm 0.08 \cdot 10^{-2} \text{ m}^4/\text{C}^2.$$

If a randomly axed arrangement is assumed in the ceramic, single crystal and ceramic electrostriction can be related as

$$\bar{Q}_{11} = 3/5 Q_{11} + 2/5 Q_{12} + 4/5 Q_{44}$$

$$\bar{Q}_{12} = 1/5 Q_{11} + 4/5 Q_{12} - 2/5 Q_{44}$$

If values of Q_{11} and Q_{12} are taken to be

$$Q_{11} = 2.60 \cdot 10^{-2} \text{ m}^4/\text{C}^2 \quad \text{within Uchino's experimental error}$$

and $Q_{12} = -0.96 \cdot 10^{-2} \text{ m}^4/\text{C}^2 \quad \text{as in Uchino's work}$

then both equations 1 and 2 can be satisfied with $Q_{44} = 0.905 \cdot 10^{-2} \text{ m}^4/\text{C}^2$.

Similarly for \bar{Q}_h in the ceramic

$$\bar{Q}_h = \bar{Q}_{11} + 2\bar{Q}_{12} = 0.68 \cdot 10^{-2} \text{ m}^4/\text{C}^2$$

in good agreement with the single crystal values.

As a further check \bar{Q}_{44} should be given by

$$\bar{Q}_{44} = \frac{1}{5} Q_{11} - \frac{1}{5} Q_{12} + \frac{3}{5} Q_{44}.$$

which taking the single crystal values above gives

$$\bar{Q}_{44} = 1.255 \times 10^{-2} \text{ m}^4/\text{C}^2$$

Since, however, the unpolarized ceramics is isotropic

$$\begin{aligned} \bar{Q}_{44} &= \frac{1}{2} (\bar{Q}_{11} - \bar{Q}_{12}) \\ &= 1.255 \cdot 10^{-2} \text{ m}^4/\text{C}^2 \end{aligned}$$

For the single crystal, however

$$\frac{1}{2} (Q_{11} - Q_{12}) = 1.78 \cdot 10^{-2} \text{ m}^4/\text{C}^2.$$

which as expected is quite different from the single crystal

$$Q_{44} = 0.905 \cdot 10^{-2} \text{ m}^4/\text{C}^2.$$

Since PMN is a relaxor ferroelectric and as evidenced from recent thermal expansion studies $\sqrt{P^2}$ is nonzero in the temperature range of these measurements, it is perhaps surprising to find such good agreement with near temperature independent electrostriction. It may be noted, however, that at low temperatures, after application of a bias PMN has rhombohedral symmetry. Thus, polarization fluctuations above T_c the dielectric maximum will be along $\langle 111 \rangle$ directions.

Thus we expect Q_{11} and Q_{12} to be normal. Q_{44} would be anomalously small if 180° reorientation of P in the polar micro-regions was the dominant process. From the good agreement observed, we speculate then that 180° rotation is difficult and that reorientation by non 180° motions is preferred. Clearly to confirm this hypothesis, it will be desirable in the future to make direct measurement of Q_{44} on 111 cut single crystals.

ACKNOWLEDGEMENT

We wish to thank Mrs. Qiyue for her assistance in the measurement and preparation of the data. Gratitude should also be extended to Mr. Umesh Kumar and Mr. Yueming Sun for their suggestions and help in both direct and converse electrostrictive measurements, respectively. Partial support for this work is acknowledged from Air Products and Chemicals on contract 063-166-P-A.

REFERENCES

1. Z.Y. Meng and L.E. Cross, J. Appl. Phys. 52(2) 488 (1985).
2. K. Uchino, S. Nomura, L.E. Cross, S.J. Jang and R.E. Newnham, J. Appl. Phys. 51(2) 1142 (1980).
3. J. Kuwata, K. Uchino and S. Nomura, Jpn. J. Appl. Phys. 19, 2099 (1981).
4. S.L. Swartz and T.R. Shrout, Mat. Res. Bull. 17, 1245 (1982).
- ~~5.~~ V.A. Bokov and I.E. Mylnikova, Soviet Physics - Solid State 3(3) 613 (1961).
- ~~6.~~ G.A. Smolenskii, V.A. Isupov, A.A. Agranovskaya and S.N. Popov, Fiz. Tverd. Tela 2, 2906 (1960).
- ~~7.~~ K. Uchino and L.E. Cross, Jpn. J. Appl. Phys. 19, L173 (1980).

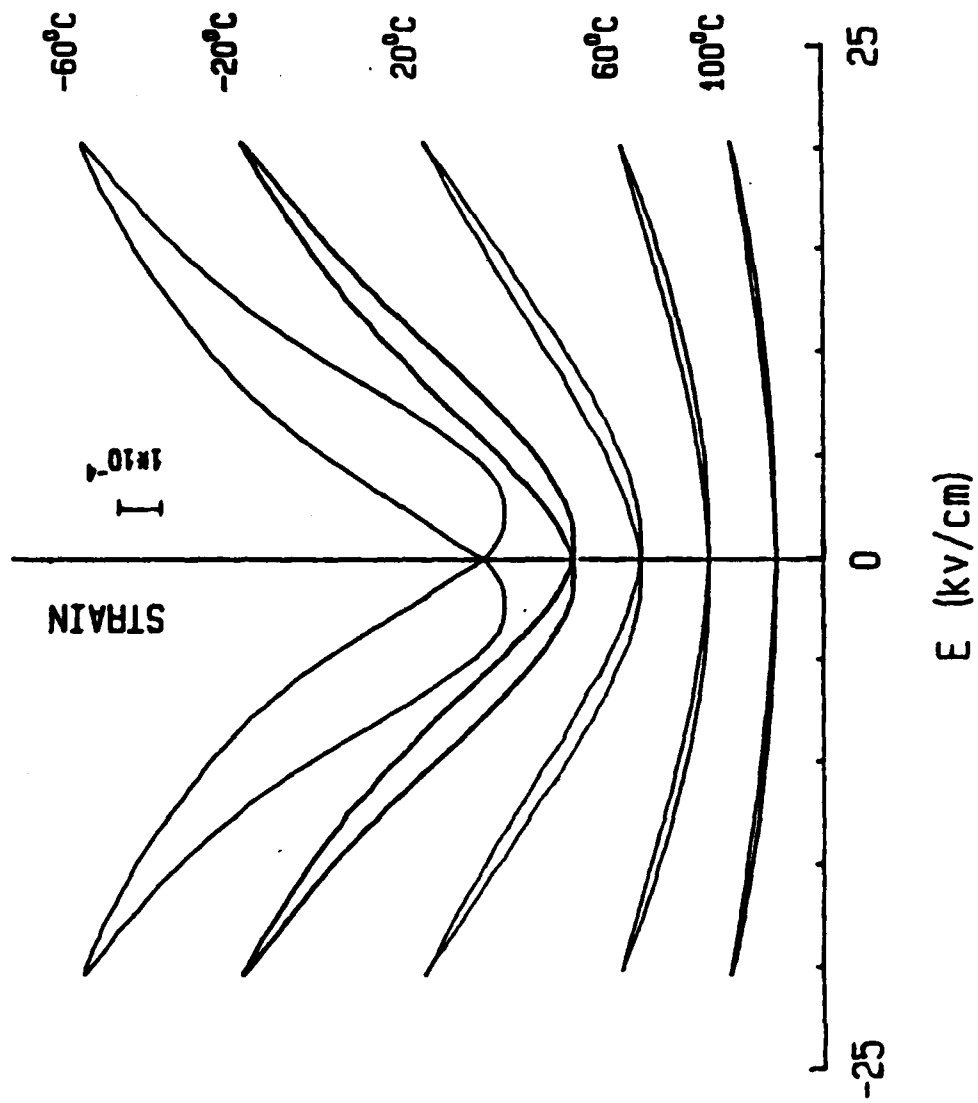


FIG.1 Electric field dependence of longitudinal strain at selected temperatures for $\text{Pb}(\text{Mg}_{1/2}\text{Nb}_{1/3})\text{O}_3$ ceramics

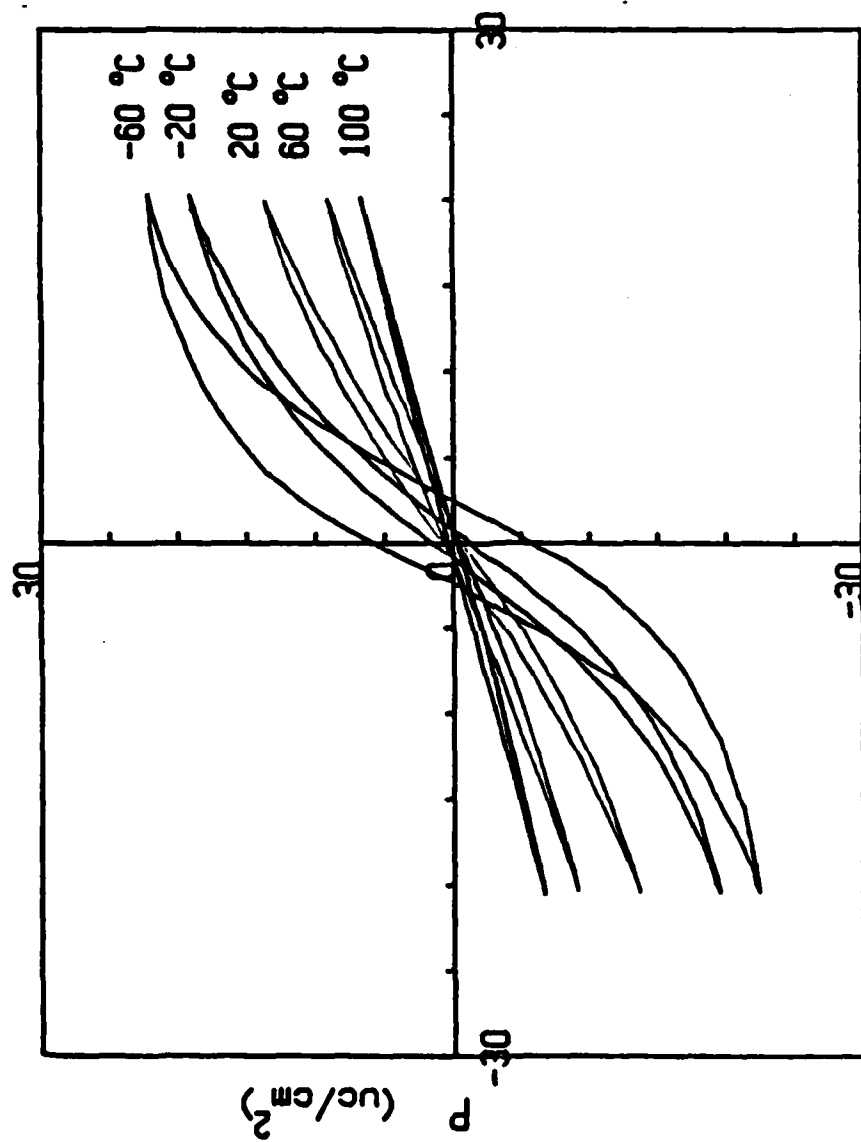


FIG.2 Electric field dependence of the induced polarization at selected temperatures for $\text{Pb}(\text{Mg}_{1/2}\text{Nb}_{1/3})\text{O}_3$ ceramics

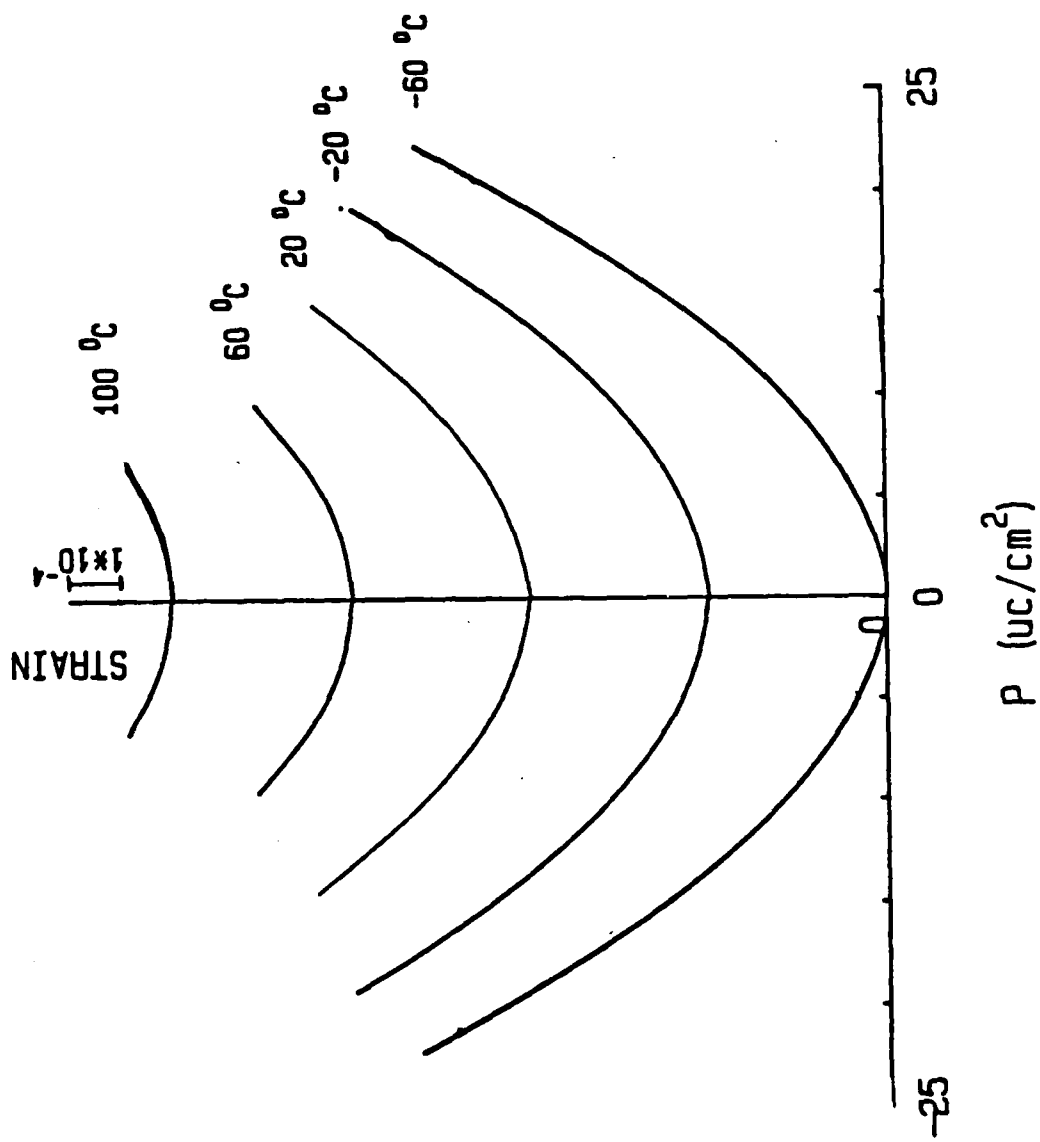


FIG.3 Polarization dependence of longitudinal strain at selected temperatures for $\text{Pb}(\text{Mg}_{1/2}\text{Nb}_{1/3})\text{O}_3$ ceramics

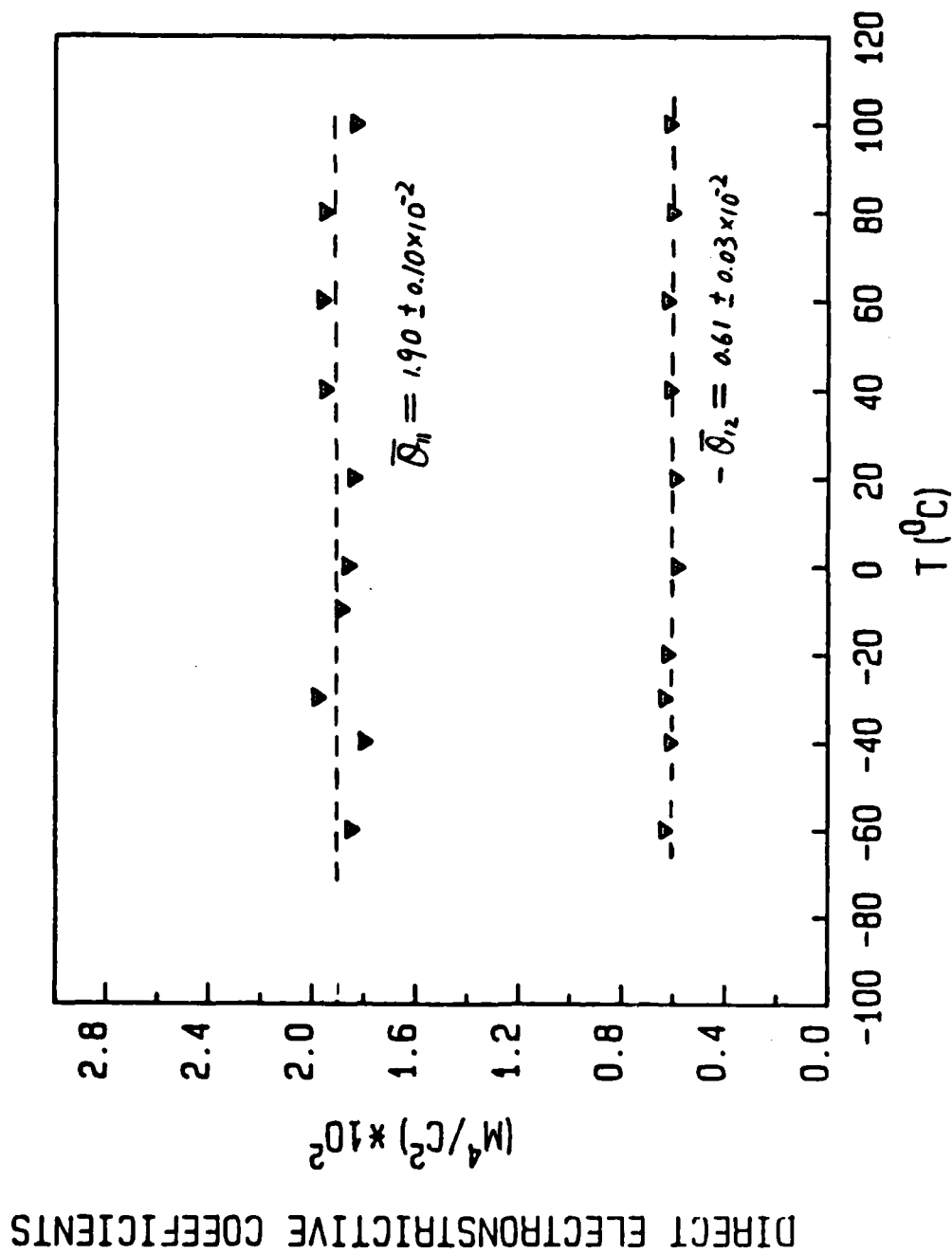


FIG.4 Temperature dependence of direct electrostrictive coefficients
for $\text{Pb}(\text{Mg}_{1/2}\text{Nb}_{1/3})_2\text{O}_3$ ceramics

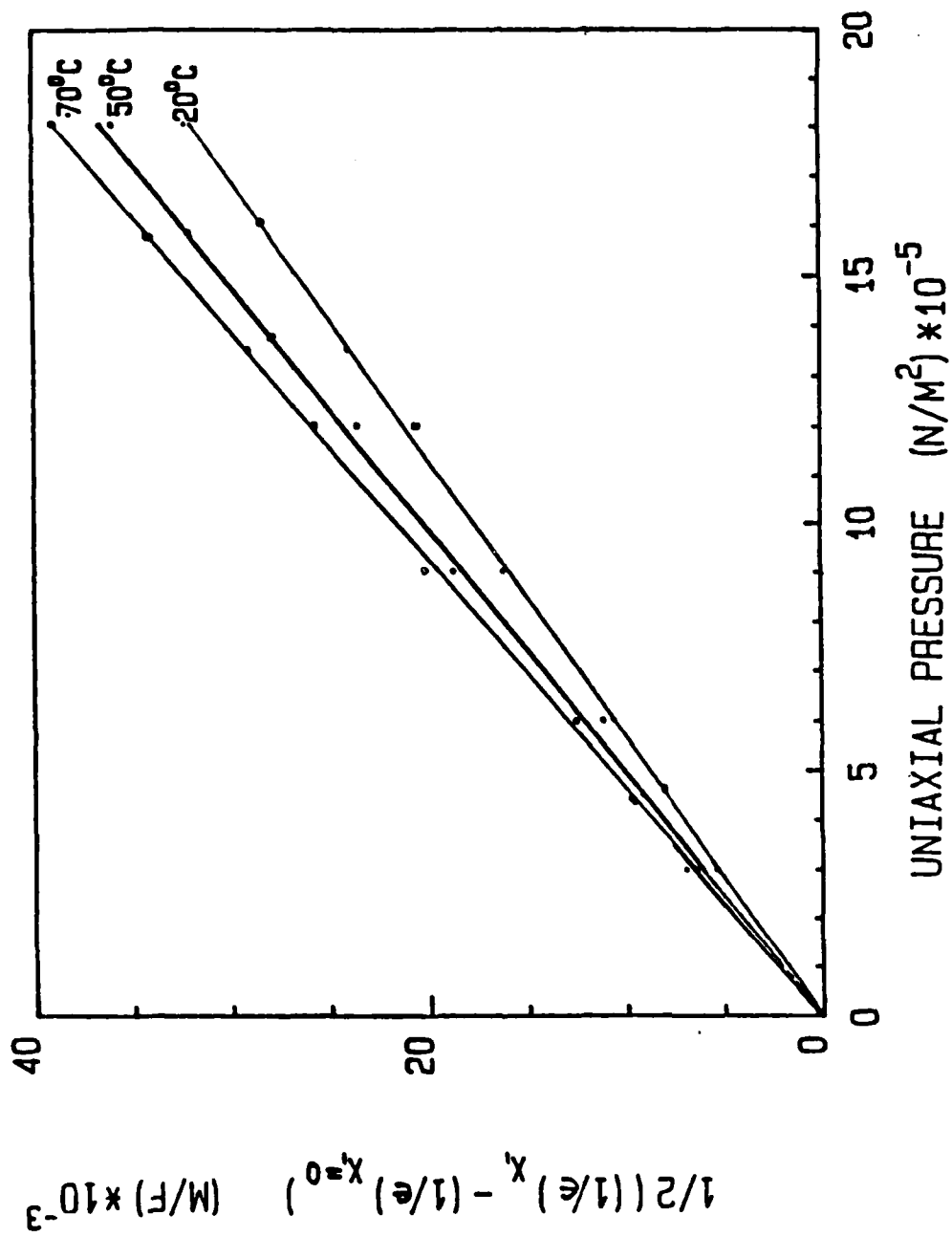


FIG.5 Dielectric stiffness change as a function of uniaxial pressure
at different temperature for $\text{Pb}(\text{Mg}_{1/2}\text{Nb}_{1/3})\text{O}_3$ ceramics

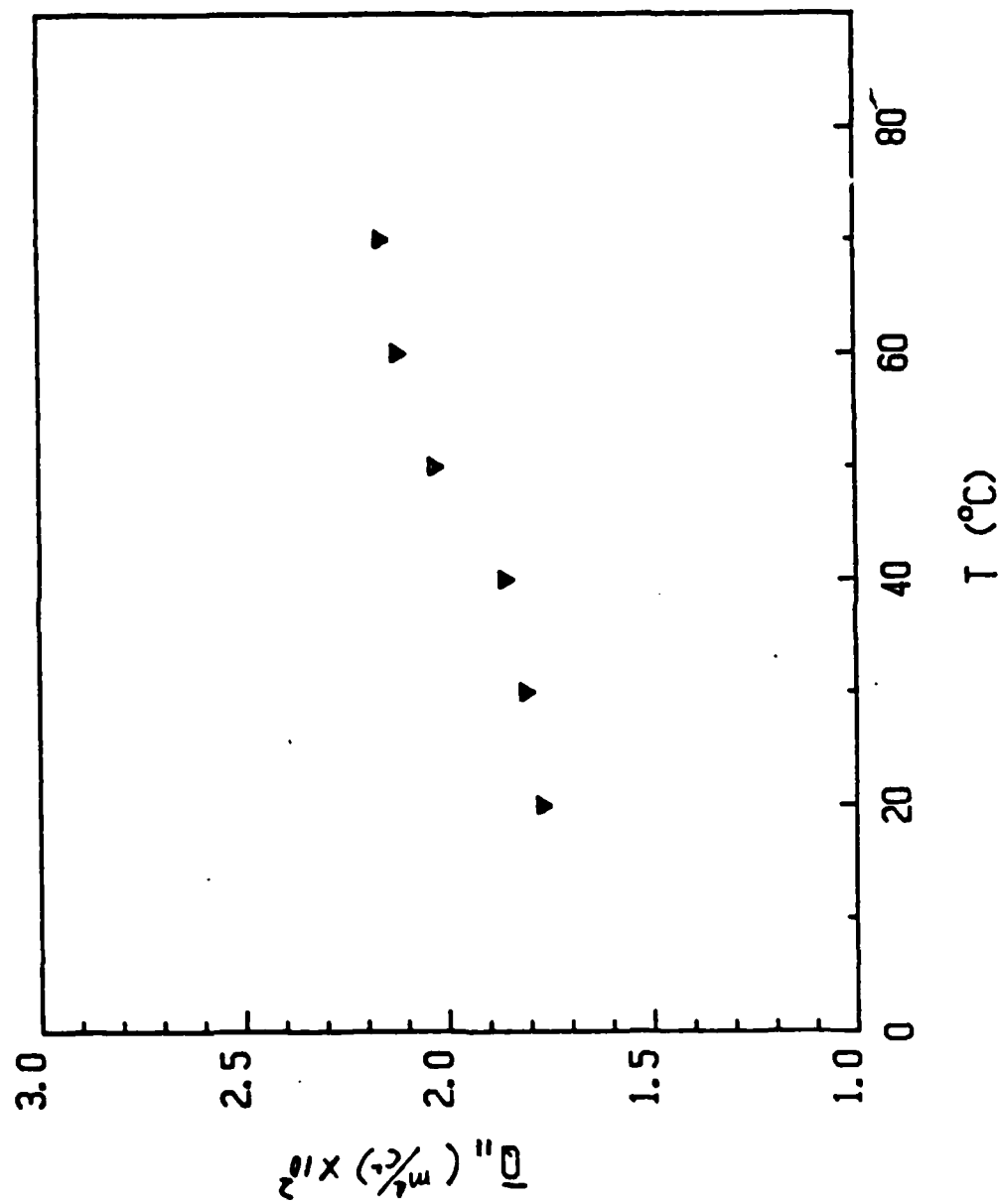


FIG. 6 Temperature dependence of converse electrostrictive coefficient Q_{11} for $\text{Pb}(\text{Mg}_{1/2}\text{Nb}_{1/3})\text{O}_3$ ceramics

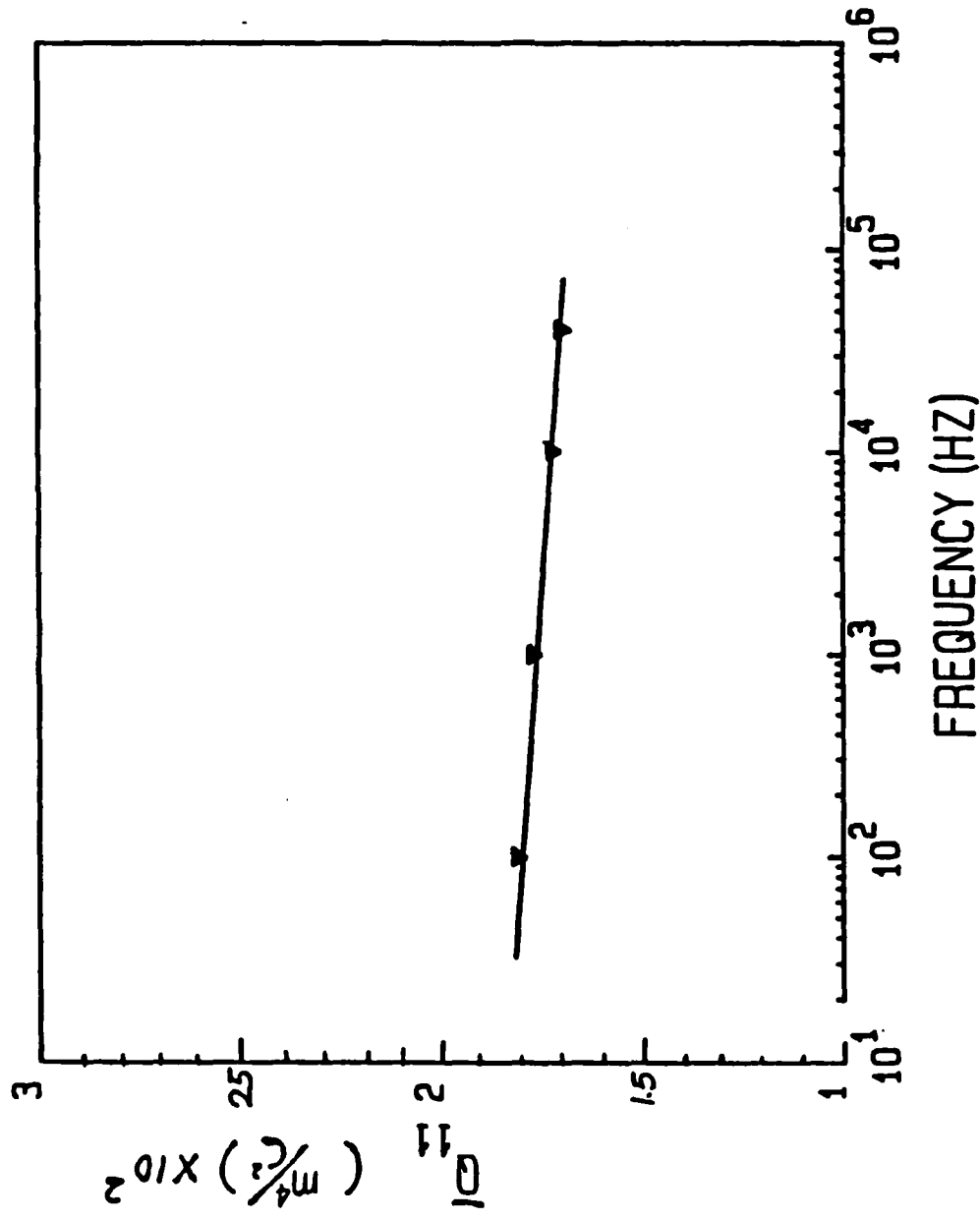


FIG. 7 Frequency dependence of converse longitudinal electrostrictive coefficients at room temperature for $\text{Pb(Mg}_{1/2}\text{Nb}_{2/3})\text{O}_3$ ceramics

ANTIFERROELECTRIC TO FERROELECTRIC SWITCHING IN LEAD
ZIRCONATE TITANATE STANNATE CERAMICS

Wuyi Pan, P. Moses and L.E. Cross

ANTIFERROELECTRIC TO FERROELECTRIC SWITCHING IN LEAD
ZIRCONATE TITANATE STANNATE CERAMICS

WuYi Pan, P. Moses and L.E. Cross
Materials Research Laboratory
The Pennsylvania State University
University Park, PA 16802, USA

ABSTRACT

Several compositions in the modified lead zirconate titanate stannate family known from earlier studies at Clevite Corporation [1] to exhibit switching from an antiferroelectric to a ferroelectric state under high electric field have been explored from the perspective of potential utility as charge controlled volume change transducers. This study has concentrated upon measurement of the magnitude of the induced volume change, the reproducibility under cyclic fields, degradation effects under repeated switching and a preliminary assessment of switching speed.

1. INTRODUCTION

Ceramics in the lead zirconate titanate stannate family have been studied extensively in the past 20 years for many actual and potential applications in energy conversion [1,2]. The interest stems from the fact that as is evident in Figure 1, there is a region in the ternary diagram at room temperature where antiferroelectric and ferroelectric phases abut and thus, for these compositions, must be of closely similar free energy. Since the different antiferroelectric and ferroelectric phases are all distinguished by small ($\sim 0.2 \text{ \AA}$) displacements of ions from a common higher temperature cubic prototypic form, switching between forms can be accomplished without breaking any energetic bonds. As the ferroelectric domains carry a large spontaneous electric polarization and the antiferroelectric are centric, it is not surprising that antiferroelectric forms close to the bounding composition, can be switched ferroelectric under high electric field. Similarly also as the

antiferroelectric arrangement is more compact than the ferroelectric counterpart, one may expect ferroelectric compositions close to the boundary to invert to antiferroelectric under suitable hydrostatic or uniaxial stress.

Pressure switching has been very extensively investigated. Upon inversion to the antiferroelectric form, a poled ferroelectric ceramic releases all polarization charge and so can supply very high instantaneous currents of voltages. Unfortunately, since the major application for such "batteries" is in fusing or ordnance of all types, much of the more detailed and interesting switching work is not accessible in the open literature. In some applications, depolarization is by an explosively driven shock front and since the charge appears before the sample disintegrates, one may speculate that the displacive phase change is very fast under these extreme conditions.

For the electric field driven phase change, the first systematic studies were at Clevite Laboratories in the 1960's [3,4] to explore the use of phase change compositions in capacitive energy storage. More recently [5,6], interest has begun to focus upon the electrostriction phenomenon in antiferroelectrics and the possible use of antiferroelectric ferroelectric switching in transduction. Here contrary to expectation, preliminary studies have suggested that the phase change under electric drive is very slow, and thus would not be of major interest [6].

It was the purpose of the studies reported here to fabricate several of the compositions shown in the original Clevite study to have electric switchability. To measure the strains s_{11} , s_{22} , s_{33} induced by the switchover, and the corresponding polarization changes in the ceramic. To explore polarization switching up to frequencies of order 10 Hz where useful applications can be envisaged but where the data will not be vitiated by temperature change, and to make preliminary measurements under pulse switching

conditions to confirm that the transition becomes fast at suitable electric drive levels.

2. SAMPLE PREPARATION

The compositions chosen for study were:

- (1) $\text{Pb}_{0.99}(\text{Zr}_{0.57}\text{Ti}_{0.05}\text{Sn}_{0.38})\text{Nb}_{0.02}\text{O}_3$
- (2) $\text{Pb}_{0.92}\text{Sr}_{0.05}\text{La}_{0.02}(\text{Zr}_{0.54}\text{Ti}_{0.16}\text{Sn}_{0.30})\text{O}_3$
- (3) $\text{Pb}_{0.92}\text{Mg}_{0.05}\text{La}_{0.02}(\text{Zr}_{0.59}\text{Ti}_{0.11}\text{Sn}_{0.30})\text{O}_3$
- (4) $\text{Pb}_{0.97}\text{La}_{0.02}(\text{Zr}_{0.66}\text{Ti}_{0.09}\text{Sn}_{0.25})\text{O}_3$
- (5) $\text{Pb}_{0.97}\text{La}_{0.02}(\text{Zr}_{0.53}\text{Ti}_{0.12}\text{Sn}_{0.35})\text{O}_3$.

The different compositions were made up from reagent grade mixed oxides by Ultrasonic Powders, Inc., of Plainfield, NJ. Calcining temperatures were in the range 750 to 900°C. Disks 1" in diameter by 0.1" thickness were cold pressed using a small amount of PVA binder and fired at 1350°C in a PbO atmosphere provided by excess PbZrO_3 in a closed container.

For initial electrical studies of the switching characteristics samples were thinned to ~0.15 mm so as to be able to accomplish the necessary field level using our generator which is limited to 1.5 K volts at high current. Electrodes were of sputtered gold, and the coating was thick enough so that edge to edge resistance across the electrode from point probes was less than 0.2 ohms.

Polarization field curves were plotted using a balanced Sawyer Tower network with sweep frequency in the range of 0.1 to 10 Hz.

For the induced strain measurement, a bonded strain guage technique was used for both longitudinal and transverse strain. Attempts to confirm the volume change using x-ray methods were not successful.

To confirm the fast switching which was evident in the lack of frequency dependence of the polarization measured by the Sawyer Tower method, the

Initial study of the switching speed was accomplished simply by increasing the cycling frequency from 0.1 to 1.0 to 10.00 Hz. Surprisingly, there was almost no change in the hysteresis figure, so clearly the transition at these field levels must be much faster than 0.1 seconds quoted by Uchino [6]. Above 10 Hz, there was evidence of some change but clearly the sample was heating due to hysteretic dissipation.

For composition (1), the characteristics are summarized in Table 1, the strain and polarization are both smaller but the switching field E_F is now less than 10 kV/cm.

Since the switching strain are large $\sim 0.25\%$, it is important to check for possible fatigue effects upon repeated switching, and for any evidence of permanent damage such as microcracking, electrode lift off or erosion. To check for such effects, samples of composition (5) which appeared to have optimum switching properties were cycled continuously for two weeks at 10 Hz, i.e. for some $24 \cdot 10^6$ switching strokes, then the transverse strain was re-measured it is evident from Figure 4 that though the switching polarization has been reduced to 50%, the transverse strain is still 77% of the original value. To check for any permanent damage, the samples was re-heated above the Curie temperature and examined again at room temperature. After this treatment, the original polarization and strain values were recovered completely.

To confirm the more rapid switching evident in the 10 Hz polarization curves, switching under step field drive was explored using a very simple relay driven transistor power switch. The rise time for this drive circuit was or order 30μ seconds (Figure 5a). From the switching transient current evident for a drive level of 47 kV/cm (Fig. 5b), it is evident that even at this field level, switching is complete after $\sim 100 \mu$ seconds. Clearly the switching as would be expected for a simple displacive transition is very fast

compared to 0.1 sec and the simple drive circuit used here is inadequate for detailed evaluation.

4. DISCUSSION OF RESULTS

For the composition 5, clear antiferroelectric to ferroelectric switching is obtained which induces a volume change of order 0.25% for an induced polarization level of $30 \mu\text{C}/\text{cm}^2$. These values are in reasonable accord with the volume change measured by Uchino [6] on a similar composition, and confirmed by x-ray measurement. The strain s_{11} is also in quite good agreement with an earlier measurement by Berlincourt [7].

Both the frequency independence of the polarization switching over the range from 0.1 to 10 Hz and the pulse switching data suggest that the switching is fast, and very different to the slow behavior observed by Uchino [6].

Since the antiferroelectric phase change is necessarily first order, it will be most interesting to explore the pulse switching in these compositions more fully so as to ascertain more information about the nucleation and growth of the phases, and their decay under reverse field drive.

In the fatigue measurements, it is puzzling to find that the switching charge Q decays faster than the switched strain. It must be remembered, however, that the volume change is that associated with the phase change is thus not itself electrostrictive, a fact which is evidenced by the observation that both s_{11} and $s_{22} = s_{33}$ are positive strains. If the transducer is to be useful in a charge control mode, it now becomes most important to explore in much more detail the relation between total switched charge and resultant induced strain.

For hydraulic amplification of stroke, it will also be important to explore the volume change induced against substantial back pressures, and the

manner in which both forward and backward switching are modified by such constraint.

Acknowledgement

We wish to thank Mrs. Qiyue for her assistance in the measurements and in the preparation of the data. Support for this work is acknowledged from Air Products and Chemicals on Contract 063-166-P-A.

REFERENCES

1. B. Jaffe, W.R. Cooke, Jr., H. Jaffe. Piezoelectric Ceramics, Academic Press, London, Monographs on Non-Metallic Solids, Editors, J.P. Roberts, P. Popper (1971).
2. D. Berlincourt, H.H. Krueger, B. Jaffe. Phys. Chem. Solids 25, 659 (1964).
3. B. Jaffe. Clevite Corporation Report, OMS 3530-11-55700, (Nov., 1962).
4. L.E. Cross. J. Phys. Soc. Japan 23, 77 (1967).
5. K. Uchino, L.E. Cross, R.E. Newnham. Japan Journal of Applied Physics 19, 425 (1980).
6. K. Uchino, S. Nomura. Ferroelectrics 50, 517 (1983).

Table 1. Summary of Switching and Strain Data for Compositions 1 and 5.

Sample Number	Batch Number	Transition Field kV/cm	Ferroelectric Polarization $\mu\text{C}/\text{cm}^2$	Strain s_{33}	Strain s_{11}	Volume Strain $\Delta V/V$
1	1	9	24	$0.8 \cdot 10^{-3}$	$4.2 \cdot 10^{-4}$	0.16%
	2	8	20			
	3	15	20			
5	1	31	31	$1.5 \cdot 10^{-3}$	$5.7 \cdot 10^{-4}$	0.26%
	2	23	28			
	3	27	27			

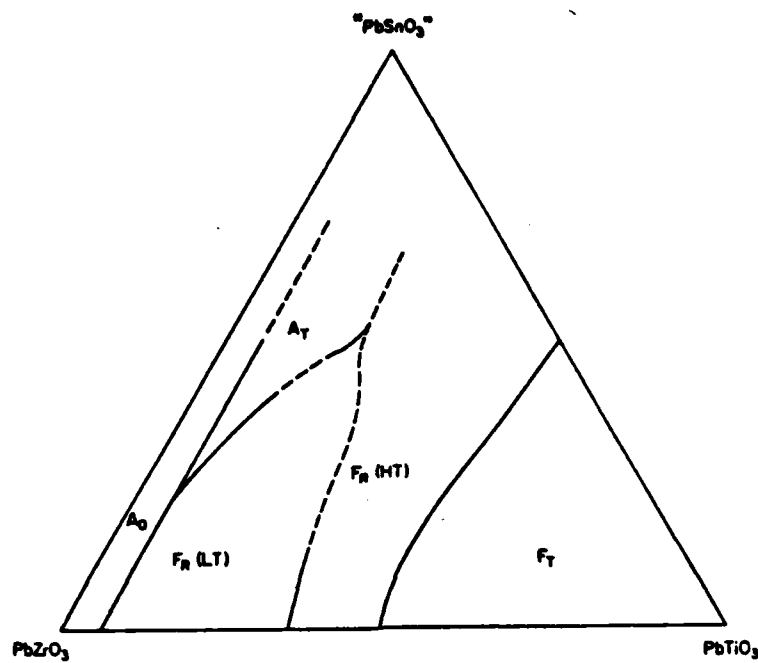


Figure 1. Phase diagram for the $\text{PbZrO}_3\text{:PbTiO}_3$ " PbSnO_3 " solid solution system.
 A_0 is antiferroelectric orthorhombic.
 A_T is antiferroelectric tetragonal.
 $FR(LT)$ is low temperature (multicell) rhombohedral ferroelectric.
 $FR(HT)$ is the high temperature (single cell) rhombohedral ferroelectric.
 F_T is the tetragonal ferroelectric phase.

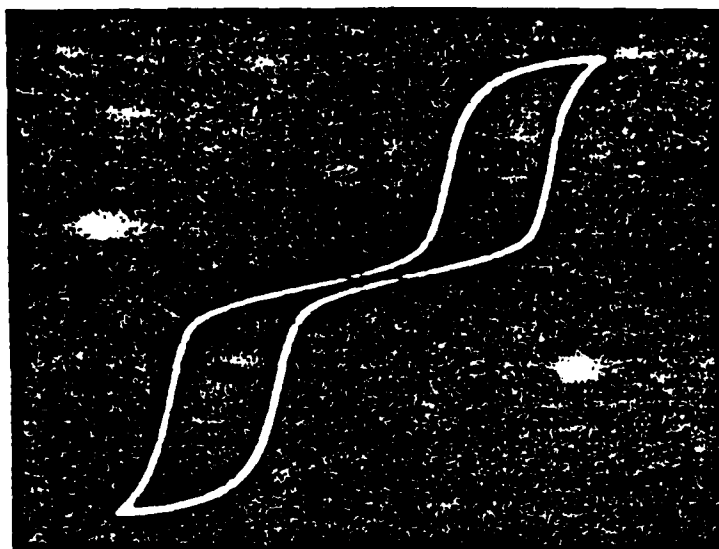


Figure 2a. Composition (5) polarization vs electric field hysteresis E_F 31 kV/cm P_S 31 $\mu\text{C}/\text{cm}^2$.

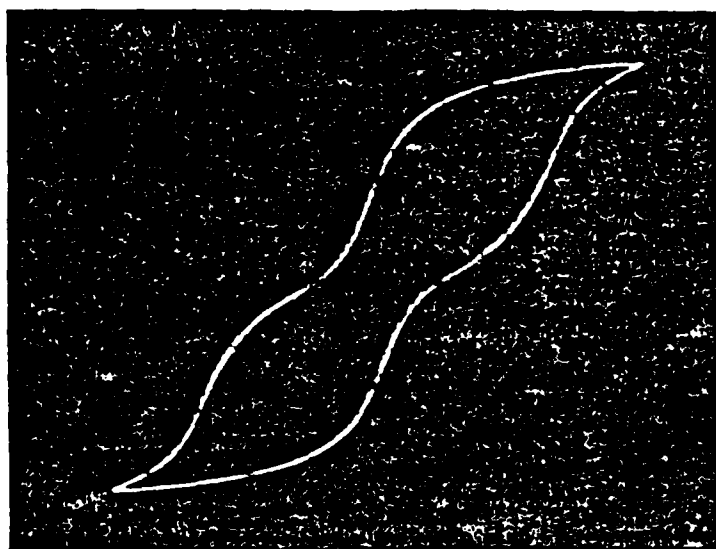


Figure 2b. Composition (1) polarization vs electric field hysteresis E_F 9 kV/cm P_S 24 $\mu\text{C}/\text{cm}^2$.

Longitudinal Strain VS Electrical Field for
 $\text{Pb}_{0.9}\text{La}_{0.02}(\text{Zr}_{0.82}\text{Ti}_{0.12}\text{Sn}_{0.02})\text{O}_3$ Antiferroelectric Ceramics

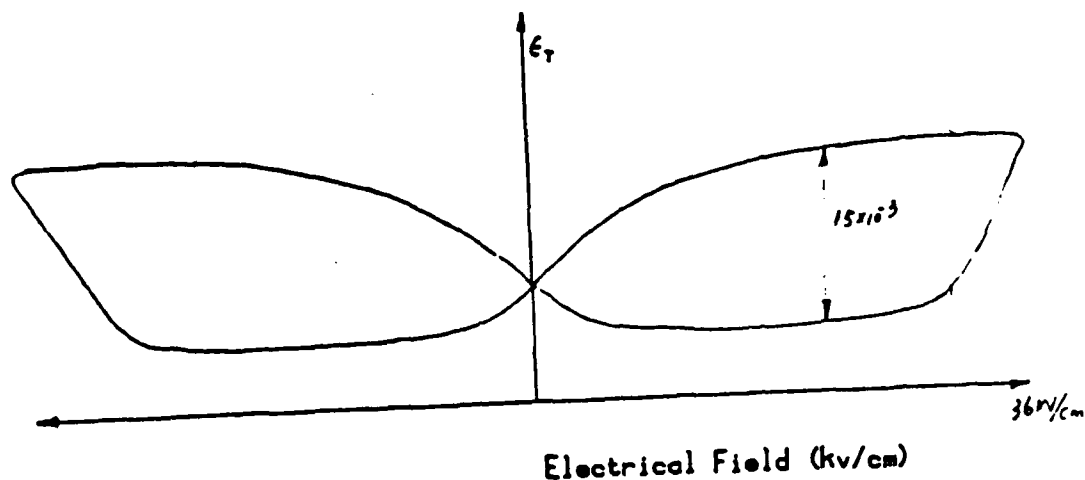


Figure 3a. Longitudinal strain as a function of driving field in composition (5).

Transverse Strain VS Electrical Field for
 $\text{Pb}_{0.9}\text{La}_{0.02}(\text{Zr}_{0.82}\text{Ti}_{0.12}\text{Sn}_{0.02})\text{O}_3$ Antiferroelectric Ceramics

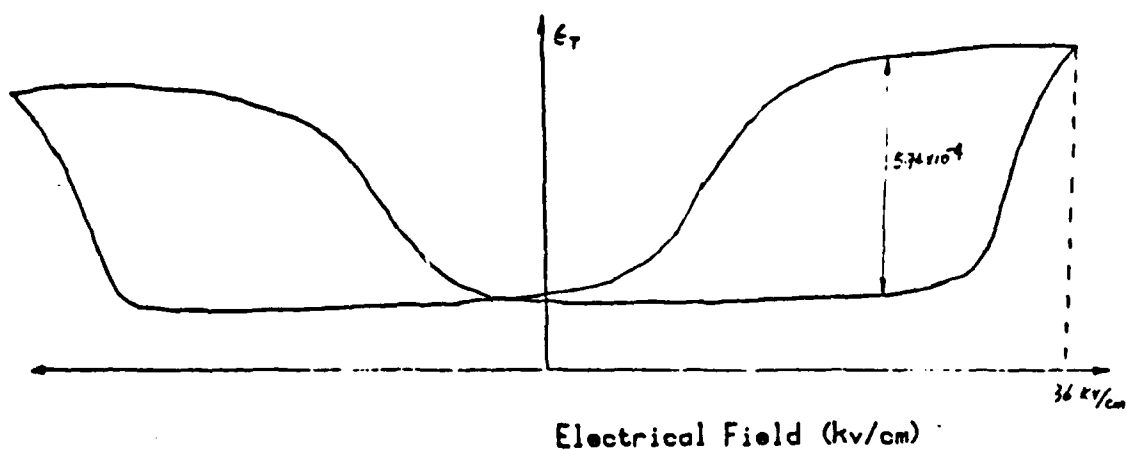


Figure 3b. Transverse strain as a function of driving field in composition (5).



Figure 4a. Polarization switching after $24 \cdot 10^6$ cycles at 10 Hz.

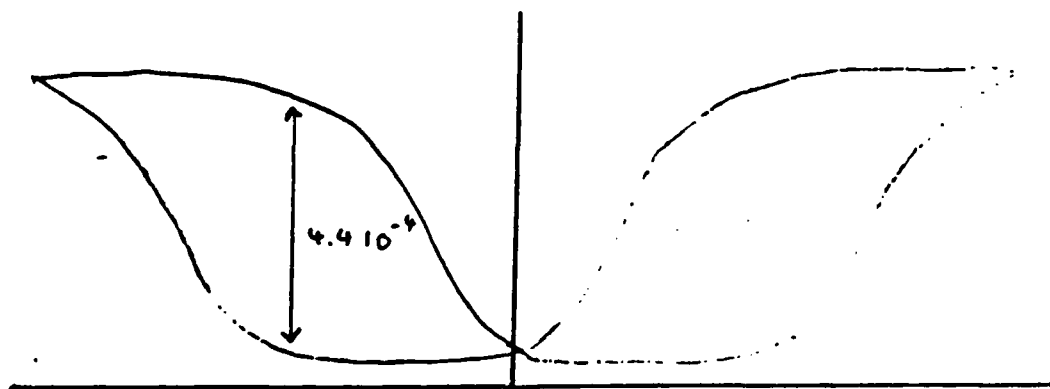


Figure 4b. Strain switching after $24 \cdot 10^6$ cycles at 10 Hz.

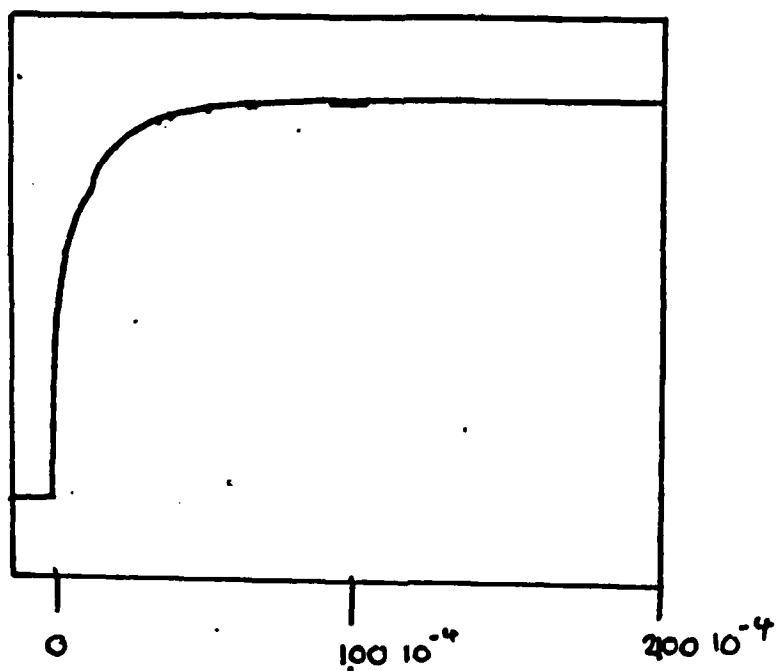


Figure 5a. Risettime of switching voltage.

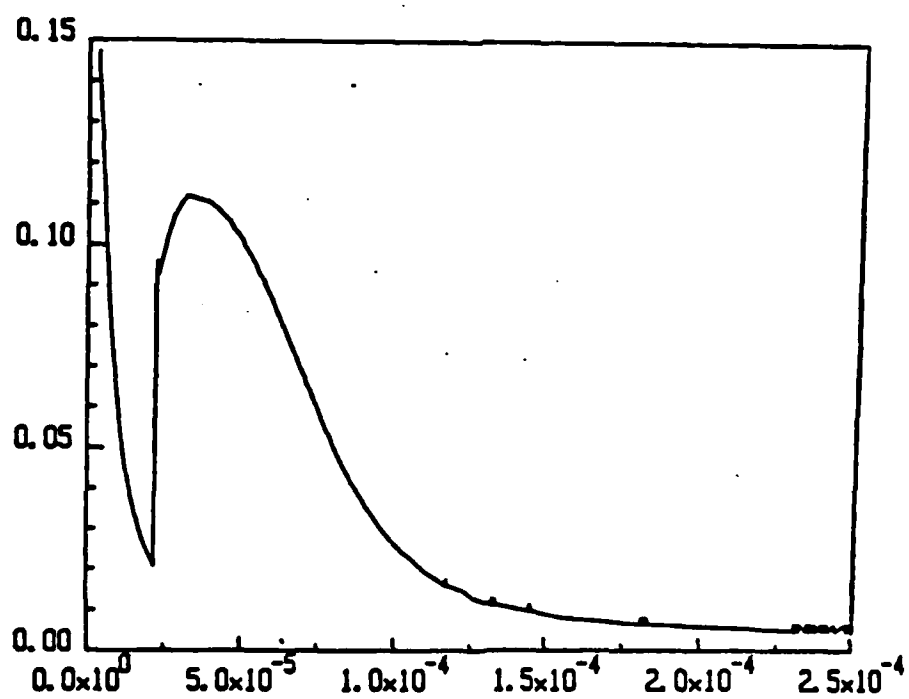


Figure 5b. Switching current in composition (5) at driving field of 47 kV/cm with time dependence of 5a.

FERROELECTRIC PHASE TRANSITIONS
IN PZT WITH OCTAHEDRAL TILTS

T.R. Halemane, M.J. Huan, L.E. Cross and R.E. Newnham

Ferroelectric Phase Transitions in PZT with Octahedral Tilts

T. R. HALEMAN[†], M. J. HAUN^{*}, L. E. CROSS^{*}
and R. E. NEWNHAM^{*}

[†]Physics Department, State University College, Fredonia, New York 14063, U.S.A.

^{*}Materials Research Laboratory, The Pennsylvania State
University, University Park, Pennsylvania 16802, U.S.A.

The lead zirconate-titanate solid solution exhibits ferroelectric phase transitions involving tilts in its oxygen octahedral chains. A theory based on the Landau-Ginsburg-Devonshire formalism has been developed and numerical calculations have been made for the $\text{Pb Zr}_{0.9}\text{Ti}_{0.1}\text{O}_3$ system. This approach involves expansion of the Gibbs free energy as a power series with polarization and tilt angle as order parameters. The results support the view that transitions are of first order in this system.

§1. Introduction

The solid solution $\text{Pb Zr}_{1-x}\text{Ti}_x\text{O}_3$ between antiferroelectric Pb ZrO_3 and ferroelectric Pb TiO_3 , named PZT, has been used extensively in the electronics industry and is of considerable theoretical interest. PZT has the perovskite structure and it exhibits phase transitions involving tilts in the oxygen octahedral chains. As seen in the PZT phase diagram,¹⁾ Figure 1, for mole fractions of Pb TiO_3 in the range 0.06 to 0.37, a phase transition from a higher temperature rhombohedral ferroelectric phase $F_{R(HT)}$ to a lower temperature rhombohedral ferroelectric phase $F_{R(LT)}$ is observed. The $F_{R(LT)}$ phase has the oxygen octahedral chain twisted, with neighboring corner-linked octahedra tilted in opposite directions. These tilts are about the [111] axis and are denoted by $a^-a^-a^-$ in the notation of Glazer.²⁾

A thermodynamic phenomenological theory³⁾ based on the Landau-Ginsburg-Devonshire approach can be developed to explain phase transitions with tilts in the oxygen octahedra. This is explained below and the theory is applied to the $\text{Pb Zr}_{0.9}\text{Ti}_{0.1}\text{O}_3$ composition.

§2. Phenomenology

Applying the first law of thermodynamics for a polarizable, deformable solid with tiltable octahedra sub-

ject to an electric field E , stress field X and a tilting torque τ , we can write assuming reversibility and extending Devonshire's treatment⁴⁾

$$dU = TdS + EdP + Xdx + \tau d\theta \quad (1)$$

where U is the internal energy, T is the temperature, S is the entropy, x is the strain and θ is the angle of octahedral tilt. The elastic Gibbs energy G can then be written in differential form

$$dG = -SdT + EdP - xdx + \tau d\theta \quad (2)$$

making it a function of T , P , X and θ . At constant temperature and zero stress conditions, we can expand G as a power series in θ and P . For a centrosymmetric paraelectric state, the odd power terms will vanish in the expansion.

Second Order Transitions:

Neglecting terms higher than the fourth powers we write

$$G = G_0 + \frac{1}{2}g_2\theta^2 + \frac{1}{4}g_4\theta^4 + \frac{1}{2}f_2P^2 + \frac{1}{4}f_4P^4 + \frac{1}{2}d\theta^2P^2 \quad (3)$$

Assuming $g_4 > 0$, $f_4 > 0$ and

$$g_2 = \gamma(T - T_\theta), \quad f_2 = \gamma_P(T - T_P) \quad (4)$$

and requiring that G be a stable minimum in the equilibrium state with values θ , and P , for θ and P , we find that four phases are possible: Phase A ($\theta=0$, $P=0$), Phase B ($\theta=0$, $P \neq 0$), Phase C ($\theta \neq 0$, $P=0$) and Phase D ($\theta \neq 0$, $P \neq 0$).

In $\text{Pb Zr}_{0.9}\text{Ti}_{0.1}\text{O}_3$, the transition sequence is $A \rightarrow B \rightarrow D$. Experimental data are available⁵⁾ for polarization (P_r) and dielectric constant (ϵ_r) at different temperatures. We derive the following temperature dependencies for P_r and ϵ_r in phases A, B, D:

$$P_r = \begin{cases} 0 & \text{in A} \\ \alpha(T_P - T) & \text{in B} \\ \beta(T_r - T) & \text{in D} \end{cases} \quad (5)$$

$$\frac{1}{\epsilon_0(\epsilon_r - 1)} = \begin{cases} \gamma(T - T_\theta) & \text{in A} \\ 2\gamma_P(T_P - T) & \text{in B} \\ 2f_4\beta(T_r - T) & \text{in D} \end{cases} \quad (6)$$

Here α , β , T_r , T_θ are constants that are functions of the

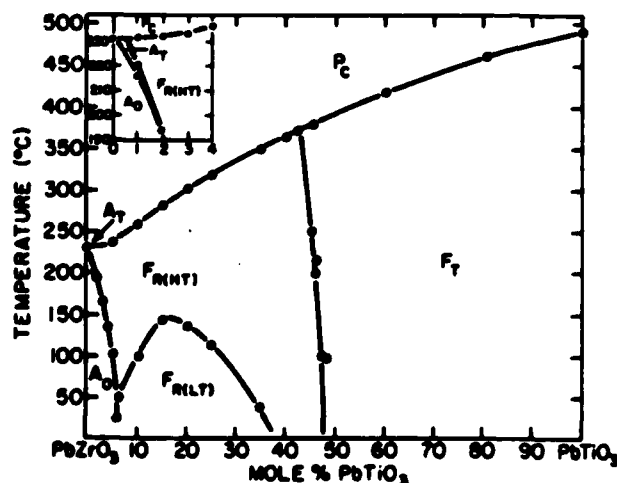


Fig. 1. $\text{Pb Zr}_{1-x}\text{Ti}_x\text{O}_3$ phase diagram (see ref. 1).

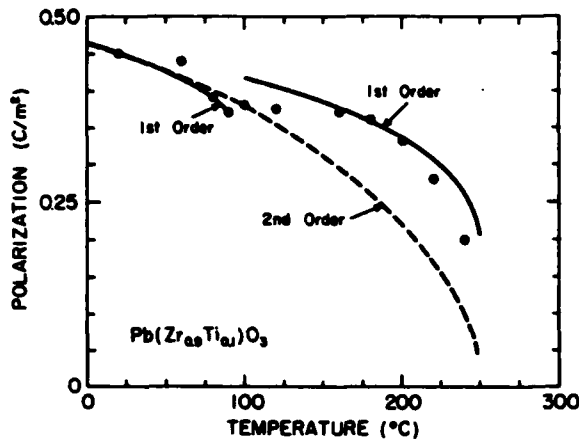


Fig. 2. The spontaneous polarization P_s is plotted versus temperature T . The solid circles denote the experimental curve, the dashed lines show the results from our second order transition calculation and the solid line represents our calculation using the first order transition theory.

expansion coefficients occurring in eq. (3). We determine the constants appearing in eqs. (5) and (6) by comparison with experimental data at a few temperatures and then plot P_s vs T , and ϵ_R vs T curves shown by the dashed lines in figures 2 and 3. The solid circles denote the experimental curves.

First Order Transitions:

Using only the minimum number of terms needed for first-order transitions, we write

$$G = G_0 + \frac{1}{2} g_2 \theta^2 + \frac{1}{4} g_4 \theta^4 + \frac{1}{2} d \theta^2 P^2 + \frac{1}{2} f_2 P^2 + \frac{1}{4} f_4 P^4 + \frac{1}{6} f_6 P^6 \quad (7)$$

Assume eq. (4) for f_2 and g_2 and in addition that $g_4 > 0$, $f_6 > 0$, $f_4 < 0$ so as to get stable energy minima and first order transitions. Once again four phases A, B, C, D are possible as before but only A, B and D are of interest in PZT. The following expressions for the temperature dependencies of P_s and ϵ_R in phases A, B and D can be derived,⁶ from (7)

$$P_s^2 = \begin{cases} 0 & \text{in A} \\ \alpha_B [1 + \sqrt{1 - \beta_B (T - T_P)}] & \text{in B} \\ \alpha_D [1 + \sqrt{1 - \beta_D (T - T_i)}] & \text{in D} \end{cases} \quad (8)$$

$$\frac{1}{\epsilon_0(\epsilon_R - 1)} = \begin{cases} \gamma_P (T - T_P) & \text{in A} \\ 2\gamma_P (T_P - T) + \frac{2\gamma_P}{\beta_B} [1 + \sqrt{1 - \beta_B (T - T_P)}]^2 & \text{in B} \\ \frac{4\alpha_D \gamma_P}{\alpha_B \beta_B} (2\alpha_D - \alpha_B) [1 + \sqrt{1 - \beta_D (T - T_i)}] - \frac{\alpha_D \beta_D (T - T_i)}{(2\alpha_D - \alpha_B)} & \text{in D} \end{cases} \quad (9)$$

The constant parameters α_B , β_B , α_D , β_D , T_i are functions of the coefficients in the expansion for G . The A \rightarrow B tran-

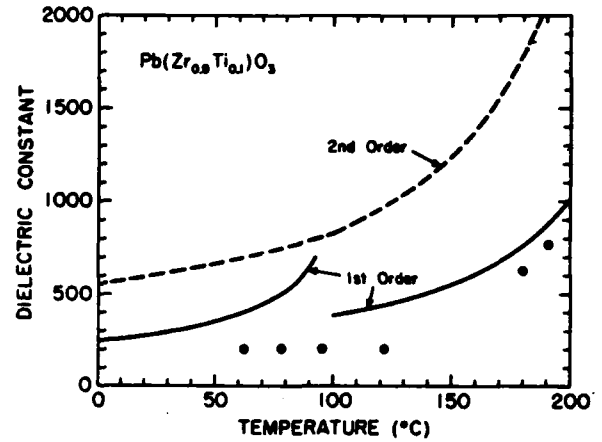
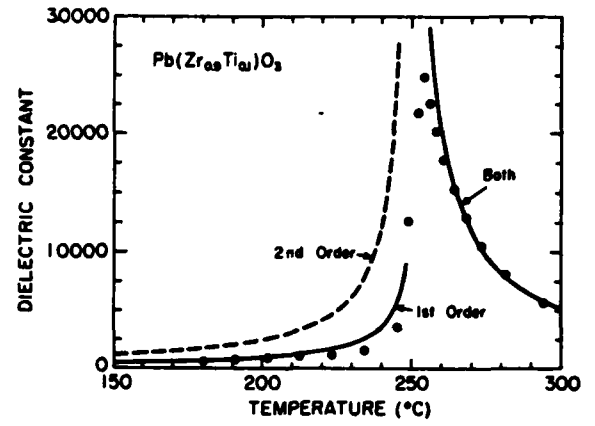


Fig. 3. The dielectric constant ϵ_R is plotted versus temperature. The solid circles, dashed lines and solid lines are experimental, second order and first order transition calculations respectively.

sition will occur at temperature T_c where the Gibbs energies of the two phases cross. Then

$$T_c = T_P + (3/4)\beta_B$$

We determine the constants in eqs. (8) and (9) by comparison with experimental data and then plot P_s and ϵ_R as functions of temperature. These are given by the solid curves in figures 2 and 3. The A \rightarrow B transition temperature T_c was 250.4°C by calculation and it seems to agree well with the available experimental data.

§3. Discussion

We have developed a phenomenological theory for phase transitions in perovskites involving tilts of the oxygen octahedra by considering the polarization and the octahedral tilt angle as the order parameters in an expansion for the Gibbs free energy. The theory is applied to the $\text{Pb(Zr}_{0.9}\text{Ti}_{0.1}\text{O}_3)$ system. The second order transition calculations while producing the general nature of the transitions correctly, do not do as well as the first order calculations. The available experimental data used here on the PZT single crystals may not be of high accuracy due to difficulties associated with growing such crystals. Also, our calculations consider only the minimum number of terms needed in the Gibbs free energy expansion to produce first order transitions, and we have neglected tensorial effects to keep calculations simple at

this stage of development. Considering all these, it is fair to say that there is good agreement between theory and experiment, as seen in the figures. A more elaborate calculation is being developed and results will be available later. Extensions to systems where the polarization direction and the direction of the tilt axis may change during the transitions, and to cases where tilts of successive octahedra along an axis may have either the same or opposite sense of tilt²⁾ will also be made in the future.

References

- 1) B. Jaffe, W. R. Cook and H. Jaffe: "*Piezoelectric Ceramics*" (Academic Press, 1971).
- 2) A. M. Glazer: *Acta Cryst.* **B28** (1972) 3384.
- 3) T. R. Halemane, M. J. Haun, L. E. Cross and R. E. Newnham: *Ferroelectrics* **62** (1985) 149.
- 4) A. F. Devonshire: *Advances in Physics* **3** (1954) 85.
- 5) A. M. Glazer, S. A. Mabud and R. M. Clarke: *Acta Cryst.* **B34** (1978) 1060.
- 6) T. R. Halemane, M. J. Haun, L. E. Cross and R. E. Newnham: (manuscript to be submitted).

A PHENOMENOLOGICAL THEORY FOR THE $\text{PbZrO}_3\text{:PbTiO}_3$ SOLID SOLUTION
SYSTEM WITH THE SPONTANEOUS POLARIZATION AND
OXYGEN OCTAHEDRAL TILT ANGLE AS ORDER PARAMETERS

M.J. Haun, T.R. Halemane, R.E. Hewnham and L.E. Cross

A Phenomenological Theory for the PbZrO_3 : PbTiO_3 Solid Solution System with the Spontaneous Polarization and Oxygen Octahedral Tilt Angle as Order Parameters

M. J. HAUN,* T. R. HALEMANE,* R. E. NEWNHAM*
 and L. E. CROSS*

*Materials Research Laboratory, The Pennsylvania State University,
 University Park, PA 16802

*Physics Department, State University College,
 Fredonia, NY 14063

The Landau-Ginsburg-Devonshire (LGD) theory for the singlecell region of the PZT solid solution system developed by Amin, *et al.*¹⁾ has been extended to include the low temperature rhombohedral phase field, which exhibits compositions having both ferroelectric polarization and tilted oxygen octahedra. An additional term has been added to the elastic Gibbs free energy to account for this tilting. The coefficients of the energy function were determined from a combination of phase boundary requirements and experimental data. The spontaneous polarization and tilt angle were calculated as a function of composition and temperature.

§1. Introduction

A phenomenological theory for the PbZrO_3 : PbTiO_3 (PZT) solid solution system would provide a method of predicting the dielectric, piezoelectric, elastic, and thermal properties for any composition and temperature. The intrinsic single domain properties could then be separated from the extrinsic domain, defect, and phase boundary contributions. The effect of mechanical and electrical boundary conditions on the properties and phase stabilities could also be investigated.

Good single domain single crystal data are unavailable for the PZT solid solution system, and thus the procedure for determining the coefficients of an energy function is complicated and must be indirect. Amin, *et al.*¹⁾ used experimental spontaneous strain data combined with phase boundary and equilibrium conditions to determine the coefficients of a modified LGD form of the elastic Gibbs free energy function. This theory was developed for the region of the PZT system from PbTiO_3 over to the morphotropic boundary between the tetragonal and high temperature rhombohedral phases, and can be extrapolated into the high temperature rhombohedral phase field.

The theory presented in this paper extends the previous theory to account for the high and low temperature rhombohedral phases. In the low temperature rhombohedral state, the oxygen octahedra tilt about the [111] axis. A theory was recently developed to account for octahedral tilting, assuming second order transitions with particular application to the $\text{PbZr}_{0.9}\text{Ti}_{0.1}\text{O}_3$ composition.²⁾ A similar theory for rotated octahedra was previously developed for the NaNbO_3 - KNbO_3 system by Darlington.³⁾

The high to low temperature rhombohedral phase transition has been experimentally shown to be first order.⁴⁾ However, at the cubic-rhombohedral boundary a tricritical point has been shown to exist at the $\text{PbZr}_{0.94}\text{Ti}_{0.06}\text{O}_3$ composition, where the transition changes from first to second order.^{5,6)} For PbZrO_3 to the tricritical point the transition was shown to be first order, and a region of second order behavior occurs from the tricritical point over to at least the

$\text{PbZr}_{0.88}\text{Ti}_{0.12}\text{O}_3$ composition.^{4,7)}

Experimental spontaneous strain data for PbTiO_3 and several PZT compositions over to $\text{PbZr}_{0.7}\text{Ti}_{0.3}\text{O}_3$ ¹⁾ indicate the transition from cubic to tetragonal and from cubic to rhombohedral to be of first order. A second tricritical point should therefore occur between the $\text{PbZr}_{0.88}\text{Ti}_{0.12}\text{O}_3$ and $\text{PbZr}_{0.7}\text{Ti}_{0.3}\text{O}_3$ compositions. This second tricritical point was not accounted for in the theory presented at this time.

All of the phase transitions were assumed to be first order over to the tricritical point at the $\text{PbZr}_{0.94}\text{Ti}_{0.06}\text{O}_3$ composition. The $T_c - \theta$ difference (T_c is the transition or Curie temperature and θ is the Curie-Weiss temperature) and the spontaneous polarization at T_c were assumed to go to zero at this tricritical point. The present theory does not describe the region between PbZrO_3 and the tricritical point, nor does it account for the antiferroelectric phases.

§2. Elastic Gibbs Free Energy Function

An additional term ($\tau d\theta$) was added to the elastic gibbs free energy G to account for the oxygen octahedra tilting:

$$dG = -SdT + EdP - xdX + \tau d\theta, \quad (1)$$

where τ is the torque responsible for the tilt $d\theta$.

Assuming isothermal and zero stress conditions, the energy function was expanded in a power series of P and θ . With the coefficients limited by the symmetry of the paraelectric phase ($m3m$ for PZT), and using reduced notation

$$\begin{aligned} \Delta G = & \alpha_1(P_1^2 + P_2^2 + P_3^2) + \alpha_{11}(P_1^4 + P_2^4 + P_3^4) \\ & + \alpha_{12}(P_1^2 P_2^2 + P_1^2 P_3^2 + P_2^2 P_3^2) + \alpha_{111}(P_1^6 + P_2^6 + P_3^6) \\ & + \alpha_{112}[P_1^4(P_2^2 + P_3^2) + P_2^4(P_1^2 + P_3^2) + P_3^4(P_1^2 + P_2^2)] \\ & + \alpha_{123}P_1^2 P_2^2 P_3^2 + \beta_1(\theta_1^2 + \theta_2^2 + \theta_3^2) + \beta_{11}(\theta_1^4 + \theta_2^4 + \theta_3^4) \\ & + \gamma_{11}(P_1^2 \theta_1^2 + P_2^2 \theta_2^2 + P_3^2 \theta_3^2), \end{aligned} \quad (2)$$

where α_1 and the α_{ij} and α_{ijk} are the dielectric stiffness and higher order stiffnesses, β_1 and β_{11} are octahedral torsion constants, and γ_{11} is a polarization-tilt angle coupling coefficient.

All of the coefficients in Equation (3) were assumed to be independent of temperature, except the dielectric stiffness constant α_1 , which was given a linear temperature dependence based on the Curie-Weiss law. Temperature independent relations for the remaining coefficients were derived at the phase transitions by equating the ΔG 's of the adjacent phases, and combining these equations with the first partial derivative equilibrium conditions.

These relations produced eight new constants, which were given compositional dependences using experimental data. The transition temperatures were determined from the experimental phase diagram.⁹ The Curie constant was given a compositional dependence based on a Gaussian distribution,¹¹ which was used to fit experimental data that was indirectly determined from a combination of calorimetric and phenomenological data.⁹

The Curie-Weiss temperature (θ) and the spontaneous polarization of the tetragonal state at T_c were determined from experimental spontaneous strain x_1 and x_2 data,¹¹ with θ given the additional requirement of becoming equal to T_c at the tricritical point.

The spontaneous polarization of the high temperature rhombohedral state at T_c was used to fit the theoretical and experimental morphotropic phase boundaries. This gave the value of the discontinuity in the spontaneous polarization at the morphotropic boundary at T_c . Using this value, along with experimental spontaneous strain x_1 data,¹¹ and the requirement that the spontaneous polarization at T_c go to zero at the tricritical point, the compositional dependence was determined.

The spontaneous polarization and tilt angle of the low temperature rhombohedral state at the high to low temperature rhombohedral phase transition were determined from experimental tilt angle data.^{10,11}

After determining the compositional dependence of the constants as described above, the ΔG 's and spontaneous polarizations and tilt angles of the tetragonal and high and low temperature rhombohedral states were calculated as shown in the next section. The derivation of the equations used and the evaluation procedure discussed above for the constants will be described in more detail in a future publication.

§3. Results

Figure 1 shows a comparison of the phenomenological and experimental phase diagrams. The solid curves are the calculated phase boundaries and the data points are from the experimental phase diagram.⁹

The spontaneous polarization is plotted versus temperature for PbTiO_3 and several PZT compositions in Figures 2 and 3. The calculated values for PbTiO_3 agree quite well with the experimental measurements of Gavril'yachenko, *et al.*¹²

For the 90:10 PZT composition, the calculated values are about one fourth the values of the experimental measurements of Clarke and Whatmore.¹³ This composition is in the region between the two tricritical points, and thus the present theory may not actually be valid here.

Figure 4 shows the oxygen octahedral tilt angle plotted versus composition at several temperatures. θ_{LT} is the

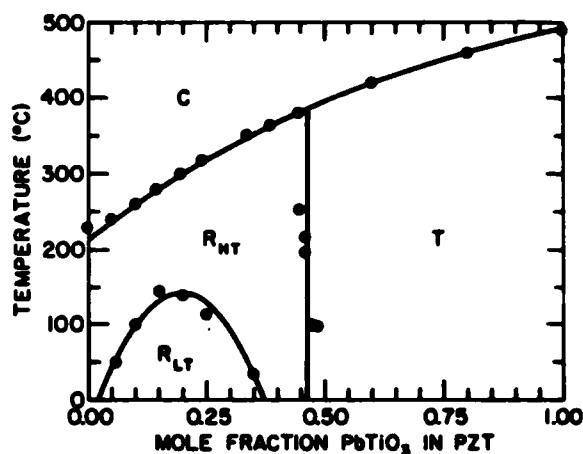


Fig. 1. Superposition of experimental and phenomenological phase diagrams.

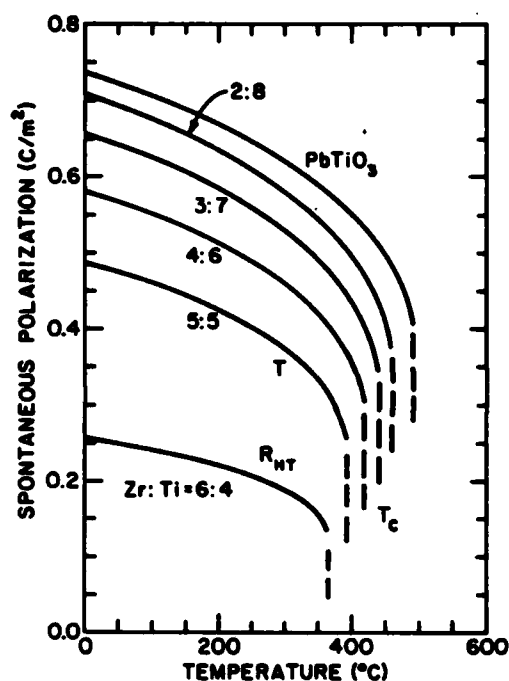


Fig. 2. The spontaneous polarization plotted versus temperature for PbTiO_3 and several PZT compositions.

spontaneous tilt angle at the high to low temperature rhombohedral phase transition. This constant was given a linear composition dependence, determined from experimental tilt angle data, which was only available at two compositions.

§4. Summary

A phenomenological theory has been developed for the PZT solid solution system for compositions from the tricritical point (at $\text{PbZr}_{0.94}\text{Ti}_{0.06}\text{O}_3$) to PbTiO_3 using the spontaneous polarization and oxygen octahedral tilt angle as order parameters. The coefficients of the energy function were determined from a combination of phase boundary requirements and experimental data, resulting in smooth continuous functions across the phase diagram.

The experimental and theoretical phase diagrams were shown to agree very well. The spontaneous polarization

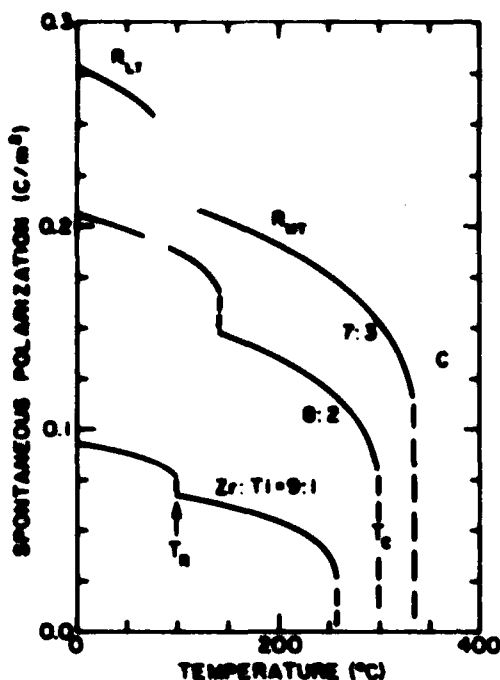


Fig. 3. The spontaneous polarization plotted versus temperature for three PZT compositions exhibiting the high to low temperature rhombohedral phase transition.

and tilt angle were calculated as a function of composition and temperature. The second order transition region between the tricritical points was not accounted for in the present theory, but will be dealt with in the future.

References

- 1) (a) A. Amin: Ph. D. Thesis, The Pennsylvania State University (1979); (b) A. Amin, M. J. Haun, B. Badger, H. McKinstry and L. E. Cross: *Ferroelectrics* 65 (1985) 107.
- 2) T. R. Halemane, M. J. Haun, L. E. Cross and R. E. Newnham:

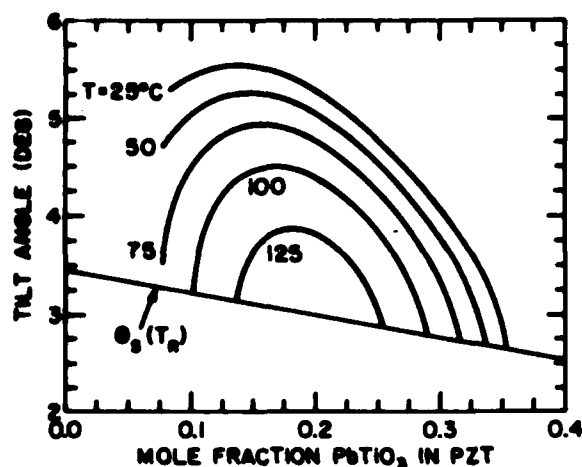


Fig. 4. The tilt angle plotted versus composition at several temperatures.

- Ferroelectrics* 62 (1985) 149.
- 3) C. N. W. Darlington: *Phil. Mag.* 31 (1975) 1159.
- 4) R. Clarke, A. M. Glazer, F. W. Ainger, D. Appleby, N. J. Poole and S. G. Porter: *Ferroelectrics* 11 (1976) 359.
- 5) R. W. Whatmore, R. Clarke and A. M. Glazer: *J. Phys. C: Solid State Phys.* 11 (1978) 3089.
- 6) K. Roleder and J. Handerek: *Phase Transitions* 2 (1982) 285.
- 7) R. Clarke and A. M. Glazer: *J. Phys. C: Solid State Phys.* 7 (1974) 2147.
- 8) B. Jaffe, W. R. Cook and H. Jaffe: *Piezoelectric Ceramics* (Academic Press, NY, 1971) p. 136.
- 9) A. Amin, L. E. Cross and R. E. Newnham: *Ferroelectrics* 37 (1981) 647.
- 10) A. M. Glazer, S. A. Mabud and R. Clarke: *Acta. Cryst.* B34 (1978) 1060.
- 11) A. Amin, R. E. Newnham, L. E. Cross and D. E. Cox: *J. Solid State Chem.* 37 (1981) 248.
- 12) V. G. Gavril'yachenko, R. I. Spinko, M. A. Martynenko and E. G. Fesenko: *Sov. Phys.-Solid State* 12 (1970) 1203.
- 13) R. Clarke and R. W. Whatmore: *J. Crystal Growth* 33 (1976) 29.

EFFECT OF ELECTRIC BOUNDARY CONDITIONS
ON MORPHOTROPIC $\text{Pb}(\text{Zr},\text{Ti})\text{O}_3$ PIEZOELECTRICS

A. Amin and L.E. Cross

Effect of Electric Boundary Conditions on Morphotropic $\text{Pb}(\text{Zr}, \text{Ti})\text{O}_3$ Piezoelectrics

A. AMIN and L. E. CROSS

Texas Instruments Incorporated, Attleboro, MA. 02703, U.S.A.
 Materials Research Laboratory, University Park, PA. 16802, U.S.A.

A phenomenological free energy function which we developed earlier is used to calculate the effect of electric boundary conditions upon the relative stability points, and the rhombohedral ($R3m$)-tetragonal ($P4mm$) degeneracy required for the morphotropy at Zr:Ti ratio approximately equal to 1:1. The free energy—composition phase diagram under applied dc fields is discussed in terms of the morphotropic phase boundary behavior.

§1. Introduction

The PZT perovskite solid solution between antiferroelectric lead zirconate (Pb Zr O_3) and ferroelectric lead titanate (Pb Ti O_3) contains a number of extremely important compositions used in the electronic industry. Piezoelectric devices such as sonar transmitters and detectors are made of poled PZT ceramics with compositions close to the morphotropic phase boundary MPB (Zr:Ti ~ 1:1 ratio) where the dielectric, and the piezoelectric coupling coefficients are unusually high.

The effect of electric boundary conditions on the single domain stability and properties of lead zirconate titanate compositions near the morphotropic phase boundary is of considerable interest, since in a polycrystalline ensemble the elastic, and electric boundary conditions are uncertain. In this work an elastic free energy function which we developed earlier^{2,3,4} is used to calculate the influence of some postulated electric boundary conditions upon the relative phase stabilities and the single domain properties for compositions close to the Zr:Ti ~ 1:1 ratio required for morphotropy at zero field.

§2. Free Energy Function

Consider the free energy function for a simple proper ferroelectric derived from a prototypic phase with symmetry $\text{Pm}3m$. For Brillouin zone center modes, the Landau-Ginsburg-Devonshire thermodynamic potential G may be written as power series in dielectric polarization P_i ($i=1, 2, 3$):

$$\begin{aligned}
 G = & \alpha_1^x(P_1^2 + P_2^2 + P_3^2) + \alpha_{11}^x(P_1^4 + P_2^4 + P_3^4) \\
 & + \alpha_{12}^x(P_1^2 P_2^2 + P_2^2 P_3^2 + P_3^2 P_1^2) + \alpha_{111}^x(P_1^6 + P_2^6 + P_3^6) \\
 & + \alpha_{112}^x(P_1^4(P_2^2 + P_3^2) + P_2^4(P_3^2 + P_1^2) + P_3^4(P_1^2 + P_2^2)) \\
 & + \alpha_{123}^x P_1^2 P_2^2 P_3^2 - 1/2 s_{11}^x(X_1^2 + X_2^2 + X_3^2) \\
 & - s_{12}^x(X_1 X_2 + X_2 X_3 + X_3 X_1) - 1/2 s_{44}^x(X_1^2 + X_2^2 + X_3^2) \\
 & - Q_{11}(X_1 P_1^2 + X_2 P_2^2 + X_3 P_3^2) \\
 & - Q_{12}(X_1(P_2^2 + P_3^2) + X_2(P_3^2 + P_1^2) + X_3(P_1^2 + P_2^2)) \\
 & - Q_{44}(X_4 P_2 P_3 + X_5 P_3 P_1 + X_6 P_1 P_2)
 \end{aligned} \quad (1)$$

where α_1^x , α_{11}^x , α_{12}^x , α_{111}^x , α_{112}^x , α_{123}^x are related to dielectric stiffness and higher order stiffness coefficients, s_{11}^x , s_{12}^x , s_{44}^x are the elastic compliances measured at constant polarization, and Q_{11} , Q_{12} , Q_{44} are the electrostriction constants written

in polarization notation. The expression is complete up to all six power terms in polarization, but contains only first order terms in electrostrictive and elastic behavior. All tensor coefficients in the free energy function (1) which fit the experimental lead zirconate-lead titanate phase diagram and the observed physical properties under zero electric field conditions have been determined² and are given in table I.

§3. Effect of Electric Boundary Conditions

For an applied dc electric field E_i ($i=1, 2, 3$), the free energy function eq. (1) takes the form:

$$\begin{aligned}
 G = & \alpha_1^x(P_1^2 + P_2^2 + P_3^2) + \alpha_{11}^x(P_1^4 + P_2^4 + P_3^4) \\
 & + \alpha_{12}^x(P_1^2 P_2^2 + P_2^2 P_3^2 + P_3^2 P_1^2) + \alpha_{111}^x(P_1^6 + P_2^6 + P_3^6) \\
 & + \alpha_{112}^x(P_1^4(P_2^2 + P_3^2) + P_2^4(P_3^2 + P_1^2) + P_3^4(P_1^2 + P_2^2)) \\
 & + \alpha_{123}^x P_1^2 P_2^2 P_3^2 - (E_1 P_1 + E_2 P_2 + E_3 P_3)
 \end{aligned} \quad (2)$$

The dielectric reciprocal susceptibilities (dielectric stiffnesses) are given by the second partial derivatives of the free energy function:

$$\frac{\partial^2 G}{\partial P_i \partial P_j} = \frac{1}{\chi_{ij}} \quad (i=1, 2, 3) \quad (3)$$

The piezoelectric coefficients d_{mkl} are given by,

$$d_{mkl} = X_{mj}(\epsilon_0) Q_{lkl} P_i \quad (4)$$

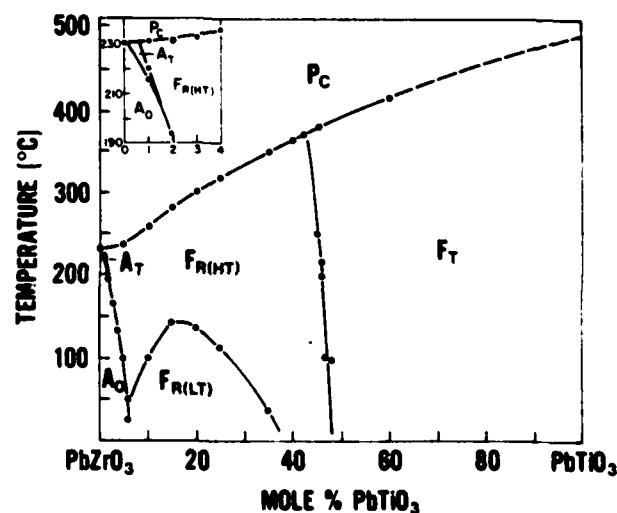


Fig. 1. Pb Zr O_3 - Pb Ti O_3 Phase diagram.¹¹

Table I. Calculated Values of T_c , θ , $P_{s(TC)}$, ϕ , and the α Stiffness Coefficients.

	Mole Fraction PbTiO ₃ in PbZrO ₃ : PbTiO ₃										
	0	0.1	0.2	0.3	0.4	0.5	0.6	0.7	0.8	0.9	1
T_c (°C)	211.8	257.7	298.4	334.4	366.1	394.1	418.7	440.3	459.5	476.7	492.2
θ (°C)	208.2	254.1	294.4	330.0	361.3	388.9	413.1	433.9	451.5	465.6	475.9
$P_{s(TC)}$ (C/m ²)	0.119	0.140	0.161	0.183	0.207	0.231	0.256	0.282	0.309	0.336	0.365
α_1^T ($\times 10^9$ m/F) at T_c	13.55	13.45	13.07	8.650	4.695	3.814	5.519	12.43	26.37	41.45	61.38
α_1^R ($\times 10^9$ m/F) at 25°C	-6.894	-8.533	-8.857	-5.938	-3.289	-2.669	-3.795	-7.963	-14.02	-16.41	-16.97
α_2^T ($\times 10^9$ m ² /C ² F)	-19.10	-13.70	-10.07	-5.153	-2.226	-1.431	-1.677	-3.139	-5.535	-7.294	-9.235
α_2^R	9.80	7.62	5.44	3.26	1.08	-1.10	-3.28	-5.46	-7.64	-9.82	-12.0
α_3^T ($\times 10^9$ m ² /C ² F)	-187.2	-104.4	-54.78	-16.80	-2.404	1.574	5.500	17.14	42.28	71.63	110.8
α_3^R ($\times 10^9$ m ² /C ² F)	67.33	35.16	19.41	7.658	2.605	1.342	1.279	1.974	2.903	3.223	3.469
α_4^T ($\times 10^9$ m ³ /C ³ F)	6.021	5.960	5.260	3.116	1.565	1.173	1.565	3.116	5.260	5.960	6.021
α_4^R ($\times 10^9$ m ³ /C ³ F)	-33.87	-31.66	-26.30	-14.60	-6.846	-4.767	-5.868	-10.71	-16.44	-16.76	-15.05

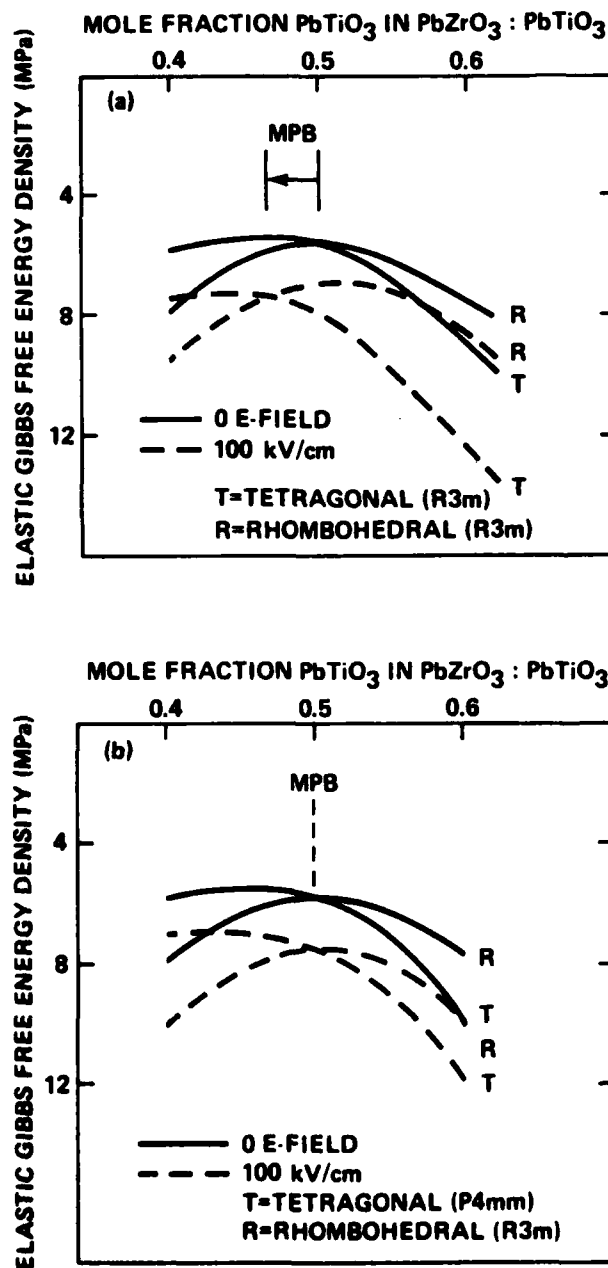


Fig. 2. Free energy function under dc fields at 25°C for composition close to morphotropy in the PZT system.
 (a) Field along [001] cubic direction
 (b) Field along [111] cubic direction

where ϵ_0 is the free space permittivity. Choosing an arbitrary value and orientation for E (applied electric field), the first partial derivative equations $(\partial G/\partial P_i) = E_i \neq 0$ ($i=1, 2, 3$) are solved to give new values of the polarization P_i under applied electric field. These values can then be reinserted in eq. (1) to delineate G as a function of composition, temperature, and applied electric field.

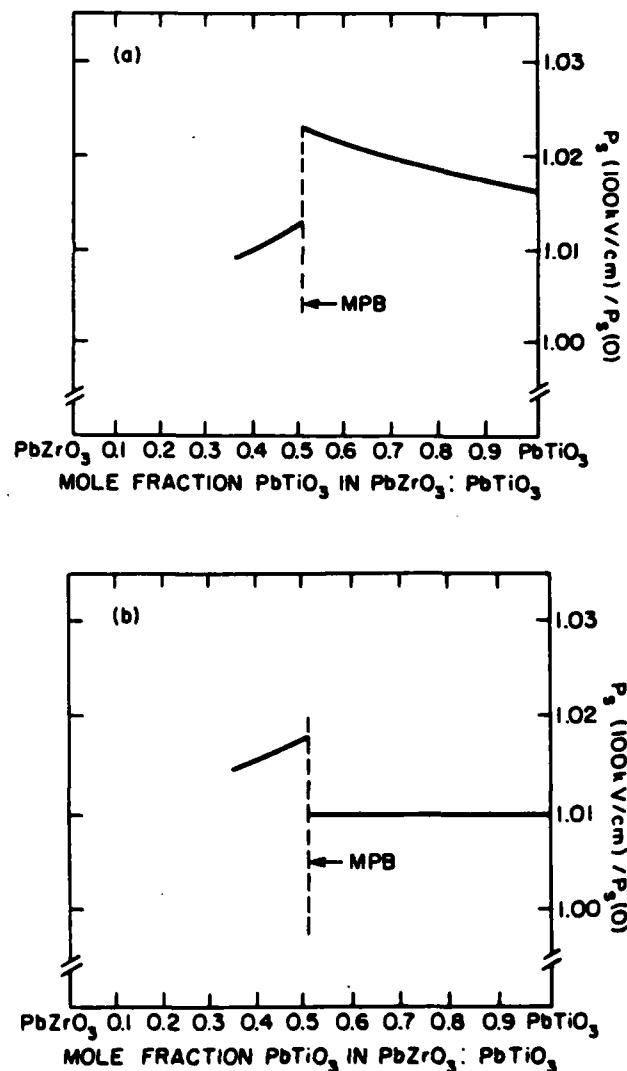


Fig. 3. Predicted compositional dependence of P_1 (100 kV/cm) / $P_1(0)$.
 (a) Field along [001] cubic direction
 (b) Field along [111] cubic direction

The free energy-composition phase diagram for dc fields applied along the cubic [001] and [111] directions are shown in Fig. 2(a) and 2(b) respectively. The orthorhombic state is found to be metastable at all field levels and has therefore been omitted for clarity. The ratio of the total polarization at 100 kV/cm to the spontaneous polarization at zero field is plotted versus composition in Fig. 3(a) and 3(b) for the two orientations of the applied electric field.

§4. Discussion

The effect of electric boundary condition changes on phase stability shows some unexpected and interesting results. It can be seen from Fig. 2(a) and 2(b) that it is rather easy to field force the rhombohedral state to the tetragonal state. However, in the tetragonal phase even

the most favorable orientation field along [111] will not force changes to the rhombohedral state. We believe that this may be part of the reason there is a rapid escalation of coercivity against poling in the tetragonal phase compositions.

References

- 1) B. Jaffe, W. R. Cook, Jr. and H. Jaffe: *Piezoelectric Ceramics* (Academic Press, London, 1971).
- 2) A. Amin, M. Huan, B. Badger, H. A. McKinstry and L. E. Cross: *Ferroelectrics* **65** (1985) 107.
- 3) A. Amin, L. E. Cross and R. E. Newnham: *Ferroelectrics* **37** (1981) 647.
- 4) A. Amin, R. E. Newnham and L. E. Cross: *The American Crystallographic Association Meeting, Snowmass, Co.* (1983) 43.
- 5) V. Ginsburg: *J. Exp. Theor. Phys. SSSR* **15** (1945) 739.
- 6) A. F. Devonshire: *Phil. Mag.* **40** (1949) 1040.

TEMPERATURE BEHAVIOR OF DIELECTRIC AND ELECTROMECHANICAL
COUPLING PROPERTIES OF SAMARIUM MODIFIED LEAD TITANATE CERAMICS

W.R. Xue, J.W. Kim, S.J. Jang, L.E. Cross and R.E. Hlawnham

Temperature Behavior of Dielectric and Electromechanical Coupling Properties of Samarium Modified Lead Titanate Ceramics

W. R. XUE,* J. N. KIM,** S. J. JANG,
 L. E. CROSS and R. E. NEWNHAM

*Nanjing Institute of Chemical Technology, The People's Republic of China

**Pusan University, Pusan, Korea

Materials Research Laboratory, The Pennsylvania State University
 University Park, PA 16802 U.S.A.

Dielectric and electromechanical coupling properties of Sm- and Mn-doped PbTiO₃ ceramics have been investigated. Small changes in the relative dielectric permittivity with frequency and temperature of rare earth modified PbTiO₃ suggest that the polarizability is mainly intrinsic. Large anisotropic electromechanical coupling has been observed with the proper poling treatment. The ratio of thickness to planar coupling coefficient, k_t/k_p , is larger than 50 near room temperature.

§1. Introduction

Large anisotropic piezoelectric coupling is a useful characteristic of transducers for high frequency array applications. Recently, the dielectric and piezoelectric properties of alkaline earth¹⁾ and rare earth²⁾ modified lead titanate ceramics were investigated in Japan. With proper processing procedures and poling conditions, both systems exhibit a large electromechanical thickness to planar coupling ratio, $k_t/k_p = 12$ to 17.^{1,2)} With a small amount of Mn doping, rare earth modified materials having k_p values of near zero were also reported.^{3,4)}

In this study, samarium doped PbTiO₃ ceramics were investigated to optimize the coupling factor ratio k_t/k_p without reducing the k_t value near room temperature. The thickness and planar coupling coefficients, k_t and k_p , were measured as a function of temperature. The influence of the poling field on k , and the piezoelectric coefficient, d_{33} , were also studied at room temperature. The relative dielectric permittivity and loss of 10 mole% Sm and 2 mole% Mn doped PbTiO₃ ceramics were measured over the temperature range from 4.2 to 300°K.

§2. Experiment and Results

Reagent grade oxides were mixed in appropriate proportions, ball-milled for six hours in alcohol, then dried and calcined in a closed alumina crucible at 900°C for one hour. After cold pressing in a die at 5000 psi to form green disks, the samples were fired at 1200°C for one hour in a closed crucible. The final density of the ceramic samples was higher than 95% of the calculated value.

The coupling coefficients, k_t and k_p , are plotted as a function of Sm dopant level in Fig. 1. The planar coupling coefficient k_p was calculated using the IRE standard method⁵⁾ based on the fundamental resonance of the planar mode measured with a HP 3585A spectrum analyzer at room temperature. The thickness coupling coefficient k_t was calculated from the ratio of the first overtone and the fundamental resonance frequencies of the thickness mode as discussed in ref. 6. As shown in Fig. 1, k_p appears to be dependent on Sm dopant level with a minimum of about 10 mole% Sm. k_t maintains a constant value of 0.45 from 8 to 14 mole% Sm.

The 10 mole% Sm and 2 mole% Mn modified PbTiO₃ composition was chosen for further investigation. The piezoelectric (d_{33}) and coupling (k_t and k_p) coefficients are shown in Fig. 2 as a function of poling field. d_{33} and k_t approach the room temperature saturation values of about 55×10^{-12} C/N and 0.45, respectively, after poling in a field of 40 kV/cm for 5 minutes at 150°C.

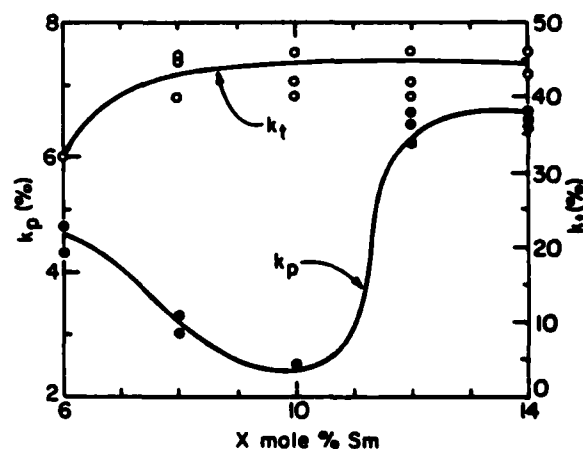


Fig. 1. The thickness (k_t) and planar (k_p) coupling coefficients of Sm-modified PbTiO₃ ceramic as a function of Sm dopant level. k_t and k_p were measured by the IRE Standard method at room temperature.

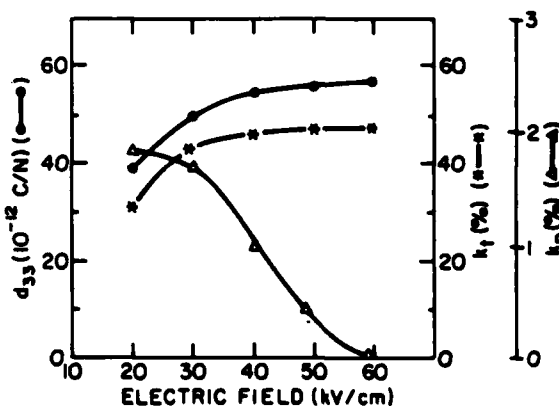


Fig. 2. The thickness (k_t) and planar (k_p) coupling and piezoelectric (d_{33}) coefficients of a 10 mole% Sm and 2 mole% Mn doped PbTiO₃ ceramic as a function of poling field at room temperature

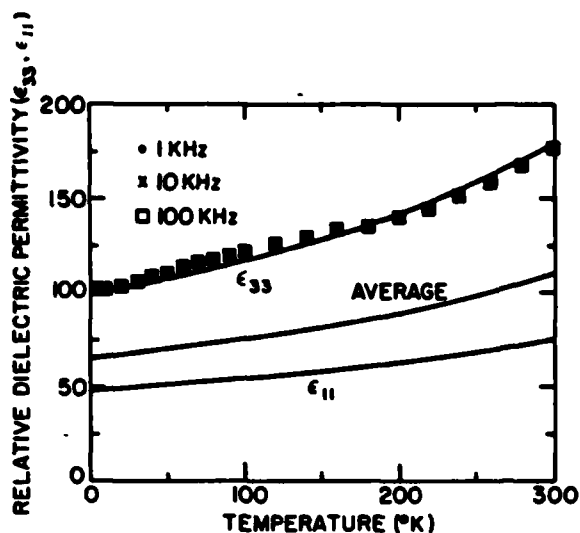


Fig. 3(a). The relative dielectric permittivity as a function of temperature. Solid lines, ϵ_{33} , ϵ_{11} , and $(\epsilon_{33} + 2\epsilon_{11})/3$, are calculated from the thermodynamic phenomenology of Ref. 8.

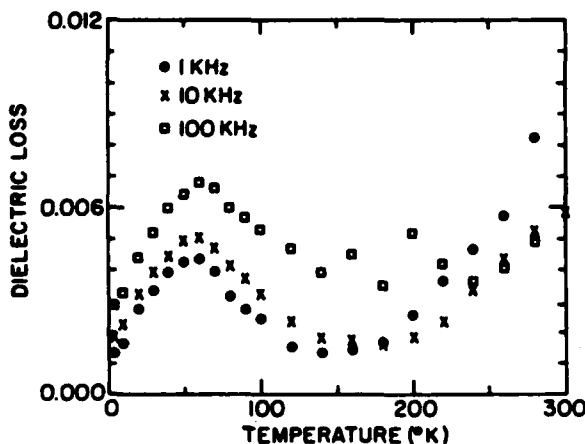


Fig. 3(b). The dielectric loss as a function of temperature.

The relative dielectric permittivity ϵ_{33} and loss tangent, measured using a HP4270A automatic capacitance bridge, are shown in Fig. 3(a) and (b). ϵ_{33} increases gradually from about 100 to 180 over the temperature span 4.2 to 300°K. It is also weakly dependent on the frequency from 1 KHz to 100 KHz. The dielectric loss is below 1% over the entire temperature range, but does show a weak peak in the vicinity of 50°K.

Figure 4 shows the coupling coefficients k_t and k_p as a function of temperature. k_t varies little over the temperature span -175°C to $+50^\circ\text{C}$. The planar coupling coefficient, k_p , becomes immeasurably small (<0.01) over the temperature range from -20°C to $+40^\circ\text{C}$. The IRE standard method is not entirely satisfactory for measuring very small magnitudes of k_p . For the exceedingly small frequency differences between parallel resonance (f_p) and series resonance (f_s) involved in the calculation of the planar coupling coefficient, $f_p - f_s \approx f_n - f_m$, where f_n and f_m are the frequencies of the maximum and minimum impedances, respectively. To obtain greater precision, the vector impedance method was used when the planar coupling coefficient k_p was small.

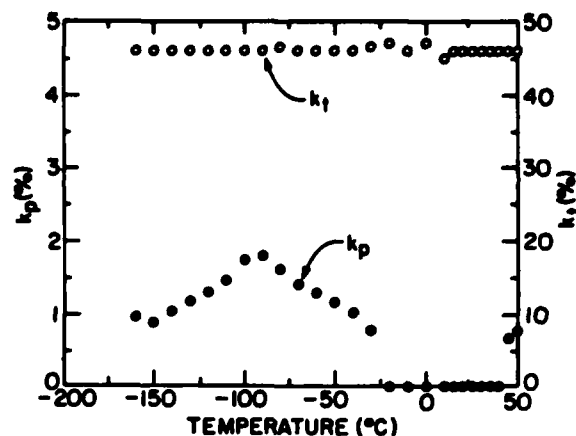


Fig. 4. The thickness (k_t) and planar (k_p) coupling coefficients of a 10 mole% Sm and 2 mole% Mn modified PbTiO₃ ceramic plotted as a function of temperature. k_p was measured by using the vector impedance method.

§3. Discussion

Lead titanate ceramics doped with 10 mole% Sm and 2 mole% Mn have coupling coefficient ratios k_t/k_p as high as 50 or more near room temperature. The poling process is important in obtaining large anisotropic electromechanical coupling. Fields of 40 kV/cm for 5 minutes at 150°C are required to achieve saturated values of the coupling factors.

The planar coupling coefficient k_p becomes exceedingly small over the temperature range from -20°C to $+40^\circ\text{C}$ as shown in Fig. 4. It has been suggested that the piezoelectric coefficient d_{31} of Sm- and Mn-modified PbTiO₃ ceramics may reverse its sign in the above temperature range. An experiment using Lissajous figure was performed to confirm whether d_{31} of the modified PbTiO₃ ceramic changes the polarity in the temperature region where k_p becomes very small. Disk-shaped samples of PZT and the modified PbTiO₃ were glued together and the PZT disk with known d_{31} was driven by a generator. A sinusoidal signal of the modified PbTiO₃ generated through the piezoelectric coupling, was compared to that of PZT with known d_{31} polarity. No sign change of d_{31} was observed in the temperature span -70°C to $+25^\circ\text{C}$.

The very minor changes in the relative dielectric permittivity with frequency and temperature as compared to PZT at compositions near the morphotropic boundary⁷⁾ suggest that the polarizability is largely intrinsic and a property of the average single domain response. To make an initial comparison, the thermodynamic phenomenology of ref. 8 has been used to calculate the intrinsic response as a function of temperature. Taking the literature 8 values of the constants for pure PbTiO₃, and simply adjusting the Curie temperature T_c to 350°C as in the Sm-doped material, the ϵ_{33} and ϵ_{11} curves of Fig. 3(a) were derived. The average is taken as the arithmetic mean $(\epsilon_{33} + 2\epsilon_{11})/3$. For this highly approximate treatment, the shape of the curve ϵ_{33} is in very good agreement with the measured values. One might speculate that in the Sm-doped material, the relative dielectric permittivity is more

nearly isotropic and that indeed the major temperature dependence is that of the single domains in the ferroelectric phase.

Acknowledgement

The authors wish to thank M. J. Haun for the theoretical calculations in Fig. 3(a). This work was supported by North American Philips Corporation.

References

- 1) Y. Yamashita, K. Yokoyama, H. Hondo and T. Takahashi: *Jpn. J. Appl. Phys.* **20** (1981) Suppl. 20-4, 183.
- 2) H. Takeuchi, S. Jyomura, E. Yamamoto and Y. Ito: *J. Acoust. Soc. Am.* **72** (1982) 1114.
- 3) T. Takahashi and Y. Yamashita: *Proc. 2nd U. S.: Japan Seminar on Dielectric and Piezoelectric Ceramics*, Williamsburg, VA, 1984, Vol. 1, p. 1.
- 4) H. Takeuchi and S. Jyomura: *Proc. 2nd U. S.: Japan Seminar on Dielectric and Piezoelectric Ceramics*, Williamsburg, VA, 1984, Vol. 2, p. 324.
- 5) IRE Standards on Piezoelectric Crystal: *Measurements of Piezoelectric Ceramics*, 1961, IEEE, New York 10021, NY.
- 6) M. Onoe, H. F. Tierstein and A. H. Meitzler: *J. Acoust. Soc. Am.* **35** (1936) 36.
- 7) J. N. Kim, M. J. Haun, S. J. Jang and L. E. Cross: paper under preparation.
- 8) A. Amin, M. J. Haun, B. Badger, H. A. McKinstry and L. E. Cross: *Ferroelectrics*, accepted.

LOW TEMPERATURE DIELECTRIC AND PIEZOELECTRIC
PROPERTIES OF DOPED PZT CERAMICS

J.N. Kim, M.J. Haun, S.J. Jang and L.E. Cross

LOW TEMPERATURE DIELECTRIC AND PIEZOELECTRIC PROPERTIES OF DOPED PZT CERAMICS

J.N. KIM

Physics Department, Pusan University, Pusan, Korea

M.J. HAUN, S.J. JANG and L.E. CROSS

Materials Research Laboratory, The Pennsylvania State
University, University Park, PA 16802

Abstract—The dielectric and piezoelectric properties (d-p properties) of four different types of PZT were investigated from 4.2 to 300°K. As discussed in previous studies, the dielectric and piezoelectric properties converge to common values near 4°K for both 'soft' and 'hard' PZT compositions. The calculated values from a phenomenological theory agree with the converged values. The reason for the large differences in the dielectric and piezoelectric properties at room temperature of the modified PZT was suggested to be mainly due to extrinsic domain or phase boundary contributions. This extrinsic contribution appears to freeze out with decreasing temperature. To confirm this hypothesis, measurements have been extended to the coercive electric field for domain switching, which is shown to escalate rapidly with decreasing temperature, going beyond our measuring range at 20°K. Below 20°K the dielectric loss also converges rapidly to a common value.

INTRODUCTION

Piezoelectric ceramics of PZT solid solutions have been widely used since their discovery in the early 1950's⁽¹⁾, because of the superior dielectric and piezoelectric properties. Most of the commercial PZT ceramics are modified by adding dopants to enhance the desired properties. Depending upon the added dopants, these modified PZT ceramics can be divided into two types, 'soft' and 'hard'⁽²⁾. The dielectric and electromechanical coupling properties of 'soft' and 'hard' materials are quite different at room temperature⁽³⁾.

An interesting question is whether these superior d-p properties of PZT ceramics and the large differences of the d-p properties between 'soft' and 'hard' materials are due to intrinsic or extrinsic response. In an earlier investigation⁽³⁾,

the d-p properties of both 'soft' and 'hard' PZT compositions converge to common values near 4°K, indicating that the large separations in the d-p properties of the modified PZT at room temperature are mainly due to extrinsic responses.

In this study, careful measurements on the d-p properties of the modified PZT ceramics were performed from 4.2 to 300°K. The coercive electric field for domain switching was measured to confirm the previous hypothesis. A phenomenology theory⁽⁴⁾ was employed to calculate the average intrinsic single-domain values of the dielectric constant, ϵ_{33}^T , and piezoelectric coefficients, d_{31} and d_{33} , of PZT. The calculated values are compared with the experimental values.

EXPERIMENTAL PROCEDURE

The basic composition of the modified PZT ceramics is lead titanate zirconate solid solution close to the morphotropic phase boundary⁽¹⁾. Navy-types I and III, which are hard materials, are modified by dopants NiO and Fe_2O_3 , respectively. Navy-types II and V, which are soft materials, are modified by dopants Nb_2O_5 and Sb_2O_3 , respectively. The samples were obtained in the form of prepoled and silver electroded large discs. However, it was necessary to cut several different shapes and dimensions to measure the various electromechanical coupling coefficients. Reshaped samples were electroded with sputtered gold and repoled. All shapes satisfied the dimensional requirements of the IRE standards on piezoelectric crystals⁽⁵⁾. Samples were carefully connected with very fine Ag wire and suspended in a vacuum in an in-house made holder on an Air Products and Chemicals Model LT-3-110 cryogenics system.

The dielectric and resonance properties were measured on a Hewlett Packard automatic capacitance bridge model 4270A and spectrum analyzer model 3585A, respectively.

RESULTS AND DISCUSSION

The dielectric constant ϵ_{33}^T and dissipation factor $\tan \delta$, measured at 1 KHz from 4.2 to 300°K, of Navy-type I, II, III, and V are shown in Figures 1(a) and (b). At room temperature, the ϵ_{33}^T and $\tan \delta$ of 'soft' and 'hard' PZT are clearly distinguishable and widely separated. Figures 2(a) and (b) show the piezoelectric coefficients, d_{31} and d_{33} . The temperature behaviors of the d_{31} and d_{33} are strikingly similar to that of the ϵ_{33}^T . There are clear separations in the d_{31} and d_{33} between 'soft' and 'hard' materials at room temperature. But both d_{31} and d_{33} converge at very low temperature in a similar manner as ϵ_{33}^T . The coupling factors, K_p , K_{31} , and K_{33} , elastic compliance, s_{11}^E , and mechanical quality factor, Q_m , are shown in Figures 3, 4, and 5, respectively, as a function of temperature. The low temperature behavior of these properties is similar to that of ϵ_{33}^T . The temperature dependences of the properties showed different trends for the hard PZTs compared to the soft PZTs. However, each of the

properties, except the dielectric loss $\tan \delta$, had similar temperature behavior for the two hard PZTs, Navy-type I and III, and also for the two soft PZTs, Navy-type II and V.

For $\tan \delta$, every composition exhibits its own characteristic peak as shown in Figure 1(b). It indicates that there are at least more than one relaxation process for each composition in this temperature range. All samples, however, show a peak near 20°K, then converge rapidly with further lowering of temperature. This phenomenon could be related to the different dopants used and with domain wall or phase boundary motions. These thermally activated contributions to the dielectric and electromechanical coupling properties of the modified PZT ceramics appears to freeze out rapidly below 20°K.

The dielectric and piezoelectric properties (i.e., ϵ_{33}^T , $\tan \delta$, d , K , s_{11}^E , and Q_m) of four kinds of doped PZT ceramics appear to converge to the average single-domain intrinsic values at very low temperature. A thermodynamic phenomenological theory for the single-cell region of the PZT solid solution systems was previously developed to predict the intrinsic single crystal properties⁽⁴⁾. Calculations from this theory were compared with the experimentally measured dielectric constant in Figure 1(a). The theoretical curve shown in this Figure is an average $(=2s_{11}^T/3 + s_{33}^T/3)$ of the calculated single crystal values. At very low temperature experimental and theoretical dielectric constants are in good agreement, indicating that the extrinsic effects have been frozen out. It is interesting to note that at room temperature even the hard PZTs have a significant extrinsic contribution to the dielectric constant. The averaging of the single crystal piezoelectric coefficients to yield ceramic values is more complicated than can be used for the dielectric constant. The calculated single crystal d_{31} and d_{33} coefficients from the phenomenological theory have similar values at low temperatures as the observed polycrystalline measurements. An averaging procedure for the piezoelectric coefficients is presently under investigation.

Finally, the coercive electric field for domain switching of 'soft' PZT (Navy-type V) was measured as a function of temperature to confirm the hypothesis of the intrinsic response at very low temperature. As shown in Figure 6, it increases very rapidly with decreasing temperature going beyond our measuring capability at 20°K, which indicates most of the thermally activated domain wall or phase-boundary contributions to the d-p properties of the modified PZT ceramics are frozen out at very low temperature.

CONCLUSIONS

The dielectric and piezoelectric properties of Navy-type I and II (hard materials), and II and V (soft materials) have been measured from 4.2 to 300°K. The dielectric permittivity (ϵ_{33}^T), loss ($\tan \delta$), piezoelectric coefficients (d_{31} and d_{33}), coupling factors (K_p , K_{31} and K_{33}), elastic compliance (s_{11}^E) and mechanical quality factor (Q_m), converge at very low temperature to a common

value which appears to be the average intrinsic single-domain response. The calculated intrinsic values, from a thermodynamic phenomenological theory, of the ϵ_{33} , d_{31} and d_{33} agree well with the observed values at very low temperature. Large differences in the d-p properties between the 'soft' and 'hard' materials at room temperature are mainly due to extrinsic contributions. The rapidly escalating coercive field of the Navy-type V sample with decreasing temperature also confirms this hypothesis.

REFERENCES

1. E. Sawaguchi, J. Phys. Soc. Jpn. 8, 615-629 (1953).
2. H. Thomann, Ferroelectrics 4, 141 (1972).
3. X.L. Zhang, Z.X. Chen, L.E. Cross and W.A. Schulze, J. Mat. Sci. 18, 968-972 (1983).
4. A. Amin, M.J. Haun, B. Badger, H. McKinstry and L.E. Cross, Ferroelectrics 65, 107-130 (1985).
5. "IRE Standard on Piezoelectric Crystals," Proc. IRE 46, 764 (1958).

FIGURE CAPTIONS

- Figure 1. (a) The dielectric constant ϵ_{33}^T and (b) the dielectric loss $\tan \delta$ plotted versus temperature. The theoretical curve is an average of the single crystal values calculated assuming a tetragonal solution to the energy function.
- Figure 2. The piezoelectric coefficients (a) d_{31} and (b) d_{33} plotted versus temperature.
- Figure 3. The coupling factors (a) K_p , (b) K_{31} and (c) K_{33} plotted versus temperature.
- Figure 4. The elastic compliance coefficient s_{11}^E plotted versus temperature.
- Figure 5. The mechanical quality factor Q_m plotted versus temperature.
- Figure 6. The coercive field of the soft PZT Navy-type V plotted versus temperature.

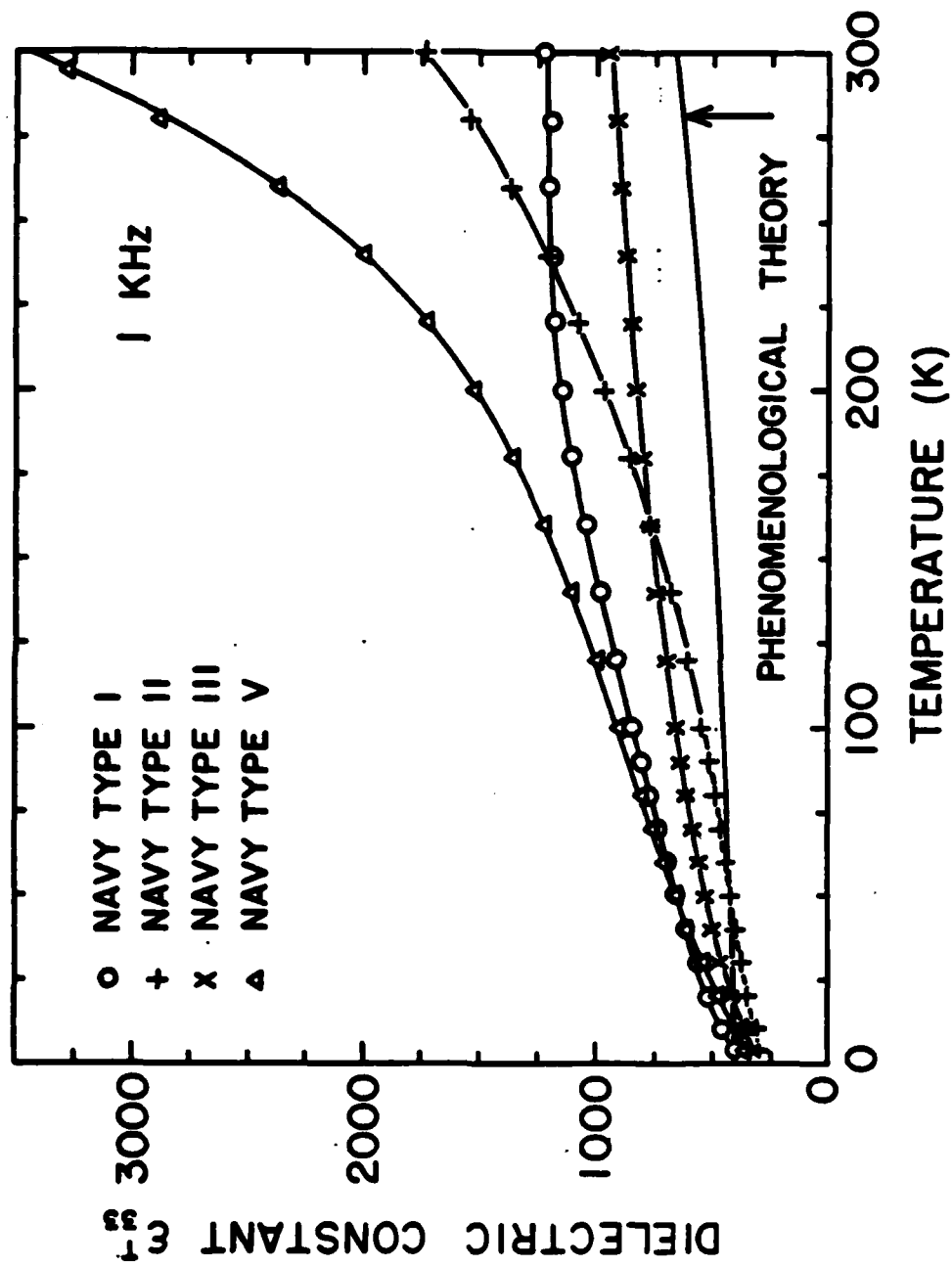


Figure 1(a)

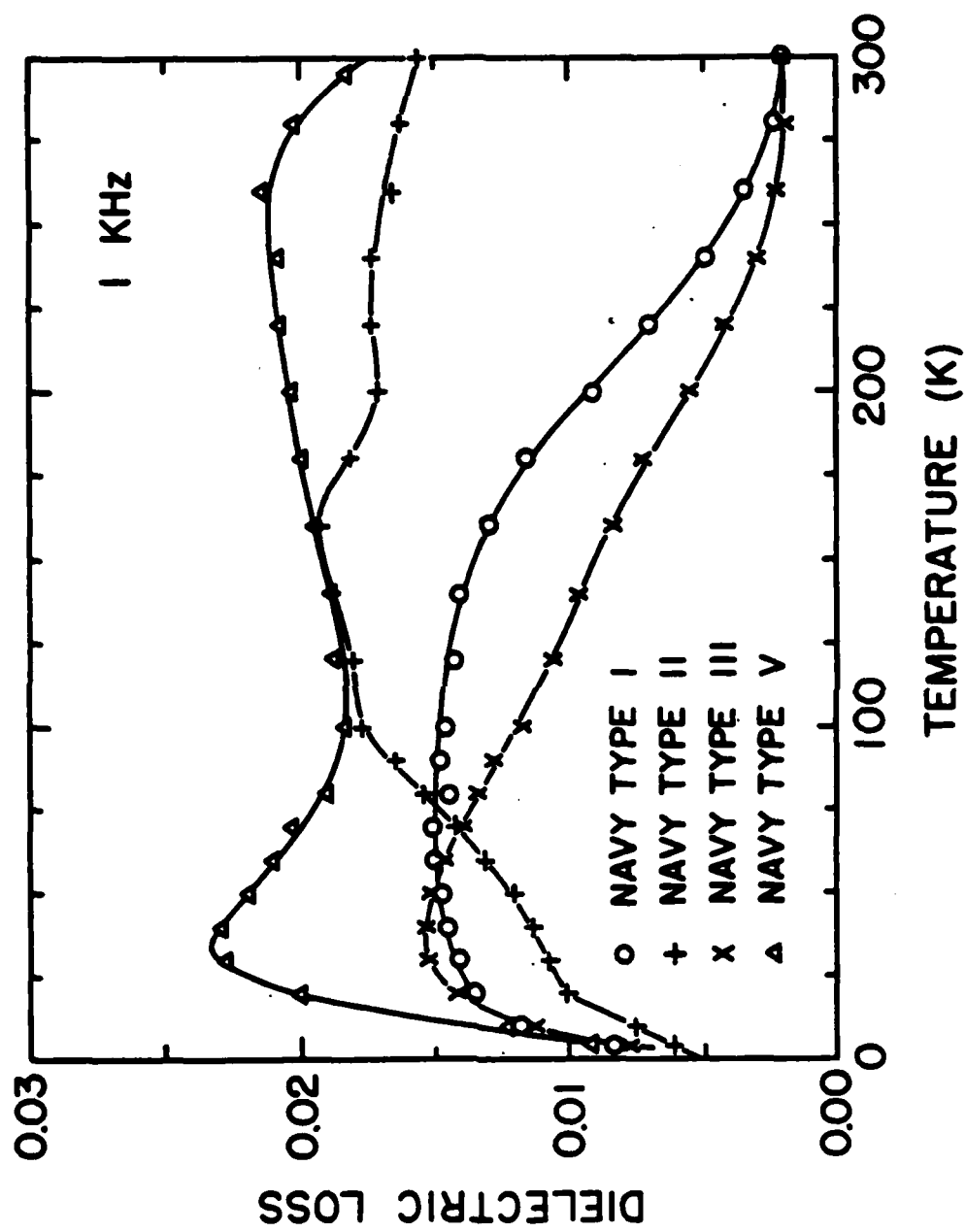


Figure 1(b)

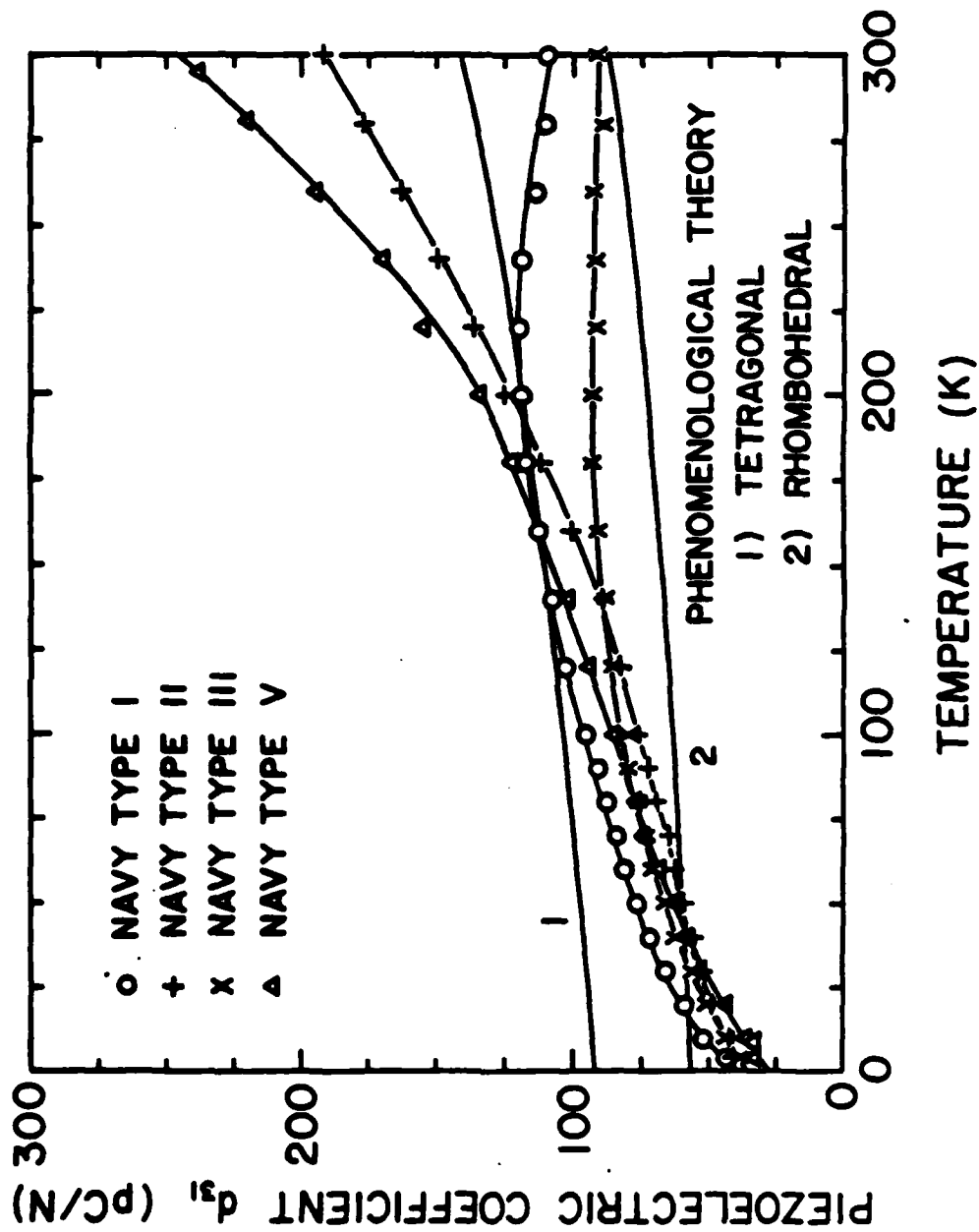


Figure 2(a)

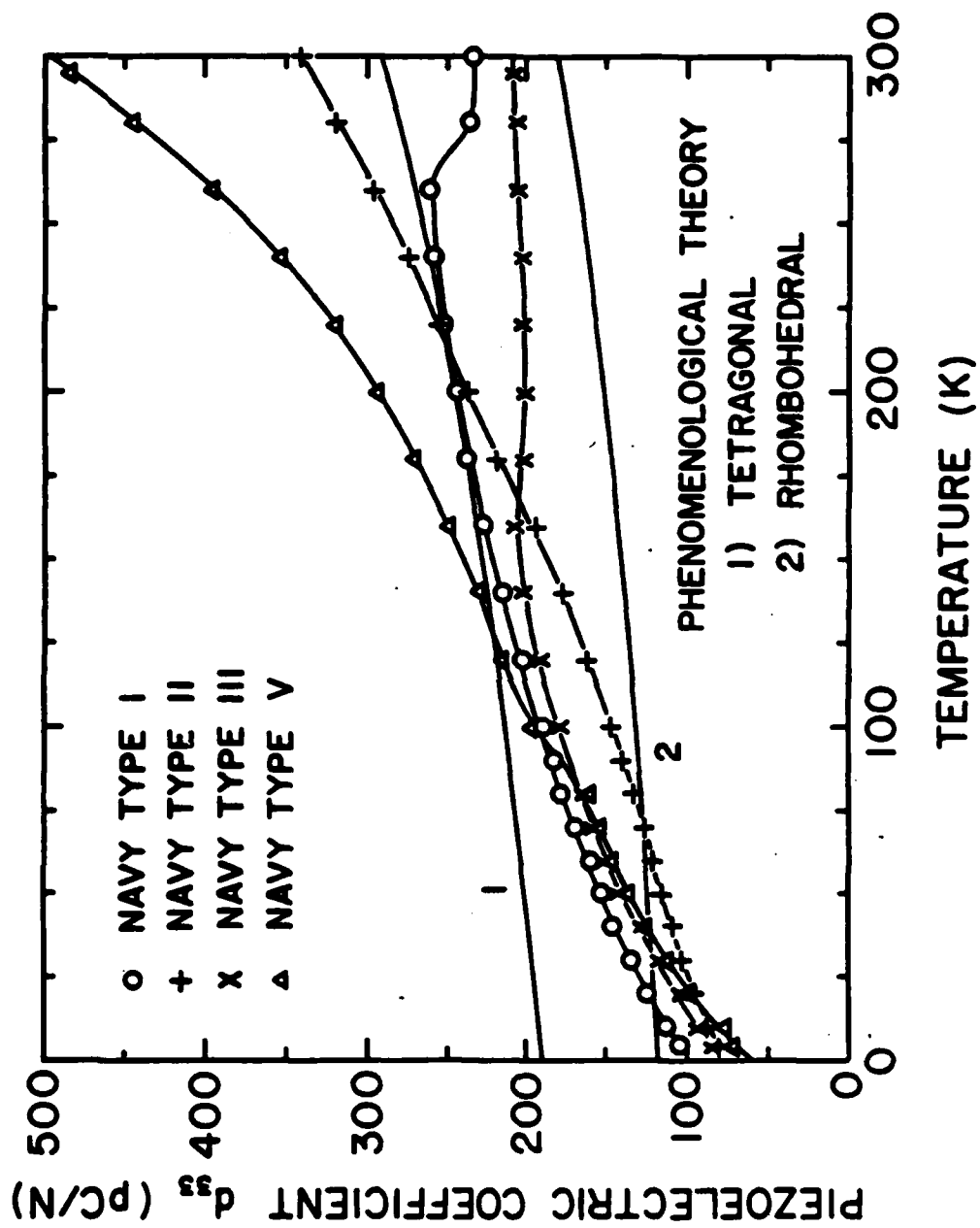


Figure 2(b)

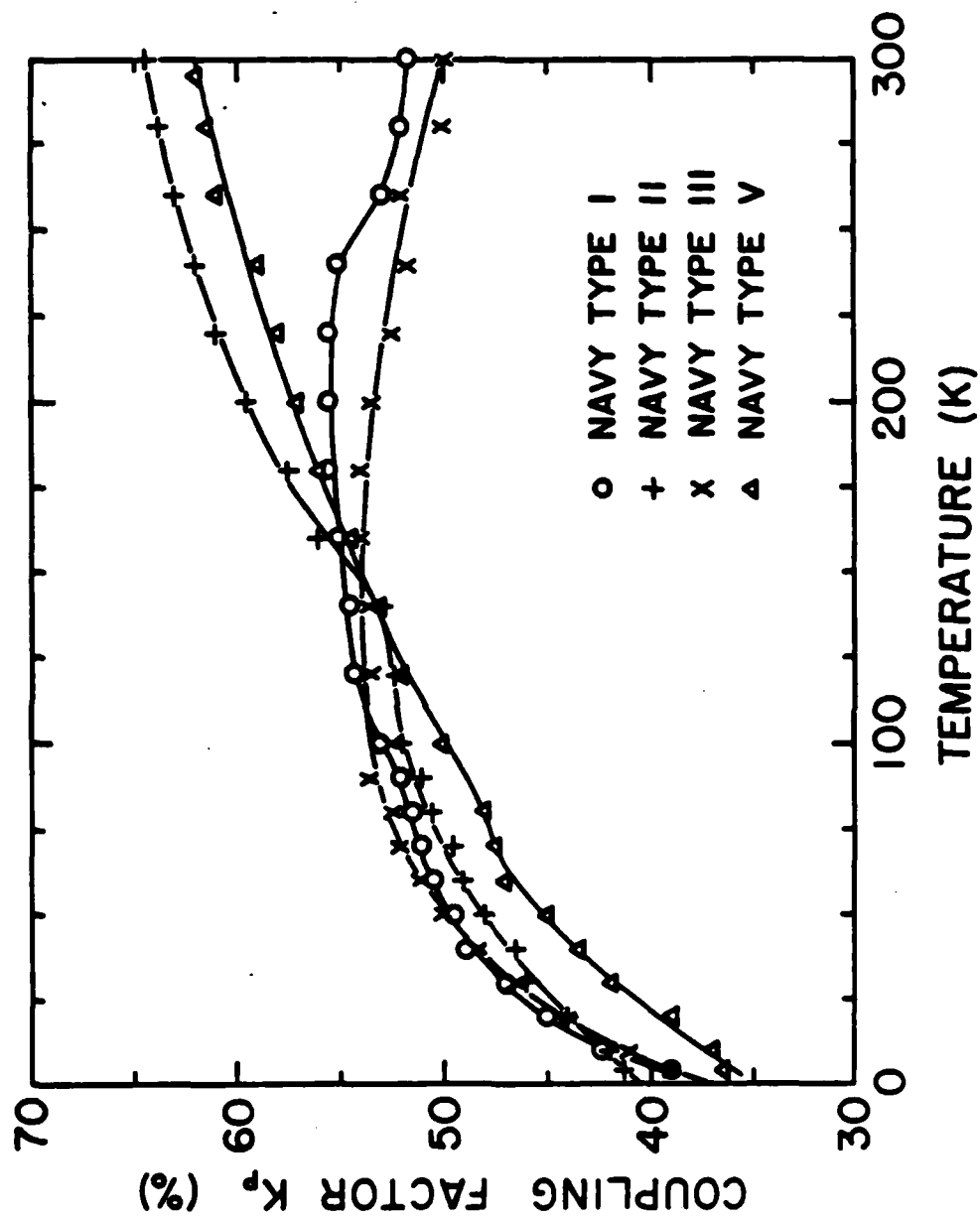


Figure 3(a)

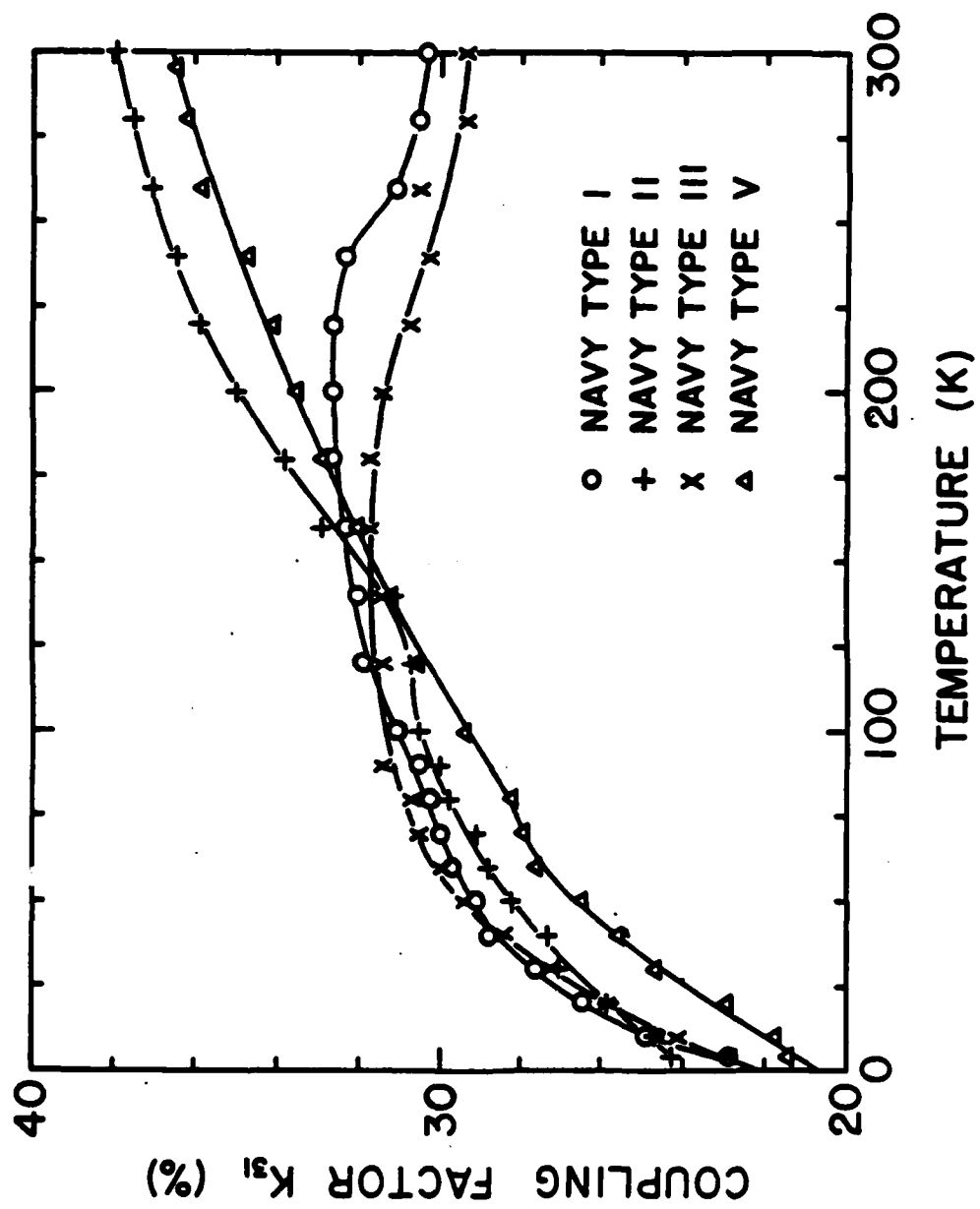


Figure 3(b)

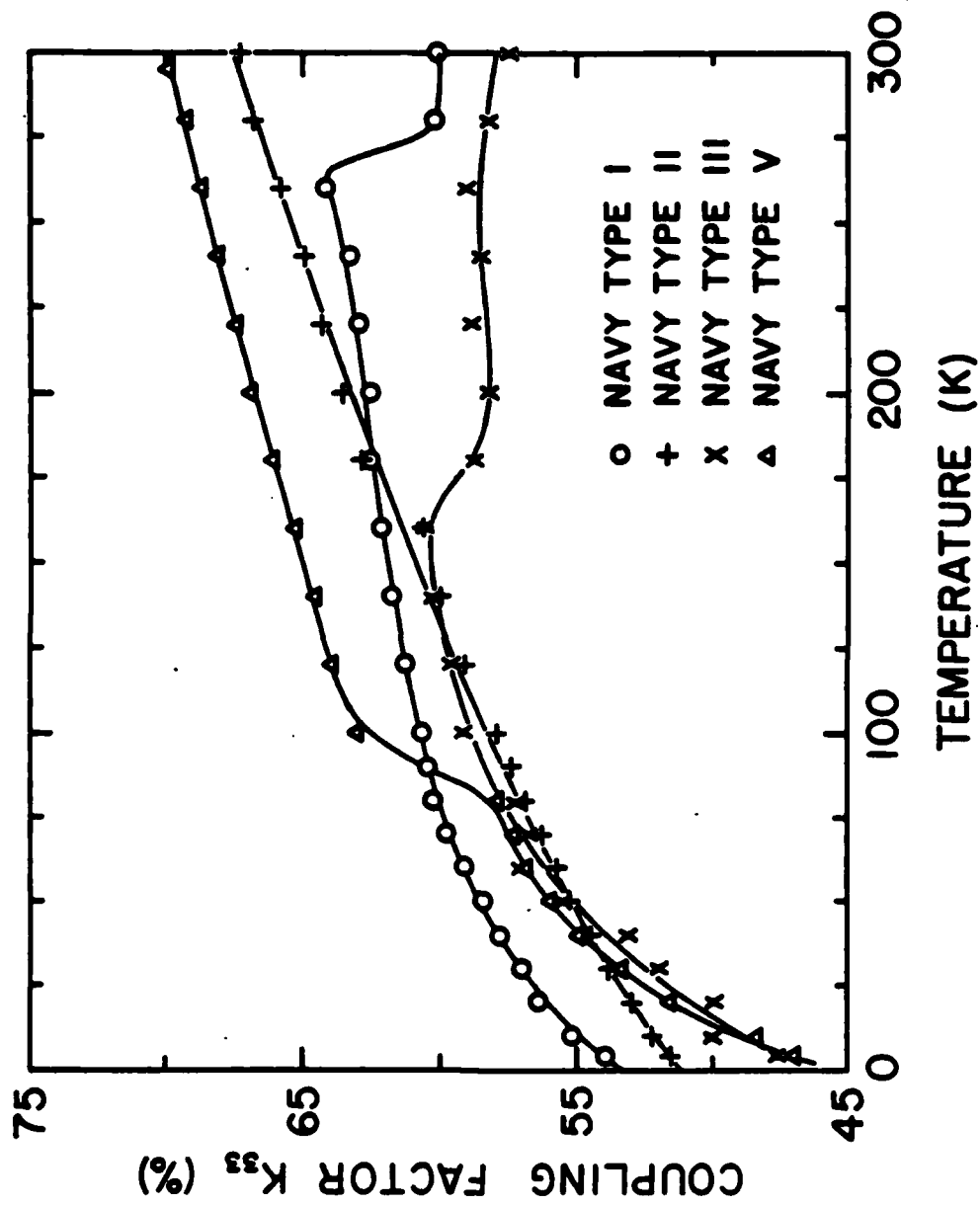


Figure 3(c)

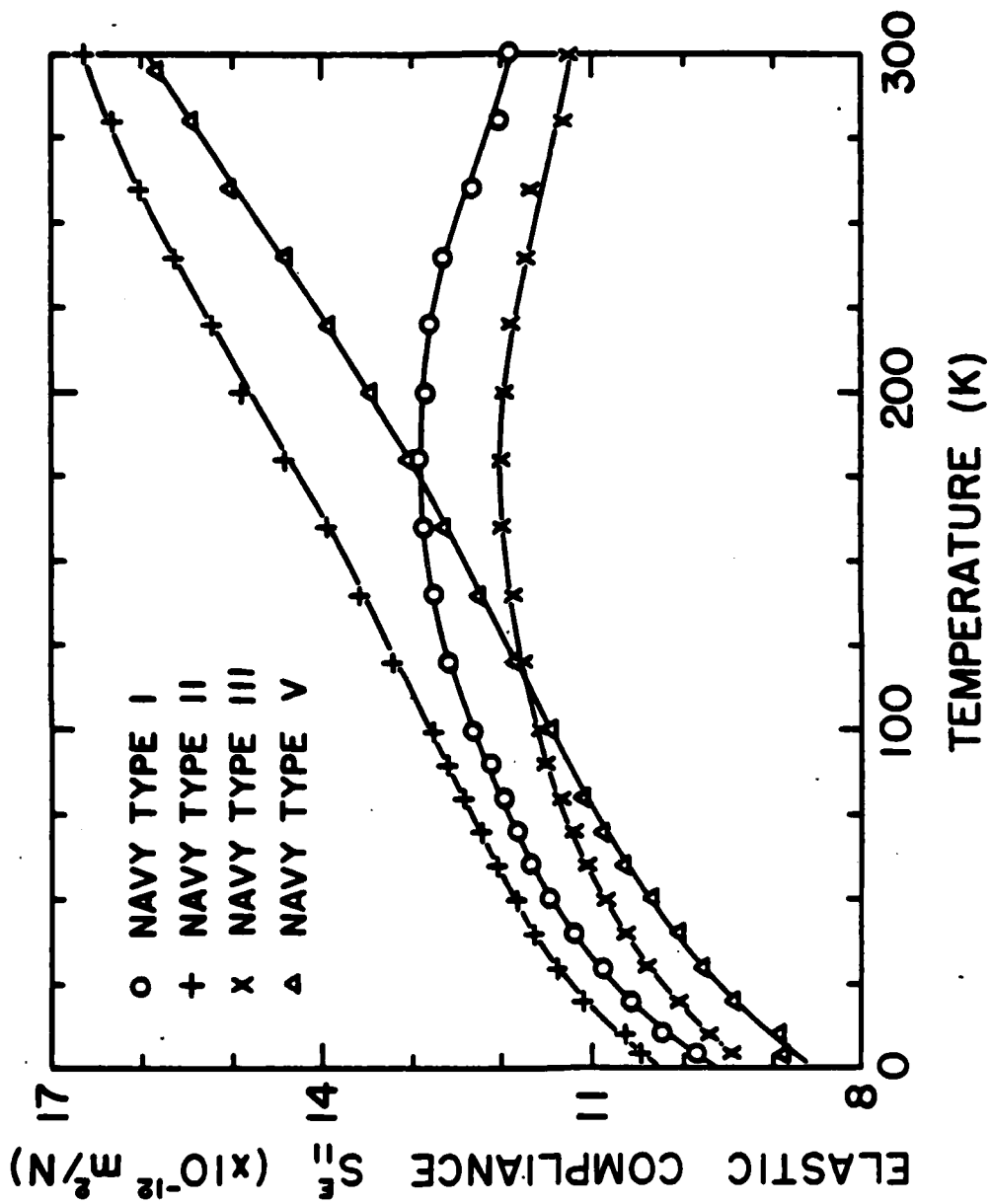


Figure 4

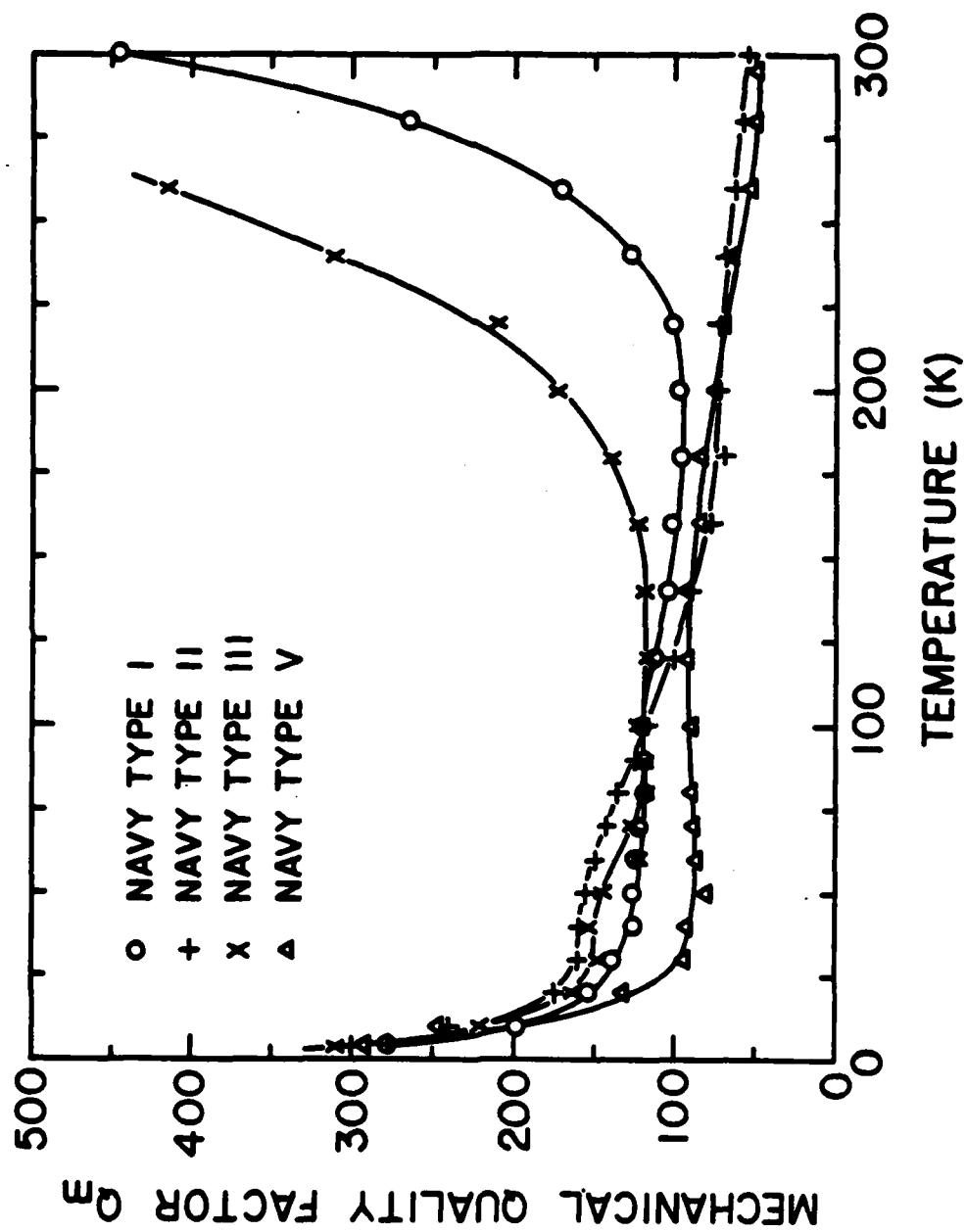


Figure 5

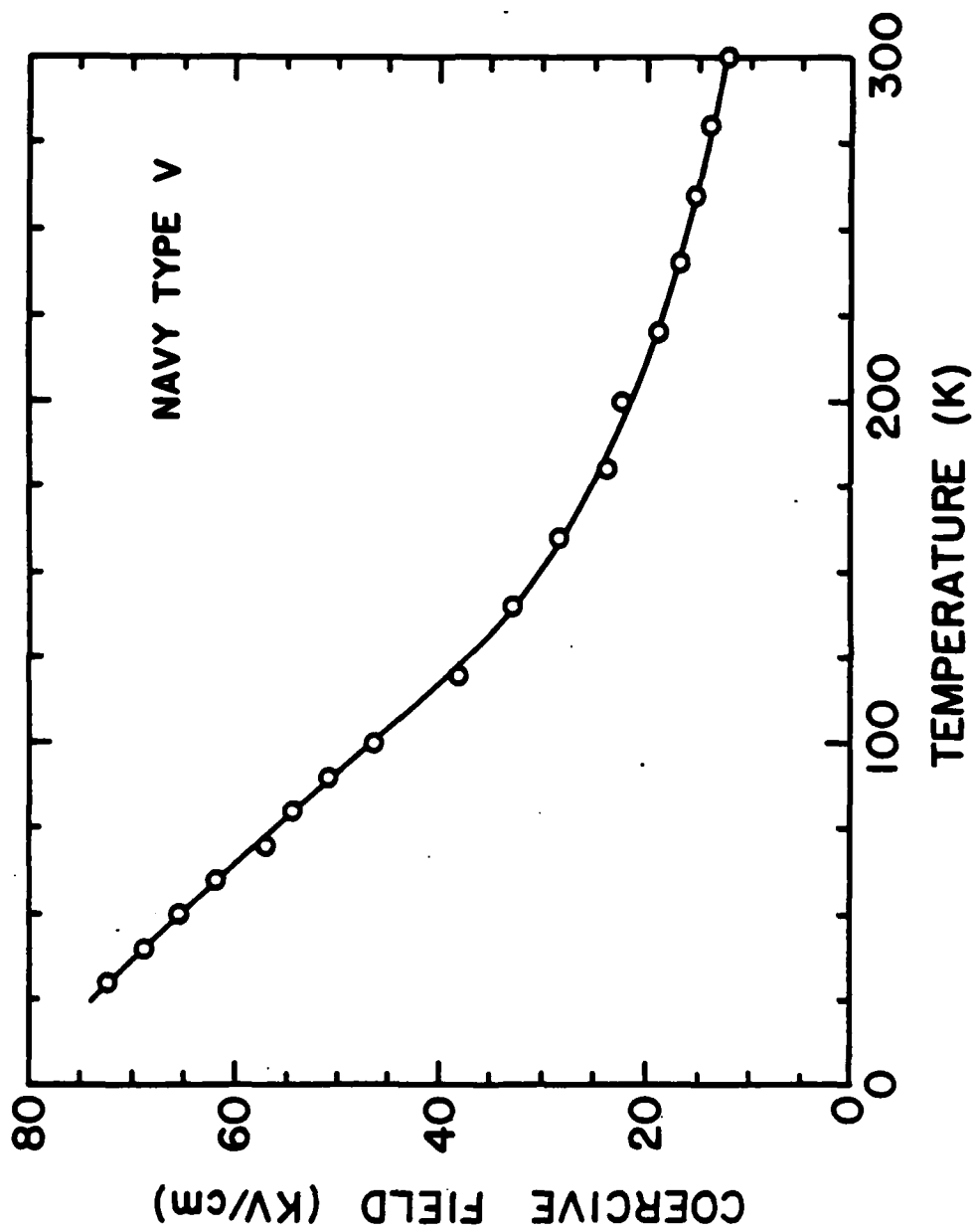


Figure 6

SOL-GEL DERIVED PbTiO_3 -POLYMER PIEZOELECTRIC COMPOSITES

D.L. Monroe, J.B. Blum and A. Safari

SOL-GEL DERIVED PbTiO_3 -POLYMER PIEZOELECTRIC COMPOSITES†

D.L. MONROE and J.B. BLUM
G.N. Howatt Laboratory, Department of Ceramics
Rutgers-The State University of New Jersey
PO Box 909 Piscataway NJ 08854

and

A. SAFARI
Materials Research Laboratory
Pennsylvania State University
University Park, PA 16802

(Received for Publication September 3, 1985)

Amorphous lead titanate powder was prepared using a sol-gel process. The powder was fired to temperatures ranging from 500°C to 1200°C and soaked for various lengths of time. X-ray diffraction confirmed that the fired powders were tetragonal PbTiO_3 . Surface area measurements indicated that the specific surface area of the powder decreased with increasing heat treatment. The powders were mixed with Eccogel polymer to make composites in which the ceramic phase constituted 60 percent by volume. Piezoelectric coefficients were found to be greatest for those composites containing powder fired to 1100°C and soaked for 1 hour. The d_{33} value obtained for this heat treatment was $540 \times 10^{-15} \text{ m}^2 \text{ N}^{-1}$.

INTRODUCTION

Lead zirconate titanate (PZT) is widely used as a transducer material because of its high piezoelectric coefficients. However, for hydrophones PZT is a poor choice for several reasons. PZT has a large piezoelectric d_{33} coefficient, but its hydrostatic strain coefficient, d_h ($=d_{33} + 2d_{31}$), is small because d_{33} and $2d_{31}$ are opposite in sign and almost cancel each other out. Moreover, the high permittivity of PZT ($K \sim 1800$) lowers the voltage coefficient, g_h , to miniscule values. In addition, the density of PZT (7.9 gm/cm^3) makes it difficult to obtain good impedance matching with water. PZT is a brittle ceramic and for some applications a more compliant material with better shock resistance is required.

†Communicated by Dr. G. W. Taylor

Other materials used for hydrophone applications are lead titanate, PbTiO_3 , and lead metaniobate, PbNb_2O_6 . Their d_h values are slightly higher than that of PZT and their g_h values are an order of magnitude better because of their modest dielectric constants. Unfortunately, PbTiO_3 and PbNb_2O_6 are also dense, brittle ceramics which undergo large volume changes at the Curie point, often fracturing during preparation.

Polyvinylidene fluoride, PVF_2 , offers several advantages over PZT and other piezoelectric ceramics. It has a low density and high flexibility. Although PVF_2 has low d_{33} and d_h , the piezoelectric voltage coefficient, g_h , is large because of its low relative permittivity.

There are, however, problems associated with the use of PVF_2 . The major problem is the difficulty in poling. A very high field is necessary to pole PVF_2 (1.2 MV/cm), this limits the thickness that can be poled. Pyroelectric phenomena in PVF_2 also produce undesirably large polarization fluctuations with temperature.

One approach to the problem is to develop composite materials in which the desired properties can be incorporated through the use of a combination of materials with different properties. In designing composite materials for hydrophone applications, a logical choice would be a piezoelectric ceramic and a compliant polymer. In such a composite, the ceramic produces a large piezoelectric effect, while the polymer phase lowers the density and permittivity yet increases the elastic compliance.

In a composite the electric flux pattern and the mechanical stress distribution, and hence the resulting physical and electromechanical properties, depend strongly on the manner in which the individual phases are interconnected. In this regard the connectivity of a composite, defined as the number of dimensions in which each component phase is continuous¹, is of crucial importance. When referred to an orthogonal axis system, each phase in a composite may be self-connected in zero, one, two, or three directions. For diphasic composites there are ten connectivity patterns, designated as 0-0, 0-1, 0-2, 0-3, 1-1, 1-2, 1-3, 2-2, 2-3, and 3-3.

During the past few years, a number of investigators have examined piezoelectric ceramic-polymer composites with different connectivity patterns. The piezoelectric properties of the composites depend, to a large extent, on the connectivity pattern of the constituent phases. A more ex-

tensive description of the work on ceramic-polymer composites can be found in recent review papers^{2,3}.

The simplest type of piezoelectric composite consists of a polymer matrix loaded with ceramic powder. In such a composite the ceramic particles are not in contact with each other while the polymer phase is self-connected in three dimensions (0-3 connectivity). Early attempts to fabricate flexible composites with piezoelectric ceramic particles were made by Kitayama⁴, Pauer⁵, and Harrison⁶. Wada and Hayakawa⁷ found the d_{33} coefficient of these composites were comparable with PVF_2 , but the d_h value was lower than those of solid PZT and PVF_2 polymer. To improve the properties of these composites Harrison fabricated a composite with much larger PZT particles (up to 2.4 mm). Here the particle size approached the thickness of the composite, and since the PZT particles extended from electrode to electrode, near saturation poling could be achieved.

An improved version of the 0-3 composite was fabricated by Banno⁸. Rather than using PZT as the ceramic filler, pure or modified PbTiO_3 was employed because of its greater piezoelectric anisotropy. The PbTiO_3 filler was prepared by water quenching the ceramic, thereby exploiting the high strain present in the material in order to produce fine powders. The average particle size was about 5 μm . To fabricate composite bodies, the piezoelectric powders and chloroprene rubber were mixed, rolled into 0.5 mm thick sheets at 40°C using a hot roller, and then heated at 190°C for 20 minutes under a pressure of 13 kg/cm^2 . The composites were poled in a field of 100-150 kV/cm for 30 minutes. The hydrostatic voltage coefficient, g_h , of pure PbTiO_3 composites was found to be comparable to that of PVF_2 polymer. The d_h value of 35 pC/N was independent of pressure and the g_h values were reduced only 2% when the pressure was increased to 40 MPa⁹.

As mentioned above, the PbTiO_3 powder used by Banno was produced by water quenching conventionally prepared ceramic samples. Recently, the sol-gel process has been used to prepare PbTiO_3 for study¹⁰⁻¹². The merits of sol-gel processing such as high purity, molecular homogeneity, and lower processing temperatures could offer advantages over conventional processing methods. The work reported is the initial study of the properties of piezoelectric composites incorporating sol-gel derived PbTiO_3 in an effort to examine its potential for technological use.

EXPERIMENTAL PROCEDURE

Gel Preparation

The procedure for preparing PbTiO_3 by the sol-gel method has been described in detail elsewhere^{10,12}. Briefly, the first step of the process was the synthesis of a "complex alkoxide", or precursor, solution. This was done by reacting lead acetate with titanium isopropoxide. Gels of the complex alkoxide were prepared by dissolving the complex in methoxyethanol. The water of hydrolysis was introduced slowly as a solution of methoxyethanol, water, and nitric acid.

For this study, the solutions were mixed in a cold bath consisting of alcohol and liquid nitrogen. This kept the temperature below 0°C and served to delay gellation. After mixing, the sol was poured into polystyrene petri dishes and allowed to gel.

Heat Treatment

The gels were dried at room temperature. Drying was complete in 3 to 4 days. The dried gels were crushed to a powder and fired in air to different temperatures and then held for various lengths of time. Samples fired to 500°C were held at that temperature for 0, 1, 2, and 4 hours. For these samples the furnace was heated to 200°C quickly, then the temperature rise was slow ($1^\circ\text{C}/\text{min}$ from 200 - 300°C) to ensure the adequate removal of water and organics. The temperature was held at 300°C for 1 hour and then increased to 500°C at $8^\circ\text{C}/\text{min}$. Powder fired to 600 and 800°C had about a $2^\circ\text{C}/\text{min}$ rise from room temperature to 300°C and a 1 hour hold at 300°C . The final soak temperature was reached at a rate of $5^\circ\text{C}/\text{min}$. Soak temperatures of 1000 , 1100 , and 1200°C were achieved by a $1^\circ\text{C}/\text{min}$ rise to 300°C , and then a $5^\circ\text{C}/\text{min}$ rise to the final temperature.

X-ray diffraction was performed on each of the fired powders. Specific surface area measurements were made using triple-point BET analysis. The quantity of powder produced was insufficient to measure the density.

The lead titanate powders were embedded into an epoxy matrix to make composites. Three samples were made from each heat treatment batch. Eccogel 1365-80 was mixed with the powder by hand. The ceramic

phase constituted 60 percent of the composite by volume. The mixtures were die pressed at 70 MPa (10,000 psi) and cured at 70°C for 8 hours. After slight polishing, air-dried silver paste electrodes were applied and the composites were poled in an 80°C silicone oil bath by applying a field of 80-100 kV/cm for 10 minutes. The piezoelectric coefficient, d_{33} , of the composites along the poling direction was measured using a Berlincourt d_{33} meter. The hydrostatic piezoelectric coefficient, g_h , was measured at a frequency of 50 Hz and a pressure of 0.7 MPa (100 psi). From the measured values of g_h , the hydrostatic piezoelectric coefficient, d_h , of the composites was calculated from the equation:

$$d_h = g_h \cdot \epsilon_0 \cdot k_{33}$$

where ϵ_0 is the permittivity of free space and k_{33} is the dielectric constant of the composite.

RESULTS AND DISCUSSION

X-ray diffraction (XRD) confirmed that all heat treatments yielded tetragonal PbTiO_3 as was expected based on previous results¹¹. As the heat treatment temperature and/or hold time was increased, the XRD peaks became narrower and more intense.

The specific surface area of the PbTiO_3 powder was found to decrease with increasing firing temperature as shown in Figure 1. This is attributed

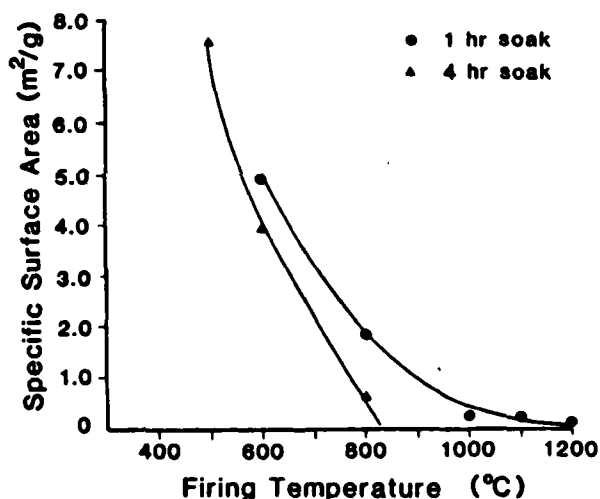


FIGURE 1 Specific Surface Area of the PbTiO_3 powders as a function of firing temperature and hold time.

to densification of the material. A hold time of 4 hours resulted in a trend similar to that of the 1 hour hold but shifted toward lower temperatures.

Though the density of the powder in this study could not be measured (insufficient amount of powder), it has been found that the density of sol-gel derived PbTiO_3 powder increases with increasing heat treatment¹³. The decrease in surface area and increase in density are accompanied by an increase in particle size. This accounts for some of the sharpening of X-ray diffraction peaks at higher temperatures.

The piezoelectric properties of the composites are given in Table 1. (The values listed are the average for three composites at each heat treatment.) Composites containing powders fired to 500°C and also 600/1 (Soak Temperature/Soak Time) were not polable. The d_{33} values rose from 11 pC/N for 600/4 and 800/1 to a maximum of 31 pC/N at 1100/1. The value dropped off to 17 for the 1200/1 treatment. Similarly, g_h rose to a maximum of $35 \times 10^{-3} \text{ VmN}^{-1}$ for 1100/1 and dropped to 16 for 1200/1. The decrease in piezoelectric properties for the higher firing temperature is probably due to the volatility of lead at this temperature.

TABLE 1 Piezoelectric Data

Heat Treatment		Properties		
Temp ($^\circ\text{C}$)	Time (hr)	d_{33} (pC/N)	g_h^a (10^{-3} Vm/N)	$d_h g_h$ ($10^{-15} \text{ m}^2/\text{N}$)
500	1,2,4	*	*	*
600	1	*	*	*
600	4	11	12	75
800	1	11	12	80
800	4	23	28	355
1000	1	28	30	420
1100	1	31	35	540
1200	1	17	16	110

^a - measured at 50 Hz, 100 psi

* - not polable

The hydrophone figure of merit $d_h g_h$ was also maximum for 1100/1. The value obtained for these composites was $540 \times 10^{-15} \text{ m}^2/\text{N}$. This, how-

ever, is only about half the value of d_{33} for other PbTiO_3 composites with 0-3 connectivity⁹.

Improving the piezoelectric properties of pure PbTiO_3 composites will be the subject of future work. Different and more consistent firing profiles will be employed in an effort to obtain higher mean piezoelectric coefficients. Though the results presented here are preliminary, they do show promise for the use of sol-gel derived lead titanate as a technological material.

SUMMARY

Pure crystalline PbTiO_3 powder was made by the sol-gel process. Heat treatment resulted in a decrease in specific surface area and an increase in density and particle size. When mixed with epoxy to form composites, fair piezoelectric properties resulted. Firing the powders to 1100°C and soaking for 1 hour gave the highest piezoelectric constants. Further research needs to be performed in this area to improve the composites.

ACKNOWLEDGEMENTS

This work was supported by the G.N. Howatt Foundation. The authors wish to thank Steve Gurkovich for his assistance in preparing the powders and for his helpful suggestions.

REFERENCES

1. R.E. Newnham, D.P. Skinner, and L.E. Cross, *Mater Res Bull*, 13, 525, (1978).
2. R.E. Newnham, A. Safari, J. Giniewicz, and B.H. Fox, *Ferroelectrics*, 60, 15, (1984).
3. R.E. Newnham, A. Safari, G. Sa-gong, and J. Giniewicz, *Proc IEEE Ultrasonics Symposium*, 501, (1984).
4. T. Kitayama and S. Sugawara, *Rept Proc Gr Inst Elec Comm Eng Japan*, CPM27-17, (1972).
5. L.A. Pauer, *IEEE Intl Conv Rec*, 1, (1973).
6. W.B. Harrison, *Proc Workshop on Sonar Transducer Materials*, Naval Research Laboratories, (1976).
7. Y. Wada and R. Hayakawa, *Japan J Appl Phys*, 15, 2041, (1976).
8. H. Banno, *Ferroelectrics*, 50, 3, (1983).

9. R.Y. Ting, Office of Naval Research, Orlando FL, unpublished.
10. S.R. Gurkovich and J.B. Blum, in *Ultrastructure Processing of Ceramics, Glasses, and Composites*, ed. by L.L. Hench and D.R. Ulrich, (Wiley-Interscience, New York, 1984), 152.
11. S.R. Gurkovich and J.B. Blum, *Ferroelectrics*, **62**, 189, (1985).
12. J.B. Blum and S.R. Gurkovich, to appear in *J Mater Sci*, (1985).
13. S.R. Gurkovich, Rutgers University, unpublished.

UNUSUAL PYROELECTRIC AND PIEZOELECTRIC PROPERTIES OF
FRESNOITE ($\text{Ba}_2\text{TiSi}_2\text{O}_8$) SINGLE CRYSTAL AND POLAR GLASS-CERAMICS

A. Halliyal, A.S. Bhalla, S.A. Markgraf, L.E. Cross and R.e. Newnham

UNUSUAL PYROELECTRIC AND PIEZOELECTRIC PROPERTIES OF FRESNOITE ($\text{Ba}_2\text{TiSi}_2\text{O}_8$) SINGLE CRYSTAL AND POLAR GLASS-CERAMICS

A. HALLIYAL, A. S. BHALLA, S. A. MARKGRAF, L. E. CROSS and
R. E. NEWNHAM

*Materials Research Laboratory, The Pennsylvania State University, University
Park, PA 16802 U.S.A.*

(Received October 17, 1984)

The dielectric, piezoelectric and pyroelectric properties of fresnoite ($\text{Ba}_2\text{TiSi}_2\text{O}_8$) single crystal and polar glass-ceramics were studied in the temperature range -150 to 200°C . The sign of pyroelectric coefficient is positive at room temperature and becomes negative at 190°C . The dielectric constant, pyroelectric coefficient and planar coupling coefficient show a maximum value at 160°C and the frequency constant shows a minimum at the same temperature. The probable reasons for the anomaly in these properties are discussed.

INTRODUCTION

Fresnoite ($\text{Ba}_2\text{TiSi}_2\text{O}_8$) has a noncentrosymmetric tetragonal structure and belongs to the polar point group $4mm$. Single crystals of fresnoite have been grown successfully by the Czochralski method by several workers.^{1,2} It has been shown that fresnoite has electromechanical coupling factors large enough for piezoelectric devices and that it is an interesting alternative substrate material for surface acoustic wave (SAW) devices.^{1,3-5} The SAW characteristics of fresnoite are intermediate between those of LiNbO_3 and LiTaO_3 . The pyroelectric coefficient of fresnoite is reported to be small and positive ($+10 \mu\text{C}/\text{m}^2 \text{ }^\circ\text{K}$). However, no detailed studies have been carried out regarding the temperature variation of piezoelectric and pyroelectric properties of fresnoite. It has also been shown that polar glass-ceramics with the fresnoite crystalline phase can be prepared by recrystallizing glasses of slightly modified compositions.^{6,7} In these glass-ceramics, the polar texture results from needle-like fresnoite crystals growing from the glass surface during crystallization. The polar glass-ceramics showed piezoelectric and pyroelectric properties comparable to the single crystal properties.

In the present work, the dielectric, piezoelectric, and pyroelectric properties of fresnoite single crystal and glass-ceramics were studied in more detail. All of the above properties were studied as a function of temperature in the range -150 to 200°C .

EXPERIMENTAL PROCEDURE

Fresnoite crystals were grown by the Czochralski method from a stoichiometric melt. Crystals were grown in a platinum crucible on a $\langle 001 \rangle$ seed. Growth conditions were as follows: seed rotation speed 10–15 rpm; pulling speed 1.0 mm/hr, crucible rotation rate: 5 rpm. The resulting boules were colorless and transparent. *c* plates were cut from the boule and circular samples were prepared (5 mm dia, 0.5 mm thick). The major surfaces of the samples were coated with sputtered gold electrodes.

Glass samples containing one mole of excess silica ($2\text{BaO} \cdot 3\text{SiO}_2 \cdot \text{TiO}_2$) were prepared by mixing reagent grade chemicals and melting the batch in a platinum crucible. Glass-ceramic samples were prepared by crystallizing the glasses in a large temperature gradient normal to the surface of glass. The details of sample preparation technique can be found in References 6–8. Microstructure studies indicated that needle-like crystals grow from the surface into the bulk along the direction of temperature gradient. For measurements of all the properties, sections were cut normal to the temperature gradient and gold electrodes were sputtered on the major surfaces.

The dielectric constant and dissipation factors were measured at different frequencies using a capacitance bridge. Pyroelectric coefficients were determined by the

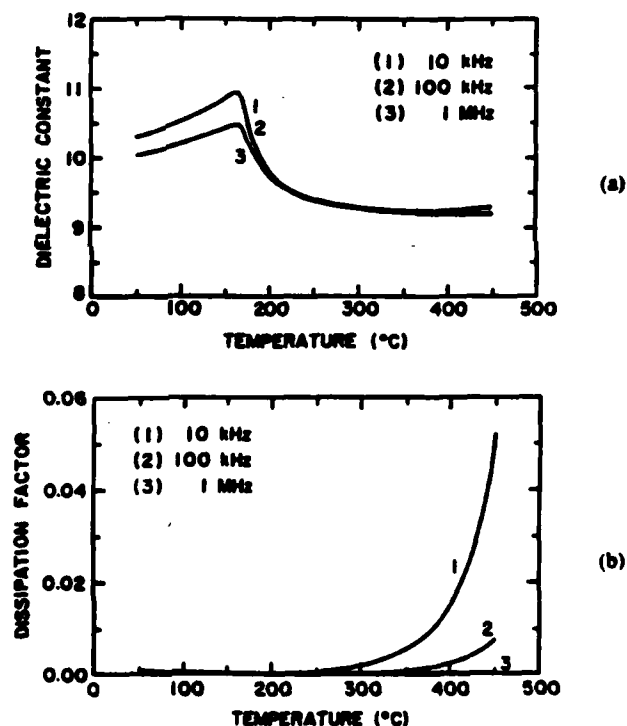


FIGURE 1 Dielectric constant (a) and dissipation factor (b) of $\text{Ba}_2\text{TiSi}_2\text{O}_9$ single crystal as a function of temperature and frequency.

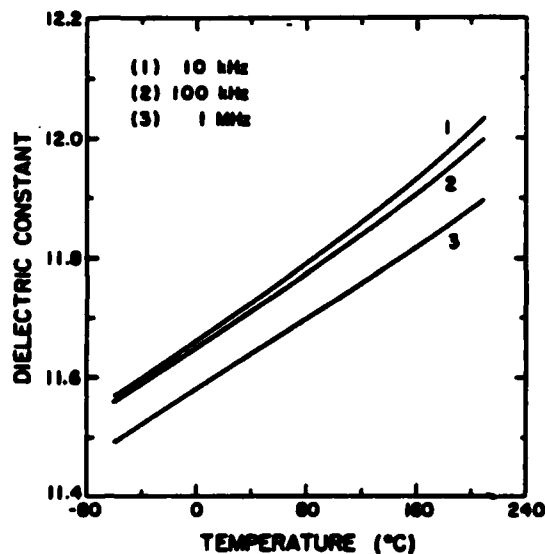


FIGURE 2 Dielectric constant of $2\text{BaO}\cdot 3\text{SiO}_2\cdot \text{TiO}_2$ glass a function of temperature and frequency.

Byer-Roundy⁹ technique. The heating and cooling rates employed were $4^\circ\text{C}/\text{min}$. The electromechanical properties were determined by standard resonance techniques. All the above properties were measured as a function of temperature in the range -150 to 200°C , both in heating and cooling cycles. Piezoelectric d_{33} coefficients were measured using a Berlincourt- d_{33} meter.

RESULTS

The dielectric constant and dissipation factor of fresnoite single crystals are shown in Figure 1. A broad peak was observed in the dielectric constant near 160°C and remained practically constant above 200°C . Surprisingly, no corresponding peak was observed in the dissipation factor curve. The dielectric losses increased at higher temperature, probably due to conduction losses. The dielectric constant of fresnoite glass (Figure 2) increases almost linearly with temperature without showing an anomaly in the temperature range -80 to 200°C . The dielectric spectrum of fresnoite glass-ceramic (Figure 3) is very similar to that of fresnoite single crystal, except that the dielectric constant peak occurs at 120°C instead of 160°C . In the glass-ceramic the only crystalline phase present was fresnoite, which indicates that the anomaly observed in the dielectric constant is an intrinsic property of fresnoite. The difference in the temperature of about 40° in the peak positions of dielectric constant of single crystal and glass-ceramics might be because of nonstoichiometric composition of glass-ceramics.

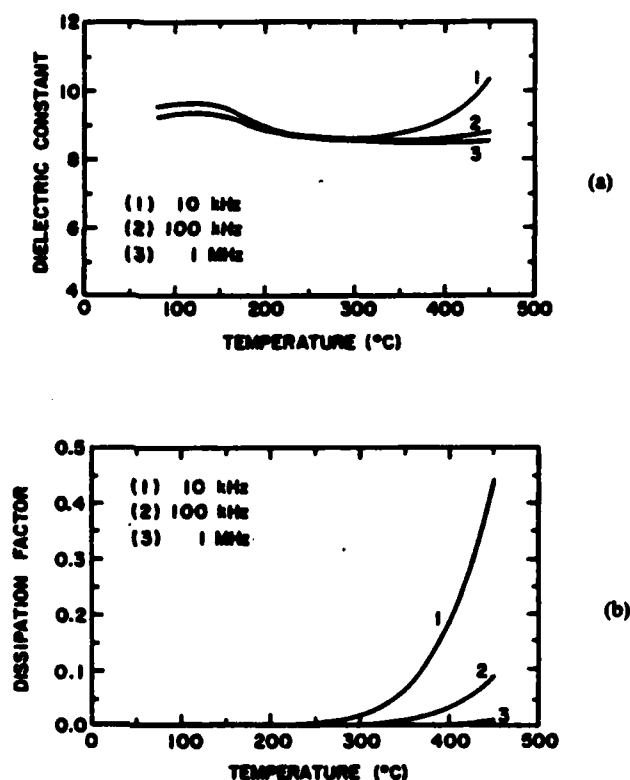


FIGURE 3 Dielectric constant (a) and dissipation factor (b) of 2BaO-3SiO₂-TiO₂ glass-ceramic as a function of temperature and frequency.

The variation of pyroelectric coefficient p_3 of fresnoite single crystal as a function of temperature is shown in Figure 4. The pyroelectric coefficient is positive at room temperature and increases with temperature, reaching a maximum at 160°C. At still higher temperatures, p_3 decreases very quickly and becomes negative. A similar behavior is observed in glass-ceramics also (Figure 5). The variation of polarization (P) with temperature is shown in Figure 6, where P is arbitrarily taken as zero at -140°C. The polarization increases with temperature in accordance with the positive sign of p_3 . A broad peak in polarization is observed at 160°C and beyond this temperature polarization decreases with temperature giving a negative pyroelectric coefficient.

The variation of planar mode frequency constant N_p and coupling coefficient k_p for single crystal and glass-ceramic are shown in Figures 7 and 8 respectively. For single crystal, the frequency constant decreases with temperature showing a minimum at 160°C and increasing sharply above 160°C. The coupling coefficient shows a maximum at 160°C. A similar behavior is observed in the case of glass-ceramics with the minimum in N_p occurring at 120°C. At the inflection point, the value of

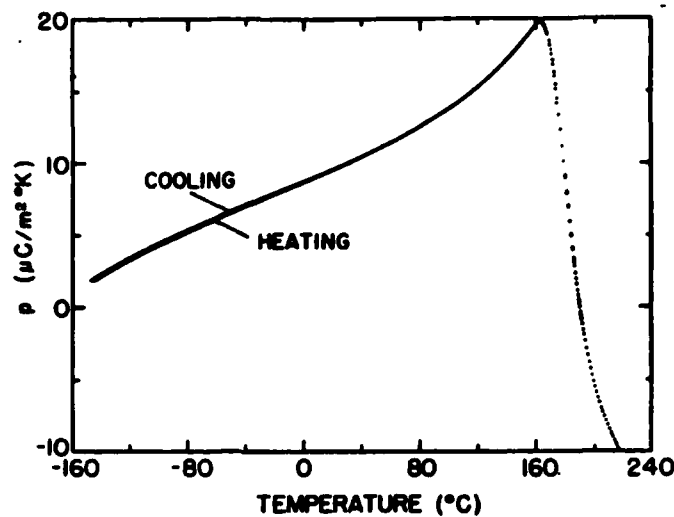


FIGURE 4 Variation of pyroelectric coefficient (p) of $\text{Ba}_2\text{TiSi}_2\text{O}_8$ single crystal as a function of temperature.

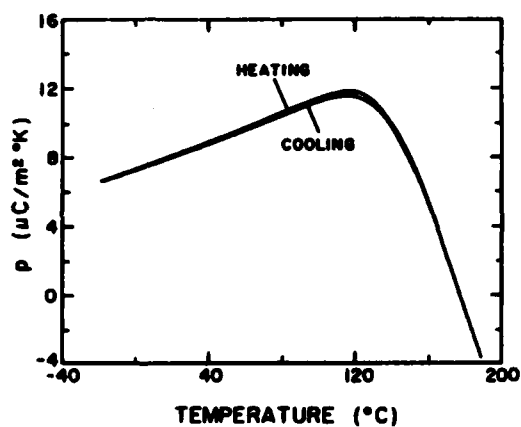


FIGURE 5 Pyroelectric coefficient as a function of temperature for $2\text{BaO}-3\text{SiO}_2-\text{TiO}_2$ glass-ceramics.

temperature coefficient of resonance (TCR), defined as

$$\text{TCR} = \frac{1}{f_r} \frac{\partial f_r}{\partial T} \quad (1)$$

is zero. Here, f_r is the resonance frequency at temperature T .

It should be noted that the minimum in N_p and the maximum in the pyroelectric coefficient and dielectric constant occur at the same temperature. The critical temperature where the anomaly in the above properties occurs is 160°C for single

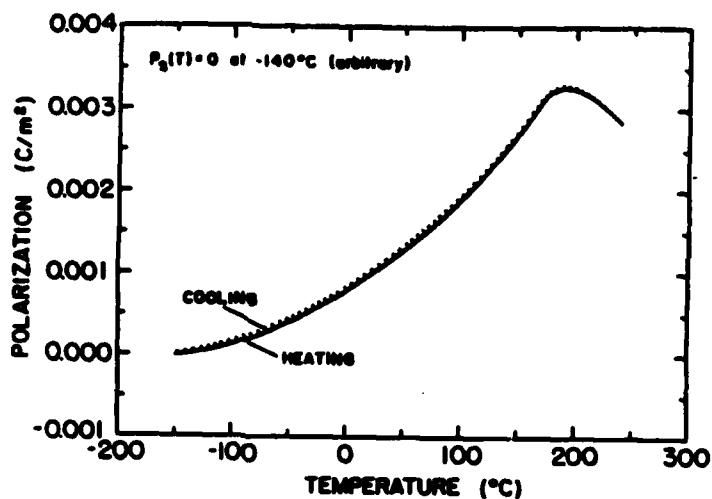
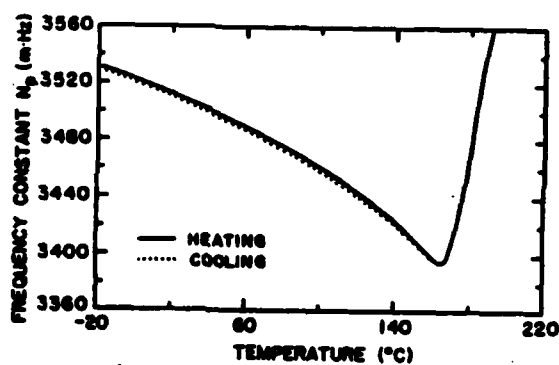
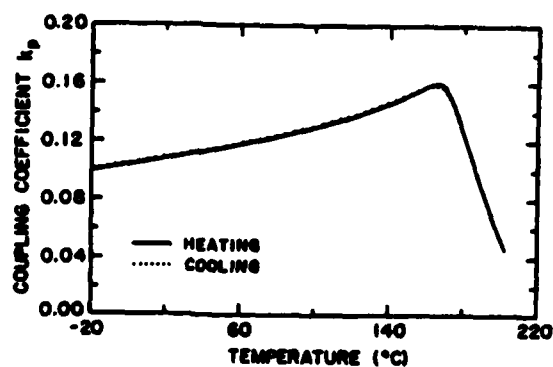


FIGURE 6 Polarization of $\text{Ba}_2\text{TiSi}_2\text{O}_9$ single crystal as a function of temperature.



(a)



(b)

FIGURE 7 Frequency constant N_p , (a) and electromechanical coupling k_p , (b) of $\text{Ba}_2\text{TiSi}_2\text{O}_9$ single crystal as a function of temperature.

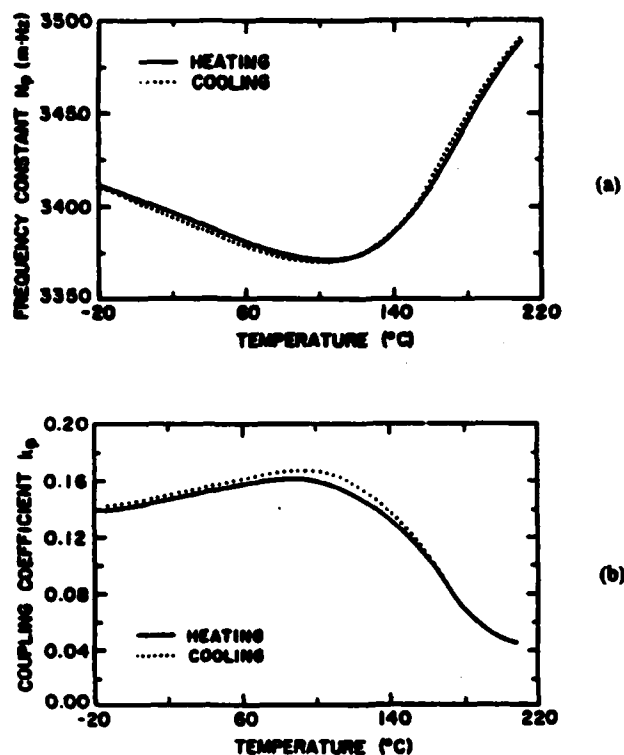


FIGURE 8 Frequency constant N_p , (a) and electromechanical coupling coefficient k_p , (b) of $2\text{BaO}-3\text{SiO}_2-\text{TiO}_2$ glass-ceramic.

crystal and 120°C for glass-ceramics. The room temperature properties of both single crystal and glass-ceramic are given in Table I.

DISCUSSION

The unusual features in the properties of both fresnoite single crystals and glass-ceramics can be summarized as follows:

- (1) In both single crystal and glass-ceramics the sign of pyroelectric coefficient is positive at room temperature and becomes negative at about 190°C .
- (2) A sharp peak in the dielectric constant, pyroelectric coefficient, and coupling coefficient are observed at 160°C in the case of single crystal and at 120°C in the case of glass-ceramics. A minimum is observed in resonance frequency at the same temperatures.

The difference in temperature between single crystal and glass-ceramics where the properties show an anomaly may be due to the nonstoichiometric composition of glass-ceramics. Hence all the properties of glass-ceramic described earlier reflect the properties of fresnoite crystalline phase.

TABLE I
Room temperature properties of fresnoite

Property	Ba ₂ TiSi ₂ O ₈ Single crystal	2BaO-3SiO ₂ -TiO ₂ Glass-ceramic
Density (gm/cc)	4.45	4.01
Dielectric constant		
K_{33} (1 kHz)	11.0	9.0
$\tan \delta$	<0.001	<0.001
Pyroelectric coefficient		
p_3 ($\mu\text{C}/\text{m}^2 \cdot ^\circ\text{K}$)	+10	+8
d_{33} (pC/N)	8	7
d_{31} (pC/N)	2.7	1.8
d_{32} (pC/N)	12.7	8.8
g_{33} (10^{-3} V m/N)	82	88
g_{31} (10^{-3} V m/N)	130	110
$d_{31}g_{31}$ (10^{-15} m ² /N)	1650	970
Frequency constants		
N_p (m · Hz)	2350	2250
N_s (m · Hz)	3500	3500
Electromechanical coupling coefficients		
k_t	0.25	0.25
k_p	0.12	0.14
Mechanical quality factor Q	3000	800
Temperature coefficient of resonance (ppm/°C)	100	100

The anomalies occurring in all the properties in fresnoite suggest the possibility of a structural phase transition near 160°C. In most ferroic crystals, structural phase transitions are invariably accompanied with anomalies in dielectric and related properties.

Several experiments were done in an attempt to detect a structural change in fresnoite near 160°C. X-ray diffractometer powder patterns were recorded at several temperatures from room temperature up to 400°C at intervals of 50°, using a high temperature x-ray diffractometer unit. No significant changes in either d spacings or intensities of different reflections could be detected. An analysis of the single crystal x-ray intensity data taken at 24° and 300°C did not indicate any change in the crystal symmetry or space group of the crystal. The results of the single crystal x-ray work will be published elsewhere.¹⁰ Thus within their resolution limit, the above experiments failed to give any indication of a structural phase change in fresnoite. However, the possibility of a subtle structural change cannot be completely ruled out. If there is a phase transition near 160°C, it is clear that it is a polar to polar type of transition. However, it is not a ferroelectric or ferroelastic type of transition, since no ferroelectric or ferroelastic properties are observed in fresnoite below the transition.

If the possibility of a phase transition near 160°C is ruled out, it is somewhat difficult to explain the origin of all the anomalies which occur at exactly the same temperature, with practically no hysteresis. In a piezoelectric polar crystal, with reasonably high electromechanical coupling all the anomalies are coupled. The observed anomalies in the properties might have their origin in either elastic, dielectric or piezoelectric nature of the crystal, but because of the coupling between these properties, we can expect changes in all the properties.

The origin of the anomaly is probably not dielectric because the change in dielectric constant from 0° to 500°C is very small. For both single crystal and glass-ceramics, the planar and thickness mode resonance frequencies were in the range 0.4 to 0.6 MHz and 4 to 6 MHz respectively. Hence the dispersion observed in the dielectric constant (Figures 1 and 3) is probably due to the mechanical resonances. To verify whether the dielectric anomaly still remains in clamped crystal, the dielectric constant was measured at 10 MHz, which is above all major resonances. A similar peak in dielectric constant was observed near 160°C, for 10 MHz measurement also. Since the anomaly in the dielectric constant was observed in clamped crystals also, the origin of the anomalies in all the properties is probably not piezoelectric. The most probable cause for the anomaly in all the properties seems to be the anomalous behavior of a few of the elastic constants near 160°C. Because of the coupling between elastic and piezoelectric properties, we might expect anomaly in the piezoelectric properties also. Measurement of the temperature dependence of all the elastic constants and thermal expansion coefficients from room temperature up to 250°C is certainly necessary to confirm the above argument.

The reversal of sign in pyroelectric coefficient is a rare phenomenon and can occur without a structural phase transition. A number of materials show a sign reversal, going from positive to negative (or vice versa) at a certain temperature: $\text{Li}_2\text{SO}_4 \cdot \text{H}_2\text{O}$,¹¹ $\text{Ba}(\text{NO}_3)_2$,¹² $\text{Ba}_2\text{TiGe}_2\text{O}_8$,¹³ and $(\text{NH}_4)_2\text{SO}_4$.¹⁴ The reason for the sign reversal of pyroelectric coefficient in many of these materials thought to be the cancellation of primary and secondary pyroelectric effects as discussed below. The magnitude and sign of secondary pyroelectric coefficient at a particular temperature can be calculated by knowing the elastic, piezoelectric and thermal expansion coefficients of the material at that temperature. Thus because of the coupling between these properties, anomalous changes in elastic or piezoelectric properties can lead to anomalies in pyroelectric properties also. A simple calculation of the sign and magnitude of secondary pyroelectric coefficient in fersite can be made is described below.

The pyroelectric coefficient (p) of a material under constant stress and electric field is defined by the relation

$$p = \left(\frac{\partial P_s}{\partial T} \right)_{E, \sigma} \quad (2)$$

where P_s is the spontaneous polarization, T is the temperature, E the electric field and σ the stress. The measured pyroelectric coefficient (at constant stress) is the sum of two terms given by

$$p_i^s = p_i^e + d_{ijk}^T C_{jkm}^T E_m^s \alpha_{im}^s \quad (3)$$

where p_i^s is the total pyroelectric effect measured at constant stress and p_i^e the pyroelectric effect at constant strain is called the primary effect. The second term is the pyroelectric contribution due to the deformation of the crystal via the expansion coefficient and the piezoelectric terms. d_{ijk}^T represents the piezoelectric tensor at constant temperature, C_{jkm}^T is the elastic stiffness coefficient at constant temperature and electric field and α_{im}^s is the thermal expansion coefficient at constant stress. All terms in the previous equation are at constant electric field.

In ferroelectric pyroelectrics the primary effect is large and negative, because the spontaneous polarization decreases with increasing temperature. The secondary effect is considerably smaller and may have either sign depending on the values of coefficients. Thus in ferroelectric materials, the experimentally observed pyroelectric coefficients are dominated by the primary effect and are negative. In nonferroelectric materials there is no simple way to predict the sign and magnitude of primary and secondary pyroelectric effects. In practice, the total pyroelectric effect can be measured and the secondary effect calculated from the coefficients d , α and C .

For the point group 4 mm of $\text{Ba}_2\text{TiSi}_2\text{O}_8$, the secondary pyroelectric coefficient is given by the following equation.¹⁵

$$p_{\text{sec}} = 2d_{31}(C_{11}\alpha_1 + C_{12}\alpha_1 + C_{13}\alpha_3) + d_{33}(2C_{13}\alpha_1 + C_{33}\alpha_3) \quad (4)$$

For $\text{Ba}_2\text{TiSi}_2\text{O}_8$ single crystals all the piezoelectric and elastic constants are known. The sign of d_{31} is positive in this material. When calculations are made using Equation (4), we obtain $p_{\text{sec}} = +16.5 \mu\text{C}/\text{m}^2 \text{ } ^\circ\text{K}$.

In Equation (3), if at a particular temperature the primary and secondary parts are equal in magnitude but opposite in sign, the pyroelectric coefficient at constant stress p'_T will be zero. This kind of behaviour has been reported in $\text{Li}_2\text{SO}_4 \cdot \text{H}_2\text{O}$.¹¹ In this material the secondary effect is positive at all temperatures whereas the primary effect is positive only above 158°K . A sign change in the pyroelectric coefficient occurs at 106°K because of the cancellation of primary and secondary parts. In addition, the pyroelectric coefficient exhibits a broad extremum at 50°K .

In the case of $\text{Ba}_2\text{TiSi}_2\text{O}_8$ crystal, the pyroelectric coefficient is positive in the temperature range -150° to $+190^\circ\text{C}$, indicating that p_{sec} is larger than p_{primary} in this temperature range. The pyroelectric coefficient goes through a maximum at about 160°C and changes its sign from positive to negative at about 190°C which implies that the primary effect dominates. A calculation of p_{primary} and p_{sec} at different temperatures can be done if we know the temperature variation of all the elastic, piezoelectric and thermal expansion coefficients of fresnoite near the anomaly.

APPLICATION IN PYROELECTRIC AND PIEZOELECTRIC DEVICES

The room temperature dielectric, piezoelectric and pyroelectric properties of fresnoite are listed in Table I. In this section a brief evaluation of the properties of fresnoite is given for pyroelectric detectors and hydrophones.

To determine the usefulness of a pyroelectric material for a specific application, different figures of merit are used which combine the pyroelectric, dielectric and thermal properties of the material.^{16,17} The commonly used figures of merit are defined below.

$$M_1 = p/K \text{ for a quick evaluation of the material}$$

$$M_2 = p/\rho cK \text{ for a fast response detector}$$

$$M_3 = \frac{p}{\rho cK^{1/2} \tan \delta^{1/2}} \text{ for vidicon}$$

TABLE II

Room temperature pyroelectric figures of merit

Property	$\text{Ba}_2\text{TiSi}_2\text{O}_9^*$ Single crystal		$2\text{BaO} \cdot 3\text{SiO}_2 \cdot \text{TiO}_2$ Glass-ceramic	LiTaO_3 single crystal
	at 25°C	at 160°C		
p_3 ($\mu\text{C}/\text{m}^2 \cdot ^\circ\text{K}$)	+10	+20	+8	-180
M_1 ($\mu\text{C}/\text{m}^2 \cdot ^\circ\text{K}$)	0.95	1.82	0.88	3.27
M_2 (10^{-12} C m/J)	0.46	0.9	0.44	1.04
M_3 (10^{-12} C m/J)	46.7	92	41.3	98

*For calculation, the values for density and specific heat were assumed to be the same at 25°C and 160°C.

In the above equations, p is the pyroelectric coefficient, K is the dielectric constant, ρ is the density, c is the volume specific heat and $\tan\delta$ is the dielectric loss. The values of M_1 , M_2 , and M_3 of both fresnoite single crystal and glass-ceramics are listed in Table II, along with the values for LiTaO_3 which is at present most widely used pyroelectric material. From the table it can be seen that at room temperature the figures of merit of fresnoite are about 25 to 30% of the corresponding values of LiTaO_3 . The transition at 160°C is highly reproducible with practically no hysteresis. The nonhysteresis behavior near the transition is a very useful feature in the high temperature pyroelectric point detector application. The values of figures of merit M_1 , M_2 , and M_3 of fresnoite at 160°C are comparable with those of LiTaO_3 . Since fresnoite is a nonferroelectric polar material, there will not be any problems of depoling which is a limitation with most of the ferroelectric materials. Fresnoite is a promising material for high temperature pyroelectric detectors.

The measured values of the dielectric constant, d_{33} , and g_h of fresnoite single crystal and glass-ceramics are listed in Table I, along with the calculated values of g_{33} , d_h and $d_h g_h$. The values of g_h and the product of $d_h g_h$ of fresnoite are comparable to PVF_2 and much higher than lead zirconate titanate (PZT) ceramics. Although the values of d_{33} and d_h of fresnoite are comparatively low, the magnitudes of g_{33} and g_h are high because of their low dielectric constant. The values of g_h remains practically constant up to a pressure of 35 MPa. Hence fresnoite can be an excellent candidate material for several piezoelectric devices like hydrophones. A more detailed discussion of the advantages of using fresnoite in piezoelectric devices can be seen in Reference 18.

ACKNOWLEDGMENTS

We thank all our colleagues in the ferroelectrics group at MRL for their help in this work. This work was supported by the Army Research Office through Contract #DAAG29-80-C-0008 and the National Science Foundation Grant No. DMR-8303906.

REFERENCES

1. M. Kimura, Y. Fujino and T. Kawamura, *Appl. Phys. Lett.*, **29**, 227 (1976).
2. S. Haussuhl, J. Eckstein, K. Reicher and F. Wallarafen, *J. Cryst. Growth*, **40**, 200 (1977).
3. M. Kimura, *J. Appl. Phys.*, **48**, 2850 (1977).

4. H. Yamauchi, *J. Appl. Phys.*, **49**, 6162 (1978).
5. J. Melngailis, J. F. Vetelno, A. Jhunjunwala, T. B. Reed, R. E. Fahey and E. Stein, *Appl. Phys. Lett.*, **32**, 203 (1978).
6. A. Halliyal, A. S. Bhalla, R. E. Newnham and L. E. Cross, *J. Mater. Sci.*, **16**, 1023 (1981).
7. A. Halliyal, A. S. Bhalla, R. E. Newnham, *Mat. Res. Bull.*, **18**, 1007 (1983).
8. G. J. Gardoee, R. E. Newnham and A. S. Bhalla, *Ferroelectrics*, **33**, 155 (1981).
9. R. L. Byer and C. B. Roundy, *Ferroelectrics*, **3**, 333 (1972).
10. S. A. Markgraf, *et al.* (to be published).
11. S. B. Lang, *Phys. Rev.*, **B4**, 3603 (1970).
12. V. V. Gladkii and I. S. Zheludev, *Sov. Phys. Cryst.*, **10**, 63 (1965).
13. H. Schmid, P. Genequand, H. Tippmann, G. Pouilly and H. Guedu, *J. Mater. Sci.*, **13**, 2257 (1978).
14. N. Yamada, *J. Phys. Soc. Jap.*, **46**, 561 (1979).
15. A. S. Bhalla and R. E. Newnham, *Phys. Stat. Sol. (a)*, **58**, K19 (1980).
16. E. H. Putley, in *Semiconductors and semimetals*, Vol. 5, Ed. by R. D. Willardson and A. C. Beer, Academic Press, NY, page 259 (1981).
17. S. G. Porter, *Ferroelectrics*, **33**, 193 (1981).
18. A. Halliyal, A. Safari, A. S. Bhalla, R. E. Newnham and L. E. Cross, *J. Am. Cer. Soc.*, **67**, 331 (1984).

PHASE TRANSITIONS, DIELECTRIC, PIEZOELECTRIC AND PYROELECTRIC
PROPERTIES OF BARIUM TITANIUM GERMANATE $\text{Ba}_2\text{TiGe}_2\text{O}_8$ SINGLE CRYSTALS

A. Halliyal, A.S. Bhalla and L.E. Cross

AD-A173 185

PIEZOELECTRIC AND ELECTROSTRICTIVE MATERIALS FOR
TRANSDUCER APPLICATIONS(U) PENNSYLVANIA STATE UNIV
UNIVERSITY PARK MATERIALS RESEARCH LAB

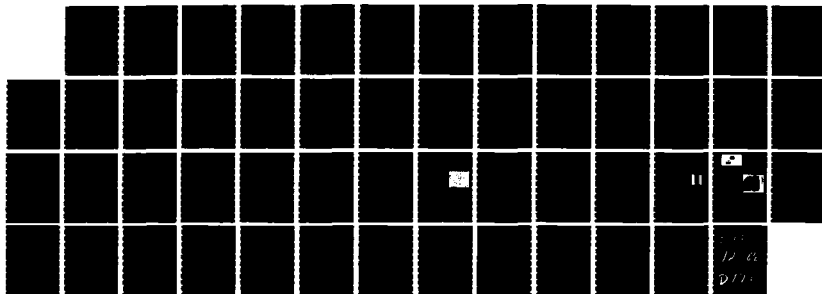
4/4

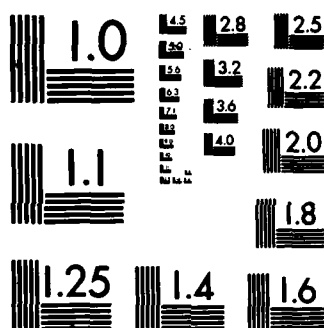
UNCLASSIFIED

L E CROSS ET AL JUL 86 N00014-82-K-0339

F/G 9/1

NL





MICROCOPY RESOLUTION TEST CHART
NATIONAL BUREAU OF STANDARDS-1963-A

PHASE TRANSITIONS, DIELECTRIC, PIEZOELECTRIC AND PYROELECTRIC PROPERTIES OF BARIUM TITANIUM GERMANATE $\text{Ba}_2\text{TiGe}_2\text{O}_8$ SINGLE CRYSTALS

A. HALLIYAL, A. S. BHALLA, and L. E. CROSS

*Materials Research Laboratory, The Pennsylvania State University, University
Park, PA 16802*

(Received September 23, 1984; in final form December 10, 1984)

Measurement of the dielectric permittivity ϵ_{33} , the pyroelectric coefficient p_3 , and the piezoelectric planar coupling k_p and frequency constant N_p in single crystal $\text{Ba}_2\text{TiGe}_2\text{O}_8$ show clear evidence of a heretofore unobserved first order phase change which occurs at -50°C on cooling and near 0°C on heating. The balance of evidence suggests that the transition is to a reorientable but irreversible ferroelectric phase, involving a tilt of the prototypic polar c axis. The inversion of the sign of the pyroelectric effect reported earlier near 135°C is confirmed and is attributed to the changing balance between primary and secondary components in the pyroelectric coefficient.

INTRODUCTION

Barium titanium germanate ($\text{Ba}_2\text{TiGe}_2\text{O}_8$ —hereafter designated BTG) was identified by Masse and Durif,¹ and also by Blasse² as having a structure similar to that of the mineral fersnoite $\text{Ba}_2\text{TiSi}_2\text{O}_8$ which has tetragonal $4mm$ symmetry. Single crystals of BTG have been grown both by Bridgman and Czochralski techniques.^{3,4} Kimura *et al.*⁵ have determined the crystal symmetry at room temperature to be orthorhombic $mm2$, with a peculiar long b -axis spacing which is reportedly $11 \times a_0$ (lattice constants: $a = 12.30 \text{ \AA}$, $b = 135.2 \text{ \AA}$, $c = 10.70 \text{ \AA}$). However, x-ray single domain data of Schmid and co-workers indicate orthorhombic symmetry ($a_{\text{o.r.}} \approx b_{\text{o.r.}} a_{\text{tet}} \sqrt{2} = 12.27 \text{ \AA}$, $c_{\text{o.r.}} = 5.35 \text{ \AA}$), whereas x-ray powder diffraction studies by Masse,¹ Guha,⁵ and Gabalica-Robert and Tarte¹⁶ reveal only the tetragonal pseudosymmetry ($a = 8.684 \pm 0.007 \text{ \AA}$, $c = 5.365 \pm 0.005 \text{ \AA}$; $a = 8.68 \text{ \AA}$, $b = 5.37 \text{ \AA}$; $a = 8.677(12) \text{ \AA}$, $c = 5.364(10) \text{ \AA}$).

Kimura *et al.*⁶ have also reported a solid state phase transition in BTG at 810°C , which they indicate reduces the point symmetry from $4mm$ to $mm2$ on cooling leading to a mimetically twinned ferroelastic structure. They confirmed ferroelasticity in the lower temperature phase by observing stress detwinning at 700°C under a uniaxial stress of 100 kg/cm^2 . Disappearance of twin domains due to the application of stress implies the exchange of crystallographic axis a and b in some domains, with the appearance of the crystallographic b axis (which is the long axis) orthogonal to the compressive stress direction. By considering the possible ferroelastic species of $4mm$ prototype symmetry, the above workers pointed out the most probable ferroelastic species as $4mmFmm2$. It has also been reported that BTG has a large

electromechanical coupling factor in the thickness shear mode³ ($k_{13} = 0.27$ and $k_{24} = 0.31$) and a small pyroelectric coefficient⁴ ($p_3 = -4 \mu\text{C}/\text{m}^2 \text{ } ^\circ\text{K}$) which reverses its sign at about 135°C . The pyroelectric coefficient increases sharply below room temperature, but in the above study, measurements were not carried out below 0°C . Measurements of the D-E relation and the temperature dependence of the dielectric constant did not indicate BTG to be ferroelectric for field applied along (c)³ in the temperature range from -180 to 1200°C . No detailed studies have been reported on the temperature variation of piezoelectric properties.

The present work was undertaken to examine the dielectric, piezoelectric and pyroelectric properties of BTG single crystals in more detail. The above properties were studied as a function of temperature in the temperature range -150 to 200°C . The present studies indicated the occurrence of a new abrupt phase transition at about -25°C , which has not been reported earlier. In this paper, the probable reasons for the sign reversal of the pyroelectric coefficient at 135°C are discussed. The properties near the low temperature phase transition are examined in detail and the possible ferroic species resulting from this transition are considered.

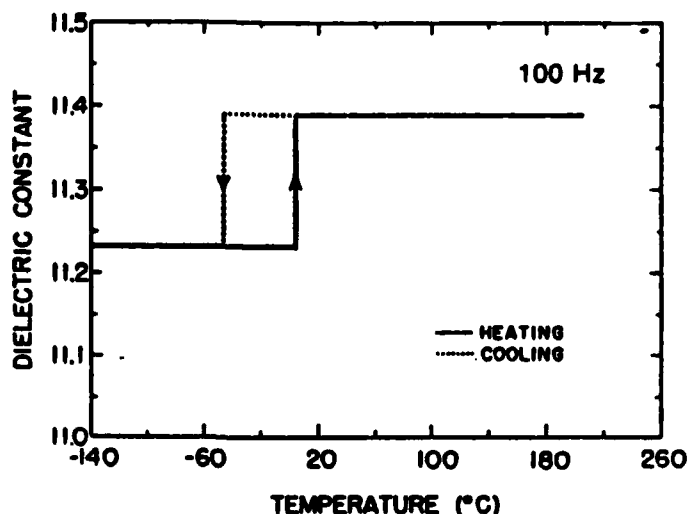
CRYSTAL GROWTH AND MEASUREMENTS

Crystals for the present study were grown by the Czochralski pulling method from stoichiometric melts contained in a platinum crucible. Growth conditions were as follows: seed rotation speed 20 rpm; initial pulling rate 10 mm/hr; final pulling rate 2 mm/hr. Crystal boules of size 8–10 mm dia \times 10–15 mm length were obtained by the above procedure. The resulting boules were colorless and transparent. c-plates were cut from the boule and circular samples of 5 mm dia and 0.5 mm thick were prepared. The major surfaces of the samples were coated with sputtered gold electrodes.

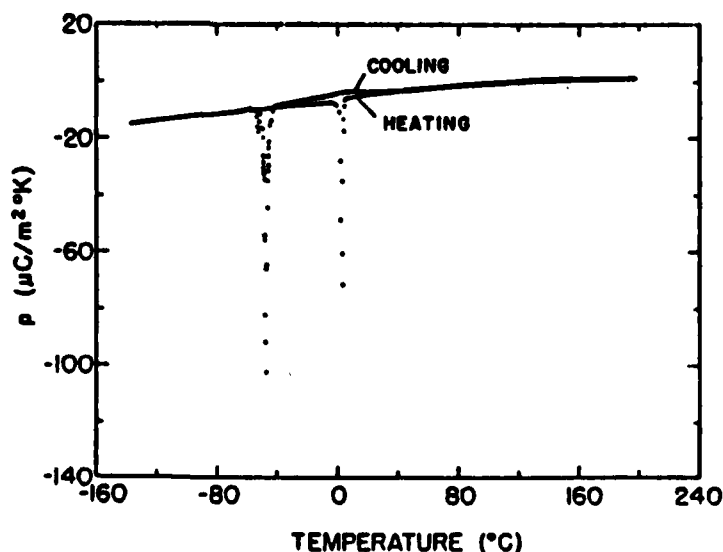
The dielectric constant and dissipation factors were measured at different frequencies using a capacitance bridge. Pyroelectric coefficients were determined by the Byer-Roundy⁷ technique. The heating and cooling rates employed were $4^\circ\text{C}/\text{min}$. The electromechanical properties were determined by standard resonance techniques. All the above properties were measured as a function of temperature in both heating and cooling cycles. Piezoelectric d_{33} coefficients were measured using a Berlincourt- d_{33} meter. The hydrostatic voltage coefficient g_h was measured by a dynamic method described in Ref. 8.

RESULTS

The variation of the dielectric constant of a BTG single crystal with temperature, measured at 100 Hz, is shown in Figure 1. There is a small but abrupt jump in the dielectric constant in both heating and cooling cycles. The jump occurs at approximately -50°C in the cooling cycle and at 0° in the heating cycle. Surprisingly, no corresponding peaks were observed in the dissipation factor curve. The dissipation factor was less than 0.001 in the temperature range -140 to 200°C . The temperature dependence of the pyroelectric coefficient p_3 is shown in Figure 2. p_3 is negative at


 FIGURE 1 Dielectric constant of $\text{Ba}_2\text{TiGe}_2\text{O}_8$ single crystal as a function of temperature.

low temperature and decreases in magnitude with increasing temperature, crossing zero at 135°C . Above 135°C , the sign of p_3 is positive and increases slightly with temperature (similar results were reported by Schmid *et al.*⁴). Very strong peaks were observed in p_3 in both heating and cooling cycles at the same temperature where there were discontinuities in the dielectric constant. The peak value of the pyroelectric coefficient at about -50°C was about $-120 \mu\text{C}/\text{m}^2 \cdot ^\circ\text{K}$. The variation


 FIGURE 2 Variation of pyroelectric coefficient (p_3) of $\text{Ba}_2\text{TiGe}_2\text{O}_8$ single crystal as a function of temperature.

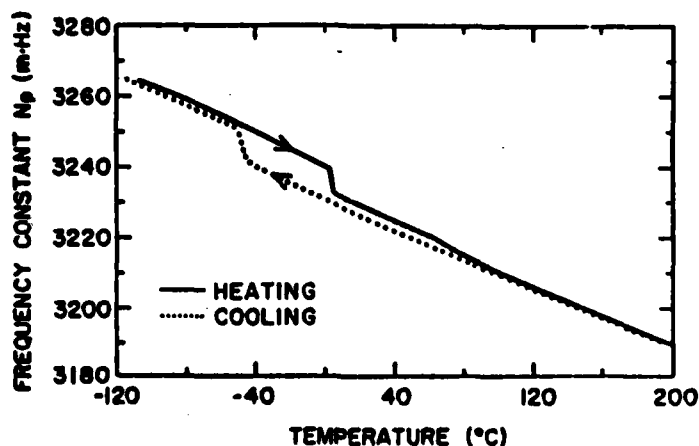


FIGURE 3 Frequency constant N_p of $\text{Ba}_2\text{TiGe}_2\text{O}_8$ single crystal as a function of temperature.

of planar frequency constants N_p and electromechanical coupling factor k_p are shown in Figures 3 and 4. Discontinuities were observed in both heating and cooling cycles, similar to the discontinuity in dielectric constant curve. It was clear that the discontinuities observed in the dielectric and piezoelectric properties were very small in comparison to the strong peaks observed in the pyroelectric coefficient curve. The reproducibility of the discontinuity in the above properties was tested by making measurements on several samples and by repeating the measurements several times on the same samples. The discontinuity in the above properties could be observed everytime with similar hysteresis. The room temperature properties of BTG are listed in Table I.

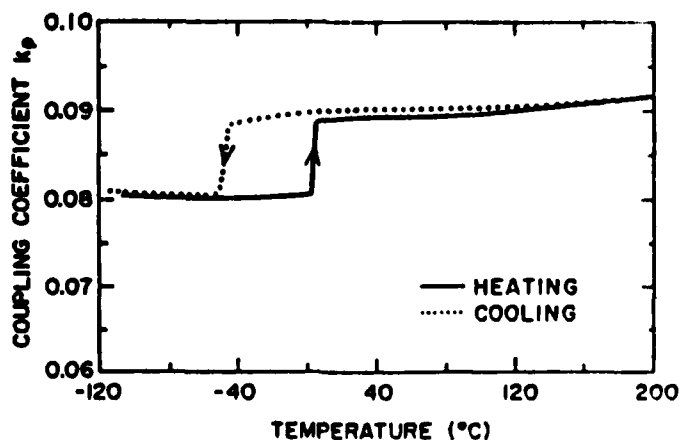


FIGURE 4 Electromechanical coupling coefficient k_p of $\text{Ba}_2\text{TiGe}_2\text{O}_8$ single crystal as a function of temperature.

TABLE I

Room temperature properties of $\text{Ba}_2\text{TiGe}_2\text{O}_8$ ^a	
Density (gm/cc)	4.84
K_{33} (1 k · Hz)	11.4
$\tan \delta$ (1 k · Hz)	< 0.001
Pyroelectric coefficient p_3 ($\mu\text{C}/\text{m}^2 \cdot ^\circ\text{K}$)	-4.0
d_{33} (pC/N)	8.0
d_{31} (pC/N)	2.0
d_h (pC/N)	12.1
g_{33} (10^{-3} Vm/N)	80
g_h (10^{-3} Vm/N)	120
$d_h g_h$ (10^{-15} Vm/N)	1450
Frequency constant N_f (m · Hz)	2150
Frequency constant N_p (m · Hz)	3200
k_p	0.09
Q (radial)	6000
TCR (ppm/ $^\circ\text{C}$)	60

^aData from the present study.

DISCUSSION

Unusual features in the properties of BTG crystals revealed in these studies may be summarized as follows:

- (1) The pyroelectric coefficient p_3 , which is negative at room temperature passes through zero at $\sim 135^\circ\text{C}$ and becomes positive at higher temperature.
- (2) The sharp and intense peaks in p_3 at -50° on cooling and at 0°C on heating suggest a first order phase change which involves a discontinuous change of the polar magnitude p_3 in the crystal.
- (3) The smaller but abrupt changes in ϵ_{33} , k_p , and N_p at the same temperatures confirm that a phase change occurs.

To discuss the results intelligently, it is first necessary to determine the symmetries in the different phases. Best evidence would suggest that BTG is orthorhombic at room temperature in the ferroelastic species $4mmFmm2$ (Aizu^{9,10}). Optical evidence of twins with the appropriate wall orientations in our crystals, taken together with the biaxial conoscopic figure in the high temperature phase would tend to confirm this $mm2$ assignment.

Additional species which are accessible from $4mm$ are $4mmFm$, $4mmF2$, and $4mmF1$ (Table II). Of these $4mmF2$ is ferroelastic, but $4mmFm$ and $4mmF1$ are both ferroelastic and divertable but irreversible ferroelectrics. Since the unique 2-fold axis of $mm2$ is preserved in the ferroelastic species it is unlikely that a major change of magnitude of P_3 would be involved in the change $mm2 \rightarrow 2$. For the species 1 and m , however, P_3 must tilt away from the 2-fold axis so that a first order change would give a finite step in P_3 and the large charge release observed. It may be noted that neither change will give rise to reversible polarity and ferroelectricity for the E field along the c axis E_3 , but only for fields orthogonal to the original c axis.

Unequivocal evidence to distinguish m and 1 from 2 can be obtained by optical measurements on crystal sections parallel to the c axis, and these measurements are now in progress.

TABLE II

Ferroic species for prototype symmetries $4mm$ and $mm2$

Prototype symmetry	Possible aizu species	Property
$4mm$	$4mmF1$	Ferroelectric and Ferroelastic
	$4mmFm$	
	$4mmF2$	Ferroelastic but not Ferroelectric
	$4mmFmm2$	
$mm2$	$mm2F1$	Ferroelectric and Ferroelastic
	$mm2Fm$	
	$mm2F2$	Ferroelastic but not Ferroelectric

We believe that the balance of evidence suggests that BTG may be a divertable but irreversible ferroelectric at temperatures below -50°C with symmetry in point group 1 or m .

For the pyroelectric sign change, there is no evidence of phase change near 135°C and we believe that the change is due to a competition between primary and secondary components of p_3 , as in $\text{Li}_2\text{SO}_4 \cdot \text{H}_2\text{O}$,¹¹ $\text{Ba}(\text{NO}_2)_2 \cdot \text{H}_2\text{O}$,¹² $\text{Ba}_2\text{TiSi}_2\text{O}_8$,¹³ and $(\text{NH}_4)_2\text{SO}_4$.¹⁴ Unfortunately, it is not yet possible to separate primary and secondary effects in BTG as the full family of elastic, piezoelectric and thermal expansion constants required to assess the secondary effect has not yet been measured.

If as in fresnoite, $\text{Ba}_2\text{TiSi}_2\text{O}_8$, the secondary effect p_{sec} is positive,¹⁵ then in BTG the primary effect must be negative and must dominate at lower temperatures. This would not be inconsistent with a low temperature phase in which P is tilted from the c axis. Since the tilt angle will be in the nature of an order parameter for this phase, it will decrease with increasing temperature, reducing the normal decrease of P and thus the normally negative p_3 primary.

We speculate that at 135°C the secondary and primary pyroelectric coefficients are equal and that above this temperature, the secondary effect dominates, but more detailed measurements are needed to verify this hypothesis.

ACKNOWLEDGMENTS

We thank all our colleagues in the ferroelectrics group at MRL for their help in this work. This work was supported by the Army Research Office through Contract #DAAG29-80-C-0008 and the National Science Foundation Grant No. DMR-8303906.

REFERENCES

1. R. Masse and A. Durit, *Bull. Soc. Fr. Min. Cryst.*, **90**, 407 (1967).
2. G. Blasse, *J. Inorg. Nucl. Chem.*, **30**, 2283 (1968).
3. M. Kimura, K. Doi, S. Nanamatsu and T. Kawamura, *Appl. Phys. Lett.*, **23**, 531 (1973).
4. H. Schmid, P. Genequand, H. Tippmann, G. Pouilly and H. Guedu, *J. Mat. Sci.*, **13**, 2255 (1978).

5. J. P. Guha, *J. Amer. Ceram. Soc.*, **60**, 246 (1977).
6. M. Kimura, K. Utsumi and S. Nanamatsu, *J. Appl. Phys.*, **47**, 2249 (1976).
7. R. L. Byer and C. B. Roundy, *Ferroelectrics*, **3**, 333 (1972).
8. A. Safari, Ph.D. Thesis, The Pennsylvania State University (1983).
9. K. Aizu, *Phys. Rev. B*, **2**, 754 (1970).
10. K. Aizu, *Phys. Rev.*, **146**, 423 (1966).
11. S. B. Lang, *Phys. Rev. B*, **4**, 3603 (1970).
12. V. V. Gladkii and I. S. Zheludev, *Sov. Phys. Cryst.*, **10**, 50 (1965).
13. A. Halliyal, *et al.*, *Ferroelectrics* (to be published).
14. N. Yamada, *J. Phys. Soc. Jpn.*, **46**, 561 (1974).
15. A. S. Bhalla and R. E. Newnham, *Phys. Stat. Sol. (a)*, **58**, K19 (1980).
16. M. Gabelica-Robert and P. Tarte, *Phys. Chem. Minerals*, **7**, 26 (1981).

X-RAY STRUCTURE REFINEMENT AND PYROELECTRIC
INVESTIGATION OF FRESHOITE, $\text{Ba}_2\text{TiSi}_2\text{O}_8$

S.A. Markgraf, A. Halliyal, A.S. Bhalla, R.E. Newnham and C.T. Prewitt

X-RAY STRUCTURE REFINEMENT AND PYROELECTRIC INVESTIGATION OF FRESNOITE, $\text{Ba}_2\text{TiSi}_2\text{O}_8$

S. A. MARKGRAF, A. HALLIYAL, A. S. BHALLA and
R. E. NEWNHAM

*Materials Research Laboratory, The Pennsylvania State University, University
Park, PA 16802 USA*

and

C. T. PREWITT

*Department of Earth and Space Sciences, SUNY at Stony Brook, Stony
Brook, NY 11794 USA*

(Received October 17, 1984)

Crystal structure parameters have been refined from single crystal x-ray intensity data collected on $\text{Ba}_2\text{TiSi}_2\text{O}_8$ at 24 and 300°C. Anisotropic refinements in space group $P4bm$ yielded residuals of 0.035 and 0.042 at 24 and 300°C, respectively. Pyroelectric measurements give a room temperature pyroelectric coefficient of $+10 \mu\text{C m}^{-2} \text{K}^{-1}$. A structural mechanism for the pyroelectric effect is discussed in terms of large oxygen displacements. A sign reversal in the pyroelectric coefficient occurs at 160°C, perhaps caused by the cancellation of primary and secondary effects.

INTRODUCTION

Fresnoite, $\text{Ba}_2\text{TiSi}_2\text{O}_8$ is a non-centrosymmetric tetragonal crystal in space group $P4bm$. It has received attention recently for its pyroelectric, piezoelectric, and surface acoustic wave properties.¹⁻⁵ In addition, the possibility of making polar glass-ceramics by the recrystallization of a glass of this composition has been demonstrated successfully.⁶ During the polar glass-ceramic study, it was observed that fresnoite glass-ceramics show a sharp sign reversal in the pyroelectric coefficient at 160°C. Single crystals also show the effect, and several other electrical properties show anomalies at 160°C (dielectric constant, K , frequency constant, N_p , electro-mechanical coupling, k_p).⁷ High temperature x-ray powder diffraction data, DTA, and specific heat measurements gave no indication of a phase transition. If a structural distortion was responsible for the sharp sign reversal in the pyroelectric coefficient it must be small in magnitude. The structure of fresnoite was solved by Moore and Louisnathan⁸ and Masse *et al.*⁹ Due to the recent technological interest in $\text{Ba}_2\text{TiSi}_2\text{O}_8$, and the unusual pyroelectric behavior, it seemed worthwhile to re-investigate the crystal structure of fresnoite, both at room temperature and above 160°C.

TABLE I

Crystallographic data for fresnoite. Estimated Standard Deviation are given in parentheses.
(This convention is followed in all tables.)

Space Group	$P4bm$ ($z = 2$)		
Lattice Parameters	$a(\text{\AA})$	$c(\text{\AA})$	Volume (\AA^3)
Temp ($^{\circ}\text{C}$)			
24	8.527(1)	5.2104(9)	378.8(1)
300	8.542(1)	5.219(1)	380.8(1)
500	8.550(2)	5.235(2)	382.6(2)
24 (after heating)	8.528(1)	5.210(1)	378.8(1)
S (Standard Deviation of an observation of unit weight)	$S = 2.48$ at 24°C $S = 2.78$ at 300°C		
Expansion Coefficients			
$\bar{\alpha}_x$	$9.9 \times 10^{-6}^{\circ}\text{C}^{-1}$ (this study)		
	$10.3 \times 10^{-6}^{\circ}\text{C}^{-1}$ (Ref. 2)		
	$9.3 \times 10^{-6}^{\circ}\text{C}^{-1}$ (Ref. 3)		
$\bar{\alpha}_y$	$5.7 \times 10^{-6}^{\circ}\text{C}^{-1}$ (this study)		
	$9.8 \times 10^{-6}^{\circ}\text{C}^{-1}$ (Ref. 2)		
	$8.7 \times 10^{-6}^{\circ}\text{C}^{-1}$ (Ref. 3)		

EXPERIMENTAL

Fresnoite crystals were grown on a $\langle 001 \rangle$ seed by the Czochralski method from a stoichiometric melt. Growth conditions were as follows: seed rotation speed of 10–15 rpm; pulling speed of 1.0 mm/hr; crucible rotation of 5 rpm. The resulting boules were colorless and transparent.

A c plate was cut from a boule, crushed, and a small fragment was chosen for x-ray investigation. An attempt was made to grind the fragment into a sphere, but proved unsuccessful. The crystal had many faces, all with rounded corners. Approximate dimensions were $140 \times 100 \times 60 \mu\text{m}$. Precession photography showed sharp, rounded spots, with no evidence of twinning.

Integrated intensity data were measured with an automated Picker four-circle diffractometer operating with graphite-monochromated $\text{MoK}\alpha$ radiation. Reflections within a quadrant of reciprocal space containing the positive and negative polar axes, with radius of $(\sin \theta)/\lambda = 0.70 \text{\AA}^{-1}$, were collected at 24 (1176 reflections) and 300°C (1180 reflections). Heating in-situ was accomplished with the heater described by Brown *et al.*¹⁰ The error in temperature was $\pm 20^{\circ}\text{C}$. Unit cell parameters were calculated at 24, 300, 500°C and again at 24°C after heating, through least-squares method on 24 reflections within the range $39^{\circ} \leq 2\theta \leq 55^{\circ}$. As the technique does not quantify possible centering and/or orientation errors, the reported standard deviations for the lattice parameters may be low (Table I).

All intensities were corrected for Lorentz and polarization factors and converted to structure factors. Since the crystal was very complex in shape, an accurate measurement of it for absorption was not possible. Therefore no absorption correction was made. A reflection was deleted if $I_{\text{obs}} < 2\sigma_I$, where σ_I is based on counting

statistics, or if the variation of a form exceeded 4σ , where σ is the standard deviation of the population. The latter is a rather stringent criterion, yet only leads to the rejection of approximately 25 symmetry-averaged reflections per data set. Most of these rejected reflections were relatively intense and at low $(\sin \theta)/\lambda$, where absorption effects would be strongest.

The structure was refined with the program RFINE IV¹¹ using starting parameters taken from Moore and Louisnathan.⁸ Atomic scattering factor curves were taken from the International Tables for X-ray Crystallography, Vol. IV,¹² as were corrections for anomalous dispersion. Strong extinction was not a serious problem, hence a correction was considered unnecessary.

RESULTS AND DISCUSSIONS

Lattice parameters and crystallographic data at various temperatures are given in Table I. Anisotropic refinements in $P4bm$ on 579 (24°C) and 575 (300°C) symmetry-averaged reflections converged in three cycles. The structural features are the same as those reported by Moore and Louisnathan⁸ and Masse *et al.*,⁹ consisting of Si_2O_7 groups linked to square pyramidal TiO_5 members, producing layers parallel to

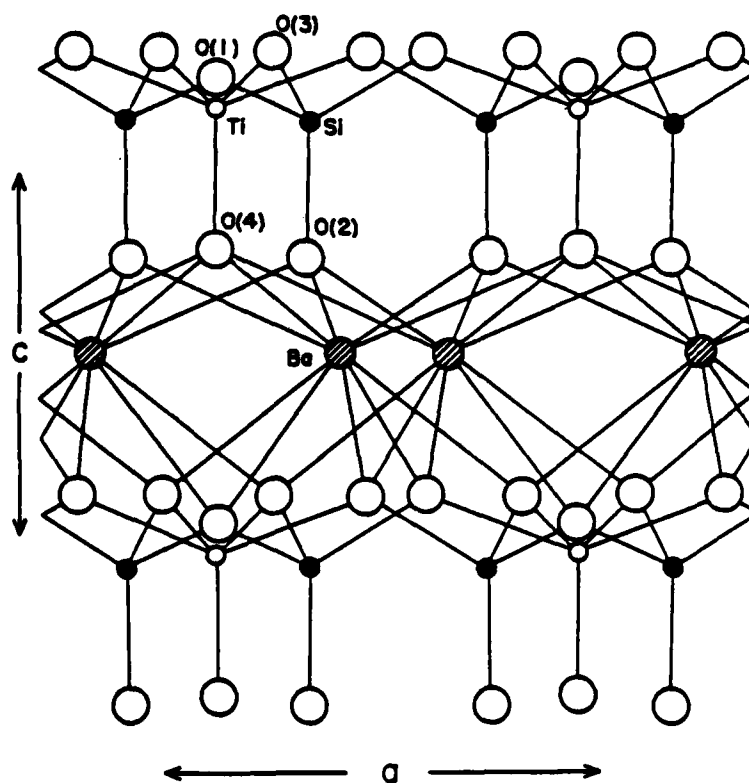


FIGURE 1 Crystal structure of fresnoite, after Moore and Louisnathan.⁸

TABLE II
Measured and calculated structure factors for selected Bijvoet pairs for $\text{Ba}_2\text{TiSi}_2\text{O}_8$

hkl	$ F_{\text{obs}} $	σ_F	$ F_{\text{calc}}^+ ^a$	$ F_{\text{calc}}^- $	$\frac{F_{\text{c}, hkl}}{F_{\text{o}, hkl}}$	$\frac{F_{\text{o}, hkl}}{F_{\text{o}, hkl}}$
127	58.434	1.371	59.076	58.902	(+)1.008	
12 $\bar{7}$	63.253	1.455	58.615	59.350	(-)0.992	:0.924
536	39.848	1.044	40.433	40.252	(+)1.009	
53 $\bar{6}$	41.951	1.080	40.056	40.673	(-)0.990	:0.950
665	51.253	1.242	52.786	53.689	(+)0.991	
66 $\bar{5}$	54.871	1.318	53.240	53.226	(-)1.009	:0.934
10, 1, 4	59.731	1.401	61.259	61.390	(+)1.003	
10, 1, $\bar{4}$	60.497	1.421	61.086	61.549	(-)0.997	:0.987
783	39.831	1.061	40.009	40.616	(+)0.991	
78 $\bar{3}$	40.902	1.075	40.380	40.244	(-)1.009	:0.974
11, 2, 2	29.339	0.965	30.523	29.559	(+)1.037	
11, 2, $\bar{2}$	30.303	0.976	29.447	30.641	(-)0.965	:0.968
5, 10, 1	35.842	0.989	34.867	35.116	(+)0.997	
5, 10, $\bar{1}$	34.824	0.982	34.966	35.015	(-)1.002	:1.029
11, 2, 1	17.569	1.099	16.746	17.246	(+)0.978	
11, 2, $\bar{1}$	18.161	1.068	17.128	16.875	(-)1.022	:0.967
10, 5, 2	49.144	1.200	52.009	51.292	(+)1.020	
10, 5, $\bar{2}$	51.927	1.247	51.002	52.326	(-)0.980	:0.946
953	22.848	1.007	21.673	23.500	(+)0.929	
95 $\bar{3}$	22.451	0.991	23.339	21.826	(-)1.077	:1.018
934	40.705	1.071	41.091	41.806	(+)0.988	
93 $\bar{4}$	41.733	1.086	41.582	41.321	(-)1.012	:0.975
815	39.228	1.041	38.837	38.925	(+)1.002	
81 $\bar{5}$	39.772	1.041	38.762	39.007	(-)0.998	:0.986
266	27.783	0.990	26.022	31.734	(+)0.985	
26 $\bar{6}$	30.698	0.980	26.411	31.229	(-)1.016	:0.905
137	27.446	0.990	25.233	27.293	(+)0.936	
13 $\bar{7}$	27.395	0.985	26.965	25.584	(-)1.067	:1.002

^a $|F_{\text{calc}}^+|$ is based on refinements with a positive z value; $|F_{\text{calc}}^-|$ from the refinement with negative z coordinates.

{001}. The Ba^{2+} cation, in ten-fold coordination, connects the layers (Figure 1). As with any polar space group, it is possible to determine the absolute configuration of the crystal structure through analysis of Bijvoet pairs. In addition, the respective R factors of each model may be used in a Hamilton significance test.¹³ Table II contains 14 Bijvoet pairs with $2\theta \geq 55^\circ$ taken from the 24°C data set. There is a clear preference for the z (negative) model, although five of the fourteen pairs do not agree with this model. However, all five are within a single standard deviation (σ_F).

TABLE III

Positional parameters, displacements and equivalent isotropic temperature factors, B_{eq} (Å²) for Ba₂TiSi₂O₈

		Positional Parameters		Displacement ^a	B_{eq}	
		24°C	300°C	$\Delta \times 10^{-4}$	24°C	300°C
Ba	x	0.32701(3)	0.32708(4)	0.7(5)		
	y	0.82701(3)	0.82708(4)	0.7(5)	0.99(1)	1.41(1)
	z	0.0	0.0	—		
Ti	x	0.0	0.0	—		
	y	0.0	0.0	—	0.70(4)	0.90(5)
	z	-0.5354(5)	-0.5355(6)	1(8)		
Si	x	0.1280(2)	0.1280(2)	0(3)		
	y	0.6280(2)	0.6280(2)	0(3)	0.70(3)	0.82(4)
	z	-0.5129(8)	-0.5133(10)	4(13)		
O(1)	x	0.0	0.0	—		
	y	0.5	0.5	—	1.44(16)	1.68(19)
	z	-0.6293(19)	-0.6284(23)	-9(30)		
O(2)	x	0.1259(5)	0.1261(6)	2(8)		
	y	0.6259(5)	0.6261(6)	2(8)	1.01(11)	1.29(13)
	z	-0.2051(12)	-0.2078(15)	27(19)		
O(3)	x	0.2924(6)	0.2924(7)	0(9)		
	y	0.5772(8)	0.5774(8)	2(11)	1.84(13)	1.77(15)
	z	-0.6429(11)	-0.6436(13)	7(17)		
O(4)	x	0.0	0.0	—		
	y	0.0	0.0	—	1.82(18)	2.46(23)
	z	-0.2096(20)	-0.2134(26)	38(33)		

^aEst. Std. Dev. of the form $(\sigma_{24}^2 + \sigma_{300}^2)^{1/2}$.

Examination of the R factors for the two models also shows a preference for the z (negative) model. With z (positive): $R_w = 0.047$, and $R = 0.040$, where $R = \Sigma(|F_o| - |F_c|)/\Sigma|F_o|$ and $R_w = [\Sigma w(|F_o| - |F_c|)^2 / (\Sigma w F_o^2)]^{1/2}$. The weighting term, w , is defined as $1/\sigma_F^2$, where σ_F is calculated from the counting statistics. Taking z (negative) yields: $R_w = 0.040$ and $R = 0.035$. To see if this difference is significant at the 0.5 percent confidence level Hamilton's tables¹³ give $R = 1.004$. The conclusion is that there is a high probability that the difference is significant. Analysis of the 300°C data yields similar results: z (positive), $R_w = 0.053$, $R = 0.045$, z (negative): $R_w = 0.047$, $R = 0.042$. All atomic coordinates, thermal parameters, interatomic distances, etc. are therefore taken from the z (negative) refinements.

Data, and the estimated standard deviations, from the 24 and 300°C refinements are given in Tables III to VI. Positional parameters and equivalent isotropic temperature factors are given in Table III. Interatomic distances and angles are listed in Table IV. Table V contains the anisotropic temperature factors. Final observed and calculated structure factors are listed in Table VI†. Mean thermal

†Table 6 is available from the authors at the Materials Research Laboratory.

TABLE IV
Interatomic distances (Å) and angles (°) for Ba₂TiSi₂O₈

	24°C	300°C
Ba-O(1)	2.843(7)	2.850(8)
Ba-O(2)	2.650(5)	2.659(6)
Ba-O(2')	2.793(5)	2.804(6)
Ba-O(3)	2.844(6)	2.846(7)
Ba-O(3')	3.008(6)	3.012(7)
Ba-O(4)	3.338(3)	3.351(5)
Ti-O(3)	1.970(6)	1.975(6)
Ti-O(4)	1.698(11)	1.681(14)
O(3)-O(4)	2.944(10)	2.937(12)
O(3)-O(3')	2.671(8)	2.677(9)
Si-O(1)	1.658(4)	1.658(5)
Si-O(2)	1.604(8)	1.595(10)
Si-O(3)	1.616(6)	1.619(7)
O(1)-O(2)	2.681(10)	2.672(12)
O(3)-O(2)	2.719(8)	2.713(10)
O(1)-O(3)	2.579(6)	2.585(6)
O(4)-Ti-O(3)	106.52(18)	106.59(21)
O(3)-Ti-O(3')	146.96(37)	146.81(42)
Si-O(3)-Ti	138.57(39)	138.45(44)
Si-O(1)-Si	137.09(69)	137.52(82)
O(2)-Si-O(1)	110.58(39)	110.44(46)
O(2)-Si-O(3)	115.09(25)	115.15(27)

expansion coefficients were calculated from the unit cell parameters with the equation $\bar{\alpha}_X = X_{24}^{-1}(X_T - X_{24})/(T - 24)$, where X is the parameter in question, T is temperature, and $(X_T - X_{24})/(T - 24)$ is the slope of X vs. temperature determined from linear regression. Results for $\bar{\alpha}_c$, $9.9 \times 10^{-6} \text{ }^\circ\text{C}^{-1}$, are in good agreement with other workers, whereas $\bar{\alpha}_a$, $5.7 \times 10^{-6} \text{ }^\circ\text{C}^{-1}$, is slightly lower than found previously^{2,3} (Table I).

Atomic coordinates and interatomic distances and angles agree with the earlier values of Moore and Louisnathan,⁸ although the present values are more precise. Previous structure refinements disagreed in the Ti-O interatomic distances, with Masse *et al.* reporting that both Ti-O interatomic distances are approximately 2.00 Å, and Moore and Louisnathan reporting a short bond, 1.634 Å, and a longer one, 2.00 Å. The current structure refinement yields results in agreement with the latter (Table IV). Fresnoite is one of the few titanates that luminesces efficiently at room temperature, and the explanation for this has centered on the short Ti-O interatomic distance within the TiO₃ group.¹⁴

STRUCTURAL MODEL FOR PYROELECTRICITY

The pyroelectric coefficient of a material in general is described as the sum of the primary and secondary effects¹⁵

$$(p_j)_T = (p_j)_{\text{prim}} + (d_j \alpha_i c_{ji})_{\text{sec}} \quad i, j = 1, \dots, 6$$

TABLE V

Anisotropic temperature factors (\AA^2) for Ba₂TiSi₂O₈^a

24°C	β_{11}	β_{22}	β_{33}	β_{12}	β_{13}	β_{23}
Ba	0.00364(5)	0.00364(5)	0.0079(2)	-0.00178(4)	0.0003(1)	0.0003(1)
Ti	0.0023(1)	0.0023(1)	0.0069(10)	—	—	—
Si	0.0024(1)	0.0024(1)	0.0064(7)	0.0002(2)	0.0003(5)	0.0003(5)
O(1)	0.0062(9)	0.0062(9)	0.006(3)	-0.0031(11)	—	—
O(2)	0.0038(5)	0.0038(5)	0.007(2)	-0.0017(7)	-0.0002(8)	-0.0002(8)
O(3)	0.0030(6)	0.011(1)	0.013(2)	0.0038(6)	0.0015(9)	0.0029(10)
O(4)	0.0076(10)	0.0076(10)	0.009(3)	—	—	—
300°C						
Ba	0.00507(6)	0.00507(6)	0.0116(2)	-0.00222(5)	0.0001(1)	0.0001(1)
Ti	0.0027(2)	0.0027(2)	0.010(1)	—	—	—
Si	0.0025(2)	0.0025(2)	0.0091(8)	0.0000(2)	0.0003(5)	0.0003(5)
O(1)	0.0066(10)	0.0066(10)	0.011(3)	-0.0031(14)	—	—
O(2)	0.0051(6)	0.0051(6)	0.008(2)	-0.0018(9)	0.0001(9)	0.0001(9)
O(3)	0.0032(7)	0.0086(10)	0.017(2)	0.0024(7)	0.001(1)	0.001(1)
O(4)	0.010(1)	0.010(1)	0.014(4)	—	—	—

^aOf the form: $\exp\{-(\beta_{11}h^2 + \beta_{22}k^2 + \beta_{33}l^2 + 2\beta_{12}hk + 2\beta_{13}hl + 2\beta_{23}kl)\}$.

where $(p_3)_{\text{prim}} = (\partial P / \partial T)_\epsilon$ is the pyroelectric coefficient under constant strain, d the piezoelectric constant, α the thermal expansion coefficients and c_{ji} the stiffness coefficients of a crystal.

Pyroelectric coefficients of single crystals of fresnoite were measured by a direct Byer-Roundy method¹⁶ (with a heating and cooling rate of 4°/minute) in a temperature range of -150 to 220°C (Figure 2). The magnitude of the pyroelectric coefficient at room temperature is 10 $\mu\text{C m}^{-2} \text{K}^{-1}$; this value includes both primary and secondary pyroelectric effects. Bhalla and Newnham,¹⁷ using the published values for the piezoelectric, compliance and thermal expansion coefficients, have calculated the secondary effect in fresnoite to be +16.5 $\mu\text{C m}^{-2} \text{K}^{-1}$, setting the primary effect at -6.5 $\mu\text{C m}^{-2} \text{K}^{-1}$.

It is possible to calculate a pyroelectric coefficient based on a point-charge model with the equation

$$p_3 = \Delta P / \Delta T = \left(ec \left| \sum_i v_i n_i \Delta z_i \right| \right) / V \Delta T$$

where e is the elementary charge, c the unit cell parameter, v_i the valence of the i th ion, n_i the number of equivalent positions for the i th ion, Δz_i the displacement of the z coordinate between the two temperatures of the i th ion, V the room temperature volume of the unit cell, ΔT the temperature range. Table III lists the atomic displacements, along with an estimated standard deviation, calculated from the refinements at 24 and 300°C. The most striking shift in the atomic coordinates is found in the O(2) Δz , 27×10^{-4} , and O(4) Δz , 38×10^{-4} , positions. Using these two displacements a pyroelectric coefficient of 30 $\mu\text{C m}^{-2} \text{K}^{-1}$ is calculated. This is greater than the room temperature value, but the calculated value is an average quantity for the temperature range 24–300°C. Also, the calculation ignores the other, rather small displacements, nor does it consider electron redistribution.

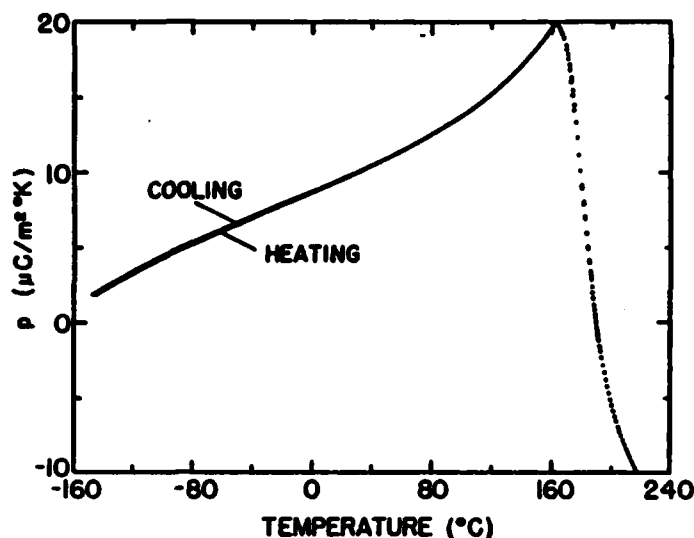


FIGURE 2 Variation of pyroelectric coefficient (p) of $\text{Ba}_2\text{TiSi}_2\text{O}_8$ single crystal as a function of temperature.

Tourmaline, another silicate mineral exhibiting pyroelectricity, has been studied in a similar manner.¹⁸ Interpretation of the structural mechanism for pyroelectricity rested on an anomalously large oxygen displacement of 0.0051. Using this feature, along with large anisotropic temperature factors for the oxygen, Donnay¹⁸ points out the agreement with Boguslawski's theory¹⁹ for pyroelectricity. In Boguslawski's analysis of pyroelectricity, the effect is caused by large anharmonic thermal vibrations.

Abrahams *et al.*²⁰ have developed a model for the pyroelectric effect in tourmaline. Using a technique similar to a normal probability plot, Abrahams and co-workers state that the large oxygen displacement found by Donnay is of low statistical significance. They find that the largest significant displacement for any z coordinate is the $\Delta z = 0.0005$ displacement for Al. A model for tourmaline was then proposed in which an average cation displacement of $5\text{--}10 \times 10^{-4}$ Å along the polar axis produced the observed pyroelectric coefficient.

The similarity in the Δz displacements of the oxygen atoms in fresnoite and tourmaline is obvious. Anisotropic temperature factors for the O(2) and O(4) atoms in fresnoite are not anomalously large. Anharmonicity does not appear to be critical, unless the large errors in the positional parameters are evidence of such. A normal probability plot is not possible on the fresnoite data, and so a direct correction to the estimated standard deviations cannot be calculated. If, however, the $\sqrt{2}$ underestimation in σ found in the IUCr single-crystal project²¹ is applied, the significance of the oxygen displacement is lessened. Still, no displacement is more significant than the O(2) and O(4) shift. It is possible to calculate a pyroelectric coefficient of approximately $19 \mu\text{C m}^{-2} \text{K}^{-1}$ based on cation displacements of $5\text{--}10 \times 10^{-4}$. It is difficult to ascertain which displacement is causing the pyroelectricity in fresnoite, and the data does not lead to a conclusive answer.

In ferroelectric materials, the total pyroelectric coefficient is large and negative. Calculated secondary coefficients are relatively small, often positive, making the primary pyroelectric coefficient negative and large. In contrast, for non-ferroelectric polar crystals the total pyroelectric coefficient is more often dominated by the secondary effect, and both are commonly positive.¹⁷ Another, albeit rare, feature of pyroelectric crystals is the reversal of the pyroelectric sign. If the crystal does not undergo a temperature related phase transition that induces a center of symmetry, the spontaneous polarization may increase or decrease with temperature. Several compounds show a sign reversal in the pyroelectric coefficients, going from positive to negative (or vice versa) at a certain temperature: $\text{Li}_2\text{SO}_4 \cdot \text{H}_2\text{O}$;²² $\text{Ba}(\text{NO}_3)_2$;²³ $\text{Ba}_2\text{TiGe}_2\text{O}_8$;²⁴ $\text{Ba}_2\text{TiSi}_2\text{O}_8$; $\text{Rb}_2\text{Cd}_2(\text{SO}_4)_3$ ²⁵ and $(\text{NH}_4)_2(\text{SO}_4)$.²⁶ Often the explanation for the sign reversal centers on the cancellation of primary and secondary pyroelectric effects. In fersnoite this appears to be the case. The structure does not undergo a phase transition at 160°C. Moreover, the reversal in the sign of the pyroelectric coefficient is reproducible between heating and cooling cycles, thus ruling out the possibility of thermal conduction. What is surprising about the reversal is its sharpness; most other reversals show a gradual slope when crossing the zero point. An example is the first sign reversal in fersnoite at -180°C.²⁷ The pyroelectric coefficient sign reversals at lower temperatures are commonly due to the secondary effect gradually becoming smaller with decreasing temperature. In the case of fersnoite, the high temperature pyroelectric coefficient reversal has a unique signature, and anomalies occur at 160°C in all the piezoelectric properties. It is possible that the large oxygen displacements change a few elastic constants enough to cause the pyroelectric sign reversal. The germanium analog of fersnoite, $\text{Ba}_2\text{TiGe}_2\text{O}_8$, undergoes a ferroelastic transition at 810°C.²⁸ It is therefore conceivable that $\text{Ba}_2\text{TiSi}_2\text{O}_8$ may have slight anomalies in the elastic constants.

ACKNOWLEDGMENTS

We wish to thank Ken Baldwin and Don Swanson for assistance in the x-ray part of the study. This work was supported by the Army Research Office through DAAG29-80-C-0008 and NSF Grant DMR-8303906.

REFERENCES

1. M. Kimura, Y. Fujino and T. Kawamura, *Appl. Phys. Lett.*, **29**, 227 (1976).
2. M. Kimura, *J. Appl. Phys.*, **48**, 2850 (1977).
3. S. Hausühl, J. Eckstein, K. Recker and F. Wallrafen, *J. Crystal Growth*, **40**, 200 (1977).
4. J. Melngailis, J. F. Vetelino, A. Jhunjhunwala, T. B. Reed, R. E. Fahey and E. Stern, *Appl. Phys. Lett.*, **32**, 203 (1978).
5. H. Yamauchi, *J. Appl. Phys.*, **49**, 6162 (1978).
6. A. Halliyal, A. S. Bhalla, R. E. Newnham and L. E. Cross, *J. Mat. Sci.*, **16**, 1023 (1981).
7. A. Halliyal *et al.* (to be published).
8. P. B. Moore and S. J. Louisnathan, *Z. Krist.*, **130**, 438 (1969).
9. R. Masse, J.-C. Grenier and A. Durif, *Bull. Soc. franc. Mineral. Cristallogr.*, **90**, 20 (1967).
10. G. E. Brown, S. Sueno and C. T. Prewitt, *Am. Mineral.*, **58**, 698 (1973).
11. L. W. Finger and E. Prince, *U.S.N.B.S. Tech. Note*, **854** (1975).
12. J. A. Ibers and W. C. Hamilton, Eds., *International Tables for X-Ray Crystallography*, Vol. IV. Revised and Supplementary Tables. Kynoch Press, Birmingham (1974).
13. W. C. Hamilton, *Acta Cryst.*, **18**, 502 (1965).
14. G. Blasse, *J. Inorg. Nucl. Chem.*, **41**, 639 (1979).
15. J. F. Nye, *Physical Properties of Crystals* (Oxford University Press, Oxford, 1979).

16. R. L. Byer and C. B. Roundy, *Ferroelectrics*, 3, 333 (1972).
17. A. S. Bhalla and R. E. Newnham, *Phys. Stat. Sol. (a)*, 58, K19 (1980).
18. G. Donnay, *Acta Cryst.*, A33, 927 (1977).
19. S. von Boguslawski, *Phys. Z.*, 15, 283, 569, 805 (1914).
20. S. C. Abrahams, F. Lissalde and J. L. Bernstein, *J. Appl. Cryst.*, 12, 104 (1979).
21. W. C. Hamilton and S. C. Abrahams, *Acta Cryst.*, A26, 18 (1970).
22. S. B. Lang, *Phys. Rev. B*, 4, 3603 (1971).
23. V. V. Gladkii and I. S. Zheudev, *Sov. Phys. Cryst.*, 10, 63 (1965).
24. H. Schmid, P. Genequand, H. Tippmann, G. Pouilly and H. Guedu, *J. Mat. Sci.*, 13, 2257 (1978).
25. N. Yamada, *J. Phys. Soc. Jpn.*, 46, 561 (1979).
26. H. G. Unruh and U. Rudiger, *J. Phys. (France)*, 33, 77 (1972).
27. A. S. Bhalla (unpublished work).
28. M. Kimura, K. Utsumi and S. Nanantsu, *J. Appl. Phys.*, 47, 2249 (1976).

DIELECTRIC, PIEZOELECTRIC AND PYROELECTRIC PROPERTIES
OF $\text{Sr}_2\text{TiSi}_2\text{O}_8$ POLAR GLASS-CERAMIC: A NEW POLAR MATERIAL

A. Halliyal, A.S. Bhalla, L.E. Cross and R.E. Newnham

Dielectric, piezoelectric and pyroelectric properties of $\text{Sr}_2\text{TiSi}_2\text{O}_8$ polar glass-ceramic: a new polar material

A. HALLIYAL, A. S. BHALLA, L. E. CROSS, R. E. NEWNHAM

Materials Research Laboratory, The Pennsylvania State University, University Park, PA 16802, USA

Polar $\text{Sr}_2\text{TiSi}_2\text{O}_8$ glass-ceramics were prepared by recrystallizing glasses in a steep temperature gradient. The dielectric, piezoelectric and pyroelectric properties were studied as a function of temperature in the temperature range -150 to 200°C . The sign of the pyroelectric coefficient is positive at room temperature and is attributed to the dominance of the secondary pyroelectric effect over the primary effect.

Anomalies were observed in the dielectric, pyroelectric and piezoelectric properties and a large hysteresis was observed in all these properties. Probable causes for the anomalies are discussed.

1. Introduction

Fresnoite ($\text{Ba}_2\text{TiSi}_2\text{O}_8$, hereafter designated BTS) is a polar but non-ferroelectric crystal with tetragonal space group $P4bm$. Single crystals of fresnoite have been grown successfully by the Czochralski technique by several workers [1-3]. Fresnoite has been shown to be a promising substrate material for surface acoustic wave (SAW) devices [1-5]. Its SAW properties are intermediate between those of LiNbO_3 and LiTaO_3 . For fresnoite z-cuts with wave propagation along the $[110]$ direction, the electromechanical coupling factor k_t^2 is 1.5% and the temperature coefficient of delay (TCD) is 50 ppm.

Recently, Ito and co-workers [6, 7] have shown that the TCD of fresnoite can be greatly lowered through the partial substitution of strontium for barium. Crystals of composition $(\text{Ba}_{2-x}\text{Sr}_x)\text{TiSi}_2\text{O}_8$ with uniform strontium concentration can be grown by edge-defined film-growth (EFG), for the compositions ranging from $x = 0$ to 0.8. It was found to be difficult to grow crystals of homogeneous composition by the Czochralski technique [7]. The strontium concentration in a Czochralski-grown crystal varies according to the normal freezing distri-

bution. Z-cut crystals with strontium concentration of $x = 0.8$ give a TCD value of 20 ppm with practically no reduction in the value of k_t^2 , and look to be very useful for SAW devices.

In compositions with $x \geq 1.0$, SrTiO_3 and SrSiO_3 also crystallize along with fresnoite, making it impossible to grow pure strontium titanium silicate ($\text{Sr}_2\text{TiSi}_2\text{O}_8$, hereafter designated STS) single crystals by the usual crystal growing techniques. However, X-ray diffraction studies on ceramic samples have shown that all compositions with $x = 0$ to 2.0 prepared by conventional ceramic processing techniques give single-phase fresnoite-type structure. The crystal symmetry of STS is the same as that of BTS. However, there are no measurements reported for the piezoelectric and pyroelectric properties of STS because of the difficulties in single-crystal growth. Moreover, since STS is a non-ferroelectric material, it is not possible to reorient the polar axes in individual crystallites and hence randomly axed ceramic samples will be of no use in studying the piezoelectric and pyroelectric properties.

In our earlier work it has been demonstrated that polar glass-ceramics with the fresnoite

structure can be prepared by recrystallizing glasses of slightly modified fresnoite compositions [8-11]. In these glass-ceramics, the polar texture results from needle-like crystals growing from the glass surface during crystallization. These fresnoite polar glass-ceramics showed piezoelectric and pyroelectric properties comparable to the single-crystal properties.

In the present study, polar STS glass-ceramics were prepared from glasses of non-stoichiometric composition. The dielectric, piezoelectric and pyroelectric properties of STS glass-ceramics were studied as a function of temperature in the temperature range -150°C to 200°C . Since our previous studies have shown that the properties of BTS single crystals and polar glass-ceramics are very similar [11], we expect that the properties of STS glass-ceramics reported in the present paper might be very similar to the single-crystal properties.

2. Experimental details

Glass samples were prepared by mixing reagent-grade chemicals followed by melting in a platinum crucible at 1400 to 1450°C . The melt was retained in the furnace for 4 to 6 h for fining and homogenization. The fined glass melt was air quenched by pouring it into graphite moulds to form cylinders of approximately 0.8 to 1 cm in diameter and 1 to 1.5 cm in length. Initially, an attempt was made to prepare glasses of stoichiometric STS composition. It was not possible to obtain clear glasses with uniform composition because of phase separation in the melt. Addition of excess silica to the composition helped to eliminate the phase separation problem. Glass samples containing one mole of excess silica (composition: $2\text{SrO}-3\text{SiO}_2-\text{TiO}_2$) were prepared for the present study. Glass-ceramic samples with polar texture were prepared by crystallizing the glasses in a temperature gradient as described elsewhere [8-11]. Microstructure studies indicated that needle-like crystals grow from the surface into the bulk along the direction of temperature gradient. X-ray powder diffraction patterns of glass-ceramic samples showed that the only crystalline phase in glass-ceramics was STS. Property measurements were carried out on sections (8 mm diameter and 0.5 mm thick) cut normal to the temperature gradient and with gold electrodes sputtered on the major surfaces.

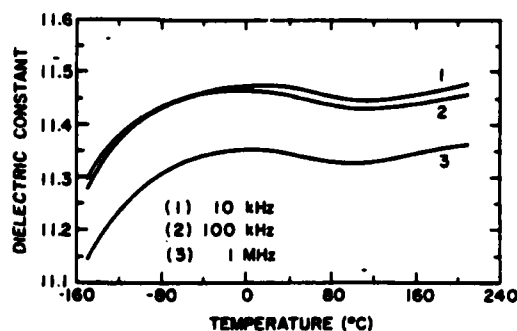


Figure 1 Dielectric constant of $2\text{SrO}-3\text{SiO}_2-\text{TiO}_2$ glass-ceramic as a function of temperature and frequency, over temperature range -150 to 200°C .

The dielectric constant and dissipation factors were measured at different frequencies using a capacitance bridge, and pyroelectric coefficients were measured by the Byer-Roundy [12] technique. The heating and cooling rates employed were $4^{\circ}\text{C min}^{-1}$. The electromechanical properties were determined by standard resonance techniques. All the above properties were measured as a function of temperature in both heating and cooling cycles. The hydrostatic voltage coefficient g_h was measured by a dynamic method described by Safari [13].

3. Results

The dielectric constant and dissipation factor of STS glass-ceramic are shown in Figs. 1 to 3. Broad peaks in dielectric constant were observed near 20 and 200°C . Below -20°C , the dielectric constant slowly decreased with decreasing temperature. There was an increase in dielectric

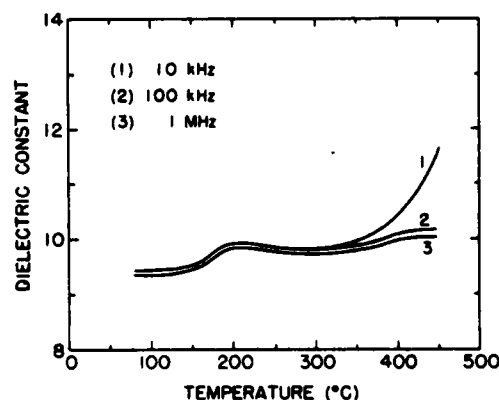


Figure 2 Dielectric constant of $2\text{SrO}-3\text{SiO}_2-\text{TiO}_2$ glass-ceramic as a function of temperature and frequency, over temperature range 80 to 450°C .

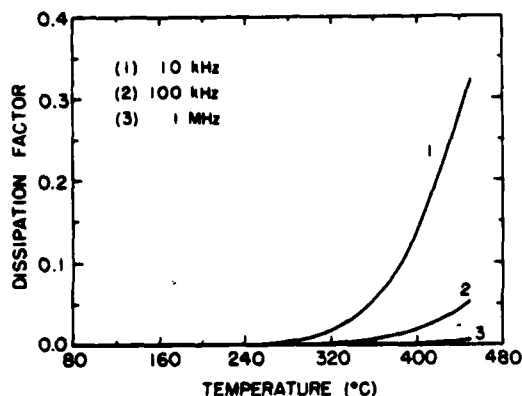


Figure 3 Dissipation factor of 2SrO-3SiO₂-TiO₂ glass-ceramic as a function of temperature and frequency.

constant and dissipation factor at higher temperatures, probably because of conduction. The dissipation factor curve was featureless up to 250°C and the losses were very low (< 0.001).

The variation of pyroelectric coefficient p_3 as a function of temperature is shown in Fig. 4. The pyroelectric coefficient p_3 is positive at room temperature and shows a very broad peak at about -20°C . An anomaly is observed in p_3 at about 120°C . A large hysteresis was observed between heating and cooling cycles above -10°C and this was particularly absent below -10°C . This behaviour in $p_3(T)$ was confirmed by repeating the heating and cooling measurements twice. Plots of $p_3(T)$ recorded during the two heating cycles were exactly the same, as were the plots for the two cooling cycles.

The variation of frequency constant N_p and electromechanical coupling factor k_p are shown in Figs. 5 and 6. Frequency constant N_p showed

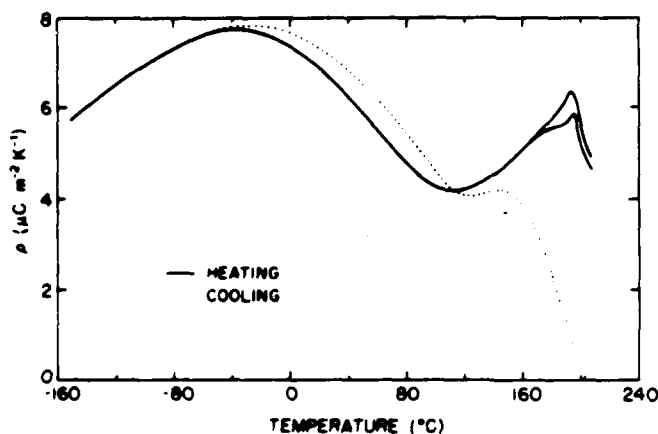


Figure 4 Variation of pyroelectric coefficient with temperature for 2SrO-3SiO₂-TiO₂ glass-ceramic.

TABLE I Room-temperature properties of 2SrO-3SiO₂-TiO₂ glass-ceramics

Density (g cm ⁻³)	3.55
Dielectric constant K_{11} , at 1 kHz	11.5
Dissipation factor	< 0.001
Pyroelectric coefficient p_3 ($\mu\text{C m}^{-2} \text{K}^{-1}$)	+ 7.5
d_{31} (pC N ⁻¹)	14
d_{32} (pC N ⁻¹)	1.6
d_{33} (pC N ⁻¹)	8.7
g_{31} ($10^{-3} \text{ V m N}^{-1}$)	138
g_{32} ($10^{-3} \text{ V m N}^{-1}$)	85
$d_h g_h$ ($10^{-15} \text{ m}^2 \text{N}^{-1}$)	740
Frequency constant N_p (m Hz)	2550
Frequency constant N_b (m Hz)	3300
k_1	0.08
k_p	0.10
Mechanical quality factor Q	700
Temperature coefficient of resonance (ppm °C ⁻¹)	50

a minimum at about 150°C in the cooling cycles and at about 200°C in the heating cycles. A large hysteresis similar to the one in pyroelectric coefficient measurement was observed between heating and cooling cycles in N_p and k_p . At the inflection point the value of temperature coefficient of resonance (TCR), defined as

$$\text{TCR} = \frac{1}{f_r} \frac{\partial f_r}{\partial T} \quad (1)$$

is zero. Here, f_r is the resonance frequency at temperature T . The minimum in N_p during the heating cycle and the small anomaly in the dielectric constant occur at the same temperature ($\sim 200^\circ\text{C}$). The room-temperature properties of STS glass-ceramics are listed in Table I.

4. Discussion

In our previous study on BTS single crystals and

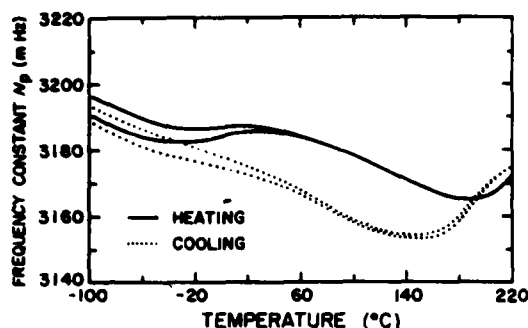


Figure 5 Temperature dependence of frequency constant N_p of $2\text{SrO}-3\text{SiO}_2-\text{TiO}_2$ glass-ceramic.

glass-ceramics [11], it was clear that all the properties of glass-ceramics containing one mole of excess silica (composition: $2\text{BaO}-3\text{SiO}_2-\text{TiO}_2$) were very similar to those of BTS single crystals. In the case of STS glass-ceramics (composition: $2\text{SrO}-3\text{SiO}_2-\text{TiO}_2$) we can also expect the properties of glass-ceramics to be similar to the properties of STS single crystals. In addition, we can expect the same anomalies in the dielectric, piezoelectric and pyroelectric properties of single crystals also.

The unusual features in all the properties of STS glass-ceramics suggest the possibility of a structural phase transition, since in most of the ferroelectric crystals structural changes are accompanied by anomalies in dielectric and related properties. In the absence of data about the properties of STS single crystals, it may be fruitful to compare the properties of STS glass-ceramics with those of BTS single crystals which show similar anomalies in properties [11]. In BTS single crystals, the sign of the pyroelectric

coefficient is positive at room temperature and becomes negative at about 190°C . Sharp peaks in K_{33} , p_3 and k_p are observed at 160°C and a minimum is observed in resonance frequency at the same temperature. A single-crystal X-ray study [14] did not indicate any phase transition in BTS. The origin of the anomaly in the dielectric and related properties of BTS is thought to be related to anomalous behaviour of some of the elastic constants near 160°C [11], and, because of the coupling between elastic and other properties, this could also lead to anomalies in the piezoelectric and pyroelectric properties.

A comparison of the properties of BTS single crystals and STS glass-ceramics indicates that it is highly unlikely that there is a phase transition in STS in the temperature range -150°C to 200°C . In STS also the reason for the anomaly in all the properties might be anomalous behaviour of some of the elastic constants. However, a detailed measurement of the temperature dependence of all the elastic constants and thermal expansion coefficients is necessary to support the above assumption.

The pyroelectric coefficient p_3 of STS is positive in the temperature range -150°C to 200°C and shows a peak value of about $8\mu\text{C m}^{-2}\text{K}^{-1}$ at about -20°C . In BTS also, p_3 is positive at room temperature and the reason for this is that the secondary component of p_3 (p_{sec}) is larger than the primary component of p_3 (p_{prim}) at room temperature [15]. The calculated value of p_{sec} in BTS is about $16.5\mu\text{C m}^{-2}\text{K}^{-1}$. Unfortunately it is not possible to separate the primary and secondary effects in STS as the full family of elastic, piezoelectric and thermal expansion constants required to assess the secondary effect have not yet been measured.

In the case of both BTS single crystals and glass-ceramics, all the properties were exactly the same in both heating and cooling cycles and the anomalies occurred at the same temperature without any hysteresis [11]. In STS glass-ceramic, there is a large hysteresis in piezoelectric and pyroelectric properties and the anomalies occur at slightly different temperatures in heating and cooling cycles. The reason for this hysteresis in STS is not clear at present. Measurement of dielectric constant and pyroelectric coefficient with an applied bias electric field might help in understanding the origin of this unusually large hysteresis.

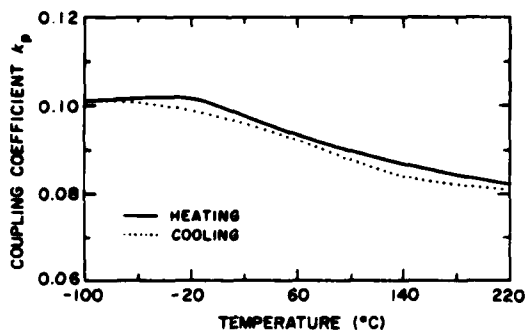


Figure 6 Variation of planar coupling coefficient k_p with temperature for $2\text{SrO}-3\text{SiO}_2-\text{TiO}_2$ glass-ceramic.

5. Summary

The present study demonstrates the usefulness of preparing polar materials by the glass-ceramic route. For several non-ferroelectric materials, which are difficult to prepare in single-crystal form and can be prepared easily as glasses, the polar glass-ceramic technique described in the present work can be used to assess the piezoelectric and pyroelectric effects in the crystalline phase. Ceramic samples of such materials will not be useful for studying the above properties since they cannot be poled by an external electric field. If it is possible to prepare glasses of the required material with minor modification in the composition, the technique of preparing glass-ceramics with oriented polar texture provides an alternative method to study the properties of such materials. In the case of $\text{Sr}_2\text{TiSi}_2\text{O}_8$ it was possible for the first time to obtain reliable data on both pyroelectric and piezoelectric properties, by the glass-ceramic technique.

Acknowledgements

We thank all our colleagues in the ferroelectrics group at MRL for their help in this work. This work was supported by the Army Research Office through Contract No. DAAG29-80-C-0008 and the National Science Foundation Grant No. DMR-8303906.

References

1. M. KIMURA, Y. FUJINO and T. KAWAMURA, *Appl. Phys. Lett.* **29**, (1976) 227.
2. M. KIMURA, *J. Appl. Phys.* **48**, (1977) 2850.
3. S. HAUSSUHL, J. ECKSTEIN, K. REICHER and F. WALLARAFEN, *J. Cryst. Growth* **40** (1977) 200.
4. H. YAMAUCHI, *J. Appl. Phys.* **49** (1978) 6162.
5. J. MELNGAILIS, J. F. VEACLINO, A. THUNJUNWALA, T. B. REED, R. E. FAHEY and E. STERN, *Appl. Phys. Lett.* **32** (1978) 203.
6. Y. ITO, K. NAGATSUMA and S. ASHIDA, *ibid.* **36** (1980) 894.
7. *Idem.* *Jap. J. Appl. Phys.* **20** (1981) 163.
8. A. HALLIYAL, A. S. BHALLA, R. E. NEWNHAM and L. E. CROSS, *J. Mater. Sci.* **16** (1981) 1023.
9. A. HALLIYAL, A. S. BHALLA and R. E. NEWNHAM, *Mater. Res. Bull.* **18** (1983) 1007.
10. A. HALLIYAL, A. SAFARI, A. S. BHALLA, R. E. NEWNHAM and L. E. CROSS, *J. Amer. Ceram. Soc.* **67** (1984) 331.
11. A. HALLIYAL, S. A. MARKGRAF, A. S. BHALLA, L. E. CROSS and R. E. NEWNHAM, *Ferroelectrics* in press.
12. R. L. BYER and C. B. ROUNDY, *Ferroelectrics* **3** (1972) 333.
13. A. SAFARI, PhD Thesis, The Pennsylvania State University, 1983.
14. S. A. MARKGRAF, A. HALLIYAL, A. S. BHALLA, R. E. NEWNHAM and C. T. PREWITT, *Ferroelectrics* in press.
15. A. S. BHALLA and R. E. NEWNHAM, *Phys. Status Solidi a* **58** (1980) K19.

Received 18 October

and accepted 22 November 1984

PYROELECTRIC AND PIEZOELECTRIC PROPERTIES OF LITHIUM
TETRABORATE SINGLE CRYSTAL

A.S. Bhalla, L.E. Cross and R.W. Whatmore

Pyroelectric and Piezoelectric Properties of Lithium Tetraborate Single Crystal

A. S. BHALLA, L. E. CROSS and R. W. WHATMORE*

Materials Research Laboratory
The Pennsylvania State University
University Park, PA 16802, USA

*Plessey Research Ltd, Allen Clark Research Center,
Caswell, Towcester, Northants

Pyroelectric, piezoelectric and dielectric properties of single crystal $\text{Li}_2\text{B}_4\text{O}_7$ (LTB) are measured in the temperature range from 50°C down through -150°C . At room temperature LTB has dielectric constant $K_3 \sim 10$ (at 100 KHz) and dielectric $\tan \delta \sim 1$ (10 KHz). At liquid nitrogen temperatures, the $\tan \delta$ decreased to $\sim 10^{-3}$. Pyroelectric coefficient at room temperature measured $\sim 30 \mu\text{C}/\text{m}^2\text{-K}$ which increased to $\sim 120 \mu\text{C}/\text{m}^2\text{-K}$ at -150°C and showed the pyroelectric figure of merit p/K comparable to the value obtained on TGS at room temperature. Primary and secondary components of pyroelectricity are separated and the results suggest that the major contribution comes from the primary effect in $\text{Li}_2\text{B}_4\text{O}_7$.

Piezoelectric measurements show high values of $g_{31} \approx 270 \times 10^{-3} \text{ V-m/N}$ and $g_{33} \approx 100 \times 10^{-3} \text{ V-m/N}$ indicating potential application of $\text{Li}_2\text{B}_4\text{O}_7$ in the area of pressure sensors.

§1. Introduction

Lithium tetraborate ($\text{Li}_2\text{B}_4\text{O}_7$) is an important non-ferroelectric piezoelectric material. At room temperature it belongs to a tetragonal symmetry 4 mm with a polar axis along the crystallographic c -axis. Recent measurements of bulk wave and surface acoustic wave propagation on $\text{Li}_2\text{B}_4\text{O}_7$ single crystal showed a promising application of this material as a SAW substrate.¹⁻³⁾

In a previous report from this Laboratory, the measurements on piezoelectric and pyroelectric properties of several silicates and germanates indicated the promising applications of such materials as hydrostatic pressure and thermal sensors. This paper describes the results of pyroelectric, piezoelectric and dielectric measurements on $\text{Li}_2\text{B}_4\text{O}_7$. At room temperature LTB has a low dielectric constant, $K_3 \approx 10$, but reasonably high $\tan \delta$ values. Therefore the pyroelectric and dielectric measurements have been extended down through -150°C .

§2. Experimental and Results

Large area, σ optically transparent single crystals of $\text{Li}_2\text{B}_4\text{O}_7$ were grown by the Czochralski method. The plates oriented perpendicular to c -axis were cut and polished to a thickness 0.4-0.6 mm. Sputtered gold electrodes were deposited on both the faces of the plates and pyroelectric, piezoelectric, dielectric measurements were made. The results of these experiments are described in the following sections and also summarized in Table I.

2.1 Dielectric measurements

The temperature dependence of the dielectric constant and $\tan \delta$ were measured by multifrequency LCR-meter. At room temperature, the samples were very lossy and thus the measurements were made down through -150°C . Figure 1 shows the plots of the dielectric constant at various frequencies and temperatures. The dielectric constant increased slightly from the room temperature $K \approx 10$ (100 kHz) when the samples were cooled

Table I. Crystallographic, Dielectric, Piezoelectric, Thermal and Pyroelectric Properties of $\text{Li}_2\text{B}_4\text{O}_7$ Single Crystal.

Crystallographic			
Crystal Class 4 mm			
Lattice Parameters		$a = 9.47 \text{ \AA}$	$c = 10.26 \text{ \AA}$
Dielectric Properties			
K	10 (-20 to -150°C)	$\tan \delta$ (30°C)	(-150°C)
(100 Hz - 100 kHz)			
	100 Hz	6	0.010
	1 kHz	2	0.003
	10 kHz	0.2	0.002
	100 kHz	0.03	0.001
Piezoelectric Constants			
d_{33}	$24.0 \times 10^{-12} \text{ C/N}$	g_{33}	$271 \times 10^{-3} \text{ V-m/N}$
d_{31}	$-4.8 \times 10^{-12} \text{ C/N}$	g_{31}	$160 \times 10^{-3} \text{ V-m/N}$
d_h	$14.4 \times 10^{-12} \text{ C/N}$	g_{hdh}	$2300 \times 10^{-12} \frac{\text{m}^2}{\text{N}}$
	$e_{33} = 0.9 \text{ C/m}^2$		
	$e_{31} = 0.2 \text{ C/m}^2$		(Ref. 2)
Expansion Coefficients (25°C)			
α_1	$12.5 \times 10^{-6}/^\circ\text{C}$	α_3	$-2.5 \times 10^{-6}/^\circ\text{C}$
Specific Heat	$cp = 3.2 \text{ Jcm}^{-3}\text{K}^{-1}$	ρ	2.45 gm/cc (Reg. 9)
Pyroelectric Properties (25°C)			
p_T	$-30 \mu\text{C}/\text{m}^2\text{-K}$	ΔP	$1.5 \mu\text{C}/\text{cm}^2$
p_{ec}	$+2.75 \mu\text{C}/\text{m}^2\text{-K}$		(from 10 to -150°C)
p_{orm}	$-32.75 \mu\text{C}/\text{m}^2\text{-K}$		
p_T	(-150°C) $= -120 \mu\text{C}/\text{m}^2\text{-K}$		

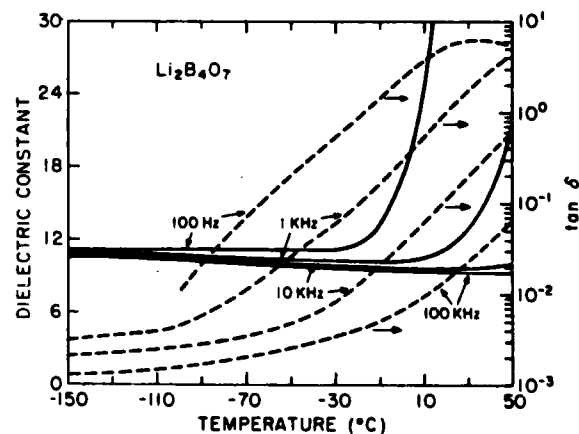


Fig. 1. K vs T and $\tan \delta$ vs T plots of $\text{Li}_2\text{B}_4\text{O}_7$ at various frequencies.

down to -150°C . The dielectric loss also dropped down to $\sim 10^{-3}$ at -150°C compared to the room temperature values of $\tan \delta = 1$ (at 10 kHz).

2.2 Piezoelectric measurements

The piezoelectric d_{33} and d_{31} were measured by the d_{33} -meter. From these values the hydrostatic piezoelectric constant ($d_h = d_{33} + 2d_{31}$) was calculated. The hydrostatic d_h and g_h constants were also measured by using an acoustic reciprocity technique.⁴⁻⁶ The results were close to the calculated values. The $g_{33} \sim 270 \times 10^{-3} \text{ V-m/N}$ of $\text{Li}_2\text{B}_4\text{O}_7$ is one of the largest known values of g_{33} and is higher than that of PVF_2 . The measured g_h values were on the range $\sim 100 \times 10^{-3} \text{ V-m/N}$ and again these are comparable to one of the favorable hydrostatic sensing material PVF_2 . The hydrostatic d_h and g_h in the case of $\text{Li}_2\text{B}_4\text{O}_7$ were independent of pressure.⁶⁻⁷

2.3 Pyroelectric measurements

The pyroelectric coefficients were measured by the Byer-Roundy method over a temperature range from 50°C down through -150°C . The temperature dependence of the pyroelectric coefficient is shown in Fig. 2 and 3. At room temperature, the pyroelectric coefficient (p_T) varied slightly for different samples giving the values in the range -35 to $-50 \mu\text{C/m}^2\text{-K}$. The pyroelectric coefficients increased with a decrease in temperature and reached the value 120 – $130 \mu\text{C/m}^2\text{-K}$ at 150°C . The measured pyroelectric coefficient p_T is generally the sum of the primary, p_{prim} , and secondary, p_{sec} , components of the pyroelectricity in the crystal. i.e.

$$p_T = p_{\text{prim}} + p_{\text{sec}}$$

If p_{sec} is positive and p_{prim} is negative, then the increase in the p_T coefficient could be due to the decrease in the secondary pyroelectricity in the crystal. The secondary pyroelectricity in the crystal class 4 mm is expressed as⁸⁾

$$p_{\text{sec}} = e_{33}\alpha_3 + 2e_{31}\alpha_1$$

or

$$p_{\text{sec}} = d_{33}(2c_{31}\alpha_1 + c_{33}\alpha_3) + 2d_{31}(c_{11}\alpha_1 + c_{12}\alpha_1 + c_{13}\alpha_3)$$

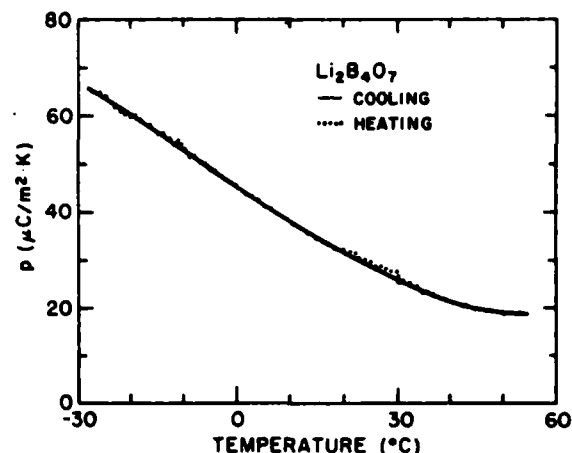
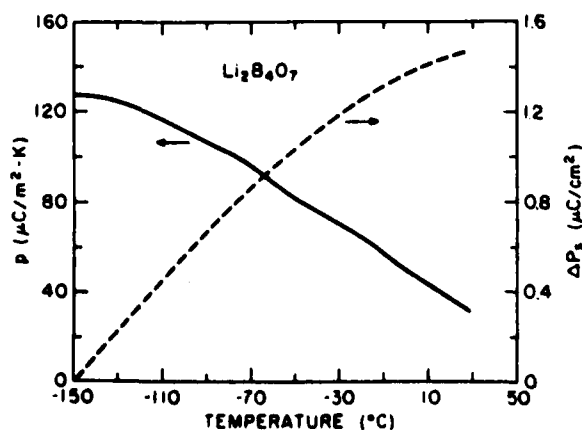


Fig. 3. p vs T plots in the heating and cooling cycles for single crystal LTB.

where c_{ij} are the elastic stiffnesses, e_{ij} the piezoelectric stress coefficients, d_{ij} the piezoelectric strain coefficients and α_i are the expansion coefficients of a single crystal.

From the experimentally determined α_i and published e_{ij} coefficients,²⁾ the calculated value of the secondary contribution was $+2.75 \mu\text{C/m}^2\text{-K}$. This result showed the small effect of the secondary pyroelectricity on the total magnitude of the coefficient. One should expect this value to be still smaller at lower temperatures as α_i generally decrease and d_{ij} stabilize as the temperature of the sample decreases provided the sample does not go through any phase transition at lower temperature. There is no documented evidence of any kind of phase transition in $\text{Li}_2\text{B}_4\text{O}_7$, but the possibility of phase transition near liquid nitrogen temperatures or the anomalous behavior in the α_i vs T and d_{ij} vs T at lower temperatures are not ruled out.

In Table II the pyroelectric properties of $\text{Li}_2\text{B}_4\text{O}_7$ at -150°C are compared to those of some favorable pyroelectric materials used for thermal sensors elements at temperature of their best performance. It is evident that both p/K and $p/\sqrt{K \tan \delta}$ figures of merit in the case of $\text{Li}_2\text{B}_4\text{O}_7$ are superior to those in other listed potential materials like TGS, LiTaO_3 , Ni-Br boracite ($\sim 100^{\circ}\text{C}$). Moreover at lower temperatures $\approx -150^{\circ}\text{C}$, most conventional ferroelectric pyroelectric materials have poor pyroelectric figures of merit for infrared vidicon and detector applications.

At -150°C , the room temperature specific heat⁹⁾ $\rho c = 3.2 \text{ Jcm}^{-3}\text{K}^{-1}$ is expected to decrease and thus will

Table II. Comparison of Pyroelectric Properties of $\text{Li}_2\text{B}_4\text{O}_7$, TGS, LiTaO_3 and Ni-Br Boracite Single Crystals.

Property	TGS (25°C)	$\text{Li}_2\text{B}_4\text{O}_7$ (-150°C)	LiTaO_3 (25°C)	Ni-Br Boracite ($< 100^{\circ}\text{C}$)
p ($\mu\text{C m}^{-2} \text{-K}$)	330	120–130	180	140
K	30	10	45	11
$\tan \delta$	5×10^{-1}	10^{-1}	10^{-1}	2×10^{-1}
c_p ($\text{Jcm}^{-3}\text{K}^{-1}$)	2.5	3 (25°C)	3.2	2.0
$p \times K$ ($\mu\text{C m}^{-2} \text{-K}$)	11.0	12–13.0	4.0	12.7
$p \times K$ ($\mu\text{C m}^{-2} \text{-K}$)	60	38	27	42
$p \times K \tan \delta$ ($\mu\text{C m}^{-2} \text{-K}$)	8.5×10^2	12×10^2	8.5×10^2	9.2×10^2

improve the figure of merit $p/(\rho c \sqrt{K \tan \delta})$ also.

Thus from above studies, it is concluded that $\text{Li}_2\text{B}_4\text{O}_7$ is one of the important materials with potential applications in hydrostatic pressure sensor, robotic pressure sensor and thermal sensor in the lower temperature environment near liquid nitrogen temperature besides its well established place in the surface acoustic wave devices.

References

- 1) R. W. Whatmore, N. M. Shorrocks, F. W. Ainger and I. M. Young: Electronics Lett. 17 (1981) 11.
- 2) N. M. Shorrocks, R. W. Whatmore and F. W. Ainger: IEEE Ultrasonic Symposium Proceedings (1981) 337.
- 3) D. S. Robertson and I. M. Young: J. Mat. Sci. 17 (1982) 1729.
- 4) R. J. Bobber: Underwater Electroacoustic Measurements GPO, Washington, DC (1970) 27-41.
- 5) C. C. Sims and T. A. Henriquez: J. Acous. Soc. Am. 36 (1984) 1704.
- 6) R. Y. Ting, A. Halliyal and A. S. Bhalla: Appl. Phys. Lett. 44 (1984) 852.
- 7) R. Y. Ting, A. Halliyal and A. S. Bhalla: IMF-VI (Kobe, Japan) proceedings.
- 8) A. S. Bhalla and S. T. Liu: "Pyroelectric Coefficients" in Landolt-Bornstein 18 (1984) 325.
- 9) R. W. Whatmore (to be published).

QUANTUM FERROELECTRICITY IN $(\text{Cd,Pb})_2(\text{Nb,Ta})_2\text{O}_7$

C.F. Clark, W.N. Lawless and A.S. Bhalla

Quantum Ferroelectricity in $(\text{Cd}, \text{Pb})_2(\text{Nb}, \text{Ta})_2\text{O}_7$

C. F. CLARK, W. N. LAWLESS and A. S. BHALLA*

CeramPhysics, Inc. Westerville, Ohio 43081, U.S.A.

*Materials Research Lab. Pennsylvania State University, U.S.A.

Quantum ferroelectricity has been induced for the first time in a pyrochlore structure. Starting with the known ferroelectric $\text{Cd}_2\text{Nb}_2\text{O}_7$, ($T_c \sim 185$ K), the transition temperature can be lowered to 0 K by a combination of Pb substitutions on the A-site and Ta substitutions on the B-site. The dielectric constants of the resulting materials have several of the typical characteristics of known quantum ferroelectrics which are all perovskites. There are, however, differences in the dielectric behavior compared to the perovskites and to renormalization-group theory results.

§1. Introduction

In recent years the transition from quantum to classic ferroelectricity has been demonstrated in several perovskite-type compounds by making ionic substitutions on either the A or B site. We report here that quantum ferroelectric effects have been found in ceramics of the pyrochlore system $(\text{Cd}, \text{Pb})_2(\text{Nb}, \text{Ta})_2\text{O}_7$ wherein the behavior of the dielectric constant as a function of composition and temperature is markedly different from the perovskites.

The dielectric behavior of the perovskites in the quantum regime is consistent from system to system and agrees in general with theory. Höchli and Rytz have studied $\text{K}(\text{Ta}, \text{Nb})\text{O}_3$ ^{1,2)} and $(\text{K}, \text{Na})\text{TaO}_3$ ^{2,4)} Bednorz and Müller³⁾ have studied $(\text{Sr}, \text{Ca})\text{TiO}_3$, and there is some literature^{6,7)} on quantum ferroelectricity in $(\text{Ba}, \text{Sr})\text{TiO}_3$. In each of these cases, quantum ferroelectric effects were studied primarily by dielectric constant measurements.

In each case above, concentration changes of the appropriate ion bring about marked changes in both the temperature of the dielectric constant maximum and the dielectric behavior at low temperatures. For example,^{1,2)} in $\text{KTa}_{1-x}\text{Nb}_x\text{O}_3$ the percentage of Nb can be taken as the interaction parameter because variations in x will cause variations in the dielectric properties of the compound. In this case, as x decreases, the ferroelectric transition temperature falls monotonically, approaching $T_c = 0$ K at about $x_c = .008$ (the "critical" concentration). At this concentration, the dielectric constant flattens around 6 K and stays relatively constant at lower temperatures; i.e., the long-range polar ordering is inhibited by quantum fluctuations (zero point motion). These features are characteristic of all quantum ferroelectrics.

For each of the perovskite systems, the relationship between the transition temperature, T_c , and the concentration follows the relationship

$$T_c \propto (x - x_c)^\phi \quad (1)$$

where $\phi = 1$ for high T_c 's (classical regime) and $\phi = 2$ for low T_c 's (quantum regime). This relationship has been predicted theoretically using renormalization-group theory^{8,9)} and has been confirmed for each of the perovskites. The critical concentration is different for each system, but is less than 1% in each case listed above.

§2. Experimental Results on the $(\text{Cd}, \text{Pb})_2(\text{Nb}, \text{Ta})_2\text{O}_7$ System

In each of the perovskite systems, the starting point is a material already known to be in the quantum regime (e.g. SrTiO_3 , KTaO_3), and substitutions raise the transition temperature into the classical ferroelectric regime. Here, in contrast, we started with a known ferroelectric, $\text{Cd}_2\text{Nb}_2\text{O}_7$, and made substitutions to induce the quantum regime. The transition temperature of $\text{Cd}_2\text{Nb}_2\text{O}_7$ was previously reported to be 185 K¹⁰⁾ and was re-measured by us to be 188 K. Adding Pb on the A site and/or Ta on the B site lowers the transition temperature¹⁰⁾ without, however, inducing a structural change. The correct combinations of substitutions can produce a range of compounds which are in the quantum regime; i.e., the dielectric constant becomes temperature-independent and the transition temperature is near 0 K. This behavior is illustrated in the phase diagram of Fig. 1 which shows isotherms of T_c as a function of the substitution concentration. The $T_c = 0$ K line is approximate and was found by extrapolation from compounds with higher T_c 's. In the region under the $T_c = 0$ line, the ferroelectric transition temperatures are predictable; i.e., increasing the Pb and/or Ta content always decreases T_c . The region with Pb concentrations greater than 70% was investigated and did show a deviation from this behavior. In particular, the $T_c = 0$ K region does not extend further

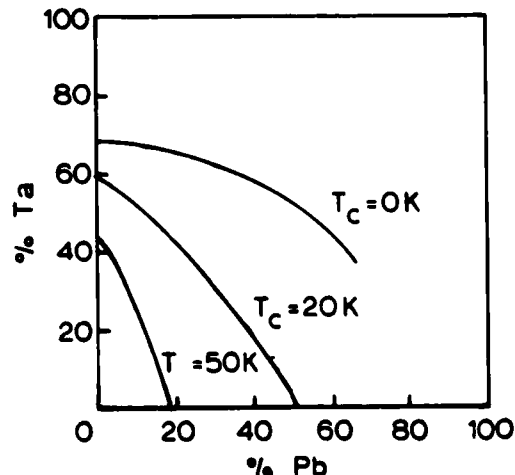


Fig. 1. Phase diagram of ferroelectric transition temperatures in the system $(\text{Cd}, \text{Pb})_2(\text{Nb}, \text{Ta})_2\text{O}_7$.

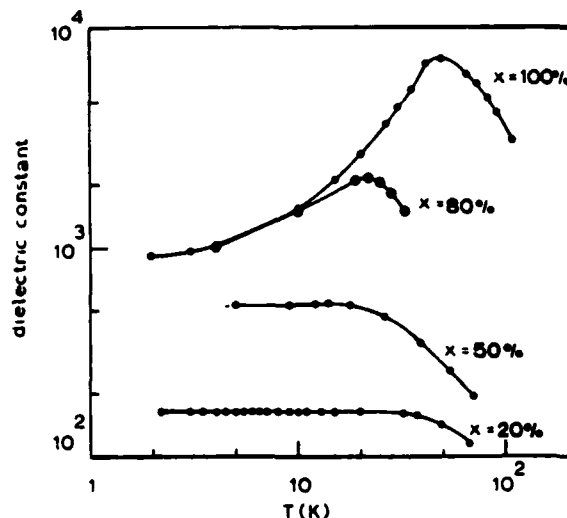


Fig. 2. Dielectric constants versus temperature for four substitution levels of $x=\text{Nb}\%$ in CPNT-20- x .

than shown since compounds at 80% Pb and low amounts of Ta still show ferroelectric features, but T_c begins to increase with $\text{Ta}\% > 20\%$ rather than decreasing as it would if the $\text{Pb}\%$ were lower. The discussion of quantum effects is limited here to the region near the $T_c=0$ K line, and the classical ferroelectric compounds considered were all below the $T_c=0$ K line.

It is convenient for this system to examine compounds with a constant Pb concentration and varying Ta (or Nb) concentration. Figure 2 shows the dielectric constant as a function of temperature for several compounds with a constant 20% Pb substitution and four different levels of Nb substitution. The nomenclature CPNT- y - x will be used and means a compound with y mole percentage of Pb and x mole percentage of Nb; i.e., $(\text{Cd}_{1-x}\text{Pb}_x)_2(\text{Nb}_y\text{Ta}_{1-y})_2\text{O}_7$. Even though we started with $\text{Cd}_2\text{Nb}_2\text{O}_7$ and added Pb and Ta to move from the classical into the quantum regime, the percentage of Nb (rather than Ta) will be used as the interaction parameter to conform to the relationship of Eq. (1) and to emphasize the analogy with the similar role of Nb in $\text{K}(\text{Ta}, \text{Nb})\text{O}_3$.

Figure 2 clearly illustrates the typical behavior of a system approaching a quantum regime. The compound CPNT-20-100 shows typical ferroelectric behavior with a transition temperature $T_c \sim 50$ K. As the Nb concentration decreases, the transition temperature approaches 0 K and the maximum dielectric constant decreases. With 50% Nb the dielectric constant flattens with a small maximum near 10 K. At 20% Nb, the dielectric constant is very nearly constant over a wide temperature range. The data in Fig. 2 are similar for any series of compounds with variable x and $0 \leq y \leq 70$. Figure 3 shows the variation in T_c as a function of Nb concentration for four different y concentrations and indicates a radical difference from the perovskite systems. As T_c approaches 0 K in Fig. 3, the curvature is opposite from that predicted by Eq. (1) with $\phi=2$. In fact a value of $\phi=1.2$ is suggested by the Fig. 3 data. No fits of Eq. (1) were made using the data of Fig. 3 since there are no good criteria for establishing a critical concentration, x_c , for each curve,

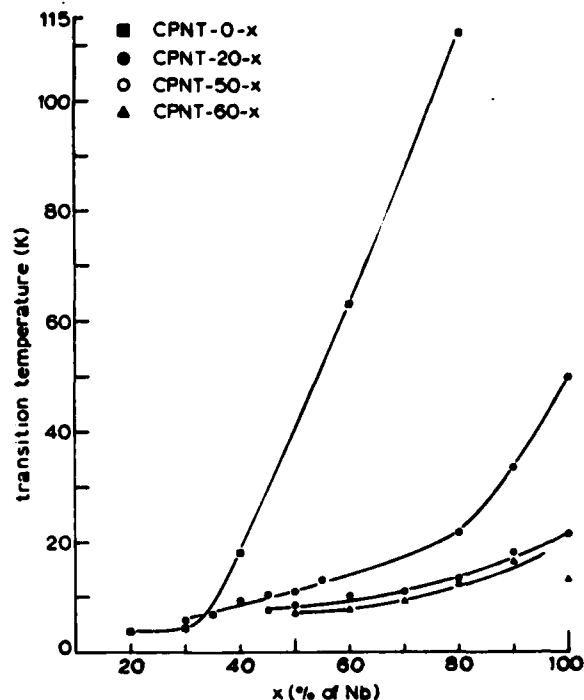


Fig. 3. Transition temperatures as a function of $x=\text{Nb}\%$ in CPNT- y - x for four different values of $y=\text{Pb}\%$.

and the fit would be very sensitive to this value. In the perovskite systems, a curve similar to Fig. 3 would show T_c approaching zero with an infinite slope; i.e., there is a well defined limit which defines x_c . There are no such criteria here.

Pyroelectric measurements were made to obtain spontaneous polarization values on a number of CPNT compounds. The accuracy of the measurements was limited to about $\pm 50\%$ in P_s , yet the data clearly indicate strong trends as T_c decreases. A check on the measurement system was made with pure $\text{Cd}_2\text{Nb}_2\text{O}_7$ and yielded a spontaneous polarization value of $4-6 \times 10^{-6} \text{ C/cm}^2$ at ~ 120 K which compares favorably to a previously measured value of $6 \times 10^{-6} \text{ C/cm}^2$ reported by Jona *et al.*¹⁰⁾

The polarization values in the classical regime here were large and typical for compounds in the classical ferroelectric regime. The spontaneous polarization decreased rapidly for compounds with decreasing Nb concentrations. For instance, CPNT-20-100 had a peak polarization of $\sim 15 \times 10^{-6} \text{ C/cm}^2$ which fell monotonically as the Nb percentage was decreased until a low value of $\sim 3 \times 10^{-9} \text{ C/cm}^2$ was reached at CPNT-20-30. These low values and the absence of any polarization peaks in the quantum regime indicate within measurement accuracy the absence of ferroelectric transitions in this regime.

§3. Conclusions

There are other differences of the pyrochlore CPNT system compared to the previously studied perovskite systems. Note that the $T_c=0$ K line of Fig. 1 is at large concentrations of Nb unlike the perovskite systems with small critical concentrations. It is also typical of the

perovskite quantum ferroelectrics that the flattening of the dielectric constant occurs no higher than about 6 K. In the CPNT system the flattening occurs over a much wider temperature range; the variation in ϵ can be as little as two parts in 10,000 between 2 K and 10 K. This flattening is not surprising considering the large concentration of Nb needed for $T_c=0$ K. Such large concentrations may imply a large range of transition temperatures within the ceramic, all of which are in the quantum regime, and the cumulative effect would be a wide range flattening of the dielectric constant.

The magnitudes of the dielectric constants near the quantum regime differ from those in the perovskites. In the (Ba, Sr)TiO₃ system, pure SrTiO₃ has the largest dielectric constant⁶⁾ (~24,000) which decreases as Ba is added. In the (Ca, Sr)TiO₃ the dielectric constant peaks rise to ~60,000 (with $T_c=30$ K) as Ca is added. In K(Ta, Nb)O₃¹³⁾ dielectric constants are again of the order 3000–4000 at the maximum for compounds in the quantum regime and the peak values rise as high as 9000 in the classical regime. On the other hand the dielectric constant peaks in the CPNT system are largest (~8,000) in the classical regime (i.e., at large Nb concentrations) and fall off rapidly as the quantum regime is approached. Along the $T_c=0$ K line in Fig. 1, the maximum dielectric constant is consistently 150–200. This variation in dielectric constant is consistent with the trend in the spontaneous polarization as noted above, and does suggest that the system may be more of a "quantum paraelectric" than a "quantum ferroelectric" for the material with low T_c 's.

Crystalline structure changes will not account for the CPNT data. It is known¹⁰⁾ that (Cd, Pb)₂Nb₂O₇ remains a pyrochlore except for a small region near pure Pb, and there are no structural changes over the 0–60% Pb substitution levels studied here. Another study¹¹⁾ of Cd₂(Nb, Ta)₂O₇, indicated there were no structural changes between 0 and 90% Ta. This is not surprising since the ionic radii of Nb⁵⁺ and Ta⁵⁺ are so similar (0.69 Å and 0.68 Å respectively). Thus there is no reason to suspect any crystallographic anomalies for any compounds below the $T_c=0$ K line of Fig. 1. There are certainly no dielectric discontinuities in any of the compounds studied.

Pressure can also be a valid interaction parameter and can lower the transition temperature following Eq. (1).

There are at least three cases of anomalous departure from Eq. (1) involving pressure in recent literature for materials in the quantum regime. In each case, the transition temperature approached 0 K at other than an infinite slope. Three different materials were involved: SbSI¹²⁾, (Ba, Sr)TiO₃¹³⁾, and K(Ta, Nb)O₃¹⁴⁾. The latter case is the most interesting because it involves the otherwise "well-behaved" system most widely studied for quantum effects. The author studied crystals with a Nb concentration of $x=.02$; (i.e., a compound well into the ferroelectric regime at zero pressure) and found the dielectric peak was not a simple ferroelectric structural phase transition, as previously assumed.

The implication for the present work on CPNT is that even though the CPNT system begins with a well-behaved ferroelectric material, (i.e., Cd₂Nb₂O₇) the introduction of ionic substitutions complicates the behavior such that Eq. (1) is no longer valid.

Finally, one must consider the possibility that the suppression in (Cd, Pb)₂(Nb, Ta)₂O₇ ceramics may not be the quantum suppression seen in single-crystal the perovskites. At such large Nb concentrations, the random fields due to compositional inhomogeneity may provide the suppression. Also, strain field in ceramics may play a role.

This work has been supported by the National Science Foundation under the SBIR Grant No. ISI-8212384.

References

- 1) U. T. Höchli, H. E. Weibel, and L. A. Boatner: Phys. Rev. Lett. **39** (1976) 1158.
- 2) D. Rytz, U. T. Höchli, and H. Bilz: Phys. Rev. **B22** (1980) 359.
- 3) J. J. van der Klink and D. Rytz: Phys. Rev. **B27** (1983) 4471.
- 4) U. T. Höchli and L. A. Boatner: Phys. Rev. **B20** (1979) 266.
- 5) J. G. Bednorz and K. A. Müller: Phys. Rev. Lett. **52** (1984) 2289.
- 6) K. A. Müller and H. Burkard: Phys. Rev. **B19** (1979) 3593.
- 7) H. Braeter, W. Windsch and V. L. Aksenov: Ferroelectrics Lett. **3** (1985) 97.
- 8) R. Oppermann and H. Thomas: Z. Phys. **B22** (1975) 387.
- 9) R. Morf, T. Schneider and E. Stoll: Phys. Rev. **B16** (1977) 462.
- 10) F. Jona, G. Shirane and R. Pepinsky: Phys. Rev. **98** (1955) 903.
- 11) A. W. Sleight and J. D. Bierlein: Solid State Comm. **18** (1976) 163.
- 12) G. A. Samara: Ferroelectrics **9** (1975) 209.
- 13) B. Pietrass and E. Hegenbarth: J. Low Temp. Phys. **7** (1972) 201.
- 14) G. A. Samara: Phys. Rev. Lett. **53** (1984) 298.
- 15) D. Rytz, A. Châtelain, and U. T. Höchli: Phys. Rev. **B27** (1983) 6830.

GLASS BONDED CRYSTALLINE BORACITE COMPOSITES
FOR PYROELECTRIC APPLICATIONS

A.S. Bhalla, L.E. Cross and R.E. Newnham

Glass Bonded Crystalline Boracite Composites for Pyroelectric Applications

A. S. BHALLA, L. E. CROSS and R. E. NEWNHAM

Materials Research Laboratory, The Pennsylvania State University
University Park, PA 16802

Polymer and glass bonded crystalline boracite composites are prepared for large area device applications. The glass bonded composites show large pyroelectric figure of merit at room temperature and at 65°C the value becomes larger than that of TGS single crystal (1×10^{-3} C/m²K) measured at room temperature. Larger area boracite composites can be prepared. Such composites are easier to pole, give quite reproducible results and give higher pyroelectric figure of merit (p/K values) than the earlier reported values on Fe-I boracite single crystals.

§1. Introduction

Improper ferroelectrics are potential candidate materials for application in pyroelectric infrared vidicon and point detectors. These materials have large pyroelectric coefficients at room temperature with a strong anomaly at the Curie point, T_c , but low dielectric constant with a weak anomaly at the transition temperature. Thus the high pyroelectric figure of merit p/K (p is the pyroelectric coefficient and K is the dielectric constant) is an attractive feature of such materials at temperatures in the vicinity of T_c .

The boracite family $M_3B_7O_{13}X$, where $M=Fe, Mn, Co, Ni, Cu$, etc. and $X=Cl, Br, I$ shows the most promising pyroelectric properties.

Based on the previous studies,¹⁻³⁾ the room temperature figure of merit of Ni-Br boracite is comparable to that of DTGFB and is probably several times larger near its transition temperature. Fe-I boracite at its Curie temperature (74°C) shows a much higher figure of merit than TGS. Despite these promising characteristics, however, there are some major limitations of using these materials for pyroelectric applications: i) larger sized crystals with homogeneous compositions are very difficult to grow, ii) there is considerable difficulty in poling, iii) ceramic samples could not be prepared. In view of these difficulties, boracite composites appear to be an attractive alternative.

In this paper we report the electrical properties of polymer and glass bonded Fe-I boracite crystalline powder composites.

§2. Experimental and Results

Our preliminary experiments were made using Fe-I boracite crystalline powder. The small crystals were crushed and screened between 100 and 200 mesh. Two kinds of second phase materials were used to prepare the Fe-I boracite composites:

a) Polymer based composite: The fine particles were loaded in a thick epoxy film. The films were polished to a thickness of 100 μm in an approximate 1:3 connectivity pattern (Fig. 1).

b) Glass bonded ceramic: Fine grained (~ 200 mesh) powder of Fe-I boracite was mixed with 2-5 wt% of low melting glass powder and pressed into a mm thick disks. The disks were sintered in order to get a high density com-

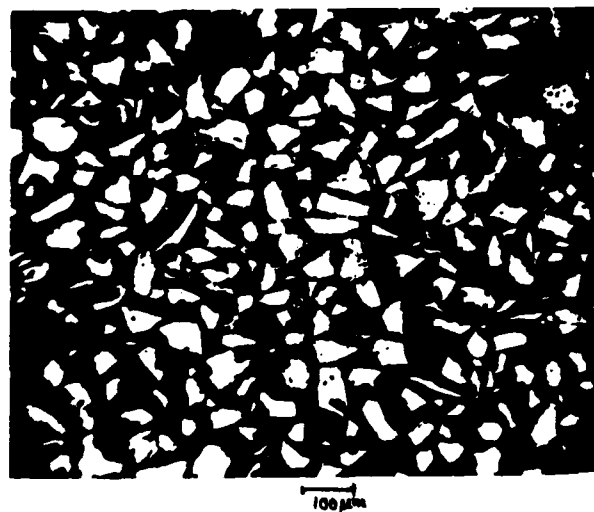


Fig. 1. Fe-I boracite: polymer composite.

posite in 3:3 connectivity pattern.

Composite samples were easy to pole. Polymer boracite composites were poled by an electric field of 10-20 kV/cm applied at various temperature in the range from room temperature to 60°C for 10-20 min. Glass bonded ceramics were poled while cooling the samples through the phase transition with the electric field applied. Dielectric and pyroelectric (by Byer-Roundy and Chynoweth methods) properties were measured in a temperature range from $-150^\circ C$ up through the Curie temperature of Fe-I boracite single crystal and are summarized in the following sections. For comparison, some Fe-I boracite single crystal samples were also selected and the similar measurements repeated on those samples.

2.1 Polymer: boracite composites

Polymer boracite composites contained approximately 50 volume percent of boracite crystals. Pyroelectric response on these samples was measured by the Chynoweth method. The following observations were made on these composites:

(1) In Fe-I boracite composites, a strong pyroelectric signal was observed after poling in a field of 20 kV/cm for two minutes. The signal increased with successive polings at room temperature.

(2) 100% reversal of the pyroelectric signal was observed when the field of 20 kV/cm was applied op-

posite to the direction in the first poling.

(3) On heating the pyroelectric signal increased. Near 60°C the signal was unstable and very sharp spikes were observed at higher temperatures. The spikes may correspond to various transitions occurring in Fe-I boracite particles differing slightly in chemical composition. This is quite possible since it is difficult to obtain chemical homogeneity in single crystals. In our composite samples, the powder used was prepared by grinding several single crystals of Fe-I boracite and polymer and boracite each were in 50 volume percent. Also the boracites have rather high electrical conductivity near the transition and thus the overall conductivity of the composite is increased accordingly.

If Fe-I boracite composites were well behaved at high temperatures, a very high figure of merit could be achieved. In this way, large area composites for pyroelectric vidicon devices could be made without the necessity of growing large single crystals.

(4) Dielectric constant of 10 and typical $\tan \delta < 10^{-2}$ were measured on composites as expected from the two phase mixing rule.

Single crystal of Fe-I boracite gave scattered values of p and K . It was difficult to pole the crystals in many cases. Efficient poling could not be achieved in several crystals. Mechanical fractures and chemical inhomogeneity seemed to be the major problem. In the best crystal, the pyroelectric signals were comparable to those of the fully poled composites at room temperature.

2.2 Glass bonded boracite composites

These composites could be poled fully by electric fields as low as 6-8 kV/cm while cooling the samples through the transition temperature. Compared to composites of several other materials, Fe-I boracite composites poled rather efficiently and thus higher pyroelectric properties could be expected. The samples poled easily, possibly because (i) the dielectric constant of boracite is about the same as that of glass, (ii) boracite has twelve domain orientations ($\langle 110 \rangle$), far more than most ferroelectrics, (iii) fracture during poling process is minimized, (iv) as a result of the smaller particle size, the degree of chemical homogeneity in the crystallites was higher.

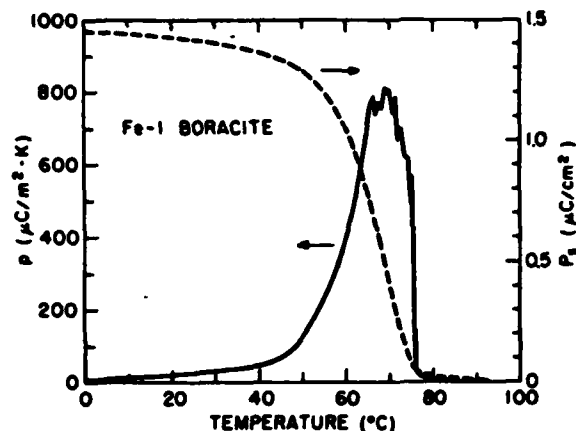
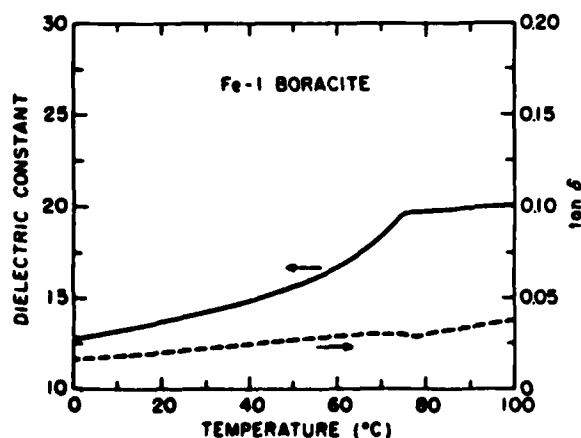


Fig. 3. p vs T and Δp , vs T plots of the Fe-I boracite: glass composites.

Figures 2 and 3 show the temperature dependence of dielectric and pyroelectric properties of the glass: boracite composites. The pyroelectric coefficient at room temperature is comparable to a value obtained on a good Fe-I boracite single crystal.

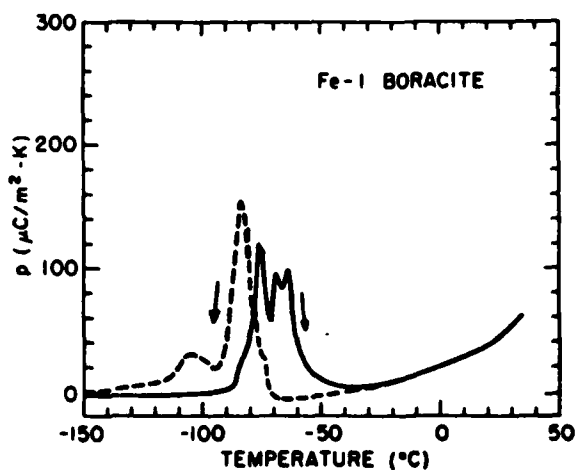
K vs T and $\tan \delta$ vs T plots in the composite are very much similar to those of single crystal indicating no effect of glass as a bonding phase on the dielectric properties.

The reported sharp jump in the K vs T curve at T_c in the single crystal apparently was not observed in the ceramic samples. Probably the composition distribution in the crystallites was the responsible factor in these measurements also.

Typical values of $\tan \delta \sim 10^{-2}$ were obtained on the composites.

The pyroelectric figure of merit p/K of these composites at 60°C is $\sim 2.5 \times 10^{-5} \mu\text{C}/\text{m}^2\text{-K}$ which is more than twice the best values obtained on single crystals of TGS.

Below room temperature, pyroelectric measurements on the composites reproduced the reported low temperature transitions $3\text{m} \times 3\text{m} \times 3\text{mm}^2$ of Fe-I boracite single crystal around -80°C (Fig. 4). Composites samples also



measured resistivity $\sim 10^9 \Omega\text{-m}$ at room temperature. The value changed little when the samples were heated to temperatures near T_c .

In our present studies, samples ≈ 6 mm in diameter were prepared. It is evident that larger area Fe-I boracite as well as the other boracite composite samples with pyroelectric figure of merit equivalent or better than those obtained on corresponding single crystals can be prepared for pyroelectric devices. Detailed results on these composites will be published in the near future.

Acknowledgements

The authors are thankful to Drs. R. W. Whatmore and F. W. Ainger (Plessey Co., U.K.) for providing single crystal samples for this study.

References

- 1) H. Schmid, P. Chan and L. A. Petermann, F. Teufel and M. Mandly: *Ferroelectrics* **13** (1976) 351.
- 2) H. Schmid, P. Genequand, G. Pouilly and P. Chan: *Ferroelectrics* **25** (1980) 539.
- 3) R. W. Whatmore, C. J. Brierley and F. W. Ainger: *Ferroelectrics* **27** (1980) 67.

FERROELASTIC BUBBLES AND PERIODIC GRATINGS IN
NEODYMIUM PENTAPHOSPHATE

S.W. Meeks, D.A. Auld and R.E. Newnham

Ferroelastic Bubbles and Periodic Gratings in Neodymium Pentaphosphate

S. W. MEEKS,* B. A. AULD* and R. E. NEWNHAM†

*Edward L. Ginzton Laboratory Stanford University, Stanford, California 94305, USA

†Materials Research Laboratory, Pennsylvania State University
 University Park, Pennsylvania 16802, USA

Tunable periodic ferroelastic domain wall gratings in neodymium pentaphosphate (NPP) are presented. These arrays have excellent diffraction patterns and may be tuned from periods of 100 microns to 0.5 microns. A free energy theory is presented which predicts the stability of the periodic arrays and their eventual collapse at very short periods. Photographs of ferroelastic bubbles are shown. These elastic bubbles are a newly-discovered domain structure and are the analog to ferromagnetic bubbles. A method of optically nucleating planar domain walls in NPP is presented. This technique may eventually lead to an optical ferroelastic domain wall memory.

§1. Introduction

Neodymium pentaphosphate (NPP) is a monoclinic ferroelastic crystal with two stable states at zero applied stress.^{1,2} NPP is switched between the two strain states by applying an appropriate shear stress. By suitably configuring the spatial pattern of shear stress, periodic domain wall arrays can be injected into the crystal in a systematic and repeatable way, and the periodicity can also be tuned. The nucleation and the tuning process of these periodic arrays is described in ref. 3. Since the abrupt change in physical properties at a ferroelastic domain wall constitutes an optical or acoustic reflecting interface⁴⁻⁶ these new arrays act as diffraction gratings and filters for optics and acoustics. Potential device applications are numerous and exciting. They include: tunable spatial filters, tunable active gratings for lasers, tunable Bragg reflection gratings, and tunable bulk and surface wave acoustic filters. This paper presents these periodic gratings, the newly-discovered ferroelastic bubbles, a free energy theory which describes the physics of the arrays, and an optical technique to inject domain walls.

§2. Discussion

Figure 1 shows a pattern with four periodic ferroelastic arrays simultaneously present in a crystal of NPP. This is a "b" plate of NPP, that is, the "b" direction is out of the paper, the "c" direction is vertical, and the "a" direction is horizontal. Typical dimensions of the "b" plates used in these experiments are 1 mm ("b"-dimension) × 5 mm ("c"-dimension) × 10 mm. The crystal is being viewed between a pair of polarizers. The domains are visible because of the birefringence of NPP. Vertical lines in the figure are planar domain walls perpendicular to the domain walls in the periodic arrays. The horizontal walls are known as "a" type walls and the vertical walls are known as "b" type walls.² These periodic gratings are stable in the absence of any external force. Arrays of approximately 25 micron period have been seen to be stable up to the Curie temperature of 145°C. It is of particular interest to note that these arrays are highly periodic and tunable (see ref. 3), making them excellent candidates for device applications. The longest period array in Fig. 1

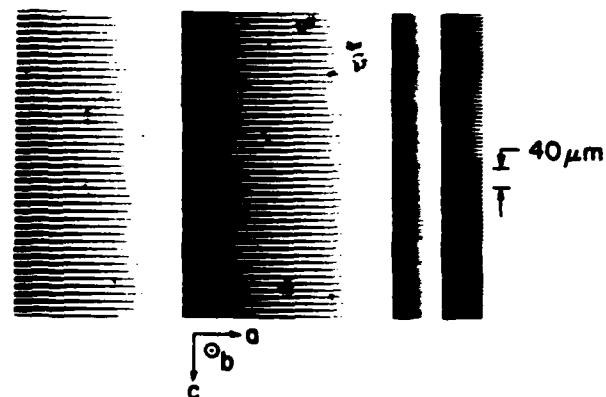


Fig. 1. Periodic arrays in NPP ranging from 20 to 6 micron period.

considerable variety of domain patterns is possible in NPP. Arrays similar to those in Fig. 1 have been reported in the ferroelastic-ferroelectric gadolinium molybdate and in the pure ferroelastic lead phosphate by Flippen and Haas,⁷ who termed them zig-zag domains. Zig-zag domains are also known to occur in ferromagnets.⁸ Figure 2 shows the diffraction pattern of a 58 micron period array in NPP which has been angled-tuned to give a Bragg spot at fifth order. The Bragg spot is the brightest spot on the left of the photograph and the undeflected spot is the next brightest spot which is roughly in the center of the photograph. Because of the anisotropic properties of the NPP crystal, the polarization of the Bragg spot and the central spot are orthogonal. The excellent periodicity of the array can be seen in the quality of the diffraction pattern. The Bragg spot contains 75% of the incident power for this uncoated crystal. An anti-reflection coated crystal would be expected to have a diffraction efficiency greater than 90%. The diffraction pattern in Fig. 2 is a typical transmission diffraction grating. It has, however, the novel feature that the period of the array may be tuned in real time, resulting in a tunable optical spatial filter or tunable Bragg grating with period varying from 100 microns to less than 0.5 microns. These periodic arrays can be rapidly tuned. The period of an NPP array has been tuned from 100 microns to about 4 microns in about 100 ms and this is not the maximum

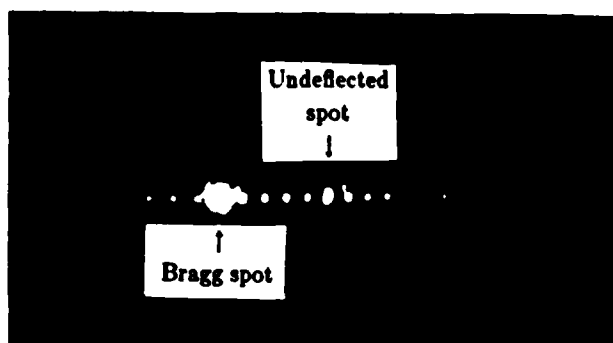


Fig. 2. Bragg diffraction in a 58 micron period NPP array.

that the Bragg spot may be switched from 5th order on the left to 5th order on the right by switching the polarization of the incident light. This is due to the nature of the transmission of light through the domain walls. This feature will allow one to make a switchable beam splitter. The power in the Bragg spot may be switched from the plus 5th order (or whatever order Bragg enhancement has been chosen to occur at) to the minus 5th order as rapidly as one can switch the polarization of the incident light.

NPP is both a ferroelastic as well as a high gain and high Nd^{+3} concentration laser material.⁹⁻¹¹ The combination of a tunable internal grating with a good infrared laser material is unique and lends itself to novel laser and active filter schemes. A tunable active grating laser based upon the above described domain gratings is currently under development.

A free energy theory has been developed to explain the stability of the periodic structures shown in Fig. 1. The total energy consists of three terms: the wall energy, the strain energy (trapped in the tips of the zig-zags), and the attractive energy between walls.¹² The coefficients of these energy terms are chosen so that they have the proper symmetry with respect to the symmetry of the periodic structure. The resulting free energy expression with four free parameters is then fit (in the least squares sense) to experimental data. The resulting fitted free energy versus domain wall density is shown in Fig. 3. The fitting was done with data taken from the periodic grating plus one "b"-type wall structure shown in Fig. 3. The varying parameter in Fig. 3 is the width W of the array. The free energy curves clearly show a metastable equilibrium at various wall densities depending upon width. The energy difference between the equilibrium point and the high point of the energy barrier (the activation energy) is clearly a function of the width. When the width of the array reaches about 66 microns (corresponding to a wall density of 485 walls/mm) the metastable equilibrium is no longer present. Thus the structure is no longer stable and it will collapse into a single "b"-type wall. The collapse is due to the attractive energy overwhelming the other energy terms. This effect is both predicted by theory and observed experimentally. Thus the shortest period for the structure in Fig. 1 is about 4 microns. The structures shown in Fig. 1 (with a periodic array trapped between two "b"-type walls) have been seen to exist down to 0.5 micron period. The difference between the structures may be due to the interaction of

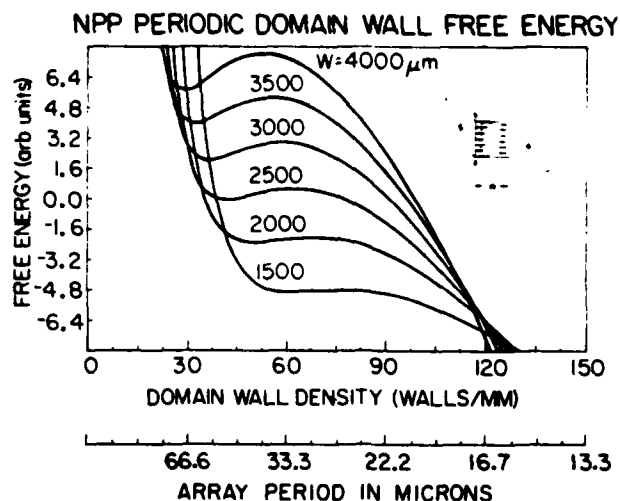


Fig. 3. Free energy of a NPP array versus domain wall density and array period.

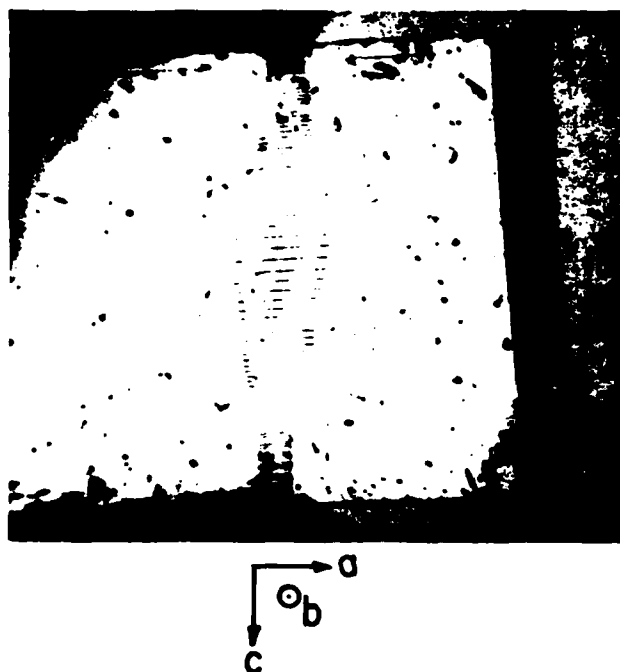


Fig. 4. Array of ferroelastic bubbles in NPP.

the additional "b"-type wall with the strain energy trapped in the tips of the zig-zags.

Figure 4 shows another type of domain pattern which can be produced in NPP. The pattern consists of an aperiodic array of lenticular domains, or, as we prefer to call them, ferroelastic bubbles. These elastic bubbles are analogous to the well-known ferromagnetic bubbles in magnetic garnets. They have a lenticular cross section of uniform strain, corresponding to one of the shear strain states, which extends through the thickness (the "b" direction in this case) of the crystal. The bubbles are lenticular because the energies of the allowed wall directions are very anisotropic. Thus the bubbles form with a maximum of the low energy wall ("a"-type) and a minimum of the high energy wall ("b"-type). Elastic bubbles share a number of properties with magnetic bubbles: they are a closed region of one (strain) polarization state which ex-

tends through the thickness of the crystal; bubbles of the same polarization state repel one another; they exist only in the presence of an external (stress) field; and they may be moved by application of an external (stress) field. The bubbles are being produced by a shear couple which can be seen at the top and bottom of Fig. 4. There are many lenticular bubbles in Fig. 4 which vary in spacing and lateral width because of the variation in stress throughout the crystal. The lateral dimensions of these elastic bubbles range from an estimated 500 microns to 100 microns. The thin dimension of the bubbles ranges from about 10 microns to 1 micron.

The domain patterns previously discussed were created by applying quasi-static mechanical shear stresses to a NPP crystal. Domain patterns can also be created optically in NPP using laser beams. This process is illustrated in Fig. 5. Thermal stresses set up by the localized heating of a focused laser beam cause blade domains to nucleate and grow as the surrounding area restrains thermal expansion. The threshold intensity for this process is about 20 kW/cm² for a 1 mm thick crystal. Near the heated portion of the crystal, the stresses are very large but it is difficult to nucleate twins (domains) inside a ferroelastic crystal. Twinning generally begins near the edge of the crystal where the thermal stresses are tangential (hoop) in orientation. These hoop stresses place the outer portions of the crystal in tension, leading to twin nucleation in the upper right and lower left quadrants of the "b" plate of NPP in Fig. 5. Hoop stresses in the $[101]$ direction favor twinning, but those in the $[\bar{1}01]$ do not. Blade-like twins begin at the edges and grow into the crystal parallel to $[100]$, eventually coalescing to a pair of planar "a"-type walls. Curved twin boundaries straighten out to lower the elastic wall energy. Minimum wall energy occurs for (001) wall orientation ("a"-type wall) where structures of the two twin states are well matched.²⁾

Laser-induced twinning has been observed previously in ferroelastic-ferroelectric gadolinium molybdate (GMO)¹³⁾ and ferrobielastic quartz.¹⁴⁾ However, the twins were much more difficult to induce in these materials,

and even more difficult to control. The laser-induced twinning in NPP appears to be far more useful than quartz or GMO for three reasons: (1) Only low beam intensities are required because the coercive stress²⁾ is much lower, (2) one domain wall orientation ("a"-type) is highly preferred, so that only a single family of stripes are produced, and (3) the domains can be moved about because of their high mobility. The stress required to initiate domain wall movement in NPP is two orders of magnitude less than that required in GMO.²⁾

The optical injection of domain walls is exciting because it opens the possibility of optically writing an optical interference pattern onto a crystal of NPP. The energy required to write a domain pattern could be greatly reduced by using a thin plate of NPP (50 microns or so) and writing with a laser tuned to one of the absorption lines of NPP where the absorption is extremely strong.¹⁰⁾ The pattern may be erased by mechanically stressing the crystal or by rotating the crystal by 180° about the "a" crystal axis and then reapplying the same optical pattern. The rotation about the "a" axis will reverse the direction of the stresses and hence erase the pattern.

This paper has presented tunable stable periodic ferroelastic arrays in NPP. These arrays have excellent diffraction patterns and should find application as tunable active gratings, tunable spatial filters, tunable acoustic filters, optical domain wall memories, and optical modulators. A new type of domain structure, namely the ferroelastic bubble, has been discovered. Ferroelastic bubbles are the analog of the well-known ferromagnetic bubbles.

Acknowledgements

This work was supported by the Office of Naval Research, and the NSF-CMR program through the Center for Materials Research at Stanford University.

References

- 1) J. Budin, A. Milatos-Roufos, N. D. Chinh and G. Le Roux: *J. Appl. Phys.* **46** (1975) 2867.
- 2) H. P. Weber, B. C. Tofield and P. F. Liao: *Phys. Rev. B* **11** (1975) 1152.
- 3) S. W. Meeks and B. A. Auld: *Appl. Phys. Lett.* **47** (1985) 102.
- 4) S. W. Meeks, B. A. Auld, P. Maccagno and A. Miller: *Ferroelectrics* **50** (1983) 245.
- 5) S. W. Meeks and B. A. Auld: *Proc. of the Ultrasonics Symposium*, Atlanta, Georgia (1983) p. 535.
- 6) T. Tsukamoto, J. Hatano and H. Futama: *J. Phys. Soc. Japan* **51** (1982) 3948.
- 7) R. B. Flippen and C. W. Haas: *Solid State Commun.* **13** (1973) 1207.
- 8) S. Hamzaoui, M. Labrune and I. B. Puchalska: *Appl. Phys. Lett.* **45** (1984) 1246.
- 9) G. Huber, W. W. Kruhler, W. Bludau and H. G. Danielmeyer: *J. Appl. Phys.* **46** (1975) 3580.
- 10) H. G. Danielmeyer and H. P. Weber: *IEEE J. Quant. Electron.* **QE-8** (1972) 805.
- 11) T. C. Damen, H. P. Weber and B. C. Tofield: *Appl. Phys. Lett.* **23** (1973) 519.
- 12) J. Bornarel and J-F. Legrand: *Ferroelectrics* **39** (1981) 1127.
- 13) R. F. Novak, T. L. Anderson and R. E. Newnham: *J. Appl. Cryst.* **10** (1977) 349.
- 14) T. L. Anderson, R. E. Newnham, L. E. Cross and J. W. Laughner: *Phys. Stat. Solidi (a)* **37** (1976) 235.

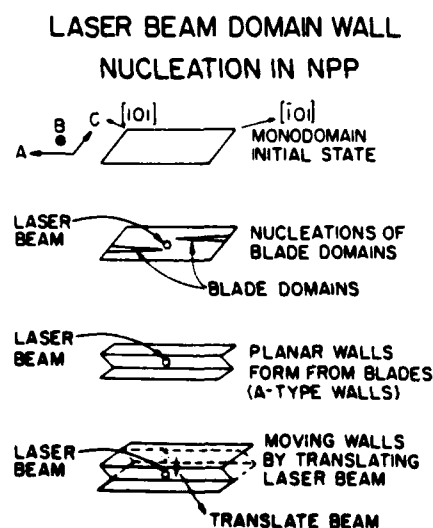


Fig. 5. Laser beam domain wall nucleation in NPP

LOW TEMPERATURE DIELECTRIC PROPERTIES
OF SrTiO_3 GLASS-CERAMICS

S.L. Swartz, A.S. Bhalla and L.E. Cross

Low Temperature Dielectric Properties of SrTiO₃ Glass-Ceramics

S. L. SWARTZ, A. S. BHALLA and L. E. CROSS

Materials Research Laboratory
 The Pennsylvania State University
 University Park, PA 16802, USA

The low temperature dielectric properties of a particular SrTiO₃-containing glass-ceramic have been investigated. This glass-ceramic exhibited a dispersive dielectric constant peak over the temperature range of 85 to 100 K and relaxation-type loss peaks at temperatures near 50 and 100 K. Arrhenius plots of dielectric loss data gave activation energies of 0.054 and 0.17 eV for the lower (50 K) and higher (100 K) temperature loss mechanisms. The higher temperature loss mechanism was further analyzed by the Cole-Cole method, and a relaxation strength ($K_1 - K_\infty$) of 41 was calculated. The dielectric constant peak was related to the higher temperature loss mechanism, and it was proposed that ferroic phenomena were responsible.

§1. Introduction

Strontium titanate glass-ceramics have been utilized for several years as cryogenic capacitive temperatures sensors.¹⁾ Their usefulness is based on a peak in the dielectric constant at a temperature near 77 K. However, the nature of this dielectric constant peak has not been clearly defined. Lawless²⁾ attributed the dielectric constant peaks to an anti-ferroelectric transition in the SrTiO₃ phase, while Siegwirth³⁾ suggested that they were caused by the relaxation of electret (defect-dipole) states in the SrTiO₃, although definitive dielectric loss data supporting these proposed mechanisms were not presented. In this paper, low temperature dielectric constant and loss measurements of a similar SrTiO₃ glass-ceramics will be reported.

§2. Glass-Ceramic Preparation and Characterization

Glass-ceramics were derived from a glass with a nominal composition consisting of 65 wt% SrTiO₃, 23 wt% SiO₂, and 12 wt% Al₂O₃, prepared by melting at 1650°C for two hours and annealing at 760°C. The crystallization and dielectric properties of these glass-ceramics have recently been investigated.⁴⁾ The dielectric measurements to be described in this paper were performed on glass-ceramic disks crystallized isothermally for 16 hours at 1100°C. Generally, in this glass-ceramic, perovskite SrTiO₃ was the primary crystalline phase. Secondary crystalline phases were anorthite SrAl₂Si₂O₈ and anatase TiO₂. The microstructure of this glass-ceramic consisted of sub-micron dispersed SrTiO₃ crystallites and large acicular anatase crystals of up to 80 microns in length. The matrix consisted of anorthite SrAl₂Si₂O₈ and a residual glass containing silica and alumina.

§3. Dielectric Measurements

The dielectric constant versus temperature at several frequencies between 10 and 1000 kHz appears in Fig. 1. The dielectric constant peak was extremely frequency-dependent. The magnitude of the dielectric constant peak varied from 204 at 10 kHz to 191 at 1 MHz, and the peak occurred near 100 K for frequencies between 10 and

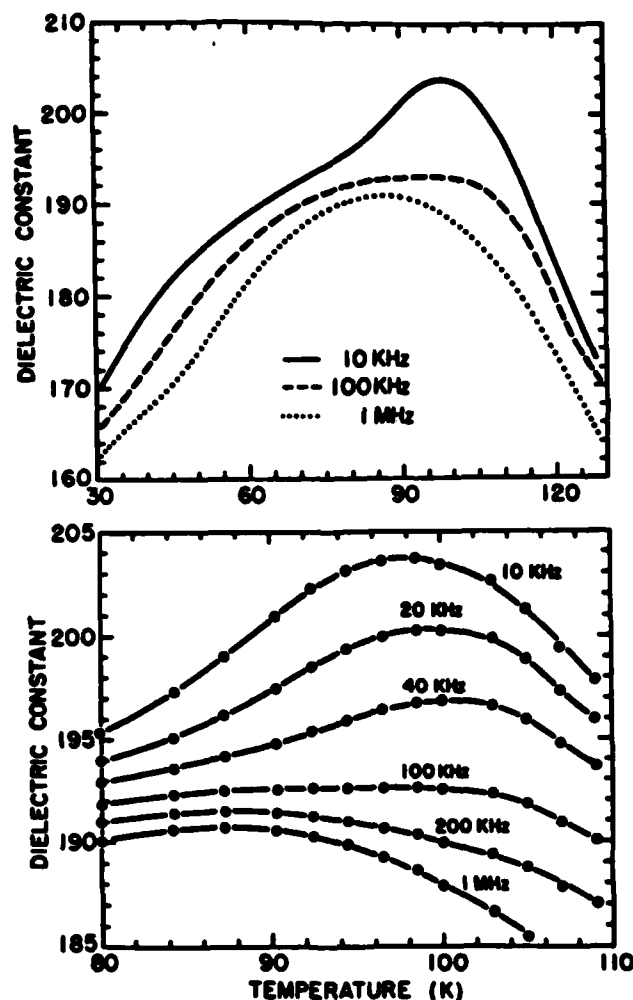


Fig. 1. Dielectric constant versus temperature for various measurement frequencies.

100 kHz, and at 85 K for a frequency of 1 MHz. The dispersive nature of the dielectric constant peaks suggested dielectric loss phenomena.

The low temperature dielectric loss behavior of this sample was dominated by two sets of relaxation-type dielectric loss peaks at temperatures near 50 and 100 K. Dielectric loss spectra (dissipation factor versus

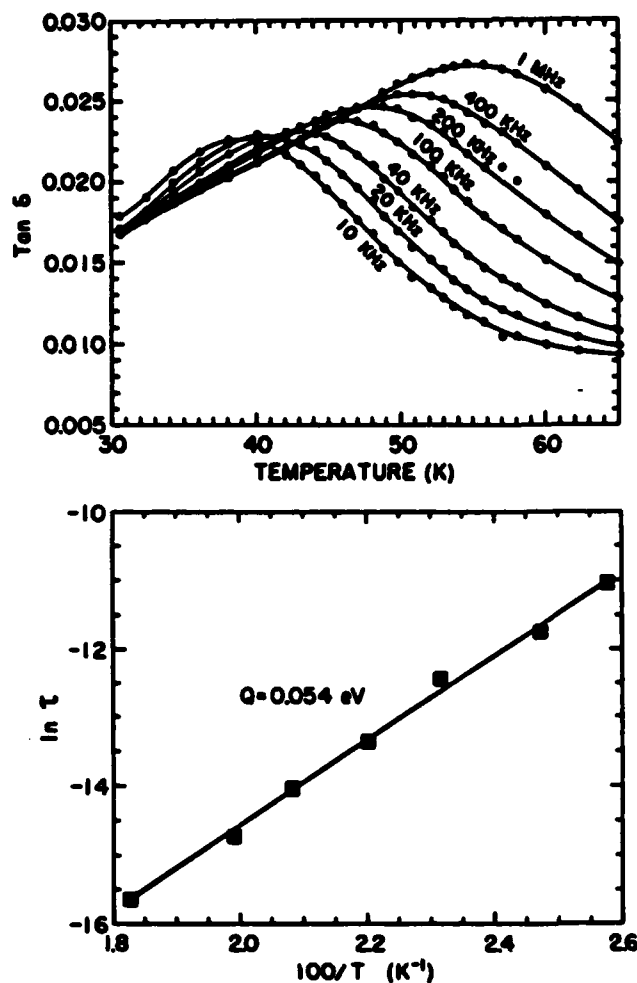


Fig. 2. Dielectric loss spectra and corresponding Arrhenius plot for the lower temperature loss mechanism.

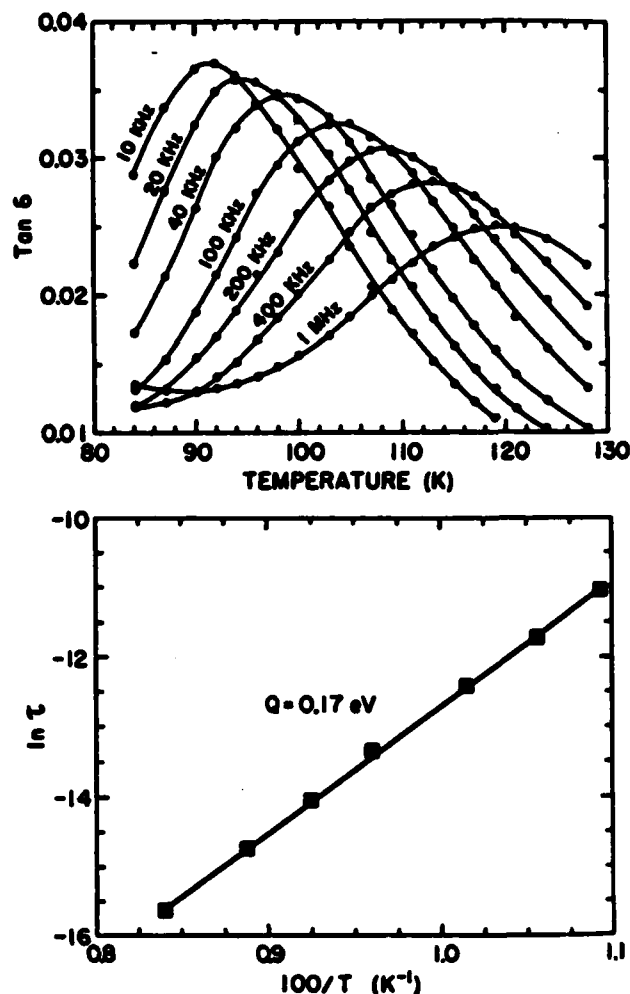


Fig. 3. Dielectric loss spectra and corresponding Arrhenius plot for the higher temperature loss mechanism.

temperature at seven frequencies between 10 and 100 kHz) in the temperature ranges of the two loss mechanisms appear along with the corresponding Arrhenius plots, in Figs. 2 and 3. For both of the dielectric loss mechanisms, the loss peak temperature increased with frequency, from about 38 to 52 K and 85 to 100 K, over the frequency range of 10 to 1000 kHz. The activation energies, calculated from the Arrhenius plots, were 0.054 and 0.17 eV for the lower (50 K) and higher (100 K) temperature loss mechanisms, respectively. The magnitude of the higher temperature loss peak decreased and the peak broadened with increasing frequency, while the magnitude of the lower temperature loss peak increased and the peak sharpened with increasing frequency.

Very precise dielectric measurements were made over the frequency range of 0.1 to 10 kHz at various temperatures, chosen so that the higher temperature dielectric loss mechanism could be studied. Dielectric data are presented as plots of dissipation factor versus log frequency at a series of temperatures between 78 and 84 K in Fig. 4. Dielectric loss peaks with frequency were observed at each of these temperatures, and the frequency of the loss peak increased with temperature, as expected for a relaxation-type loss mechanism.

The low frequency dielectric data were further analyzed

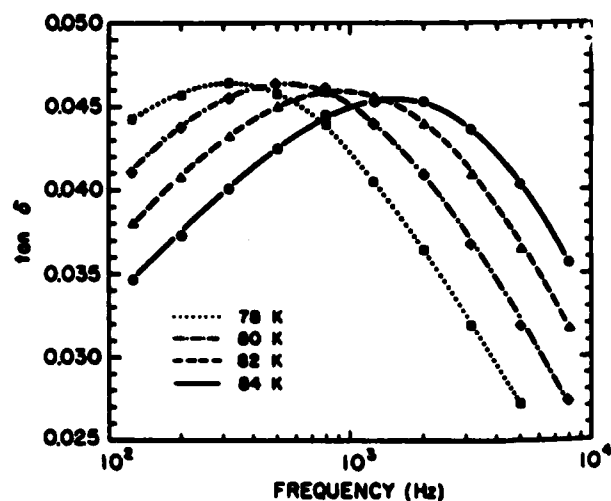


Fig. 4. Dissipation factor versus log frequency at various temperatures.

by the Cole-Cole method. A Cole-Cole plot, constructed from dielectric data taken at 82 K, is presented in Fig. 5; the line between the K_{∞} intercept and the origin of the arc is shown, defining the tilt angle. The effect of temperature on the relaxation process was determined by

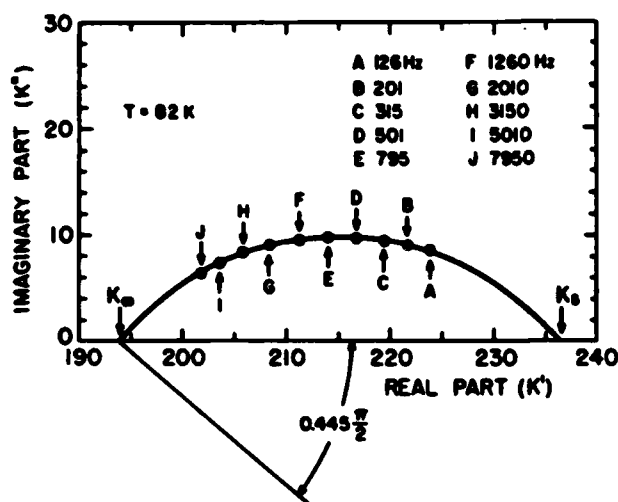


Fig. 5. Cole-Cole plot constructed from dielectric data taken at 82 K, corresponding to the higher temperature loss mechanism.

performing the Cole-Cole analysis on the dielectric data taken at temperatures of 75, 78, 80, 82, and 84 K. The data indicated a relaxation strength ($K_\infty - K_0$) of about 41, and that K_0 (the value of the dielectric constant without the contribution of the loss mechanism) decreased from 196.3 to 192.6 as the temperature was increased from 75 to 84 K. The latter observation was in contradiction with the original data, in which the dielectric constant increased with temperature at constant frequency in this range. This can be explained by the shift in the relative positions of the data points along the Cole-Cole arc with increasing temperature, as shown in Fig. 6 for a series of Cole-Cole arcs for five temperatures between 75 and 84 K. At 75 K, the dispersion corresponding to this loss mechanism occurred on the high frequency portion of the arc. As the temperature was increased, the dispersion shifted to lower frequencies, thus increasing the contribution of the loss mechanism to the dielectric constant. From these data it can be concluded that the anomalous shape of the dielectric constant peak was related to the higher temperature loss mechanism.

§4. Discussion

From the above data, and in data not presented in this paper, it was clear that the dielectric constant peaks were the result of an interaction of the SrTiO₃ phase with the matrix. The defect-dipole mechanism proposed by Siegwarth³⁾ is immediately ruled out for two reasons: 1)

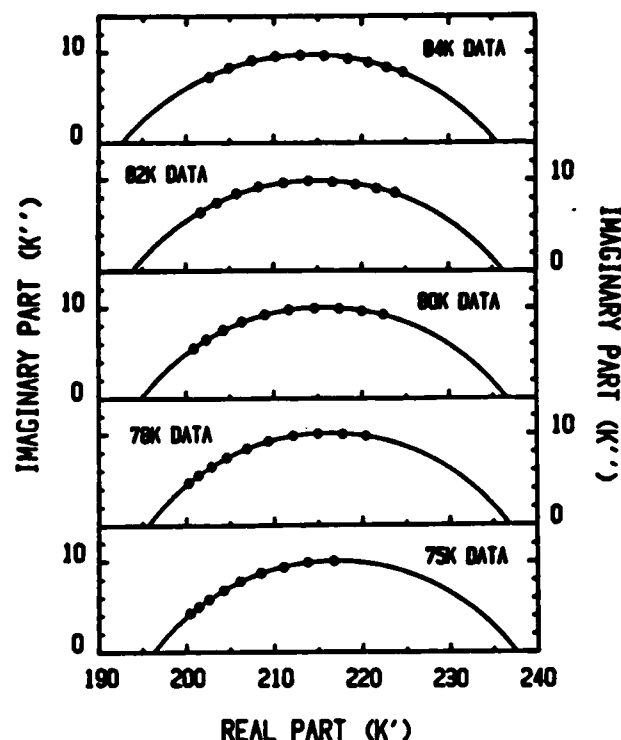


Fig. 6. Comparison of Cole-Cole arcs, constructed from dielectric data taken at various temperatures between 75 and 84 K.

the dielectric constant peaks would not have been as sensitive to the nature of the matrix; and 2) the decrease of the dielectric constant with an applied electric field of 20 kV/cm was much larger than the relaxation strength ($K_\infty - K_0$). Some sort of ferroic phenomenon was suggested by the data. The higher temperature loss mechanism was consistent with ferroic domain effects, and the temperature of this loss mechanism was close to the known ferroelastic transition at 110 K in SrTiO₃. The complicated stresses exerted by the matrix on the SrTiO₃ as the glass-ceramic was cooled below the 110 K transition of SrTiO₃ could have resulted in a number of possible ferroic interactions. The exact natures of these phenomena are still under investigation.

References

- 1) W. N. Lawless and U. S. Patent No. 3, 649, 891 (1972).
- 2) W. N. Lawless, *Ferroelectrics* 7 (1974) 379-381.
- 3) J. D. Siegwarth, *J. Appl. Phys.* 48 (1) (1977) 1-4.
- 4) S. L. Swartz, Ph. D. Thesis, The Pennsylvania State University (1985).

BASIC DISTRIBUTION LIST

Technical and Summary Reports

<u>Organization</u>	<u>Copies</u>	<u>Organization</u>	<u>Copies</u>
Defense Documentation Center Cameron Station Alexandria, VA 22314	12	Naval Air Propulsion Test Center Trenton, NJ 08628 ATTN: Library	1
Office of Naval Research Department of the Navy 800 N. Quincy Street Arlington, VA 22217 ATTN: Code 471 Code 470	1 1	Naval Construction Battalion Civil Engineering Laboratory Port Hueneme, CA 93043 ATTN: Materials Division	1
Commanding Officer Office of Naval Research Branch Office Building 114, Section D 666 Summer Street Boston, MA 02210	1	Naval Electronics Laboratory San Diego, CA 92152 ATTN: Electron Materials Sciences Division	1
Commanding Officer Office of Naval Research Branch Office 536 South Clark Street Chicago, IL 60605	1	Naval Missile Center Materials Consultant Code 3312-1 Point Mugu, CA 92041	1
Office of Naval Research San Francisco Area Office One Hallidie Plaza Suite 601 San Francisco, CA 94102	1	Commanding Officer Naval Surface Weapons Center White Oak Laboratory Silver Spring, MD 10910 ATTN: Library	1
Naval Research Laboratory Washington, DC 20375 ATTN: Codes 6000 6100 6300 2627	1 1 1 1	Commander David W. Taylor Naval Ship Research and Development Center Bethesda, MD 10084	1
Naval Air Development Center Code 606 Warminster, PA 18974 ATTN: Mr. F.S. Williams	1	Naval Oceans Systems Center San Diego, CA 92132 ATTN: Library	1
Naval Weapons Center China Lake, CA 93555 ATTN: Library	1	Naval Underwater System Center Newport, RI 02840 ATTN: Library	1
		Naval Postgraduate School Monterey, CA 93940 ATTN: Mechanical Engineering Dept.	1

<u>Organization</u>	<u>Copies</u>	<u>Organization</u>	<u>Copies</u>
Naval Air Systems Command Washington, DC 20360 ATTN: Codes 52031 52032	1 1	NASA Lewis Research Center 21000 Brookpark Road Cleveland, OH 44135 ATTN: Library	1
Naval Sea System Command Washington, DC 20362 ATTN: Code 05R	1	National Bureau of Standards Washington, DC 20234 ATTN: Metals Science and Standards Division	1
Naval Facilities Engineering Command Alexandria, VA 22331 ATTN: Code 03	1	Ceramics Glass and Solid State Science Division Fracture and Deformation Division	1 1 1
Scientific Advisor Commandant of the Marine Corps Washington, DC 20380 ATTN: Code AX	1	Director Applied Physics Laboratory University of Washington 1013 Northeast Fortthieth Street Seattle, WA 98105	1
Army Research Office P.O. Box 12211 Triangle Park, NC 27709 ATTN: Metallurgy and Ceramics Program	1	Defense Metals and Ceramics Information Center Battelle Memorial Institute 505 King Avenue Columbus, OH 43201	1
Army Materials and Mechanics Research Center Watertown, MA 02172 ATTN: Research Programs Office	1	Metals and Ceramics Division Oak Ridge National Laboratory P.O. Box X Oak Ridge, TN 37380	1
Air Force Office of Scientific Research/NE Building 410 Bolling Air Force Base Washington, DC 20332 ATTN: Chemical Science Directorate Electronics and Materials Sciences Directorate	1 1	Los Alamos Scientific Laboratory P.O. Box 1663 Los Alamos, NM 87544 ATTN: Report Librarian	1
Air Force Materials Laboratory Wright-Patterson AFB Dayton, OH 45433	1	Argonne National Laboratory Metallurgy Division P.O. Box 229 Lemont, IL 60439	1
Library Building 50, Room 134 Lawrence Radiation Laboratory Berkeley, CA 94720	1	Brookhaven National Laboratory Technical Information Division Upton, Long Island New York 11973 ATTN: Research Library	1
NASA Headquarters Washington, DC 20546 ATTN: Code RER	1	Office of Naval Research Branch Office 1030 East Green Street Pasadena, CA 91106	1

SUPPLEMENTARY DISTRIBUTION LIST A

Electronic, Magnetic, and Optical Ceramics

Advanced Research Project Agency
Materials Science Director
1400 Wilson Boulevard
Arlington, VA 22209

Dr. Don Berlincourt
Channel products
16722 Park Circle Drive W.
Chagrin Falls, OH 44022

Dr. J.V. Biggers
The Pennsylvania State University
Materials Research Laboratory
University Park, PA 16802

Mr. George Boyer
Sensor Systems Program
Office of Naval Research
Code 222
Arlington, VA 22217

Dr. Dean Buckner
Piezo Products Division
Gulton Industries
P.O. Box 4300
Fullerton, CA 92634

Dr. Robert Callahan
Channel Products
839 Ward Drive
Box 3680
Santa Barbara, CA 93105

Professor L.E. Cross
Materials Research Laboratory
The Pennsylvania State University
University Park, PA 16802

Mr. N. Coda
Vice President for Engineering
Erie Technological Products
West College Avenue
State College, PA 16801

Dr. N. Perrone
Code 474
Office of Naval Research
800 N. Quincy Street
Arlington, VA 22217

Dr. Gene Haertling
Motorola Corporation
3434 Vassar, NE
Albuquerque, NE 87107

Dr. W.B. Harrison
Honeywell Ceramics Center
1885 Douglas Drive
Golden Valley, MN 55422

Dr. C.M. Stickley, V.P.
The BDM Corporation
7915 Jones Branch Drive
McLean, VA 22102

Dr. L.L. Hench
Department of Metallurgy
University of Florida
Gainesville, FL 32603

Dr. B.F. Rider
Rockwell International
400 Collins Road NE
Cedar Rapids, IA 52406

Dr. F. Robert Hill
Marine Resources
755 Highway 17 and 92
Fern Park, FL 32730

Dr. B.G. Koepke
Honeywell, Inc.
Corporate Research Center
10701 Lyndale Avenue South
Bloomington, MN 55420

Dr. R. Lapetina
Edo Western Corporation
2645 South 300 West
Salt Lake City, UT 84115

Mr. C. LeBlanc
Naval Underwater Systems Center
TD 121
Newport, RI 02840

Professor R. Roy
Materials Research Laboratory
The Pennsylvania State University
University Park, PA 16802

Dr. Frank Recny
General Electric
Court Street
Plant Building C
Box 1122
Syracuse, NY 13201

Dr. J.H. Rosolowski
General Electric Company
Research and Development Center
P.O. Box 8
Schenectady, NY 02301

Dr. P.L. Smith
Naval Research Laboratory
Code 6361
Washington, DC 20375

Dr. R.W. Tizme
Naval Research Laboratory
Code 8275
Underwater Sound Reference Division
P.O. Box 8337
Orlando, FL 32806

Dr. Charles C. Walker
Naval Sea Systems Command
National Center #3
2531 Jefferson Davis Highway
Arlington, VA 20390

Dr. Paul D. Wilcox
Sandia Laboratories
Division 2521
Albuquerque, NM 87115

The State University of New York
at Alfred
Materials Science Division
Alfred, NY 14802

Dr. R. Rice
Naval Research Laboratory
Code 6360

Dr. David C. Hill
Member, Technical Staff
Texas Instruments, Inc.
Attleboro, MA 02703

Dr. S.K. Kurtz, V.P.
Clairol, Inc.
2 Blachley Road
Stamford, CT 06902

Dr. N. Tallan
AFML Wright-Patterson AFB
Dayton, OH 45433

Dr. H.E. Bennett
Naval Weapons Center
Code 3818
China Lake, CA 93555

Dr. Michael Bell
Inorganic Materials Division
National Bureau of Standards
Washington, DC 20234

Dr. R. Bratton
Westinghouse Research Laboratory
Pittsburgh, PA 15235

Dr. Joe Dougherty, Dir. Eng.
Gulton Industries
212 Durham Avenue
Metuchen, NJ 08840

Dr. James Pappis
Raytheon Co.
Research Division
28 Seyon Street
Waltham, MA 02154

Dr. Perry A. Miles
Raytheon Co., Res. Div.
28 Seyon Street
Waltham, MA 02154

Dr. P.E.D. Morgan
Rockwell Science Center
1049 Camino Dos Rios
P.O. Box 1085
Thousand Oaks, CA 91360

Dr. G. Ewell
MS6-D163
Hughes Aircraft Company
Centinela and Teale Streets
Culver City, CA 90230

Dr. George W. Taylor
Princeton Resources, Inc.
P.O. Box 211
Princeton, NJ 08540

Mr. John J. Thiermann
Physics International
2700 Merced Street
San Leandro, CA 94577

Dr. Herb Moss
RCA Laboratories
Princeton, NJ 08540

Dr. R.E. Newnham
Materials Research Laboratory
The Pennsylvania State University
University Park, PA 16802

Dr. Charles S. Sahagian, Chief
EM Technology Branch, SSS Division
HQ Rome Air Dev. Center (AFSC)
Deputy for Electronic Technology
Hanscom AFB, MA 01731

Dr. J. Smith
GTE Sylvania
100 Endicott Street
Danvers, MA 01923

Dr. Wallace A. Smith
North American Philips Laboratories
345 Scarborough Road
Briarcliff Manor, NY 10510

Mr. Raymond E. Sparks
Technology Library R220
Delco Electronics Division/GMC
P.O. Box 1104
Kokomo, IN 46901

Dr. Manfred Kahn
Senior Scientist, Prod. Dev.
AVX Ceramics
Myrtle Beach, SC 29577

Mr. G. Goodman, Manager
Corporation of Applied Research Group
Globe-Union, Inc.
5757 North Green Bay Avenue
Milwaukee, WI 53201

Dr. A.E. Clark
Naval Surface Weapons Center
White Oak Laboratory
Silver Spring, MD 20910

Director
Applied Research Laboratory
The Pennsylvania State University
University Park, PA 16802

Dr. D. Carson
Code 7122
Naval Ocean Systems Center
San Diego, CA 92152

Dr. C. Hicks
Code 631
Naval Ocean Systems Center
San Diego, CA 92152

Dr. R. Smith
Code 7122
Naval Ocean Systems Center
San Diego, CA 92152

Professor R. Buchanan
Department of Ceramic Eng.
University of Illinois
Urbana, IL 61801

Professor B.A. Auld
Stanford University
W.W. Hansen Laboratories
of Physics
Stanford, CA 94306

Dr. S. Musikant
General Electric Co.
3188 Chestnut Street
Philadelphia, PA 19101

Dr. A. Gentile
Hughes Research Labs
3011 Malibu Canyon Road

Dr. J. Harrington
Hughes Res. Labs.
3011 Malibu Canyon Road
Malibu, CA 90265

Professor G. Kino
Stanford University
Stanford, CA 94305

Dr. Gordon Martin
2627 Burgener
San Diego, CA 92110

Deborah Graves
Ceramic Engineer
Endevco
Rancho Vie Jo Road
San Juan Capistrano, CA 92675

Army Research Office
Box CM, Duke Station
ATTN: Met. and Ceram. Div.
Durham, NC 17706

National Bureau of Standards
Inorganic Matls. Division
Washington, DC 20234

National Bureau of Standards
Metallurgy Division
Washington, DC 20234

Naval Air Systems Command
Code 320
Washington, DC 20360

Pacific Missile Test Center
Materials Consultant
Code 4121
Pt. Mugu, CA 93042

Naval Research Lab
Code 6400
Washington, DC 20390

Naval Sea System Command
Code 035
Washington, DC 20362

Naval Ship Engr. Center
Code 6101, CTR BG #2
3700 East-West Highway
Prince Georges Plaza
Hyattsville, MD 20782

Office of Naval Research
Department of the Navy
Code 102
Arlington, VA 22217

Dr. G. Bansal
Battelle Laboratories
505 King Avenue
Columbus, OH 43201

Dr. F.F. Lange
eRockwell International
P.O. Box 1085
1049 Camino Dos Rios
Thousand Oaks, CA 91360

Dr. G. Denman, Code LPJ
AFML, Wright-Patterson AFB
Dayton, OH 45433

Sheldon Detwiler, Disp. Mgr.
Adv. Technol. Laboratories
13208 Northrup Way
P.O. Box 6639
Bellevue, WA 98007

Dr. W.G.D. Frederick
AFML, Wright-Patterson AFB
Dayton, OH 45433

Dr. P. Giellisse
University of Rhode Island
Kingston, RI 02881

Mr. G. Hayes
Naval Weapons Center-
China Lake, CA 93555

Dr. R.N. Katz
Army Materials and Mechanics
Research Center
Watertown, MA 02171

Dr. P.L. Lall
Office of Naval Research
666 Summer Street
Boston, MA 02210

Dr. P. Land
AFML, Wright-Patterson AFB
Dayton, OH 45433

Dr. Eugene A. Larson, Pres.
Blue River Laboratories
P.O. Box 442
Lewistown, PA 17044

Dr. George Benthien
Naval Ocean Systems Center
Code 212
San Diego, CA 92152

Mr. K. Letson
Redstone Arsenal
Huntsville, AL 35809

Mr. G. Schmitt
AFML, Wright-Patterson AFB
Dayton, OH 45433

Dr. N. Macmillan
Materials Research Laboratory
The Pennsylvania State University
University Park, PA 16802

Mr. F. Markarian
Naval Weapons Center
China Lake, CA 93555

Mr. K.D. McHenry
Honeywell Corp. Tech. Center
10701 Lyndale Avenue South
Bloomington, MN 55420

Dr. R.R. Neurgaonkar
Rockwell International Science Ctr.
1049 Camino Dos Rios
P.O. Box 1085
Thousand Oaks, CA 91360

Norton Company - Library
Industrial Ceramics Division
Worcester, MA 01606

James W. Pell
Manager of Development
Rohe Scientific Corporation
2722 S. Fairview Street
Santa Ana, CA 92704

Dr. R.C. Pohanka
Room 619 Ballston Tower
800 N. Quincy Street
Arlington, VA 22217

Dr. R.A. Queeney
126 Hammond Building
The Pennsylvania State University
University Park, PA 16802

J.J. Rasmussen, Manager
Applied Research Division
Montana Energy and MHD R and D
P.O. Box 3809
Butte, MT 59701

Dr. R. Ruh
AFML, Wright-Patterson AFB
Dayton, OH 45433

James Runt
313 Steidle Bldg.
The Pennsylvania State University
University Park, PA 16802

Dr. T. Sentementes
GTE Sylvania
100 Endicott Street
Danvers, MA 01923

State University of New York
College of Ceramics
Alfred University
ATTN: Library
Alfred, NY 14802

Dr. R.E. Tressler
Ceramic Science Section
226 Steidle Building
The Pennsylvania State Univ.
University Park, PA 16802

Eric Udd
McDonnell Douglas Astron.
5301 Bolsa Avenue
Huntington Beach, CA 92647

Dr. T. Vasilos
AVCO R and Adv. Dev. Div.
201 Lowell Street
Wilmington, MA 01887

Mr. J.D. Walton
Engineering Experiment Station
Georgia Institute of Technol.
Atlanta, GA 30332

Mr. L.B. Weckesser
Applied Physics Laboratory
Johns Hopkins Road
Laurel, MD 20810

Mertan Brooks
Sandia National Labs
Division 7472
P.O. Box 5800
Albuquerque, NM 87185

Darnall P. Burks
Sprague Electric Company
Ceramic Capacitor Operations
P.O. Box 5327
Wichita Falls, TX 76307

Dr. Kim Ritchie
AVX Corporation
P.O. Box 867
Myrtle Beach, SC 29577

Roger T. Dirstine
Unitrode Corporation
580 Pleasant Street
Watertown, MA 02172

END

12-86

DTIC